UAB

Universitat Autònoma de Barcelona

Improved synthesis routes and coating
approaches of anisotropic magnetite
nanoparticles for theranostics

Javier Muro Cruces

Improved synthesis routes and coating approaches of anisotropic magnetite nanoparticles for theranostics

Javier Muro Cruces

Doctoral thesis

Doctoral Program in Materials Science

Supervised by:

Josep Nogués Sanmiquel

Alejandro Gómez Roca

Department of Physics

Faculty of Science

2019

Acknowledgements

I would like to express my gratitude to anyone that ever contributed no matter how to support me in this project, either helping to carry out experiments, to develop new ideas or even just helping to chill out during a break. In first place, I would like to give thanks to my directors, Josep and Álex and to my tutor, Santiago Suriñach, to allow me to do the PhD in such a high quality research centre and, of course, for their supervision. I would also like to thank the technicians belonging to UAB Microscopy Service for their technical support and personal warmth, in particular to Alejandro Sánchez and Emma Rosinyol for being so supportive. Also those belonging to the microscopy service of ICN2 deserve a special mention, like Belén Ballesteros, Marcos Rosado and Francisco Belarre for their highly efficient work and good mood. I would also give thanks to Javier Saiz for helping me to understand better the organic chemistry behind the synthetic processes, apart from, of course, his work as technician; and to Borja Sepúlveda, to help importantly with the optics part of the project. Despite not being physically so close, I would also like to give thanks to our abroad collaborators, like Elvira and Alberto López and, very especially, to Miryana, who, thanks to her continuous feedback, made the project advance astonishingly fast. I would also like to remind that this thesis has been possible thanks to the financial support received from the Spanish Ministry of Economy and Competitiveness. Finally, I want to give thanks to my group mates, to Li, Yue, Pau, Guba and Nour and also to those from other groups like José de la Cruz and José Fran, for making these years much more pleasant and funny, encourage me to carry on and being good friends.

Resumen

Esta tesis aborda la síntesis, caracterización y funcionalización de nanoestructuras magnéticas biocompatibles y anisótropas de óxido de hierro (Fe_3O_4) para su aplicación en diagnóstico biomédico mediante imagen de resonancia magnética (MRI) y uso terapéutico en dos modalidades de hipertermia: magnética y fototérmica. Para ello, se escogieron dos tipos de estructuras: nanocubos y nanorods. Para sintetizar los nanocubos, se probaron varios métodos ya publicados. Sin embargo, ninguno de ellos proporcionó resultados completamente satisfactorios en cuanto a monodispersión de tamaños, reproducibilidad, pureza de fase, alta cristalinidad y definición de forma. Por ello, desarrollamos una estrategia nueva basada en la introducción de oleato de sodio y una mezcla de disolventes que permitían el control de la temperatura de reflujo y la polaridad del medio, lo que además mejoró la estabilidad química del entorno en el que tenía lugar el crecimiento, dando lugar a una síntesis más reproducible. Estos resultados mostraron el éxito a la hora de producir partículas cúbicas en un rango de tamaños muy amplio, con unas excelentes propiedades y reproducibilidad. En cuanto a los nanorods, la síntesis fue especialmente complicada, ya que la estructura cúbica del Fe_3O_4 dificulta la formación de morfologías tan alargadas. De entre todos los procedimientos probados, solo la síntesis solvotermal dio buenos resultados. Para tener un mejor control sobre el tamaño y la relación de aspecto, se desarrollaron nuevas estrategias basadas en el ajuste de la presión y del ratio entre surfactantes. La superficie de las partículas sintetizadas es hidrófoba y por tanto fue necesario modificarla para que éstas pudieran dispersarse en medios biológicos. Además, el recubrimiento de las partículas debería proporcionar grupos funcionales para conjugar biomoléculas y así dirigirlas contra células malignas. Se probaron varias estrategias y los resultados mostraron que, a pesar de que la repulsión electrostática puede ser suficiente para estabilizar nanopartículas pequeñas o no magnéticas, en nuestro caso era necesario combinarla con impedimento estérico para evitar la agregación irreversible. Con este fin, se desarrolló un nuevo procedimiento de encapsulación basado en la formación de bicapas lipídicas que, a pesar de dar resultados prometedores, fue descartado finalmente al tener en cuenta el tiempo que se necesitaría para optimizar completamente todo el protocolo. En su lugar, se usó un procedimiento basado en la encapsulación con copolímeros anfipáticos, que también dio unos resultados excelentes, garantizando la estabilidad coloidal en entornos biológicos. El potencial biomédico de las partículas se evaluó primero como herramienta diagnóstica midiendo el contraste T_2 para resonancia magnética de partículas de diferentes tamaños y formas, resaltando el mayor contraste de las nanopartículas anisótropas respecto a

las isótropas (esferas). En cuanto al uso terapéutico, se evaluó también el potencial de las partículas en hipertermia magnética. Los resultados mostraron una buena capacidad de calentamiento a pesar de las suaves condiciones que usamos en nuestro estudio. Además, gracias a un amplio estudio espectroscópico teórico y experimental, se vio que las nanopartículas de Fe_3O_4 son adecuadas para fototermia, sobre todo en la segunda ventana biológica del infrarrojo cercano (1000-1350 nm). Esta región espectral es especialmente interesante porque permite la aplicación de mayores potencias de irradiación y tiene una mayor penetración en los tejidos humanos. A 1064 nm se consiguieron eficiencias de calentamiento óptico similares a los mejores agentes fototérmicos. Además, se aprovecharon las anisotropías magnética y óptica para medir la temperatura local en tiempo real mediante un método relativamente nuevo. Los experimentos in vitro usando células tumorales HeLa demostraron que las nanopartículas son internalizadas fácilmente y que no son tóxicas para concentraciones inferiores a 4 mM de hierro y que la fototermia usando nanocubos de Fe_3O_4 es una terapia excelente para destruir células tumorales.

Abstract

This thesis tackles the synthesis, characterisation and functionalisation of biocompatible anisotropic iron oxide (Fe_3O_4) magnetic nanostructures for their application in biomedical diagnosis by means of magnetic resonance imaging (MRI) and therapy by two different modalities of hyperthermal therapy: magnetic fluid hyperthermia and photothermia. Two different types of structures were chosen for these purposes: nanocubes and nanorods. Several approaches published in literature were tested to synthesize the nanocubes. However, none of them rendered fully satisfactory results in size monodispersity, reproducibility, phase purity, high crystallinity and well-defined shape. Thus, we developed a new strategy based on the introduction of sodium oleate and a solvent mixture enabling the control of the reflux temperature and the polarity of the medium, which also resulted in an improvement of the chemical stability of the growth environment, leading to a more reproducible synthesis. The results demonstrate the successful synthesis of highly cubic particles in a very broad size range, with excellent properties and reproducibility. Concerning the nanorods, their synthesis was particularly challenging since the cubic crystal structure of Fe_3O_4 complicates the formation of such elongated morphologies. Among all the tested procedures, only the solvothermal synthesis provided good results. To have a better control on the size and aspect ratio new approaches based on adjusting the pressure and surfactants have been developed. The surface of the freshly synthesized particles is hydrophobic and therefore it was necessary to modify the surface to make them dispersible in biological media. In addition, the coating should provide functional groups to attach biomolecules for targeting malignant cells. Several approaches were tested and the results showed that, despite electrostatic repulsion can be enough to stabilize smaller or non-magnetic nanoparticles, in our case it was necessary to combine it also with steric hindrance to avoid irreversible aggregation. For this purpose, a novel procedure based on the formation of a lipid bilayer coating was developed which, despite providing promising results, was eventually discarded considering the time that would be required to fully optimise the protocol. Instead, a procedure based on the coating with amphiphilic copolymers was used, which also provided excellent results, ensuring colloidal stability in biological environments. The biomedical potential of the particles was evaluated first as a diagnostic tool by measuring the MRI T_2 contrast of particles of different sizes and shapes, evidencing the enhanced contrast of anisotropic nanoparticles with respect to isotropic ones (spheres). In terms of therapy, the potential of the particles in terms of magnetic hyperthermia was also evaluated. The results showed the good heating capacity of the particles despite the mild conditions used in our study.

In addition, thanks to a comprehensive theoretical and experimental spectroscopic study, it was established that Fe_3O_4 nanoparticles are suitable for photothermia, particularly in the near infrared second biological window (1000-1350 nm). This spectral range is especially appealing because it allows the application of higher powers and has a deeper penetration in human tissues. At 1064 nm were measured some heating efficiencies similar to the best photothermal agents. In addition, the magnetic and optic anisotropies were exploited for a relatively new approach for *in situ* local temperature sensing. The *in vitro* experiments using HeLa cancerous cells demonstrated that the nanoparticles are easily internalized and are not toxic for concentrations below 4 mM Fe and that photothermia using Fe_3O_4 nanocubes at 1064 nm is an excellent therapy for destroying cancerous cells.

Table of contents

CHAPTER 1: INTRODUCTION

1. NANOTECHNOLOGY AND MAGNETIC NANOSTRUCTURES

1.1 Introduction to the nanoscale

Since 1959 when Richard Feynman gave his seminal lecture, "There is plenty of space at the bottom; An Invitation to Enter a New Field of Physics", the interest for the research in nanoscience and nanotechnology has kept growing continuously. Although the term "nanotechnology" was originally introduced by Norio Taniguchi in 1974, as years passed and the popularity of the term arose, a more specific definition for the word nanotechnology became necessary and eventually in the 90's it was the National Nanotechnology Initiative of United States that defined nanotechnology as "the manipulation of matter with at least one dimension sized from 1 to 100 nanometers".[1] This criterion is so specific about size because generally it is considered that when one of the dimensions of the material is smaller than 100 nm, this dimension is "lost" and thus nanomaterials can be named as two-dimensional (e.g., thin films), one-dimensional (*i.e.*, nanowires) and zero-dimensional materials (like nanoparticles). A characteristic feature of nanomaterials is that due to their small size, the behaviour can be quite different from that of the bulk material, lying somewhere between the macroscopic and atomic realms. Consequently, this allows new ways of intentionally tuning the properties for specific applications. Some of these differences are somehow easily inferable and are merely an extrapolation of the macroscopic properties. For example, nanomaterials can have a very large surface area because as the particle size decreases, the surface to volume ratio increases (see **Fig. 1**).
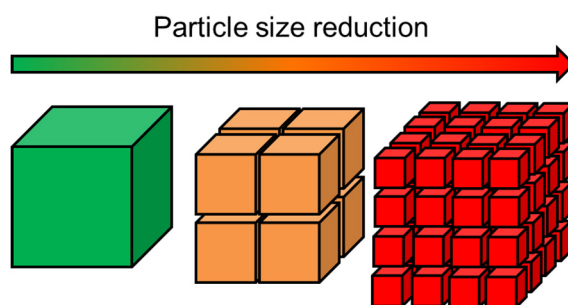
Figure 1. Effect of the particle size reduction on the specific surface area of the nanostructures. Although in the three cases the volume keeps constant, as the particle size decreases, the surface increases because more facets are exposed. In the case of small cubes (in red), whose edge is 4 times smaller than the large green particle, the surface is 64 times larger.

In fact, as the size decreases the surface atom number of a nanoparticle can become similar to the core atom number (see **Fig. 2**).[2]

Decrease of Surface-to-volumen ratio

92%   76%   63%   52%
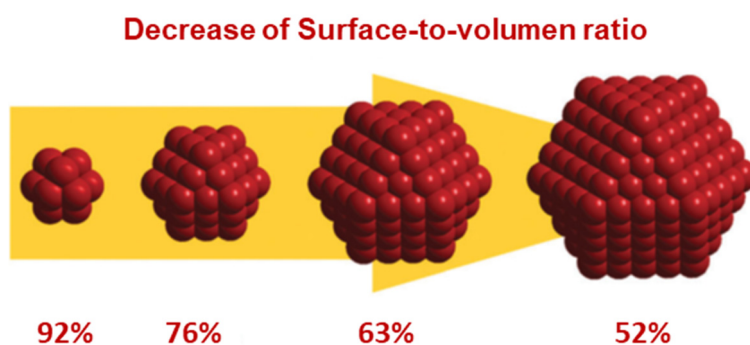
Figure 2. Percentage of surface atoms as a function of the particle size in a cuboctahedral particle.[2] Note that as the particle size increases, this percentage is reduced.

Having a high surface to volume ratio offers new possibilities in diverse fields such as sensing or catalysis, as it involves an increase of efficiency compared to their bulk counterpart because the large surface-to-volume ratio of small nanoparticles can help to minimize the amount of ''unused'' material in the core of the catalyst and thus increase the number of active sites on the surface.

From a physical point of view, having a large number of surface atoms also involves other changes such an increase of the chemical potential, reduced lattice constant, a decrease in the melting point with respect to the bulk material, or lower phase transition temperatures.[3]

One more factor that leads to important physicochemical differences in nanostructures with respect to the *macro* scale is their commensurability with the length scale of some physical phenomena, such as electron and phonon mean free path, domain wall width, exciton Bohr radius or diffusion length to name some of them.[3] For example, when the size of a structure is commensurate with the phonon mean free path its thermal conductivity will be drastically affected, which is one of the main issues in nanoelectronics.[4]

A particular case is when the new properties of nanostructured materials have no equivalent in the *macro*-scale. For example, because of the small size, quantum mechanics phenomena can dominate over bulk behaviour, leading to completely novel effects. This would be the case of the quantum dots, which are particles of semiconductor materials whose size is so small (only a few nanometers), that their optical and electronic properties are radically different from the original material and closer to those of discrete atoms or molecules. For example, if a

particle is small enough so that the radius of the semiconductor nanocrystal is smaller than the exciton Bohr radius, electrons remain confined in a small space (which is called *quantum box*) and there is a quantization of the energy levels according to Pauli's exclusion principle.[5] As a result, the energy band gap between both the valence and the conduction bands is increased as size is decreased so optically exciting an electron from the valence to the conduction band requires more energy and therefore more energy is released when returning to the ground state (**Fig. 3 a**)[6]. Consequently, the photons emitted in the process are of a very specific wavelength, yielding radiation of "pure colours" (i.e., discrete wavelengths) with very high efficiencies, long lifetimes and high extinction coefficients.
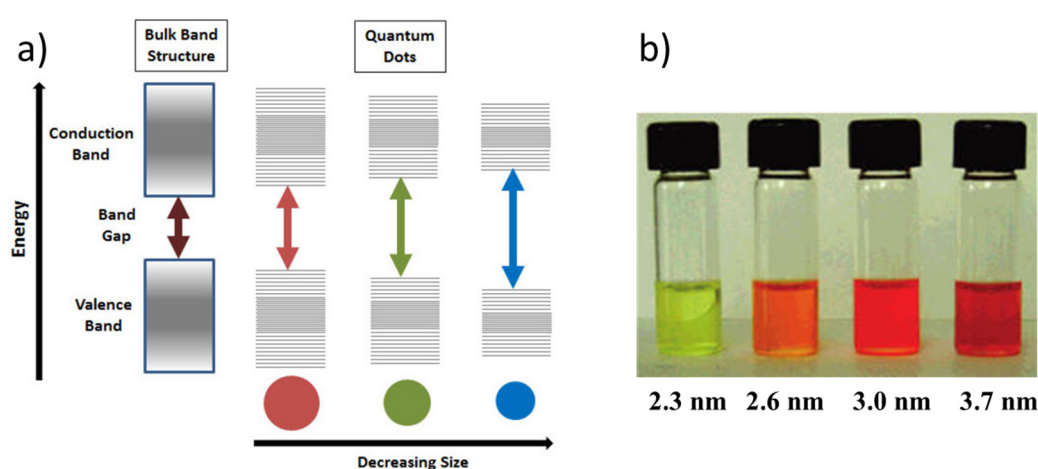
Figure 3. a) Size-dependent band gap energy and quantization of energy levels in quantum dots;[6] b) image of 2.3, 2.6, 3.0, and 3.7 nm diameter CdSe quantum dots in dispersion.[7]

In addition, because fundamental biomolecules such as proteins and DNA are *nano-sized* (i.e. proteins are in the 3-20 nm range),[8] working with elements that are in the same size range allows the selective manipulation and interaction with biomolecules, such as grafting nanoparticles for cell tracking, targeting, drug delivery, among others.[9] Actually, *nanomedicine* is one of the most promising and exciting fields stemming from nanotechnology and, for example, more than 50 nanotechnology-based drugs have been approved by the Food and Drugs Administration (FDA).[10]

In summary, due to the four effects described before (namely, surface area enhancement, commensurability between the nanostructure size and critical physicochemical length scales, quantum phenomena and scale convergence between technological and biological realms), nanoparticles have led to a wide number of opportunities in both fundamental and applied research. Some examples of these applications in our daily life are: orthopaedic implants and

supercapacitors (carbon nanotubes); cosmetics and anti-viral therapies (fullerenes); sunscreen lotions and paints (TiO_2 nanoparticles); gas purification and contamination sensors (ZnO nanoparticles); combustion catalyst in diesel fuels and eye drops (CeO_2 nanoparticles); textile industry and disinfectant sprays (silver nanoparticles); telecommunications and photovoltaic cells (quantum dots) to name only a few.[11]

1.2 Introduction to magnetic nanostructures

Magnetic nanoparticles deserve special attention, as the magnetic properties are especially sensitive to size effects. In addition, magnetic nanoparticles can be synthesized from many different materials with a wide variety of functional properties, e.g., saturation magnetization, coercivity, transition temperature or susceptibility. This versatility has attracted the interest of researchers from very diverse fields and disciplines such as data storage,[12] biotechnology,[13] sensors,[14] magnetic resonance imaging,[15] environmental remediation[16] or catalysis.[17]

Basic magnetic properties

The magnetic properties of atoms (and, consequently, those of materials) are the result of the contribution of the individual orbital and intrinsic magnetic moments of electrons orbiting the nucleus of the atom. However, because electrons are combined into pairs with opposite intrinsic moments as a result of the Pauli Exclusion Principle and placed into subshells without a net orbital motion, most of times the magnetic moments of the electrons are cancelled out between each other.[18] As a result, only a few atoms (e.g., cobalt, nickel, gadolinium and neodymium) show a net magnetic moment. At the same time, the final magnetic properties of the materials containing any of these elements depend also on the chemical composition and the crystal structure. As a consequence, different materials show dissimilar responses to the application of an external magnetic field. According to the nature of this response, materials can be classified into five general categories:

- *Diamagnetic:* In diamagnetic materials, there are no unpaired electrons, but yet the orbital electron motion of the electrons is present, resulting in a (very weak) magnetic response that opposes to the application of an external magnetic field. Thus, diamagnetic materials can be repelled by a magnet. Some examples are copper and carbon. Although diamagnetism is present in every material, the opposed response is so weak that it is usually not noticeable and if any other magnetic behaviours are possible in a material (*i.e.,* paramagnetism or

ferromagnetism), the latter will predominate. Some examples of diamagnetic materials are copper and carbon, silica, water.

- *Paramagnetic:* Unlike diamagnetic materials, some electrons in atoms of paramagnetic materials are unpaired hence carrying a net magnetisation. However, despite the atoms carry a magnetic moment, when atoms order in a crystal structure, the magnetic moment of each atom is randomly oriented and therefore the net sum of all of the contributions is zero, resulting in a null total magnetisation unless an external magnetic field is applied. The field-induced magnetisation is usually weak and is linearly proportional to the applied field. Some examples of paramagnetic substances are aluminium and oxygen.

- *Ferromagnetic:* In ferromagnetic materials the atoms have uncompensated spins (similar to paramagnetic materials). However, in ferromagnetic materials there is a quantum-mechanical long-range ordering phenomenon at the atomic level (exchange interaction) that causes the spins to align parallel with each other when the atoms are arranged in a crystal lattice, resulting in a permanent net magnetic moment even at zero fields. After the application of an external magnetic field, ferromagnets keep the magnetization in the same direction as the last applied field. This tendency to *remember* their magnetic history is called hysteresis. Some examples of ferromagnetic substances are iron, cobalt and nickel.

- *Antiferromagnetic:* Antiferromagnetic substances are similar to ferromagnetic materials. However, in this case exchange interactions induce an antiparallel alignment of the magnetic moment of the atoms. Consequently, the overall magnetic moments cancel each other, resulting in a null magnetisation at zero field. The magnetic response is quite different and is more similar to that of paramagnetic materials, with a weak linear dependence of the magnetisation respect to the applied field. An example of an antiferromagnetic material is chromium.

- *Ferrimagnetic:* Ferrimagnetic materials show the same magnetic response as the antiferromagnetic ones, where exchange interactions induce an antiparallel coupling. However, ferrimagnetic materials are composed of (at least) two different types of atoms with different magnetic response. This results in only a partial cancelation of the magnetic moments. Consequently, ferrimagnets possess a net magnetic moment at zero field similar to ferromagnetic materials. The magnetic response of ferrimagnets is, hence, similar to that of ferromagnets, including hysteresis. An example of a ferrimagnetic material is Fe_3O_4, in which the magnetic moments of the Fe^{3+} atoms placed in the octahedral and tetrahedral sites

cancel each other but due to the Fe^{2+} ions in the octahedral sublattice there is still a net magnetic moment.

In any case, it is important to understand that even a same material can show different magnetic states depending on the temperature and other variables such as pressure and the applied magnetic field. For example, ferri-, antiferro- and ferromagnetic materials behave like paramagnets above a critical temperature: at high temperatures, when the thermal fluctuations become stronger than the exchange interactions, which keep the magnetic moments aligned, the material loses its net magnetic moment since the moments in the crystal lattice become random.

Ferro- and ferrimagnetic materials have many interesting properties. For example, their magnetic behaviour can depend on the shape of the constituent particles: keeping all the moments aligned along the easy axis of a particle is energetically costly (due to the magnetostatic energy); however, the shape can play a major role, as the structural anisotropy creates a favourable energy term for magnetization along the longest axis of non-isotropic structures, thus favouring the generation of a net magnetisation.

As a consequence of magnetostatic energy, usually materials are composed of different regions where magnetic spins are aligned in the same direction, but different from the rest of the regions unless an external magnetic field is applied. Each of these regions is called domain and the interface between them is called domain wall (**Fig. 4**). The number of different domains (and thus spin orientations) in a material depends on the balance between the magnetostatic energy and the domain-wall energy. In a multi-domain particle, the net magnetization of the particle is the vector sum of all the magnetic moments of the domains in the material.

For a demagnetized state (*i.e.*, zero net macroscopic magnetization) if an external magnetic field is applied to a ferro- or ferrimagnetic material, the value of its magnetization (M) due to the reorientation of its domains will increase with the intensity of the applied field (H) up to a maximum value (*i.e.*, when all the domains are aligned in the direction of the magnetic field). This state is called saturation magnetization (M_S; Fig. 4). When the applied is reduced back to zero not all the domains return to the original state and there appears a remnant magnetization (M_R; Fig. 4) that can only be removed by applying a coercive field (H_c; Fig. 4) in the opposite direction to the initially applied field. By applying a sufficiently large field in this opposite direction the magnetization will saturate at a negative M_S. When increasing the field back to positive values, the inverse process from $-M_S$ to $+M_S$ takes place (Fig. 4). Consequently, the

magnetization as a function of the applied field (M vs H) shows hysteresis and the corresponding M vs H curve is called hysteresis loop (**Fig. 4**).
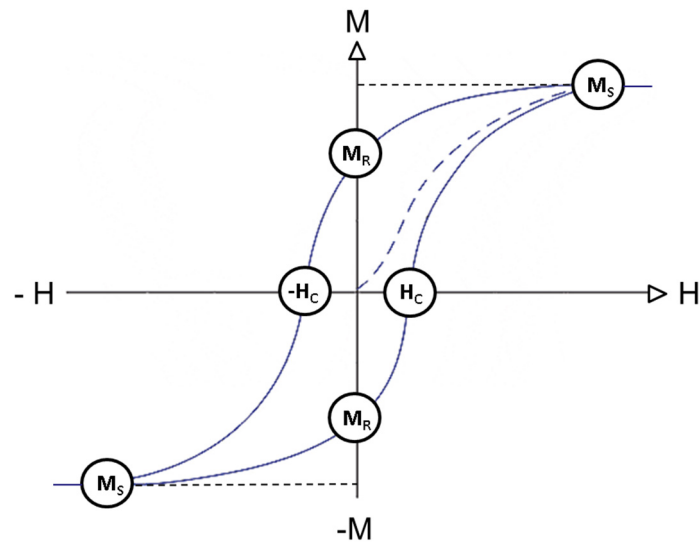
Figure 4. Magnetization as a function of the intensity of the applied field in a ferromagnetic nanoparticle. The highlighted points represent M_S, M_R and H_c, as indicated.

Size effects on magnetic nanoparticles

To fully understand the interest on magnetic nanoparticles, first one should understand how magnetism is altered by the particle size reduction into the nanoscale. Overall, depending on their origin, one can classify magnetic effects on the nanoscale into two big categories: finite-size effects and surface effects.

Finite-size effects: These are effects arising from the particle size reduction. Some of the most representative effects are the apparition of single-domain limit and superparamagnetism. If the volume of the particle is reduced below a critical size (single-domain limit), the magnetostatic energy decreases so that the generation of a wall is energetically disfavoured. At this point, all of the spins in the particle will align in the same direction even in the absence of an external magnetic field (**Fig. 5** right).
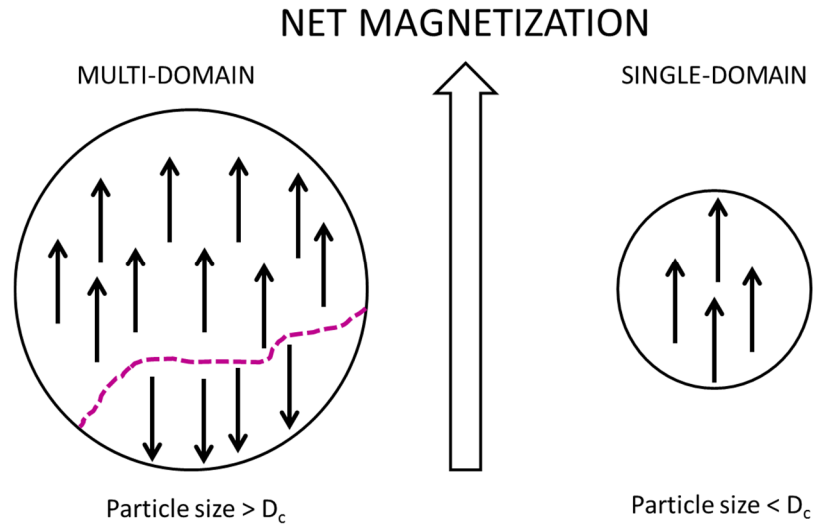
Figure 5. Two particles of different size but with the same net magnetization direction as indicated by the arrow. On the left, a large particle (particle size>D_c) with several magnetic domains. Small arrows represent the orientations of the magnetic moments within the domains, while the purple dashed line represents a domain wall. On the right, a small single-domain particle (particle size<D_c).

One of the consequences of having single-domain nanoparticles is that, as there are no domain walls to move the reversal should take place by magnetization rotation, which is energetically most costly, and causes the coercivity enhancement typical of small single-domain nanoparticles.[19]

Another factor that can be used to adjust the coercivity is shape anisotropy. In general, higher shape anisotropies trend to increase coercivity and also the D_c, favouring a single-domain regime. This coercivity enhancement can be used for a number of applications such as permanent magnets and magnetic recording, for example.[20]

Superparamagnetism is a phenomenon that can take place in single-domain nanoparticles and leads to a loss of a permanent magnetization at a given temperature in the absence of an external field even if the constituent bulk material shows ferro- or ferrimagnetic behaviour. The energy that holds the magnetic moments in a fixed direction is called magnetic anisotropy energy and is proportional to the volume of the particle (V) and the effective anisotropy K_{eff}, which comprises all the anisotropies of the particle including, e.g., magnetocrystalline, shape, surface or strain anisotropies). Actually, the product of $K_{eff}V$ is related to the energy barrier that separates the two possible orientations of magnetization in a single-domain particle and which are energetically equivalent along the direction of the easy axis (**Fig. 6**).[21]
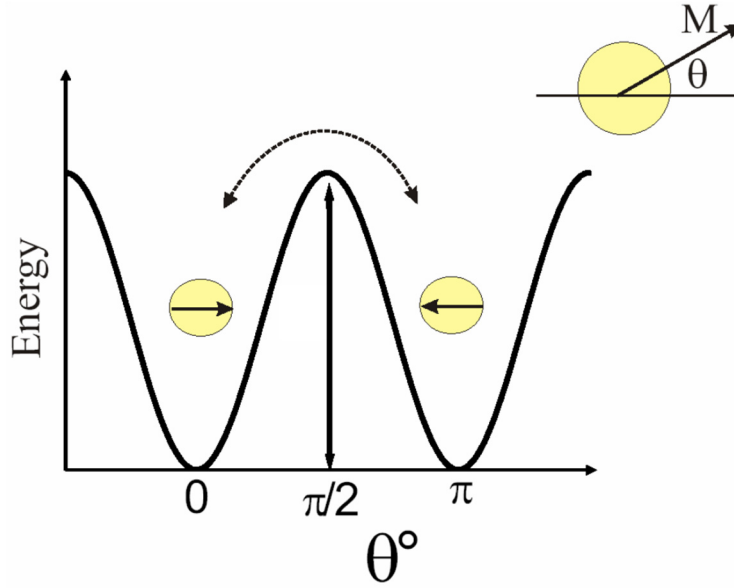
Figure 6. Representation of the energy of a single-domain particle as a function of the magnetisation direction for two possible orientations along the easy axis that are energetically equivalent (right and left). Θ represents the angle between the magnetisation and the easy axis. Adapted from Bedanta.[21]

If the size (and thus V) of the particle is reduced sufficiently this energy barrier can become of the order of the thermal energy (given by k_BT) and thermal agitation is sufficient to make the moment overcome the energy barrier. Therefore, if $K_{eff}V < k_BT$, the spins fluctuate randomly but still all coupled parallel to each other, leading to a net zero magnetization at zero field. In contrast, in the paramagnetic regime the spins fluctuate independent from each other.

Obviously, as this is the result of a balance between both the magnetic anisotropy and the thermal energies, if temperature decreases sufficiently so that the thermal energy becomes smaller than the magnetic anisotropy energy, the particle will show a permanent magnetization; at this state it is usually said that the particle is *blocked* (**Fig. 7a)** because the direction of the magnetization is fixed. The temperature at which this happens is called blocking temperature, T_B. The particles that remain unblocked (i.e., fluctuating with time) (**Fig. 7b**) above a given temperature as a consequence of particle size reduction are called *superparamagnetic*. In this state, if no external magnetic field is applied, the time required to measure the magnetization might be much longer than the fluctuation time and thus the magnetisation is flipping randomly within the time frame of the measurement; consequently it appears to be zero in average. Thus, particles will show no hysteresis ($H_c = 0$) nor remanence ($M_R = 0$) and therefore the magnetization becomes 0 when in the absence of an external magnetic field (**Fig. 7c**). Note that the required time for a fluctuation of the magnetic moment is typically in the range of 10^{-9} s, while the measuring times depend on the technique, e.g., whereas magnetization measurements

9

typically range in the 10-100 s range, other techniques like Mössbauer or neutron diffraction range in 10^{-8}-10^{-12} s.

Interestingly, superparamagnetism (due to $M_R = 0$) is a way to prevent inter-particle magnetic dipolar interactions and consequently magnetically driven aggregation, which can be very useful for purposes where colloidal stability is crucial, such as injectable probes, catalysis or removal of toxic metals from aqueous solutions.[22]
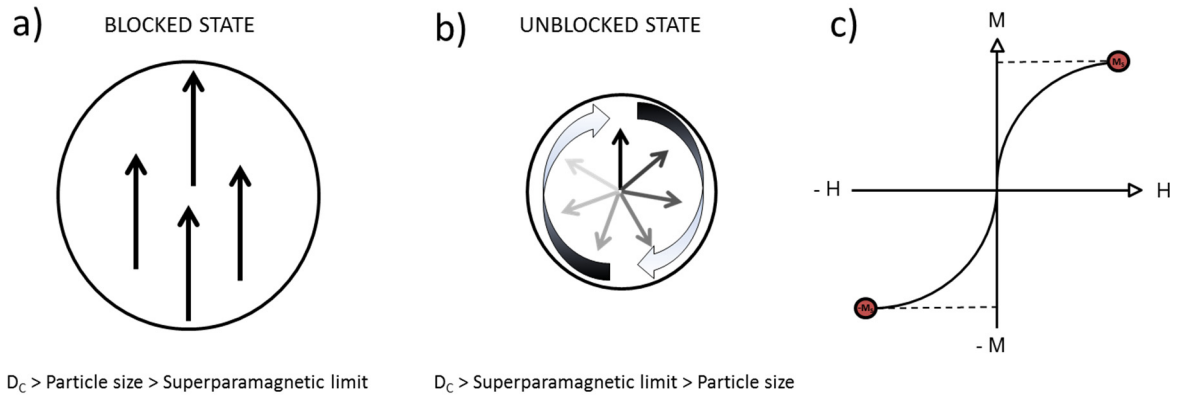
Figure 7. a) Single-domain particles of sizes beyond and b) under the superparamagnetic limit in the absence of an external magnetic field. The curved arrows indicate the fluctuation with time; c) Hysteresis loop of superparamagnetic nanoparticles. Note that there is no coercivity or remanence.

To summarize, **Fig. 8** shows the different magnetic behaviours (in H_c vs size) that can arise from finite-size effects in magnetic nanoparticles.
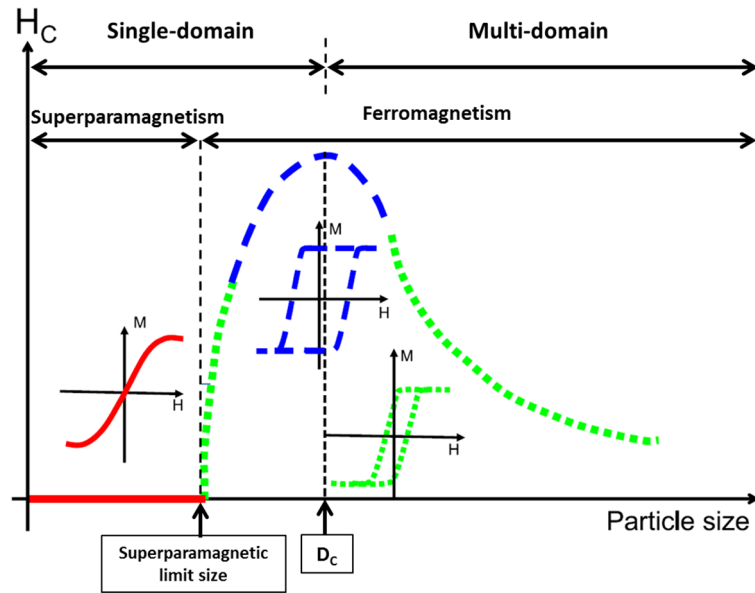
Figure 8. Schematic representation of the dependence of H_C on the particle size. The colours of the hysteresis loops correspond to different size particle regions (i.e. red hysteresis loop corresponds to superparamagnetism, etc.). Adapted from Paunović et al.[23]

Surface effects: as mentioned before, the smaller a particle is, the larger surface to volume ratio it has. Consequently, given higher number of atoms at the surface, their influence in the overall behaviour of the particle becomes more prominent. Generally speaking, the local disruption of the symmetry can induce changes in the crystallographic parameters such as lattice constant or atom coordination. Therefore, some effects can arise such as surface anisotropy, spin frustration, or core-surface exchange anisotropy.[24] These effects can alter the magnetic properties of the particles in such a complex way that sometimes the resulting consequences seem contradictory. For example, size reduction can result in a decrease of the magnetization for metal oxide nanoparticles, whereas in metal nanoparticles (like cobalt)[25] can lead to an increase of the magnetization. In any case, since the nature of these effects is beyond the scope of this thesis, we will only give a general overview on a few of them.

Surface anisotropy: This effect arises from the breaking of the atomic boundaries at the surface of the particle and can actually depend on factors such as the presence of ligands or the shape of the particle.[26] The overall anisotropy of a nanoparticle can be taken as the result of the sum of two different contributions: one from the core of the particle (K_V) and another from the surface (K_S). For example, for a spherical structure, the total anisotropy would be given by: $K_{eff} = K_V + \frac{6}{D}K_S$. A direct effect of the surface anisotropy enhancement could be, for example, a non-monotonic change of the blocking temperature with size.

11

Spin canting: because some changes on lattice constants and atom coordination can take place at the surface of the particle, sometimes the magnetic spins appear slightly tilted respect to the easy axis rather than being exactly parallel (**Fig. 9**). This phenomenon is called spin-canting. One of the consequences of this effect is the change of how the magnetization approaches saturation at high fields and the need of much higher fields to reach saturatuion.[27,28]
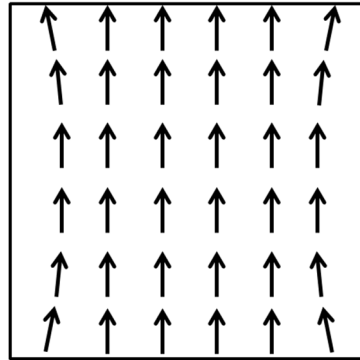
Figure 9. Spin canting on a cubic particle. Note how the spins (arrows) slightly tilt in the surface of the particle.

Finally, note that magnetic nanoparticles can be made of a variety of materials and the constituent material has a critical influence on the properties. Generally, magnetic materials are based on iron, cobalt, nickel and compounds containing these materials.[29] The combination of materials will dictate their functional magnetic properties and thus their possible applications. However, other factors like the shape or crystallinity may be critical for certain applications.

2. SYNTHESIS AND COATING OF MAGNETIC NANOPARTICLES

2.1 Synthesis of magnetic nanoparticles

Since for a given material the magnetic properties of the particles depend on the particle size, shape and crystallinity, it becomes obvious that a well-defined structure and a narrow size distribution is desirable so as to have optimal, uniform and reproducible properties and behaviour. Therefore, a "*good* synthesis" should yield size-specific, controlled shape, crystalline and monodisperse particles with a controlled aggregation in a reproducible way, while allowing a tight control over the size in order to tune the properties as required. Although there are many methodologies to synthesize magnetic nanoparticles, they can be classified into two broad categories: top-down and bottom-up approaches.

In top-down strategies, the dimensions of the bulk material are gradually reduced into the nanoscale by using either physical or chemical methods.[30] Some examples of these methodologies are ball milling, lithography and acid etching. Approaches based on lithography are often slow and expensive thus they are not usually used to obtain large quantities of nanoparticles.[25] Although some of the other top-down methods are relatively easy to scale up for a large production (e.g., ball-milling), some top-down strategies have certain issues like for example offering a poor control on size.[31] Moreover, it has been observed that the techniques used in the process of size reduction can damage the crystallographic structure of the processed material, introducing defects and impurities, which could have a significant impact on physical properties and surface chemistry of nanomaterials.[32] As these problems are opposite to the criteria we set on what a *good* synthesis should be, in this work we will not focus any further in top-down strategies.

On the other hand, in bottom-up approaches, nanomaterials emerge from smaller building blocks that generally are atoms or molecules. The chemical reactions involved in these processes offer a large number of control points to regulate the growth and thus the size of the resulting particles, allowing, in general, a better size-control than top-down strategies. In addition, bottom up syntheses yield a material with less defects and a more homogeneous chemical composition. This is due to the fact that bottom-up processes are driven by the decay in Gibbs free energy, so the resulting nanostructures are continuously closer to the thermodynamic equilibrium state, as opposite to top-down strategies where, often stress is induced to achieve size reduction, which leads to heterogeneity.[3] The mechanism of the bottom-up liquid-phase syntheses can be described in a general manner by the LaMer diagram, which is a representation of the concentration of precursors (monomers) a function of time (**Fig. 10**). The concentration of monomers increases, up to a point that nucleation occurs. The subsequent growth of the particles is the result of a combination of diffusion of atoms onto the nuclei and the aggregation of several nuclei. The growth stops when the concentration of precursors decays under the solubility threshold.
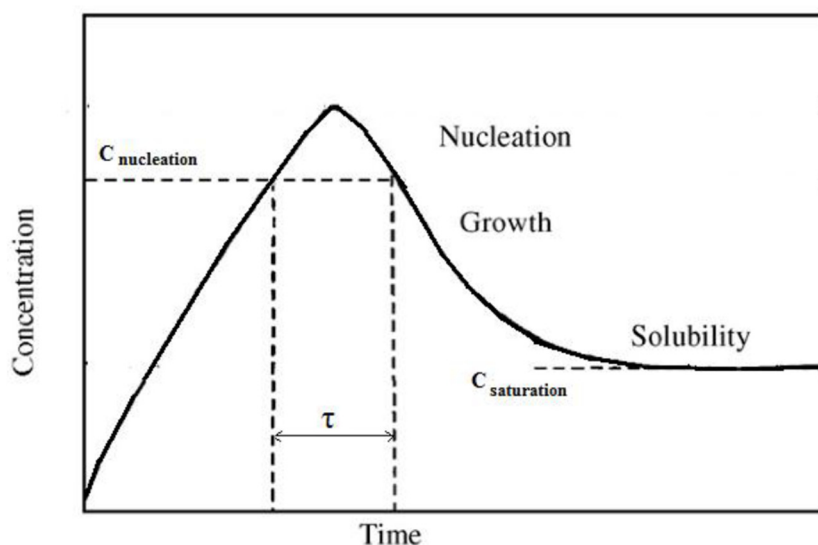
Figure 10. LaMer diagram. τ represents the time in which nucleation can take place.[33]

From this diagram, some considerations can be inferred, for example, on how to improve the particle size distribution of the syntheses. For instance, the nucleation stage should be as fast as possible so i) all of the nuclei are formed at the same time and grow during the same time in equal conditions, increasing the homogeneity and ii) the concentration of precursors decays quickly under the nucleation threshold, so only a limited number of nuclei is generated. On the other hand, to narrow the particle size distribution, the growth rate should be slow so that this stage is much longer than the nucleation phase. Taking into account these simple considerations and the high number of parameters that can be tuned in a chemical synthesis (*i.e.*, temperature, solvents, reagents, etc.) to improve the conditions and kinetics of the process, it is not difficult understand why bottom-up approaches are so popular.

 Some of the most important types of bottom up syntheses are: microemulsion, co-precipitation, solvothermal synthesis and thermal decomposition.

Microemulsion: a microemulsion is a dispersion of droplets of one liquid in another liquid with which it is immiscible (*i.e.* micelles and reverse micelles); the interface between both liquids is usually stabilised by surfactants. Generally, in this approach one of the droplets carries one of the reactants, *i.e.*, a salt which acts as metal precursor and the other one a precipitating agent (a reductor), so when both of them collide and coalesce, nucleation starts and further particle growth takes place within the confined space of the droplet, thus resulting in a limited particle growth. The addition of a third solvent with an intermediate polarity between the other two solvents (typically ethanol or acetone) causes the breakage of the micelles and the precipitation

14

of the particles (**Fig. 11**).[34] The amount of surfactant, the ratio between both polar and non-polar solvents and the total reactant concentration are some of the parameters that can be used to tune the particle size.[35] Using this methodology, some spinel ferrites have been synthesized. For example, manganese ferrite particles with sizes ranging from 4 to 15 nm were synthesized in an emulsion of water in toluene using sodium dodecylbenzenesulfonate as surfactant and $Mn(NO_3)_2$ and $Fe(NO_3)_2$ as metal precursors.[36] In this example, it was the ratio of water to toluene what determined the size of the particles. Although some examples of other materials that have been synthesized using this approach can be found in literature (*i.e.*, metallic cobalt, platinum cobalt alloys...)[37], microemulsion syntheses face some disadvantages with respect to the current modern techniques that has resulted in a decrease in their use. For example, despite the size distribution is relatively narrow and the shape control is moderately good, the conditions can only be tuned within a small range. In addition, the yield is very low and large amounts of solvents are usually required to produce an reasonable amount of material, making it a difficult process to scale up.[24]
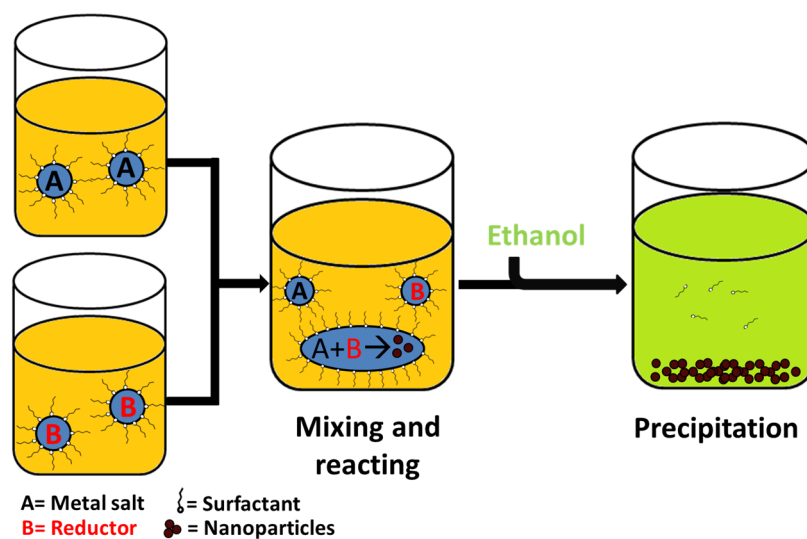
Figure 11. General scheme on a microemulsion nanoparticle synthesis. Yellow colour represents a non-polar solvent while blue represents water.

Coprecipitation: it is perhaps the most popular method for synthesizing iron oxide nanoparticles for sizes below 50 nm.[38] The mechanism lying behind this approach is very simple: For example, for iron oxides, salts of Fe^{3+} and Fe^{2+} are mixed with a base in an aqueous solution, carrying the reaction either at room temperature or heating for several hours. In this reaction, magnetite (Fe_3O_4) is the obtained iron phase, although it can be adapted to obtain maghemite (γ-Fe_2O_3) by further oxidizing the original product. The general scheme for a coprecipitation reaction is as follows:

$$Fe^{2+} + 2Fe^{3+} + 8OH^- \rightarrow Fe_3O_4 + 4H_2O$$

The size can be controlled by adjusting the Fe^{2+}/Fe^{3+} ratio, the reaction temperature, the ionic strength or the pH among other parameters. For specific experimental conditions, this synthesis is highly reproducible which, together with the experimental simplicity of this approach, the high yield per reaction and the easy scalability, are the main reasons why coprecipitation is a popular approach. This synthesis pathway can also be used to obtain non-spherical particles, where for instance, Han *et al.*, developed an inexpensive synthesis for obtaining magnetite nanowires with high magnetic saturation.[39] In addition, this approach has been also applied for synthesizing cobalt, nickel, manganese, zinc and copper ferrites by replacing the Fe^{2+} salts by the corresponding bivalent cation.[33] However, achieving a narrow size distribution and controlling the shape and size in coprecipitation syntheses remains a challenge. This difficulty often leads to wide particle size distributions (in both size and shape) with the corresponding spread in magnetic properties. Moreover, using this approach particles trend to aggregate during the synthesis.[40] Although the use of some anionic surfactants can improve the colloidal stability issues, the poor control over size and the irregular morphologies obtained make this synthesis not very suitable for applications where a controlled response is required.[41]

Solvothermal synthesis: in solvothermal syntheses, the metal precursors, reductors and surfactants are mixed in a solvent and the resulting mixture is heated above the solvent boiling temperature. Because of the high pressure generated (which can be as high as 2000 psi), these reactions must be carried out inside an autoclave. The main advantages of working at such high pressure and temperatures are that i) as a result, nucleation is very fast, resulting in an improvement of the size distribution and ii) that the kinetics of the process is accelerated.[41] Using this versatile approach, Li *et al.* synthesized nanoparticles of several materials such as Fe_3O_4, $CoFe_2O_4$ or $BaTiO_3$ among others. Although the typical reaction times require from several hours to several days, the introduction of microwave-assisted heating can improve this drawback due to the induction fast local super heating, where, for example, γ-Fe_2O_3 10 nm spheres were synthesized in only 25 min instead of requiring several hours.[42] However, since the chemical reactions take place automatically inside a closed container, the mechanisms behind these processes remain unclear, hindering the systematic study on how to find the optimal conditions. The advantages of this method are the scalability, the narrow size distributions and shape control (the best ones compared with all of the previously described methods) but the moderate yield, which is better than the microemulsions but still lower than

co-precipitation, the long reaction times required in most of cases and the difficulty to elucidate the exact mechanisms, make it a less common synthetic approach.

Thermal decomposition: this approach is based on the decomposition of organometallic compounds or metal carboxylates in the presence of surfactants at high temperatures in heavy non-polar solvents. Some of the precursors include metal acetylacetonates, cupferronates and carbonyls. The surfactants are usually fatty acids such as decanoic or oleic acid but sometimes long chain alkylamines like oleylamine, hexadecylamine can be used. The growth of the particles is carried out at the boiling temperature of the mixture and under inert atmosphere, resulting in highly monodisperse nanocrystals. Some of the parameters that can be used to tune the size and morphology of the particles are the ratios and total concentration of reagents, the solvents and the temperature and times of the reaction.[41] The decomposition of precursors with metal cations (like acetylacetonates or carboxylates) leads directly to metal oxide nanoparticles, while organometallic precursors in which metal has zero valence (like carbonyls) lead to the formation of metal nanoparticles.[43] The exact chemical mechanisms behind thermal decomposition are complex and still under debate, but in general it is accepted that the electrons needed for the redox reactions come from the oxidative decarboxylation of the fatty acids.[44] The global process can be described according to the La Mer model. Namely, the concentration of monomers increases in the first stages up to supersaturation and at the point of the boiling of the mixture a burst nucleation is triggered and the subsequent growth is driven by diffusion, thus achieving a complete separation between nucleation and growth.[45]Although initially, this approach was developed in the early 90's for the synthesis of semiconductor nanocrystals such as CdS or CdSe,[46] later it was adapted for the synthesis of magnetic nanomaterials. For example, in 2002 Sun and co-workers developed a synthesis of magnetite nanoparticles with sizes ranging from 3 to 20 nm using iron acetylacetonate as precursor, oleic acid as surfactant and reductor and phenyl ether as solvent.[47] The main drawbacks of thermal decomposition are that (i) except in a few cases, the obtained product is hydrophobic, which is a limitation for biomedical applications, where water-dispersible particles are necessary and (ii) that the needed experimental conditions are complex, requiring high temperatures, pressures and inert atmospheres. Nevertheless, because of the high yield per synthesis and the accurate control on both size and shape, some authors have regarded thermal decomposition as the best method to date for synthesizing magnetic nanoparticles with an optimal response.[33]

2.2 Coating of magnetic nanoparticles

Although the controlled synthesis of the particles is crucial, the coating also plays a major role for almost any application of magnetic nanoparticles. In fact, the coatings do not only serve as protection layers to avoid chemical changes over time (e.g., oxidation), but they can also be used to tune the magnetic properties of the particles. Indeed, by comparing particles of equal size and composition but different coatings, it has been established that the coating can influence the magnetic behaviour and properties such as susceptibility, barrier energy, effective anisotropy and the surface magnetic moment.[48] The coating is also necessary to prevent long-term instability, e.g., a loss of dispersibility. Namely, due to magnetic interparticle interactions, magnetic nanoparticles trend to aggregate and precipitate. The coatings physically separate the particles from each other, thus weakening the magnetic interactions and, consequently, reducing aggregation. Note that uncontrolled aggregation can limit the applications of magnetic nanoparticles in many applications. For example, in biomedicine it is important that particles with high magnetic saturation remain stable in aqueous media at physiological conditions of pH and ionic strength. Interestingly, chemical instability will result in deviations from the optimal properties while colloidal instability can lead to uncontrolled aggregation and blockage of blood vessels.[49] Importantly, some coatings can also prevent or reduce toxicity by avoiding non-specific interactions between the particle and biomolecules in the host organism.[50] Another key aspect of the coatings is that they allows the introduction of functional groups like carboxyls, amines, thiols, etc. These groups can be used to increase colloidal stability by electrostatic repulsion or to confer the particles some special functionalities. For example, amine and carboxyl groups can be used to covalently link biomolecules such as peptides, proteins, nucleic acids or antibodies to nanoparticles so they can be targeted towards specific types of cells.[51] Essentially, coatings can be classified in two groups: organic and inorganic. Although there is a vast variety of available coating procedures according to the intended functionality of the nanoparticles, we will only focus on a few of them, as a complete review is beyond the scope of this thesis.

Organic coatings: magnetic nanoparticles coated with organic materials are used in a variety of applications and especially in the biomedical field (e.g., magnetic resonance imaging (MRI), cell sorting, drug delivery, etc.).[52] These coatings are usually performed during or after the synthesis to prevent aggregation by either electrostatic or steric repulsion, countering both the Van der Waals and magnetic interparticle attractive forces. Additionally, some of these

molecules allow the introduction of special groups such as alcohols, carboxyls and amines. The main two types of organic shells are those based in the use of either surfactants or polymers.

a) *Surfactants:* small molecules are often directly attached to the nanoparticle surface by adsorption. The most common organic ligands are fatty acids and alkyl-amines with a cis-9 unsaturated 18 carbon long chain. The coordination of the ligands to the surface takes place usually by coordination bonds. For example, carboxylates such as oleic acid can coordinate to metal oxides surface by sharing electron density with the cations in the surface[53] while amines can donate the non-shared electrons of the nitrogen atom.[54]

b) *Polymers:* the use of polymers provides a strong interaction between the coating and the particle due to the numerous interactions and/or cross-linkage between monomers. Compared to surfactants, polymer coatings provide a higher colloidal stability.[55] Despite polyethylene glycol and its derivatives are likely the most used polymer, there is a large number of available both synthetic (such as polyacrylic acid or polymethylmethacrylate) and natural polymers (such as chitosan or polysaccharides).[52] Although some strategies have been developed to directly coat the nanoparticles during the synthesis, the thickness of the polymeric shell remains difficult to control, which results in a poor colloidal stability. This is why nowadays coating is usually carried out as a separated process after the synthesis.[56] In some cases the polymers are not directly attached to the surface of the particle, but to the surfactant that is used during the synthesis. Interestingly, the coating with polymers is often used to make the particles to go from hydrophobic (e.g., the ones synthesized by thermal decomposition) to hydrophilic.[57] The main advantages of some of the polymers are that, on the one hand, there is no needed to remove the original coating and, on the other hand, a secondary layer of molecules is added, which enhances the steric hindrance (reducing the dipolar interactions). The large variety of commercially available polymers with functional groups such as carboxyls, amines, alcohols, thiols or phosphonates among others can be used not only the improve the colloidal stability but also the specific applications, especially in medicine.

Inorganic coatings: although coating with organic molecules seems to be the preferred choice for biological applications, it has been shown that this is not enough to prevent air or acid induced oxidation of metallic nanoparticles (*e.g.*, iron nanoparticles) and that polymers face stability problems at high temperatures.[58] This is why in some situations, an inorganic coating is preferred. Moreover, inorganic materials can confer some special properties to the raw

nanoparticles, such as higher electron density and strong optical absorption (gold coating)[59] or enhanced magnetic moment (cobalt oxide coating).[60] Some of the most frequently used inorganic coatings are gold and silica coating.

a)   *Gold coating*: gold is a noble metal that can provide a powerful shell to prevent the oxidation of the core. In addition, it is a plasmonic material, so it can be used for sensors based in surface enhanced Raman spectroscopy[61] or for biomedical applications.[62] Due to its inertness, it is expected to be a biocompatible coating and highly stable under different chemical conditions. Moreover, the gold surface can strongly link to thiolated molecules, which can be useful in catalysis and optical applications.[63] Despite the potential interest, coating with gold some magnetic materials like iron oxides can be particularly challenging due to the differences in the crystal structures.[64]

Silica coating: this coating provides particles a shield for avoiding etching in acidic environments. It can also enhance the colloidal stability of magnetic nanoparticles by increasing the distance between magnetic cores and also because of the negative charges in the silica surface, resulting in water-dispersible nanoparticles without the need of any other surfactants. Furthermore, the presence of silanol groups enables the linkage to other molecules and functional groups. However, silica can be etched in basic environments and its porous structure can allow the diffusion of oxygen molecules that could lead to the oxidation of the core. In addition, the reproducible synthesis of a silica shell with a well-controlled and homogeneous thickness in every particle is still difficult and sometimes some core-free silica particles can also be generated in the process. This can be critical in biomedical applications like drug delivery, where the differences in core in the shell thickness and core-free silica particles have been pointed out as the major cause for an uneven tissue distribution.[52] In addition, because the magnetic attraction increases with particle size, a thicker shell is required for stabilizing large particles. However, it has been shown that the increase of the silica thickness can lead to a decrease in the performance of particles, like for example as contrast agents.[65]

3. BIOMEDICAL APPLICATIONS OF MAGENTIC NANOPARTICLES

Although magnetic nanoparticles have been extensively used for very diverse applications, it is in biomedicine where a great research effort is currently ongoing. Specifically, one of the main aims of the research of magnetic nanoparticles in biomedicine is in the diagnosis and therapy of diseases, particularly cancer. The diagnosis and treatment of

cancer is one of the major current societal challenges since every sixth death in the world is due to cancer, making it the second leading cause of death after cardiovascular diseases.[66] Rather than a single disease, cancer should be understood as a group of diseases where certain types of cells grow uncontrollably and tend to invade and spread to other parts of the body, as opposite to benign tumours.[67] More than one hundred types of cancer have been described in humans according to the affected type of cells. This diverse etiology originates a great variety of symptoms, making cancer very difficult to diagnose and treat. In addition, cancer can show no symptoms in the first stages, making it more difficult to detect. However, an early diagnosis can actually make the difference between death and survival. For instance, in lung cancer, which is the most common cause of cancer deaths in developed countries (29% of all cancer deaths and more deaths than from prostate, breast, and colorectal cancer combined in the United States),[68] survival rate is higher than 80% for patients diagnosed at the earliest stage, whereas it decays to 15% for those diagnosed in an advanced stage.[69] This effect becomes even more dramatic in ovarian cancer, where 90% or patients can survive at least for 5 years if diagnosed in the earliest stage compared to approximately only 5% that are diagnosed in the most advanced stages.[70] These statistics make it clear that finding new tools that allow an earlier diagnosis is a priority for fighting cancer, as it could notably improve the survival rate.

The most common strategies to treat cancer nowadays are based on conventional methods such as chemotherapy, surgery and radiotherapy. They are usually combined to enhance the effectiveness of the treatment and thanks to years of scientific research, nowadays the success rate has improved drastically. However, despite the technical advances in these techniques, the multiple side-effects and the aggressiveness of these techniques makes it necessary to develop more specific and efficient therapies that can overcome these issues.[71] For example, chemotherapy usually involves the administration of drugs that interfere with the cell division such as platinum-based derivatives. Although, harnessing the cell division should affect preferentially to cancer cells, the systemic diffusion of these chemicals can result in damages in several organs and tissues, such as nervous and renal systems.[72] Despite some differences are known in malignant cells (*i.e.*, a lower differentiation degree,[67] the overexpression of certain receptors[73,74] or a higher need of glucose),[75] the difficulty to selectively attack cancer cells lies in the similarity between both healthy and malignant cells (after all, they all are own cells of the same organism).

In summary, the two main challenges to deal with in the fight against cancer are: (i) improving current diagnosis tools and (ii) finding more specific and less aggressive therapies to reduce side effects.

3.1 Cancer and nanotechnology

In fact, since the second half of the last century, researches in nanotechnology pointed out that magnetic nanoparticles could be very useful to overcome these problems and diagnose and treat cancer in more efficient ways. For example, due to their magnetic properties, they can work as contrast agents in MRI and as therapeutic mediators in thermal therapies, selective drug and gene delivery as they allow magnetic active targeting, etc. However, the number of materials that can be used for these purposes is strongly restricted by biocompatibility issues since some magnetic materials have shown cytotoxicity to some extent.[76] Indeed, among all the available magnetic materials, only two have been approved so far by the FDA for their application in humans, magnetite and maghemite.[77] The metabolism of iron oxides has been studied and its biochemistry is well-established. For example, it has been observed that approximately 24 hours after injection, iron oxide nanoparticles are usually internalised and confined within the lysosomes of both liver and spleen cells.[78] Afterwards, particles become etched and the released iron is captured by ferritin molecules, which store it in a safe way, avoiding the formation of unstable and reactive iron species. Iron captured in this way will be released from these proteins depending on the metabolic requirements of the body.[79] Another advantage of working with iron oxide nanoparticles is that iron is a relatively cheap material due to the iron abundance (the fourth most abundant element on Earth's crust).

Some of the main reported applications of iron oxides in biomedicine are:

MRI: magnetic resonance imaging is a technique used to explore the inside of the body in a non-invasive way and it is based on the same principles as nuclear magnetic resonance. Due to its magnetic properties, iron oxide nanoparticles can induce significant susceptibility effects, which results in a shortening of the spin-spin relaxation time (T_2) of the surrounding water protons. This generates a negative contrast, leading to an image darkening in the regions where particles are accumulated. In the last years, however, an effort has been made on enhancing the properties of iron oxide nanoparticles to be used as a positive contrast agent by reducing the T_1 (due to spin-lattice relaxation processes), which would improve the sensitiveness of the technique.[80] This can be achieved by reducing the particle size below 5 nm. However,

controlling their synthesis while preserving chemical stability of such small structures still remains a challenge. Contrast agents based on iron oxide nanoparticle benefit from the low toxicity of iron oxide. This is an advantage over the conventional contrast agents based on gadolinium, which can induce nephrotoxicity in some cases.[81] Other advantages are i) a very short delay time (around 10 min) from injection to imaging, ii) cross section flow void in narrow vessels may impede the differentiation from small liver lesions; and iii), aortic pulsation artefacts become more pronounced.[52] In addition, due to their magnetic character, by the application of an external magnetic field, the particles can be efficiently guided and accumulated in the region of interest, which is one of the limitations of conventional contrast agents. Due to these advantages MRI is a promising application of iron oxide nanoparticles in biomedicine. Indeed, they have been widely used for imaging tumours in spleen, liver and lymph modes[82] and atherosclerotic plaques[83] as well as for angiography.[84] Furthermore, iron oxide nanoparticles have also been used for *in vivo* cell tracking[85] and monitoring cell therapy.[86] Despite since the mid-1990's several products have been commercialized (such as Feridex®, Resovist® or Endorem®), their production has been stopped because of both the possible side effects on the immune system and their inability to compete with the much higher relaxivities of the state of the art contrast agents.[87] Actually, both effects are related, as a higher efficiency would increase the resolution and require a lower dosage, thus avoiding the side-effects. This clearly indicates that further research must be carried out to take advantage of the full potential of magnetic iron oxide nanoparticles in MRI applications.

Drug delivery: In conventional chemotherapy, drugs are usually administered orally or intravenously and nonspecifically distributed through systemic blood circulation. As a result, two non-desirable effects arise: i) the portion of the drug that reaches the target tissue is quite small and ii) there is lower drug diffusion through the biological barriers, causing a high incidence of adverse effects. Magnetic nanoparticles are potential candidates to overcome these problems and enhance the accumulation of drugs at specific sites. Drugs can be attached onto the surface of the nanoparticles in different ways. For example, using some small ligands that act as bridge between the drug and the nanoparticle, coating the particles with polymers that can covalently bind or embed drugs, or using chemical methods like the creation of a sulphide or an amide bond between the drugs and the functional groups of the coating of the nanoparticle.[88] In magnetic active targeting, an external magnetic field is applied on the region of interest, leading to an effective guiding of particles loaded with drugs and a local concentration increase in the area of interest.[89] In addition, in this way, the concentration of

drugs that remain circulating in the bloodstream and tissues could be virtually eliminated while they could be driven beyond certain biological barriers, such as the blood-brain barrier.[90] Particles intended for drug delivery should be small enough to diffuse through the capillary system but large enough to avoid an exceedingly fast renal clearance. On the other hand, large particles can aggregate very fast and are thus difficult to stabilize. Therefore, it has been estimated that the optimal size of magnetic iron oxide particles for injectable suspensions should be between 10 and 100 nm.[91] The cell uptake of the particles varies according to both the target cells and the particle coating. For example, it has been shown that human breast cells internalize more efficiently positively charged nanoparticles.[92] Therefore, depending on the target, the coating material should be carefully selected from a wide variety of choices such as biocompatible polymers, liposomes, silica… etc. In addition, some of these materials can be functionalized with molecules to achieve a higher precision in the targeting (*e.g.*, antibodies). Once the particles have reached the target region, drug release and action can be triggered as a response to different stimuli such as temperature, pH and salinity changes, optical or magnetic stimulation, etc.[93] For example, while in human healthy tissues pH is slightly basic (typically 7.4), hypoxia in the tumour leads to an anaerobic carbohydrate-based metabolism, thus increasing the lactic acid production and, consequently, a local low pH. This physiological feature can be used to release drugs specifically in tumour sites. For example, in 2007 Zhang *et al.*, used a pH-sensitive linker (hydrozone) to release deliver doxorubicin (an anti-cancer drug) specifically to tumour cells.[94] Another proposed application of magnetic active targeting is the carriage of chemicals beyond the blood-brain-barrier, which is a limitation for conventional drug administration.[95] Despite the great expectations on magnetic nanoparticles-based drug delivery, to date there are no significant clinical applications yet. Firstly, although generally iron oxide nanoparticles are regarded as a non-toxic material, it is not clear whether their conjugation with drugs could trigger an immune response. In addition, *in vivo* experiments have shown unclear results concerning the success of targeting. Indeed, only one nanocarrier has been tested in humans for treating liver carcinoma and yet the clinical experiments were stopped in phase II due to poor evidences of efficacy.[96] The truth is that active targeting requires the application of a magnetic field in a very precise way (which can be a limitation for tumours that are deep inside the body), very strong magnetic field gradients and/or particles with a high magnetic saturation, which can be a problem considering the important restrictions on both the available constituent materials and sizes.[97] Therefore, while more research is carried out on how to address these issues, alternative ways of using iron oxide nanoparticles as therapeutic effectors should be investigated.

Hyperthermia: Hyperthermia is defined as the induced temperature increase up to 41-47 °C in tissues so as to cause local damage (by protein denaturation, apoptosis, increasing the sensitivity to drugs, etc.). In tumours, this results in a preferential death of malignant cells because they are more sensitive against prolonged exposures to higher temperatures.[99] The traditional use of hyperthermia involves applying heat externally to relatively large areas around the tumour, which can cause side effects in the surrounding healthy tissues surrounding the tumour. In contrast, hyperthermia can be induced using nanoparticles, which can generate *local* heat under the application of different stimuli (*e.g.,* magnetic or optical) only in the tumour area. This approach represents some advantages. For example, due to the poorly organized vasculature (leaky and with blind ends) that is usually present in tumours heat dissipation will be less efficient than in normal tissues. This effect is called Enhanced Permeation and Retention and it is also responsible for the preferential accumulation of nanoparticles in tumours, making nanoparticle-based hyperthermia an appealing therapy against cancer.[100] Another important advantage of hyperthermia is that it does not require invasive surgical procedures as, in principle, only an injection and the application of an external stimulus is necessary to trigger the heating. Hyperthermia can by classified depending on the external stimulus used to trigger the activity of the nanoparticles. The two main approaches applied to nanoparticles are magnetic hyperthermia and photothermia.

Magnetic Hyperthermia: For example, the exposure of magnetic nanoparticles to an alternating external magnetic field can trigger the heat release as a result of magnetic fluctuations. The first documented case on the utilisation of magnetic particles for magnetic hyperthermia in cancer patients, dates from the year 1957,[101] and, since then, many experiments have been carried out both *in vivo* and *in vitro* and great advances have been achieved. Perhaps one of the most relevant and relatively recent examples are the clinical trials performed by Van Landeghem *et al.*, where patients with glioblastoma where treated with magnetite nanoparticles for the first time.[102] However, despite these clinical trials were conducted in 2009, currently magnetic hyperthermia has not become yet a common tool in modern medicine and it somehow remains restricted to the academic world. The truth is that, although magnetic nanoparticles are considered as a very promising therapeutic agent, their application in real situations still requires improvements in aspects such as the reproducibility, and size and shape control in order to have optimal heating properties. For example, it has been shown that the temperature increase obtained from intravenously injections of targeted nanoparticles is not enough to provide clinical results because of the insufficient accumulation of particles in the tumour

site.[103] For this reason, nanoparticles usually need to be injected directly into the tumour. Nevertheless, the required dosage is considerably high. For instance, in the above-mentioned example of Landeghem *et al.*, concentrations as high as 155 mg of particles per mL were employed. Another limiting factor for *in vivo* applications of magnetic hyperthermia is related to the intracellular processing of endocytosed nanoparticles. After internalisation, particles are stored within endosomes. The confinement in such a small space causes their aggregation, which affects the magnetic properties and results in a susceptibility decrease and hysteresis loop opening due to the magnetic dipolar interactions, as well as the inhibition of Brownian motion. As a consequence of these effects, the heating efficiency can be severely affected.[104] Nevertheless, as not all the particles are endocytosed or cleared by the circulatory system, particles that remain in the extracellular matrix of the affected tissue can also be heated enough so as to have a clinical effect (*i.e.*, destroying the collagen fibres, which allow a better permeability for chemotherapeutic drugs).[105] Indeed, in a clinical phase II study performed in 2011, an increase of median survival of 13.4 months for glioblastoma patients that received a combined therapy of magnetic hyperthermia and radiotherapy was achieved, which is a considerable difference respect to the average 6.2 months for the control group (patients that had received only chemotherapy in a previous study).[106] Indeed, more recently, in 2018 a commercial product based on iron oxide nanoparticles (Nanotherm®), entered the clinical phase II trials after being tested in several types of tumours such as glioblastoma or prostate. However, to date yet there are no commercially available treatments for magnetic hyperthermia Moreover, the limited heating efficiency of the particles in clinical trials results in other issues such as the need to use very high magnetic fields or due to the huge amount of particles that is required, following the progression of the tumour by MRI is not possible due to the artifacts of the remaining particles in the tumour.[106]

Photothermia: An alternative to magnetic hyperthermia is to induce the temperature increase by optical excitation, *i.e.*, photothermia. In this approach, particles are irradiated with a laser, typically in the infrared region. As a response to the absorption of the radiation, particles release heat. Due to the relatively simple mechanism of this approach, there are not as many restrictions as in the case of magnetic hyperthermia when it comes to choose the constituent material for the particles (apart from, of course, being biocompatible) and thus there is a moderately big variety of substances that can be used in photothermia, like semiconductor nanocrystals, carbon based nanoparticles (such as graphene), organic dye molecules, organic semiconducting polymer nanoparticles, chalcogenides, etc.[107] Because the energy that can be transformed into

heat depends on the energy that is initially absorbed, plasmonic materials (like noble metallic nanoparticles) are very popular, since their plasmon resonance can be tuned so as to match the laser wavelength that is going to be used for the irradiation, thus maximizing the absorption. In addition, due to its high stability and inertness (and consequently, expected biocompatibility) gold has become one of the most widespread plasmonic materials. Indeed, thanks to its enhanced optical properties, the achieved temperature increases can be huge with very low dosages of particles, as opposite to magnetic hyperthermia. For example, in 2009, Schwartz *et al.* achieved temperatures of up to 65 °C in the brain tumours of dogs using gold nanoshells and a laser at 808 nm.[108] Another advantage of optical hyperthermia is that unlike magnetic hyperthermia, the heating properties are not harnessed by the cell endocytosis. Even more, some authors report that the confinement of particles within cell vesicles can have an enhancing effect on optical hyperthermia.[109]

On the other hand, the major disadvantages of optical hyperthermia are i) limited penetration (as the tissues between the laser source and the particles can also absorb part of the energy before reaching the particles); and ii) the little versatility due to the lack of magnetic properties in the materials that can be employed, which otherwise could enable magnetic active targeting, contrast enhancement in MRI, magnetic hyperthermia, etc. For example, despite gold particles have become the standard in this kind of therapies, their use is limited to therapeutic effectors. In addition, they can be less biocompatible due to its biopersistency,[110] unlike iron-based nanoparticles, which even have their own biochemical pathway for its metabolism.

A possible solution to overcome this disadvantage is to combine materials with good optical properties with magnetic elements, creating hybrid nanoparticles. For example, although not as efficient as their plasmonic competitors, recently some magnetic non-plasmonic materials have shown certain potential as optical heaters. For instance, in 2013, Chen *et al.*, used FePt nanoparticles for hyperthermia, achieving an efficiency comparable to gold nanorods.[111] However, the tunability of the optical properties of plasmonic materials contrasts with the staticity of non-plasmonic materials, where the properties are determined by the chemical composition and essentially independent from the particle size or shape. This might represent an inconvenience in biomedicine, where the irradiation conditions that can be used are quite restricted for safety reasons. Therefore, optimisation of the properties in non-plasmonic materials to enhance the heating properties might be challenging. For instance, in the particular case of the above mentioned example, FePt nanoparticles showed a maximum in their spectrum in the ultraviolet region. However, due to the absorbance of water and biological tissues, the

wavelengths that can be used for optical heating are limited to the so-called biological windows,[112] which are two regions in the infrared where tissues have an absorbance minimum. Hence, irradiating at the wavelength where these particles show a maximum is not feasible. Other approaches involve the combination of plasmonic and magnetic materials. For example, Li *et al*., employed lithography to deposit gold onto structures of magnetic elements such as iron or cobalt.[113] These particles did show a magnetic response while preserving the optical heating properties of gold. However, this approach has a major issue, as none of these magnetic elements is approved for its use on humans.

Probably motivated by the need of biocompatible but yet versatile materials, recently, some other researchers tried to achieve optical heating using iron oxide nanoparticles. Perhaps, one of the most relevant studies in the field is the one of Espinosa *et al*. who, in the year 2016, achieved tumour regression in mice by combining both magnetic and optical hyperthermia.[114] Since the wavelengths that can be used in optical hyperthermia are restricted, usually laser sources in the range of 800 nm are employed. Unfortunately, the spectra of both magnetite and maghemite show a minimum absorbance in that region, which makes them less efficient heaters than plasmonic particles.

In summary, the current dichotomy with photothermia therapies is to choose whether to use a highly biocompatible and multi-functional material but less efficient heater like iron oxide; or to choose one that can provide more heating power (at least as long light can penetrate to the target) but not as versatile nor biocompatible, like gold. Consequently, it would be advantageous to merge into one single type of particle the best of the two worlds (*i.e.*, high heating efficiency, good magnetic properties and high biocompatibility).

4. STRATEGIES TO OPTIMIZE THE POTENTIAL OF IRON OXIDE NANOPARTICLES IN BIOMEDICINE

Given the huge potential of magnetic nanoparticles for biomedicine, there is an increasing interest towards the enhancement of some of their properties to improve the performance in, for example, hyperthermia and/or MRI. For this aim, many different approaches have been used. Some of the most relevant are:

Doping with transition metal ions: changing the chemical composition can be a way to tune the magnetic properties as desired. In the particular case of iron oxides, some cations (usually bivalent) can be introduced to produce ferrites. Perhaps the most common example of metal

doping in magnetite is cobalt ferrite. Despite having a slightly lower M_s than that of magnetite (80 vs 90 emu/g), cobalt ferrite has a much larger magnetocrystal anisotropy, which causes a great H_c enhancement respect to magnetite. As a result, cobalt ferrite nanoparticles have shown a great improvement in both magnetic heating efficiency and performance as contrast agent.[115] However, cobalt is a somewhat *exotic* element for the organism, at least compared with iron. Therefore, its biocompatibility remains unclear. Certainly, some studies have reported reactivity of cobalt ferrite nanoparticles against the red blood cell membranes.[116] In any case, at this point it is important to remember that so far only magnetite and maghemite are approved by the FDA for their use in humans, so changing the chemical composition of iron oxides to include other metals is currently perhaps not the best choice to enhance the performance.

Combination with plasmonic materials: although maybe magnetic hyperthermia as a stand-alone therapy might not be powerful enough to provide clinical effects at low-dosages, an alternative to increase the heating power is to combine magnetic with optical heating. In this kind of approaches, although sometimes a plasmonic material is decorated with iron oxide nanoparticles, most often iron oxide particles are synthesized separately and then coated with plasmonic materials.[117] Using chemical methods, the coating with plasmonic substrates such as aluminium[118] or CuS[119] was successfully achieved. However, once again the issues concerning the toxicity restrict the number of elements that can be used. Hence, when intended for biomedicine, gold is mainly the material of choice in plasmonics. Although some authors have claimed that they successfully attached or coated iron oxide nanoparticles with gold,[62,120] blending both materials in a reproducible, homogeneous and fully controllable manner, which is critical to tune the resonance of the plasmon, still remains an experimental challenge. The reasons for this difficulty lies in the fact that both iron oxides and gold have very different crystal structures.[121] Alternative approaches to chemical synthesis involve, for example, the utilisation of physical methods such as lithography for depositing vaporised metals onto a substrate. In this way, some authors reported great heating capacities for bimetallic (iron and gold) particles, with a really tight control over the gold shell thickness.[122] Unfortunately, so far, lithography is not a sufficiently scalable process and only moderate amounts of particles are obtained.

Particle clustering: although random aggregation is usually detrimental for biomedical applications,[123] controlled aggregation of small clusters can be advantageous for several applications (*i.e.*, drug delivery and photonic crystals) [124] and also for magnetic hyperthermia.[125,126] For example, the formation of chain-like arrays of magnetic nanoparticles

boosts the effective anisotropy and susceptibility, leading to an enhancement of hysteresis losses.[127] Some studies reported a two-fold increase in hyperthermia efficiency for aligned particles with respect to randomly ordered states.[128] However, controlling and preserving in biological environments the amount of particles that build up the aggregates in a precise way might be rather complex, which can lead to polydisperse aggregates. This can be a problem for injectable materials, where large aggregates can obliterate blood vessels. An alternative could be the clustering of small iron oxide nanoparticles into one single nanostructure, as in the so called "nanoflowers". Actually, some authors reported an improvement in hyperthermia of one order of magnitude in nanoflowers respect to non-clustered individual particles.[129] Unfortunately, unlike "single entity" nanoparticles, once endocytosed nanoflowers have been proven to rapidly decompose into smaller and much less effective particles that can be metabolised much quicker and therefore their *in vivo* lability limits their applications.[78]

Reducing polydispersity and improving crystallinity: as mentioned in earlier, magnetic properties depend on the particle size. In particular, H_c reaches its maximum in the transition size between superparamagnetism and ferrimagnetism. This means that heating by hysteresis losses will be maximized for particles of this size. Actually, some authors confirmed that magnetite particles of this size show a much better performance than others slightly smaller or slightly larger.[130] However, despite the improvement in chemical synthesis, the particle size is usually spread over several nanometres. This deviation is typically represented by the standard deviation or the polydispersity index (PDI). It is commonly accepted that when the PDI is equal to or smaller than 10%, the nanoparticles can be considered as monodisperse.[131] However, in most of the syntheses the PDI is considerably higher than this value, leading to a reduction of the performance for biomedical applications. This effect can be easily understood if one just considers that every particle that has a different size than the ideal one will not have the optimal properties. For example, some studies showed that substantially higher hyperthermia performance can be achieved by decreasing the polydispersity of iron oxide nanoparticles and optimizing the size.[132] For hyperthermia and other applications increasing the M_S could be also an alternative way to enhance the performance. To obtain M_S values as close as possible to bulk values in iron oxides it is very important to have highly crystalline nanoparticles and minimize surface disorder.[133] Consequently, more efforts should be devoted to trying to develop new synthetic strategies to reduce polydispersity and improve crystallinity so as to get particles with optimal properties.

Anisotropic structures: changing the morphology of the particles into non-spherical structures can be very effective to tune the magnetic properties. Briefly, shape anisotropy increases the tendency of the magnetisation to align in a particular direction. As a result, the blocking temperature and H_c increase, favouring the single-domain state for smaller particles than those of similar volume but with a spherical structure (see Section 1.1). These effects can have a positive influence on the performance for biomedical applications. For example, a direct consequence of these changes is the increase of the squareness of the hysteresis loop,[134] which can be beneficial for magnetic hyperthermia. Several studies have reported great enhancements in hyperthermia for anisotropic nanoparticles compared to spheres of similar volume.[135,136] Also for MRI shape anisotropy can be important. For example, Nikitin et al., reported higher relaxivities for anisotropic nanoparticles compared to spherical analogues, which were explained as a consequence of their enhanced magnetic properties but also from their large effective surface area.[137] Finally, and although it is not related to magnetism, anisotropic nanoparticles could have higher efficiency as photothermal heaters: because of the shape anisotropy, some structures (such as rods) can have an optical cross-section one order of magnitude larger than spherical particles, resulting in an enhancement of the optical absorbance.[138,139] However, the synthesis of high quality anisotropic magnetic nanoparticles is still a challenge, since isotropic growth is usually more favoured. Moreover, due to the higher surface exposure, anisotropic nanoparticles will trend to aggregate more easily than particles of similar size so as to minimize the surface energy. Consequently, when working with this kind of structures, special attention should be paid to control the colloidal stabilisation by i) thoroughly controlling the size so as to avoid working with exceedingly large particles with a large remanent magnetization and ii) carefully selecting the coating.

5. GOALS OF THIS WORK

After taking into account the potential and current challenges in the use of iron oxide nanoparticles in nanomedicine, the goals of this work are defined as: to synthesize monodisperse, colloidally stable, shape anisotropic iron oxide nanoparticles (such as nanocubes and nanorods) with a well-defined structure and high crystallinity for their potential use in cancer diagnosis and therapy. For these purposes, several synthetic strategies will be tested to produce nanoparticles with optimal properties, which will involve an extensive characterisation. In addition, the surface of the nanoparticles will be modified as required to

31

ensure colloidal stability in biological environments. Eventually, the potential of the particles for cancer diagnosis and therapy in different modalities will be carefully evaluated.

6. References

(1)   Caruso, G.; Merlo, L.; Caffo, M. UK: Woodhead Publishing: Cambridge. *Innovative Brain Tumor Therapy: Nanoparticle-Based Therapeutic Strategies*; Elsevier, **2014**; 167–173

(2)   Sonström, P.; Bäumer, M. Supported Colloidal Nanoparticles in Heterogeneous Gas Phase Catalysis: On the Way to Tailored Catalysts. *Phys. Chem. Chem. Phys.* **2011**, 13 (43), 19270-19284.

(3)   M. L. T. Cossio, L. F. Giesen, G. Araya, M. L. S. Pérez-Cotapos, R. L. Vergara, M. Manca, R. A. Tohme, S. D. Holmberg, T. Bressmann, D. R. Lirio, J. S. Román, R. G. Solís, S. Thakur, S. N. Rao, E. L. Modelado, A. D. E. La, C. Durante, U. N. A. Tradición, M. En, E. L. Espejo, D. E. L. A. S. Fuentes, U. A. De Yucatán, C. M. Lenin, L. F. Cian, M. J. Douglas, L. Plata, & F. Héritier, Large-Area Synthesis of High-Quality and Uniform Graphene Films on Copper Foils. Science Mag, XXXIII (**2012**) 81–87.

 (4)   Ju, Y. S. Phonon Heat Transport in Silicon Nanostructures. *Appl. Phys. Lett.* **2005**, 87 (15), 153106.

(5)   Reimann, S. M.; Manninen, M. Electronic Structure of Quantum Dots. *Rev. Mod. Phys.* **2002**, 74 (4), 1283–1342.

(6)   Brkić, S. Applicability of Quantum Dots in Biomedical Science. In Ionizing Radiation Effects and Applications; InTech, **2018**; 2, 21-36

(7)   Kongkanand, A.; Tvrdy, K.; Takechi, K.; Kuno, M.; Kamat, P. V. Quantum Dot Solar Cells. Tuning Photoresponse through Size and Shape Control of CdSe−TiO 2 Architecture. *J. Am. Chem. Soc.* **2008**, 130 (12), 4007–4015.

(8)   Erickson, H. P. Size and Shape of Protein Molecules at the Nanometer Level Determined by Sedimentation, Gel Filtration, and Electron Microscopy. *Biol. Proced. Online* **2009**, 11 (1), 32–51.

(9)   C. Grossman, J. A Little Bit about Nanotechnology. **2007**. *http://web.mit.edu/jcg/www/Outreach_files/a_little_bit_about_nano.pdf*

(10)   Bobo, D.; Robinson, K. J.; Islam, J.; Thurecht, K. J.; Corrie, S. R. Nanoparticle-Based

Medicines: A Review of FDA-Approved Materials and Clinical Trials to Date. *Pharm. Res.* **2016**, 33 (10), 2373–2387.

(11) Universite Concordia. Nanomaterials Safety Guidelines. **2017**, 1–33.

(12) Terris, B. D.; Thomson, T. Nanofabricated and Self-Assembled Magnetic Structures as Data Storage Media. *J. Phys. D. Appl. Phys.* **2005**, 38 (12), R199–R222.

(13) Reddy, L. H.; Arias, J. L.; Nicolas, J.; Couvreur, P. Magnetic Nanoparticles: Design and Characterization, Toxicity and Biocompatibility, Pharmaceutical and Biomedical Applications. *Chem. Rev.* **2012**, 112 (11), 5818–5878.

(14) Haun, J. B.; Yoon, T.-J.; Lee, H.; Weissleder, R. Magnetic Nanoparticle Biosensors. *Wiley Interdiscip. Rev. Nanomedicine Nanobiotechnology* **2010**, 2 (3), 291–304.

(15) Zhou, Z.; Yang, L.; Gao, J.; Chen, X. Structure-Relaxivity Relationships of Magnetic Nanoparticles for Magnetic Resonance Imaging. *Adv. Mater.* **2019**, 1804567.

(16) Tang, S. C. N.; Lo, I. M. C. Magnetic Nanoparticles: Essential Factors for Sustainable Environmental Applications. *Water Res.* **2013**, 47 (8), 2613–2632.

(17) Phan, N. T. S.; Jones, C. W. Highly Accessible Catalytic Sites on Recyclable Organosilane-Functionalized Magnetic Nanoparticles: An Alternative to Functionalized Porous Silica Catalysts. *J. Mol. Catal. A Chem.* **2006**, 253 (1–2), 123–131.

(18) Cornell, R. M.; Schwertmann, U. *The Iron Oxides: Structure, Properties, Reactions, Occurences and Uses*, 2nd ed.; Wiley-VCH GmbH & Co. KGaA, **2003**.

(19) Iwaki, T.; Kakihara, Y.; Toda, T.; Abdullah, M.; Okuyama, K. Preparation of High Coercivity Magnetic FePt Nanoparticles by Liquid Process. *J. Appl. Phys.* **2003**, 94 (10), 6807–6811.

(20) Wang, D.; Doyle, W. D. High Coercivity FeSmN Thin Films for Longitudinal Magnetic Recording Media. *IEEE Trans. Magn.* **1994**, 30 (6), 4032–4034.

(21) Bedanta, S. Supermagnetism in Magnetic Nanoparticle Systems. **2006**, 1–188. https://duepublico2.uni-due.de/receive/duepublico_mods_00014868

(22) Devi, S. M.; Nivetha, A.; Prabha, I. Superparamagnetic Properties and Significant Applications of Iron Oxide Nanoparticles for Astonishing Efficacy—a Review. *J. Supercond. Nov. Magn.* **2018**, 3, 1–18.

(23) Paunović, N.; Popović, Z. V.; Dohčević-Mitrović, Z. D. Superparamagnetism in Iron-

Doped CeO_{2-y} Nanocrystals. *J. Phys. Condens. Matter* **2012**, 24 (45), 456001.

(24) Lu, A.-H.; Salabas, E. L.; Schüth, F. Magnetic Nanoparticles: Synthesis, Protection, Functionalization, and Application. *Angew. Chemie Int. Ed.* **2007**, 46 (8), 1222–1244.

(25) Respaud, M.; Broto, J. M.; Rakoto, H.; Fert, A. R.; Thomas, L.; Barbara, B.; Verelst, M.; Snoeck, E.; Lecante, P.; Mosset, A.; Osuna, J.; Ely, T. O.; Amiens, C.; Chaudret, B. Surface Effects on the Magnetic Properties of Ultrafine Cobalt Particles. *Phys. Rev. B* **1998**, 57 (5), 2925–2935.

(26) Bødker, F.; Mørup, S.; Linderoth, S. Surface Effects in Metallic Iron Nanoparticles. *Phys. Rev. Lett.* **1994**, 72 (2), 282–285.

(27) Wetterskog, E.; Tai, C.-W.; Grins, J.; Bergström, L.; Salazar-Alvarez, G. Anomalous Magnetic Properties of Nanoparticles Arising from Defect Structures: Topotaxial Oxidation of $Fe_{1-x}O|Fe_{3-\delta}O_4$ Core|Shell Nanocubes to Single-Phase Particles. *ACS Nano* **2013**, 7 (8), 7132–7144.

(28) Tobia, D.; Winkler, E.; Zysler, R. D.; Granada, M.; Troiani, H. E. Size Dependence of the Magnetic Properties of Antiferromagnetic Cr_2O_3 Nanoparticles. *Phys. Rev. B - Condens. Matter Mater. Phys.* **2008**, 78 (10), 1–7.

(29) Kudr, J.; Haddad, Y.; Richtera, L.; Heger, Z.; Cernak, M.; Adam, V.; Zitka, O. Magnetic Nanoparticles: From Design and Synthesis to Real World Applications. *Nanomaterials* **2017**, 7 (9), 243-244.

(30) Chen, G.; Roy, I.; Yang, C.; Prasad, P. N. Nanochemistry and Nanomedicine for Nanoparticle-Based Diagnostics and Therapy. *Chem. Rev.* **2016**, 116 (5), 2826–2885.

(31) Kwon, S. G.; Hyeon, T. Colloidal Chemical Synthesis and Formation Kinetics of Uniformly Sized Nanocrystals of Metals, Oxides, and Chalcogenides. *Acc. Chem. Res.* **2008**, 41 (12), 1696–1709.

(32) Poncharal, P.; Wang, Z. L.; Ugarte, D.; De Heer, W. a. Electrostatic Deflections and Electromechanical Resonances of Carbon Nanotubes. *Science.* **1999**, 283 (5407), 1513–1516.

(33) Faraji, M.; Yamini, Y.; Rezaee, M. Magnetic Nanoparticles: Synthesis, Stabilization, Functionalization, Characterization, and Applications. *J. Iran. Chem. Soc.* **2010**, 7 (1), 1–37.

(34) Gupta, A. K.; Gupta, M. Synthesis and Surface Engineering of Iron Oxide Nanoparticles

for Biomedical Applications. *Biomaterials* **2005**, 26 (18), 3995–4021.

(35) Klier, J.; Tucker, C. J.; Kalantar, T. H.; Green, D. P. Properties and Applications of Microemulsions. *Adv. Mater.* **2000**, 12 (23), 1751–1757.

(36) Liu, C.; Zhang, Z. J. Size-Dependent Superparamagnetic Properties of Mn Spinel Ferrite Nanoparticles Synthesized from Reverse Micelles. *Chem. Mater.* **2001**, 13 (6), 2092–2096.

(37) Carpenter, E. E.; Sims, J. a.; Wienmann, J. a.; Zhou, W. L.; O'Connor, C. J. Magnetic Properties of Iron and Iron Platinum Alloys Synthesized via Microemulsion Techniques. *J. Appl. Phys.* **2000**, 87 (9), 5615–5617.

(38) Cardoso, V. F.; Irusta, S.; Navascues, N.; Lanceros-Mendez, S. Comparative Study of Sol-Gel Methods for the Facile Synthesis of Tailored Magnetic Silica Spheres. *Mater. Res. Express* **2016**, 3 (7), 075402.

(39) Han, C.; Ma, J.; Wu, H.; Hu, K. A Low-Cost And High-Yield Production Of Magnetite Nanorods With High Saturation Magnetization. **2015**, 1, 2799–2802.

(40) F. Hasany, S.; Ahmed, I.; J, R.; Rehman, A. Systematic Review of the Preparation Techniques of Iron Oxide Magnetic Nanoparticles. *Nanosci. Nanotechnol.* **2013**, 2 (6), 148–158.

(41) Ribeiro, C.; Cardoso, V. F.; Francesko, A.; Martins, P.; Bañobre-López, M.; Lanceros-Mendez, S. Advances in Magnetic Nanoparticles for Biomedical Applications. *Adv. Healthc. Mater.* **2017**, 7 (5), 1700845.

(42) Sreeja, V.; Joy, P. a. Microwave-Hydrothermal Synthesis of γ-Fe$_2$O$_3$ Nanoparticles and Their Magnetic Properties. *Mater. Res. Bull.* **2007**, 42 (8), 1570–1576.

(43) Frey, N. A.; Peng, S.; Cheng, K.; Sun, S. Magnetic Nanoparticles: Synthesis, Functionalization, and Applications in Bioimaging and Magnetic Energy Storage. *Chem. Soc. Rev.* **2009**, 38 (9), 2532-2533.

(44) Kemp, S. J.; Ferguson, R. M.; Khandhar, A. P.; Krishnan, K. M. Monodisperse Magnetite Nanoparticles with Nearly Ideal Saturation Magnetization. *RSC Adv.* **2016**, 6 (81), 77452–77464.

(45) LaMer, V. K.; Dinegar, R. H. Theory, Production and Mechanism of Formation of Monodispersed Hydrosols. *J. Am. Chem. Soc.* **1950**, 72 (11), 4847–4854.

(46) Murray, C. B.; Norris, D. J.; Bawendi, M. G. Synthesis and Characterization of Nearly

Monodisperse CdE (E = Sulfur, Selenium, Tellurium) Semiconductor Nanocrystallites. *J. Am. Chem. Soc.* **1993**, 115 (19), 8706–8715.

(47) Sun, S.; Zeng, H. Size-Controlled Synthesis of Magnetite Nanoparticles. *J. Am. Chem. Soc.* **2002**, 124 (28), 8204–8205.

(48) Haracz, S.; Hilgendorff, M.; Rybka, J. D.; Giersig, M. Effect of Surfactant for Magnetic Properties of Iron Oxide Nanoparticles. *Nucl. Instruments Methods Phys. Res. Sect. B Beam Interact. with Mater. Atoms* **2015**, 364, 120–126.

(49) Tartaj, P.; Morales, M. P.; Veintemillas-Verdaguer, S.; Gonzalez-Carreno, T.; Serna, C. J. The Preparation of Magnetic Nanoparticles for Applications in Biomedicine. *J. Phys. D Appl. Phys.* **2003**, 36 (22), R182–R197.

(50) Markides, H.; Rotherham, M.; El Haj, A. J. Biocompatibility and Toxicity of Magnetic Nanoparticles in Regenerative Medicine. *J. Nanomater.* **2012**, 1–11.

(51) Chang, D.; Lim, M.; Goos, J. A. C. M.; Qiao, R.; Ng, Y. Y.; Mansfeld, F. M.; Jackson, M.; Davis, T. P.; Kavallaris, M. Biologically Targeted Magnetic Hyperthermia: Potential and Limitations. *Front. Pharmacol.* **2018**, 9-10.

(52) Wu, W.; Wu, Z.; Yu, T.; Jiang, C.; Kim, W.-S. Recent Progress on Magnetic Iron Oxide Nanoparticles: Synthesis, Surface Functional Strategies and Biomedical Applications. *Sci. Technol. Adv. Mater.* **2015**, 16 (2), 023501.

(53) Bronstein, L. M.; Huang, X.; Retrum, J.; Schmucker, A.; Pink, M.; Stein, B. D.; Dragnea, B. Influence of Iron Oleate Complex Structure on Iron Oxide Nanoparticle Formation. *Chem. Mater.* **2007**, 19 (15), 3624–3632.

(54) Wood, M. H.; Welbourn, R. J. L.; Charlton, T.; Zarbakhsh, A.; Casford, M. T.; Clarke, S. M. Hexadecylamine Adsorption at the Iron Oxide–Oil Interface. *Langmuir* **2013**, 29 (45), 13735–13742.

(55) Yang, X.; Grailer, J. J.; Rowland, I. J.; Javadi, A.; Hurley, S. a.; Steeber, D. a.; Gong, S. Multifunctional SPIO/DOX-Loaded Wormlike Polymer Vesicles for Cancer Therapy and MR Imaging. *Biomaterials.* **2010**, 31 (34), 9065–9073.

(56) Pimpha, N.; Chaleawlert-umpon, S.; Sunintaboon, P. Core/Shell Polymethyl Methacrylate/Polyethyleneimine Particles Incorporating Large Amounts of Iron Oxide Nanoparticles Prepared by Emulsifier-Free Emulsion Polymerization. *Polymer.* **2012**, 53 (10), 2015–2022.

(57) Pellegrino, T.; Manna, L.; Kudera, S.; Liedl, T.; Koktysh, D.; Rogach, A. L.; Keller, S.; Rädler, J.; Natile, G.; Parak, W. J. Hydrophobic Nanocrystals Coated with an Amphiphilic Polymer Shell: A General Route to Water Soluble Nanocrystals. *Nano Lett.* **2004**, 4 (4), 703–707.

(58) Farrell, D.; Majetich, S. a; Wilcoxon, J. P. Preparation and Characterization of Monodisperse Fe Nanoparticles. *J. Phys. Chem. B* **2003**, 107 (40), 11022–11030.

(59) Jain, P. K.; Xiao, Y.; Walsworth, R.; Cohen, A. E. Surface Plasmon Resonance Enhanced Magneto-Optics (SuPREMO): Faraday Rotation Enhancement in Gold-Coated Iron Oxide Nanocrystals. *Nano Lett.* **2009**, 9 (4), 1644–1650.

(60) Ye, Y.; Kuai, L.; Geng, B. A Template-Free Route to a Fe_3O_4–Co_3O_4 Yolk–shell Nanostructure as a Noble-Metal Free Electrocatalyst for ORR in Alkaline Media. *J. Mater. Chem.* **2012**, 22 (36), 19132-19138.

(61) Henry, A.-I.; Bingham, J. M.; Ringe, E.; Marks, L. D.; Schatz, G. C.; Van Duyne, R. P. Correlated Structure and Optical Property Studies of Plasmonic Nanoparticles. *J. Phys. Chem. C* **2011**, 115 (19), 9291–9305.

(62) Robinson, I.; Tung, L. D.; Maenosono, S.; Wälti, C.; Thanh, N. T. K. Synthesis of Core-Shell Gold Coated Magnetic Nanoparticles and Their Interaction with Thiolated DNA. *Nanoscale* **2010**, 2 (12), 2624-2630.

(63) Colvin, V. L.; Goldstein, a. N.; Alivisatos, a. P. Semiconductor Nanocrystals Covalently Bound to Metal Surfaces with Self-Assembled Monolayers. *J. Am. Chem. Soc.* **1992**, 114 (13), 5221–5230.

(64) Gu, H.; Zheng, R.; Zhang, X.; Xu, B. Facile One-Pot Synthesis of Bifunctional Heterodimers of Nanoparticles: A Conjugate of Quantum Dot and Magnetic Nanoparticles. *J. Am. Chem. Soc.* **2004**, 126 (18), 5664–5665.

(65) Pinho, S. L. C.; Laurent, S.; Rocha, J.; Roch, A.; Delville, M.-H.; Mornet, S.; Carlos, L. D.; Vander Elst, L.; Muller, R. N.; Geraldes, C. F. G. C. Relaxometric Studies of γ-Fe_2O_3@SiO_2 Core Shell Nanoparticles: When the Coating Matters. *J. Phys. Chem. C* **2012**, 116 (3), 2285–2291.

(66) Naghavi, M.; Abajobir, A. A.; Abbafati, C.; Abbas, K. M.; Abd-Allah, F.; Abera, S. F.; Aboyans, V.; Adetokunboh, O.; Afshin, A.; Agrawal, A.; Ahmadi, A.; Ahmed, M. B.; Aichour, A. N.; Aichour, M. T. E.; Aichour, I.; Aiyar, S.; Alahdab, F.; Al-Aly, Z.; Alam,

K.; et al. Global, Regional, and National Age-Sex Specific Mortality for 264 Causes of Death, 1980–2016: A Systematic Analysis for the Global Burden of Disease Study 2016. *Lancet* **2017**, 390 (10100), 1151–1210.

(67)   Defining Cancer. **2018**. *https://www.cancer.gov/about-cancer/understanding/statistics*

(68)   Greenlee, R. T.; Murray, T.; Bolden, S.; Wingo, P. A. Cancer Statistics, 2000. **2000**, 50 (1), 7–33.

(69)   Hirsch, F.; Wilbur, A.; Franklin, A.; Gazdar, F.; Bunn, P. Early Detection of Lung Cancer: Clinical Perspectives of Recent Advances in Biology and Radiology. *Clin. Cancer Res.* **2001**, 7 (1), 5–22.

(70)   Why Is Early Diagnosis Important? **2018**. *https://www.cancerresearchuk.org/about-cancer/cancer-symptoms/why-is-early-diagnosis-important*

(71)   Hehr, T.; Wust, P.; Bamberg, M.; Budach, W. Current and Potential Role of Thermoradiotherapy for Solid Tumours. *Oncol. Res. Treat.* **2003**, 26 (3), 295–302.

(72)   Hartmann, J. T.; Lipp, H.-P. Toxicity of Platinum Compounds. *Expert Opin. Pharmacother.* **2003**, 4 (6), 889–901.

(73)   Hemming, A. W.; Davis, N. L.; Kluftinger, A.; Robinson, B.; Quenville, N. F.; Liseman, B.; Lcriche, J. Prognostic Markers of Colorectal Cancer: An Evaluation of DNA Content, Epidermal Growth Factor Receptor, and Ki-67. *J. Surg. Oncol.* **1992**, 51 (3), 147–152.

(74)   Mihai, R.; Stevens, J.; McKinney, C.; Ibrahim, N. B. N. Expression of the Calcium Receptor in Human Breast Cancer—a Potential New Marker Predicting the Risk of Bone Metastases. *Eur. J. Surg. Oncol.* **2006**, 32 (5), 511–515.

(75)   Shaw, R. J. Glucose Metabolism and Cancer. *Curr. Opin. Cell Biol.* **2006**, 18 (6), 598–608.

(76)   Jiang, Z.; Shan, K.; Song, J.; Liu, J.; Rajendran, S.; Pugazhendhi, A.; Jacob, J. A.; Chen, B. Toxic Effects of Magnetic Nanoparticles on Normal Cells and Organs. *Life Sci.* **2019**, 220, 156–161.

(77)   Anselmo, A. C.; Mitragotri, S. A Review of Clinical Translation of Inorganic Nanoparticles. *The AAPS Journal.* **2015**, 17 (5), 1041–1054.

(78)   Kolosnjaj-Tabi, J.; Lartigue, L.; Javed, Y.; Luciani, N.; Pellegrino, T.; Wilhelm, C.; Alloyeau, D.; Gazeau, F. Biotransformations of Magnetic Nanoparticles in the Body.

Nano Today **2016**, 11 (3), 280–284.

(79) Beaumont, C.; Delaby, C. Recycling Iron in Normal and Pathological States. *Semin. Hematol.* **2009**, 46 (4), 328–338.

(80) Song, C.; Sun, W.; Xiao, Y.; Shi, X. Ultrasmall Iron Oxide Nanoparticles: Synthesis, Surface Modification, Assembly, and Biomedical Applications. *Drug Discov. Today* **2019**, 24 (3), 835–844.

(81) Luo, Y.; Yang, J.; Yan, Y.; Li, J.; Shen, M.; Zhang, G.; Mignani, S.; Shi, X. RGD-Functionalized Ultrasmall Iron Oxide Nanoparticles for Targeted T 1 -Weighted MR Imaging of Gliomas. *Nanoscale* **2015**, 7 (34), 14538–14546.

(82) Chen, F.; Ward, J.; Robinson, P. . MR Imaging of the Liver and Spleen: A Comparison of the Effects on Signal Intensity of Two Superparamagnetic Iron Oxide Agents. *Magn. Reson. Imaging* **1999**, 17 (4), 549–556.

(83) Neuwelt, A.; Sidhu, N.; Hu, C.-A. A.; Mlady, G.; Eberhardt, S. C.; Sillerud, L. O. Iron-Based Superparamagnetic Nanoparticle Contrast Agents for MRI of Infection and Inflammation. *Am. J. Roentgenol.* **2015**, 204 (3), W302–W313.

(84) Wang, Y.-X. J.; Hussain, S. M.; Krestin, G. P. Superparamagnetic Iron Oxide Contrast Agents: Physicochemical Characteristics and Applications in MR Imaging. *Eur. Radiol.* **2001**, 11 (11), 2319–2331.

(85) Wu, Y. L.; Ye, Q.; Foley, L. M.; Hitchens, T. K.; Sato, K.; Williams, J. B.; Ho, C. In Situ Labeling of Immune Cells with Iron Oxide Particles: An Approach to Detect Organ Rejection by Cellular MRI. *Proc. Natl. Acad. Sci.* **2006**, 103 (6), 1852–1857.

(86) Asanuma, T.; Ono, M.; Kubota, K.; Hirose, A.; Hayashi, Y.; Saibara, T.; Inanami, O.; Ogawa, Y.; Enzan, H.; Onishi, S.; Kuwabara, M.; Oben, J. a. Super Paramagnetic Iron Oxide MRI Shows Defective Kupffer Cell Uptake Function in Non-Alcoholic Fatty Liver Disease. *Gut* **2010**, 59 (2), 258–266.

(87) Shah, A.; Mankus, C. I.; Vermilya, A. M.; Soheilian, F.; Clogston, J. D.; Dobrovolskaia, M. a. Feraheme® Suppresses Immune Function of Human T Lymphocytes through Mitochondrial Damage and MitoROS Production. *Toxicol. Appl. Pharmacol.* **2018**, 350 (April), 52–63.

(88) Mout, R.; Moyano, D. F.; Rana, S.; Rotello, V. M. Surface Functionalization of Nanoparticles for Nanomedicine. *Chem. Soc. Rev.* **2012**, 41 (7), 2539-2544.

(89) Ma, H.; Qi, X.; Maitani, Y.; Nagai, T. Preparation and Characterization of Superparamagnetic Iron Oxide Nanoparticles Stabilized by Alginate. *Int. J. Pharm.* **2007**, 333 (1–2), 177–186.

(90) Shao-Wen C; Ying-Jie Z; Ming-Yan M; Liang L; Ling Z. Hierarchically Nanostructured Magnetic Hollow Spheres of Fe_3O_4 and γ-Fe_2O_3: Preparation and Potential Application in Drug Delivery. *J. Phys. Chem. C* **2008**, 112 (6), 1851–1856.

(91) Laurent, S.; Forge, D.; Port, M.; Roch, A.; Robic, C.; Vander Elst, L.; Muller, R. N. Magnetic Iron Oxide Nanoparticles: Synthesis, Stabilization, Vectorization, Physicochemical Characterizations, and Biological Applications. *Chem. Rev.* **2010**, 110 (4), 2574–2574.

(92) Zhu, C.; Liu, L.; Yang, Q.; Lv, F.; Wang, S. Water-Soluble Conjugated Polymers for Imaging, Diagnosis, and Therapy. *Chem. Rev.* **2012**, 112 (8), 4687–4735.

(93) Zhu, X.-M.; Yuan, J.; Leung, K. C.-F.; Lee, S.-F.; Sham, K. W. Y.; Cheng, C. H. K.; Au, D. W. T.; Teng, G.-J.; Ahuja, A. T.; Wang, Y.-X. J. Hollow Superparamagnetic Iron Oxide Nanoshells as a Hydrophobic Anticancer Drug Carrier: Intracelluar PH-Dependent Drug Release and Enhanced Cytotoxicity. *Nanoscale* **2012**, 4 (18), 5744-5754.

(94) Zhang, J.; Misra, R. D. K. Magnetic Drug-Targeting Carrier Encapsulated with Thermosensitive Smart Polymer: Core–shell Nanoparticle Carrier and Drug Release Response. *Acta Biomater.* **2007**, 3 (6), 838–850.

(95) Pangestuti, R.; Kim, S.-K. Neuroprotective Properties of Chitosan and Its Derivatives. *Mar. Drugs* **2010**, 8 (7), 2117–2128.

(96) Wilson, M. W.; Kerlan, R. K.; Fidelman, N. a; Venook, A. P.; LaBerge, J. M.; Koda, J.; Gordon, R. L. Hepatocellular Carcinoma: Regional Therapy with a Magnetic Targeted Carrier Bound to Doxorubicin in a Dual MR Imaging/ Conventional Angiography Suite—Initial Experience with Four Patients. *Radiology* **2004**, 230 (1), 287–293.

(97) Tay, Z. W.; Chandrasekharan, P.; Chiu-Lam, A.; Hensley, D. W.; Dhavalikar, R.; Zhou, X. Y.; Yu, E. Y.; Goodwill, P. W.; Zheng, B.; Rinaldi, C.; Conolly, S. M. Magnetic Particle Imaging-Guided Heating in Vivo Using Gradient Fields for Arbitrary Localization of Magnetic Hyperthermia Therapy. *ACS Nano* **2018**, 12 (4), 3699–3713.

(98) Glazer, E. S.; Curley, S. a. The Ongoing History of Thermal Therapy for Cancer. *Surg.*

Oncol. Clin. N. Am. **2011**, 20 (2), 229–235.

(99) Thomas, L. A.; Dekker, L.; Kallumadil, M.; Southern, P.; Wilson, M.; Nair, S. P.; Pankhurst, Q. A.; Parkin, I. P. Carboxylic Acid-Stabilised Iron Oxide Nanoparticles for Use in Magnetic Hyperthermia. *J. Mater. Chem.* **2009**, 19 (36), 6529-6535.

(100) Rakesh, K. J. Determinants of Tumor Blood Flow: A Review. *Cancer Res.* **1988**, 48 (10), 2641–2658.

(101) Gilchrist, R. K.; Medal, R.; Shorey, W. D.; Hanselman, R. C.; Parrott, J. C.; Taylor, C. B. Selective Inductive Heating of Lymph Nodes. *Ann. Surg.* **1957**, 146 (4), 596–606.

(102) van Landeghem, F. K. H.; Maier-Hauff, K.; Jordan, A.; Hoffmann, K.; Gneveckow, U.; Scholz, R.; Thiesen, B.; Brück, W.; von Deimling, A. Post-Mortem Studies in Glioblastoma Patients Treated with Thermotherapy Using Magnetic Nanoparticles. *Biomaterials* **2009**, 30 (1), 52–57.

(103) Dadfar, S. M.; Roemhild, K.; Drude, N. I.; von Stillfried, S.; Knüchel, R.; Kiessling, F.; Lammers, T. Iron Oxide Nanoparticles: Diagnostic, Therapeutic and Theranostic Applications. *Adv. Drug Deliv. Rev.* **2019**, 138, 302–325.

(104) Ovejero, J. G.; Cabrera, D.; Carrey, J.; Valdivielso, T.; Salas, G.; Teran, F. J. Effects of Inter- and Intra-Aggregate Magnetic Dipolar Interactions on the Magnetic Heating Efficiency of Iron Oxide Nanoparticles. *Phys. Chem. Chem. Phys.* **2016**, 18 (16), 10954–10963.

(105) Kolosnjaj-Tabi, J.; Di Corato, R.; Lartigue, L.; Marangon, I.; Guardia, P.; Silva, A. K. A.; Luciani, N.; Clément, O.; Flaud, P.; Singh, J. V.; Decuzzi, P.; Pellegrino, T.; Wilhelm, C.; Gazeau, F. Heat-Generating Iron Oxide Nanocubes: Subtle "Destructurators" of the Tumoral Microenvironment. *ACS Nano* **2014**, 8 (5), 4268–4283.

(106) Maier-Hauff, K.; Ulrich, F.; Nestler, D.; Niehoff, H.; Wust, P.; Thiesen, B.; Orawa, H.; Budach, V.; Jordan, A. Efficacy and Safety of Intratumoral Thermotherapy Using Magnetic Iron-Oxide Nanoparticles Combined with External Beam Radiotherapy on Patients with Recurrent Glioblastoma Multiforme. *J. Neurooncol.* **2011**, 103 (2), 317–324.

(107) Hu, J.-J.; Cheng, Y.-J.; Zhang, X.-Z. Recent Advances in Nanomaterials for Enhanced Photothermal Therapy of Tumors. *Nanoscale* **2018**, 10 (48), 22657–22672.

(108) Schwartz, J. A.; Shetty, A. M.; Price, R. E.; Stafford, R. J.; Wang, J. C.; Uthamanthil, R. K.; Pham, K.; McNichols, R. J.; Coleman, C. L.; Payne, J. D. Feasibility Study of Particle-Assisted Laser Ablation of Brain Tumors in Orthotopic Canine Model. *Cancer Res.* **2009**, 69 (4), 1659–1667.

(109) Espinosa, A.; Kolosnjaj-Tabi, J.; Abou-Hassan, A.; Plan Sangnier, A.; Curcio, A.; Silva, A. K. A.; Di Corato, R.; Neveu, S.; Pellegrino, T.; Liz-Marzán, L. M.; Wilhelm, C. Magnetic (Hyper)Thermia or Photothermia? Progressive Comparison of Iron Oxide and Gold Nanoparticles Heating in Water, in Cells, and *In Vivo*. *Adv. Funct. Mater.* **2018**, 28 (37), 1803660.

(110) Chen, Y.-S.; Hung, Y.-C.; Liau, I.; Huang, G. S. Assessment of the In Vivo Toxicity of Gold Nanoparticles. *Nanoscale Res. Lett.* **2009**, 4 (8), 858–864.

(111) Chen, C. L.; Kuo, L. R.; Lee, S. Y.; Hwu, Y. K.; Chou, S. W.; Chen, C. C.; Chang, F. H.; Lin, K. H.; Tsai, D. H.; Chen, Y. Y. Photothermal Cancer Therapy via Femtosecond-Laser-Excited FePt Nanoparticles. *Biomaterials* **2013**, 34 (4), 1128–1134.

(112) Smith, A. M.; Mancini, M. C.; Nie, S. Bioimaging: Second Window for in Vivo Imaging. *Nat. Nanotechnol.* **2009**, 4 (11), 710–711.

(113) Li, Z.; Lopez-Ortega, A.; Aranda-Ramos, A.; Tajada, J. L.; Sort, J.; Nogues, C.; Vavassori, P.; Nogues, J.; Sepulveda, B. Simultaneous Local Heating/Thermometry Based on Plasmonic Magnetochromic Nanoheaters. *Small* **2018**, 14 (24), 1800868.

(114) Espinosa, A.; Di Corato, R.; Kolosnjaj-Tabi, J.; Flaud, P.; Pellegrino, T.; Wilhelm, C. Duality of Iron Oxide Nanoparticles in Cancer Therapy: Amplification of Heating Efficiency by Magnetic Hyperthermia and Photothermal Bimodal Treatment. *ACS Nano* **2016**, 10 (2), 2436–2446.

(115) Sathya, A.; Guardia, P.; Brescia, R.; Silvestri, N.; Pugliese, G.; Nitti, S.; Manna, L.; Pellegrino, T. Co x Fe 3– x O 4 Nanocubes for Theranostic Applications: Effect of Cobalt Content and Particle Size. *Chem. Mater.* **2016**, 28 (6), 1769–1780.

(116) Drašler, B.; Drobne, D.; Novak, S.; Valant, J.; Boljte, S.; Otrin, L.; Rappolt, M.; Sartori, B.; Iglič, a.; Kralj-Iglič, V.; Šuštar, V.; Makovec, D.; Gyergyek, S.; Hočevar, M.; Godec, M.; Zupanc, J. Effects of Magnetic Cobalt Ferrite Nanoparticles on Biological and Artificial Lipid Membranes. *Int. J. Nanomedicine* **2014**, 9 (1), 1559–1581.

(117) Lim, J.; Tilton, R. D.; Eggeman, A.; Majetich, S. a. Design and Synthesis of Plasmonic

Magnetic Nanoparticles. *J. Magn. Magn. Mater.* **2007**, 311 (1), 78–83.

(118) Huang, W.; Tsai, P.; Chen, Y. Multifunctional Fe$_3$O$_4$@Au Nanoeggs as Photothermal Agents for Selective Killing of Nosocomial and Antibiotic-Resistant Bacteria. *Small* **2009**, 5 (1), 51–56.

(119) Wu, Z. C.; Li, W. P.; Luo, C. H.; Su, C. H.; Yeh, C. S. Rattle-Type Fe$_3$O$_4$@CuS Developed to Conduct Magnetically Guided Photoinduced Hyperthermia at First and Second NIR Biological Windows. *Adv. Funct. Mater.* **2015**, 25 (41), 6527–6537.

(120) Abdulla-Al-Mamun, M.; Kusumoto, Y.; Zannat, T.; Horie, Y.; Manaka, H. Au-Ultrathin Functionalized Core–shell (Fe$_3$O$_4$@Au) Monodispersed Nanocubes for a Combination of Magnetic/Plasmonic Photothermal Cancer Cell Killing. *RSC Adv.* **2013**, 3 (21), 7816 -7827.

(121) Espinosa, A.; Bugnet, M.; Radke, G.; Neveu, S.; Botton, G.; Wilhelm, C.; Abou-Hassan, A. Can Magneto-Plasmonic Nanohybrids Efficiently Combine Photothermia with Magnetic Hyperthermia? *Nanoscale* **2015**, 7 (45), 18872–18877.

(122) Li, Z.; Aranda-Ramos, A.; Güell-Grau, P.; Tajada, J. L.; Pou-Macayo, L.; Lope Piedrafita, S.; Pi, F.; G. Roca, A.; Baró, M. D.; Sort, J.; Nogués, C.; Nogués, J.; Sepúlveda, B. Magnetically Amplified Photothermal Therapies and Multimodal Imaging with Magneto-Plasmonic Nanodomes. *Appl. Mater. Today* **2018**, 12, 430–440.

(123) Guibert, C.; Dupuis, V.; Peyre, V.; Fresnais, J. Hyperthermia of Magnetic Nanoparticles: Experimental Study of the Role of Aggregation. *J. Phys. Chem. C* **2015**, 119 (50), 28148–28154.

(124) Kralj, S.; Makovec, D. Magnetic Assembly of Superparamagnetic Iron Oxide Nanoparticle Clusters into Nanochains and Nanobundles. *ACS Nano* **2015**, 9 (10), 9700– 9707.

(125) Niculaes, D.; Lak, A.; Anyfantis, G. C.; Marras, S.; Laslett, O.; Avugadda, S. K.; Cassani, M.; Serantes, D.; Hovorka, O.; Chantrell, R.; Pellegrino, T. Asymmetric Assembling of Iron Oxide Nanocubes for Improving Magnetic Hyperthermia Performance. *ACS Nano* **2017**, 11 (12), 12121–12133.

(126) Cho, M.; Cervadoro, A.; Ramirez, M.; Stigliano, C.; Brazdeikis, A.; Colvin, V.; Civera, P.; Key, J.; Decuzzi, P. Assembly of Iron Oxide Nanocubes for Enhanced Cancer Hyperthermia and Magnetic Resonance Imaging. *Nanomaterials* **2017**, 7 (4), 72

(127) Conde-Leborán, I.; Serantes, D.; Baldomir, D. Orientation of the Magnetization Easy Axes of Interacting Nanoparticles: Influence on the Hyperthermia Properties. *J. Magn. Magn. Mater.* **2015**, 380, 321–324.

(128) Myrovali, E.; Maniotis, N.; Makridis, A.; Terzopoulou, A.; Ntomprougkidis, V.; Simeonidis, K.; Sakellari, D.; Kalogirou, O.; Samaras, T.; Salikhov, R.; Spasova, M.; Farle, M.; Wiedwald, U.; Angelakeris, M. Arrangement at the Nanoscale: Effect on Magnetic Particle Hyperthermia. *Sci. Rep.* **2016**, 6 (1), 37934.

(129) Hugounenq, P.; Levy, M.; Alloyeau, D.; Lartigue, L.; Dubois, E.; Cabuil, V.; Ricolleau, C.; Roux, S.; Wilhelm, C.; Gazeau, F.; Bazzi, R. Iron Oxide Monocrystalline Nanoflowers for Highly Efficient Magnetic Hyperthermia. *J. Phys. Chem. C* **2012**, 116 (29), 15702–15712.

(130) Guardia, P.; Di Corato, R.; Lartigue, L.; Wilhelm, C.; Espinosa, A.; Garcia-Hernandez, M.; Gazeau, F.; Manna, L.; Pellegrino, T. Water-Soluble Iron Oxide Nanocubes with High Values of Specific Absorption Rate for Cancer Cell Hyperthermia Treatment. *ACS Nano* **2012**, 6 (4), 3080–3091.

(131) Konno, M.; Nagao, D. Monodisperse Polymer Particles. *Encycl. Polym. Sci. Technol.* **2014**, 1–2.

(132) Gonzales-Weimuller, M.; Zeisberger, M.; Krishnan, K. M. Size-Dependant Heating Rates of Iron Oxide Nanoparticles for Magnetic Fluid Hyperthermia. *J. Magn. Magn. Mater.* **2009**, 321 (13), 1947–1950.

(133) Nemati, Z.; Alonso, J.; Rodrigo, I.; Das, R.; Garaio, E.; García, J. Á.; Orue, I.; Phan, M.-H.; Srikanth, H. Improving the Heating Efficiency of Iron Oxide Nanoparticles by Tuning Their Shape and Size. *J. Phys. Chem. C* **2018**, 122 (4), 2367–2381.

(134) Chen, M.; Kim, J.; Liu, J. P.; Fan, H.; Sun, S. Synthesis of FePt Nanocubes and Their Oriented Self-Assembly. *J. Am. Chem. Soc.* **2006**, 128 (22), 7132–7133.

(135) Suriyanto; Ng, E. Y. K.; Kumar, S. D. Physical Mechanism and Modeling of Heat Generation and Transfer in Magnetic Fluid Hyperthermia through Néelian and Brownian Relaxation: A Review. *Biomed. Eng. Online* **2017**, 16 (1), 36.

(136) Nemati, Z.; Alonso, J.; Martinez, L. M.; Khurshid, H.; Garaio, E.; Garcia, J. a.; Phan, M. H.; Srikanth, H. Enhanced Magnetic Hyperthermia in Iron Oxide Nano-Octopods: Size and Anisotropy Effects. *J. Phys. Chem. C* **2016**, 120 (15), 8370–8379.

(137) Nikitin, A. A.; Khramtsov, M. A.; Savchenko, A. G.; Abakumov, M. A.; Mazhuga, A. G. Anisotropic Iron-Oxide Nanoparticles for Diagnostic MRI: Synthesis and Contrast Properties. *Pharm. Chem. J.* **2018**, 52 (3), 231–235.

(138) Jain, P. K.; Lee, K. S.; El-Sayed, I. H.; El-Sayed, M. a. Calculated Absorption and Scattering Properties of Gold Nanoparticles of Different Size, Shape, and Composition: Applications in Biological Imaging and Biomedicine. *J. Phys. Chem. B* **2006**, 110 (14), 7238–7248.

(139) Lisjak, D.; Mertelj, A. Anisotropic Magnetic Nanoparticles: A Review of Their Properties, Syntheses and Potential Applications. *Prog. Mater. Sci.* **2018**, 95, 286–328.

CHAPTER 2: EXPERIMENTAL TECHNIQUES

In this chapter, the experimental techniques used during this thesis will be briefly described: from the fundamental principles to the particular experimental details used in this thesis. These techniques include (i) electron microscopies, such as transmission and scanning electron microscopy (TEM and SEM, respectively) combined with energy-dispersive x-ray spectroscopy (EDX; in the SEM) and electron energy loss spectroscopy (EELS; in the TEM), which were used to perform morphological analysis and to learn about the chemical composition of the particles; (ii) x-ray diffraction (XRD) to get information about the crystal structure; (iii) magnetometry using a superconducting quantum interference device (SQUID) to study the magnetic properties; (iv) dynamic light scattering (DLS) and Z-potential to study the colloidal stability; (v) visible (vis)-near infrared (NIR) spectroscopy to learn about optical absorption properties focused on optical hyperthermia; (vi) magnetic and optical hyperthermia to evaluate the heating efficiency; and (vii) magnetic resonance imaging (MRI) to gain information on the transverse relaxation time (T_2).

1. Electron microscopy

Transmission electron microscopy (TEM)

This technique allows the study of particle morphology (size, shape, size distribution). In TEM, electrons are emitted from a source and accelerated to go through a thin specimen to form an image. Typically, samples need to be thinner than 100 nm, since electrons need to be able to go through the specimen. As electrons pass through, their interaction with the sample will modify their trajectory, being scattered either elastically or inelastically. The strength of this interaction will depend on the electron density of the studied material and thus, denser materials will yield higher contrast. The beam of transmitted electrons is magnified and focused onto an imaging device, typically a CCD camera connected to a computer. The principles of transmission electron microscopy are essentially the same as those of optical microscopy. However, unlike optical microscopy, whose maximum resolution power is around 0.2 µm, the maximum in TEM is the subnanometric scale because electrons have a much smaller wavelength than visible photons (*i.e.*, de Broglie wavelength; 0.1-0.01 nm compared to 400-700 nm).[1] As a consequence, the resolution is literally thousands of times better than typical optical microscopes.

In this work, images obtained by TEM were used for the morphological characterisation of the particles. For example, measuring the dimensions of the particles, such as edge-length in cubes or width and length in rods we can get information about the shape specificity (*i.e.*, the *cubicity* in nanocubes or the aspect ratio in nanorods) and, importantly, the particle size distribution. This information is highly valuable since it gives an idea of the efficiency of the synthesis parameters.

The TEM Images were acquired using a JEOL JEM-1400 transmission microscope operating at 80 kV. The specimens for TEM imaging were prepared by dipping a carbon copper grid into a freshly sonicated dilute suspension of particles in toluene. The toluene remains were quickly removed by depositing the grid on a sorbent Whatman® filter paper. The average particle size and its standard deviation were estimated by measuring the size of at least 100 particles. The data were fitted to a log-normal function and the average size and polydispersity index (PDI were calculated for all the samples. To assess the morphological quality of the cubic particles, we used a simple "cubicity" parameter. Namely, since the ratio between the diagonal of a perfect square and its side is $\sqrt{2}$, by comparing the diagonal/side ratio with $\sqrt{2}$ we can have a quantitative idea on how close we are to an ideal cube. Thus, for a perfect cube the cubicity = diagonal/($\sqrt{2}\times$edge) $\times$ 100 should be 100%.

These experiments and the subsequent analysis were carried out by me using the TEM in the Servei de Microscopia of the Universitat Autònoma de Barcelona.

On the other hand, using high resolution transmission electron microscopy (HRTEM), it is possible to obtain images with atomic resolution. Such a high resolution allows the determination of the distances between crystal planes and the presence of defects (dislocations, stacking faults, antiphase boundaries, etc.), thus providing information about the crystallinity of the material.

High-resolution TEM images have been obtained using a FEI Tecnai F20 operating at 200 kV. Fast Fourier transform (FFT) of the high resolution images generated a spot pattern that was used to calculate the interplanar distance. The as-obtained values were compared with those of references.

These experiments were carried out at the Microscopy Service of the Catalan Institute of Nanoscience and Nanotechnology with the assistance of Dr. Belen Ballesteros. I performed the

analysis of the results with the help of Dr. Pau Torruella and Dr. Alejandro Sánchez from the Servei de Microscopia de la Universitat Autònoma de Barcelona.

Scanning electron microscopy (SEM)

With SEM, it is possible to study the topography of the synthesized nanoparticles. In this technique, the sample is scanned with a focused beam of electrons to generate an image of the surface using reflected electrons, as opposite to transmission microscopy, where the image is obtained using transmitted electrons. For this reason, the detector is placed over the sample and not after (which is the case of TEM). The incident electrons interact with the atoms and produce signals that contain information about the topography of the material. In the typical scanning electron microscopy, the surface atoms are excited by the electron beam, emitting secondary electrons. The quantity of secondary electrons depends on the topography of the sample, thus, images with field depth can be obtained with a resolution typically over 1 nm.

In our case, the specimens for SEM imaging were prepared by diluting the particles in toluene and dipping a carbon copper grid into a freshly sonicated dispersion. The images were acquired using a FEI Magellan 400L XHR scanning electron microscope, operating at 2 kV. These experiments were carried out by Marcos Rosado, at the Microscopy Service of the Catalan Institute of Nanoscience and Nanotechnology (ICN2).

Energy dispersive x-ray spectroscopy (EDX)

This technique is used to study the atomic composition of a sample. When radiation (electrons, x-rays, etc.) interacts with a sample, it excites the electrons of the inner shell of the atoms, which in the ground state remain in discrete energy levels or electron shells bound to the nucleus. When an electron is excited, it is ejected from the shell, thus creating a vacancy. Then, an electron from the outer shell (and therefore higher energy) fills that vacancy. The energy difference between these two electrons is released as x-ray radiation. The energies of the X-rays are characteristic of the difference in energy between the two shells and of the atomic structure of the atom, resulting in a characteristic peak pattern for each element. The intensity and wavelength of the emitted x-rays are measured by a spectrometer, allowing the determination of the elemental composition of the sample. In our case, we use the electron beam of the SEM to generate the EDX signal. Thus, we use the same SEM microscope as for the topography experiments and the Oxford Instruments Ultim Extreme EDX detector system

integrated on it. The experiment does not require any additional sample preparation with respect to that of conventional SEM.

These experiments and analysis were carried out by Marcos Rosado, with my assistance, at the Microscopy Service of the Catalan Institute of Nanoscience and Nanotechnology (ICN2).

Electron energy loss spectroscopy (EELS)

With this technique it is possible to obtain element mapping of the nanoparticles. Moreover, this technique unravels the oxidation state of the element. In EELS, the sample is irradiated with a focused beam of electrons. As electrons collide with the sample, some of them will go through, some others will be elastically scattered and a fraction will be inelastically scattered. The latter will have a lower energy than the incoming electrons and will be randomly deflected. The energy difference is due to several factors, such as phonon excitations, plasmon resonances, inter- and intra-band transitions or inner shell ionizations. The latter are very useful for identifying the chemical elements of the sample: in an analogous way to EDX, the emission peak pattern is characteristic for each element and therefore an elemental analysis can be performed. Although an EELS spectrum could include a wide range of energies (from 0.1 to 10 keV), the emitted radiation from the sample consists mainly of elastically scattered electrons, that is, electrons that have not lost energy in the process, giving the so-called *zero-loss peak*. A smaller portion is scattered with lower energies than initially (typically, at 50 eV lower energy) is caused by plasmonic resonances. This region is called *low-loss region*. The emission due to the inner shell ionizations represents only a small fraction of the total emitted radiation (between 100 and 2000 eV) and can be used for element identification. Moreover, since the size and the intensity of the peaks in this region is proportional to the number of atoms, quantitative analysis can also be performed to find out the ratios between different elements and have an idea on the chemical composition of the sample. In addition, the shape of the EEL spectra carries information not only about the type of atom but also about its valence state. Remarkably, owing to the high resolution of TEMs, it is possible to acquire spectra at discrete intervals (approximately, every 0.5 nm) to generate maps with the chemical composition in every point. This is interesting for our work, as it allows as to discriminate between different iron oxidation states according along different regions of the particle (*i.e.*, to know if we have a homogeneous structure or a core-shell, to find impurities and metal inclusions, etc.).

The sample preparation is the same that for TEM. The measurements were collected in a FEI-TECNAI F30 microscope, equipped with a Quantum GIF EELS spectrometer to perform the EELS analysis. The experiments were carried out at 200 kV. The EEL spectra were analysed using the Oxide Wizard script.[2,3]

These experiments were carried out by Dr. Belen Ballesteros, with my assistance, in the TEM at the microscopy service of the Catalan Institute of Nanoscience and Nanotechnology (ICN2).The analysis of the results was performed by Mr. Daniel del-Pozo-Bueno, Dr. Sonia Estradé and Prof. Francesca Peiró of the Universitat de Barcelona.

2. X-ray diffraction (XRD)

This technique is used for the determination of the atomic structure of materials. It is based on the fact that crystals can diffract when an incident x-ray beam is irradiated, into specific directions. Although in principle diffraction can occur with every radiation wavelength, the effect becomes more intense as the incident wavelength becomes commensurate with the size of the diffracting object. Thus, considering that the typical interatomic distances are in the Å range, x-rays, whose wavelengths range between 0.01-10 nm, become the light of choice for structural determination based on diffraction. Consequently, when x-rays collide with an atom, they make the electronic cloud oscillate. These oscillating charges produce new waves with the same wavelength as the incident radiation, which can then interfere with each other either constructively or destructively. As if it was a mirror, in crystalline structures, the as-generated waves are scattered from crystal planes separated by the interplanar distance (d). When these waves interfere constructively, they remain in phase since the difference between the path lengths of the two waves is equal to an entire multiple of the wavelength. Consequently, the path difference between two interfering waves is given by $2d \cdot sin\,\theta$, where θ is the scattering angle. The effect of the constructive or destructive interference is enhanced because of the cumulative effect of reflection in successive crystallographic planes of the crystal. This leads to Bragg's law, which describes the condition on θ for the constructive interference (also called Bragg's condition) (Equation 2.1):

Eq. 2.1 $$n\lambda = 2d \cdot \sin\theta,$$

where n is a positive integer and λ is the wavelength of the incident wave, which depends on the material of the x-ray source. As a consequence of this law, reflections will take place only at the angles that Bragg's condition is satisfied. Consequently, a characteristic diffraction

pattern can be obtained by representing the intensities of the scattered waves as a function of the scattering angle, with intense peaks at the angles that satisfy Bragg's condition. Since the resulting pattern is the consequence of the interaction between the x-ray beam and the electronic clouds of the atoms, by applying Fourier transform a spatial reconstruction of the electron density distribution within the crystal can be obtained and hence the average positions of each atom can be inferred. In a typical measurement, the sample is placed on a goniometer, which is used to rotate it at precise angles while irradiating with a focused x-ray beam and registering the scattered radiation. In our case, the measured peak patterns from our samples were compared to literature references to find out information about the purity (by studying the present iron oxide phases in the particles) or the crystallinity. For this purpose, the crystal size was calculated and compared with the particle size: the closer these two values are, the higher the crystallinity is and, in an ideal, case both values would be the same. In this situation, it is said that the particles are *single-crystal*. To calculate the crystal size, Scherrer equation was applied, which is a formula that relates the crystal size (τ) with the broadening of the peaks in the diffraction pattern and is written as (Equation 2.2):

Eq. 2.2
$$\tau = \frac{\kappa \cdot \lambda}{\beta \cdot \cos \theta},$$

where κ is the shape factor, which varies according to the shape of the grain but for simplification, typically is assumed to be 0.9; λ is the wavelength of the incident x-ray, β is the width of the peak at half of the maximum intensity (in radians); and θ is the angle at which the peak centre is located.

In this work, samples were deposited as dry powder on a holder, usually made of Si, to reduce the background signal. The measurements were then carried out using an X'pert PRO MPD from PANalytical with a Cu Kα radiation ($\lambda = 0.15406$ nm).

These experiments and the analysis were carried out by me at the Catalan Institute of Nanoscience and Nanotechnology (ICN2).

3. Magnetic measurements

The magnetic properties such as saturation magnetization (M_S), remanence (M_R) or coercivity (H_c) (obtained from hysteresis loops at a set temperature) and the dependence of the magnetisation with the temperature were measured using a magnetometer equipped with a

superconducting quantum interference device (SQUID). SQUIDs are very sensitive detectors based on the Josephson effect (the flow of an electric current between two separated superconductors by tunnel effect). Usually, the detectors are formed by two Josephson junctions and the generated current depends on the magnetic flux inside them, owing to which they are capable of measuring ultrasmall magnetic fields. The sample is placed inside the pair of Josephson junctions and moved in-and-out, thus generating a magnetic flux that induces voltage changes in the junctions from which the magnetisation can be inferred.

In this work, two types of magnetic measurements were performed: to investigate the dependence of the magnetisation with temperature [M(T)] and with the applied field [M(H)], which are also referred to as hysteresis loops. For the M(T) studies, measurements have been performed in two different ways:

- *Zero-field cooling (ZFC):* Samples are cooled from room temperature to low temperatures (around 10 K) without applying any magnetic field. Then, a small magnetic field is applied and the temperature is increased while recording the magnetisation.
- *Field-cooling (FC):* the sample is cooled from room temperature while applying a magnetic field and then, the magnetisation is recorded while warming and keeping the applied magnetic field.

Both curves are later represented as magnetisation as a function of T and information about Neel or Curie transition, blocking temperatures or presence of interactions can be obtained and evaluated. For example, in magnetite nanoparticles, a kink in the ZFC at low temperatures (near 120 K) is caused by a structural change called Verwey transition.[4] The temperature at which Verwey transition takes place (T_V) is very sensitive to the different factors such as the stoichiometry. Small deviations from stoichiometry (*i.e.,* by cation substitutions or a partial oxidation) can lead to dramatic decrease in the T_V or even completely inhibit it.[5,6] Although the possible origins for a decrease in the T_V are quite complex, in this work the presence of the Verwey transition is considered as an indicator of the purity of the magnetite. Conversely, the absence of other transitions is taken as a sign of purity. For example, the appearance of the Néel transition (from antiferromagnetism into paramagnetism) of FeO at about $T_N = 200$ K, would indicate the presence of FeO in the sample.

On the other hand, hysteresis loops can provide other information about the magnetic behaviour (*i.e*, superparamagnetism, ferrimagnetism, etc.) and the susceptibility, saturation, remanence and coercivity values. In this type of measurements, the sample is saturated by

applying a strong magnetic field in one direction. Afterwards, the field is stepwise reversed and the magnetisation of the sample is registered after every step until it is completely reversed. Then, the magnetisation is gradually reversed to the original direction while registering the magnetisation.

In this work, both the M(T) and M(H) were evaluated on tightly packed powdered samples encapsulated in Teflon and placed in gelatine capsules using a MPMS 7 T SQUID magnetometer (Quantum Design). The measurements of the temperature dependence of magnetization, M(T), were carried out from 10 to 300 K or 350 K typically at 25 Oe after cooling in the absence (ZFC) of a field. The hysteresis loops were carried out either at room temperature or at 10 K applying a maximum field of 70 kOe.

These experiments were carried out by Dr. Alberto López-Ortega at CIC nanoGUNE. I carried out the posterior analysis of the data.

4. Dynamic light scattering (DLS) and Z-Potential

DLS allows the determination of the particle size distribution profile in dispersion. In this technique, the sample (*i.e.*, a dispersion of particles) is irradiated with a monochromatic polarized laser beam. The incident photons are scattered elastically in random directions due to Rayleigh scattering. A detector is used to collect the scattered light from the sample, whose intensity fluctuates over time due to the Brownian motion of the particles. As a consequence of this motion, the distance between the scattering particles is constantly changing over time and thus the interferences generated between the light that is scattered by every particle will continuously vary. Smaller particles will move faster across the solvent, resulting in faster intensity variations (**Fig. 1**)[7] and hence, it is possible to get information about the aggregate size.
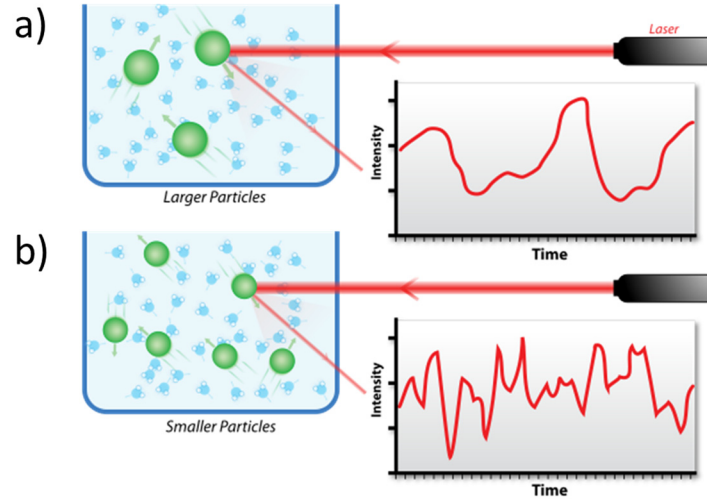
Figure 1. Dispersion of large particles (a) vs dispersion of small particles (b). Note that in the case of smaller particles, the intensity of the scattered laser varies much more the than in the case of large particles for a given time. [7]

The hydrodynamic diameter of the particles (D_H) and aggregates can be estimated using the Stokes-Einstein equation (Eq. 2.3):

Eq. 2.3
$$D_H = \frac{k_B T}{3\pi\eta D_{dif}},$$

where k_B is the Boltzmann constant, T is the temperature, η is the viscosity of the medium and D_{dif} is the translational diffusion coefficient of the particles.[8]

The Z-potential gives an idea of the surface charge and is calculated indirectly by measuring the electrophoretic mobility (U_e) of the particles. The presence of a net charge on their surface affects the distribution of the nearby ions, leading to an increase of ions of opposite charge to that of the particles. As a consequence of this gradient, two regions appear: an inner one where the ions are interacting strongly with the surface charges (Stern layer); and an outer one where the interactions are weak (diffuse layer). Thus, every particle is surrounded by an electrostatic double layer (inner Stern layer and outer diffuse layer). When particles move (due to Brownian motion, gravity, etc.), ions in the Stern layer move with it. However, ions in the diffuse layer don't. The boundary within these two regions is called slipping plane and its potential is called Z-Potential. Its value is considered as an indicator of stability and values larger than $\pm$ 30 mV are usually considered stable.[9] In Z-Potential measurements, an electric potential difference is applied and the electrophoretic mobility of the particles is monitored by laser Doppler velocimetry. Then, Z-potential (ζ) is calculated by applying the Henry equation (Eq. 2.4):

$$Eq.\ 2.4 \qquad\qquad U_e = \frac{2\varepsilon\zeta f(ka)}{3\eta},$$

where ε is the dielectric constant of the solvent, η is the viscosity and *f(ka)* is the Henry function, whose value depends on both the ionic strength of the medium and the particle size and is typically either 1 for particles in non-polar media (Hückel approximation); or 1.5 for particles in polar media (Smoluchowsky approximation).[10]

The measurements of both hydrodynamic diameter and Z-Potential were carried out in a Zetasizer Nano ZS (Malvern Panalytical).The samples were dispersed either in toluene or mili-Q water prior to the measurements.

These experiments and the analysis were carried out by me using the DLS apparatus at the Catalan Institute of Nanoscience and Nanotechnology (ICN2). The results were analysed with the help of Dr. Javier Saiz.

5. Vis-NIR absorption spectroscopy

Absorption spectroscopy refers to the study of the absorption of radiation by matter. In this work, the regions of the electromagnetic radiation spectrum that will be exploited for the absorption properties of the particles are two: visible (400-700 nm) and near infrared (780-2500 nm). The absorption in each of these regions is driven by different processes. For example, the absorption of visible and ultraviolet radiation is due to the excitation of electrons from lower to higher energy levels. Since the energy levels where electrons can move to are quantized, only the radiation with the precise amount of energy (and thus wavelength) can induce the transition from one level to another. This means that only some very specific wavelengths will be absorbed and thus UV-vis spectroscopy can provide very accurate information about the chemical composition of a sample. On the other hand, near-infrared absorption is mainly due to overtones or combinations of the tension vibrational bands produced in the region between 3333 and 5882 nm. The typical bonds that are involved are C-H, N-H and O-H. However, some electronic transitions can also cause absorption in this region, like the Fe^{2+}-Fe^{3+} transitions in Fe_3O_4.[11]   To know how much radiation has been absorbed at a set wavelength, the ratio between the absorbed and incident intensities (I and I_0, respectively), referred to the absorbance (A), is calculated as (Eq. 2.5)

$$Eq.\ 2.5 \qquad\qquad A = log\frac{I_0}{I}$$

The spectrophotometers are composed of basically four types of elements: an emission source, an optical system to collimate, select and focus the desired wavelength, etc.; a sample holder and a detector, which is usually connected to a computer (**Fig. 2**).[12]
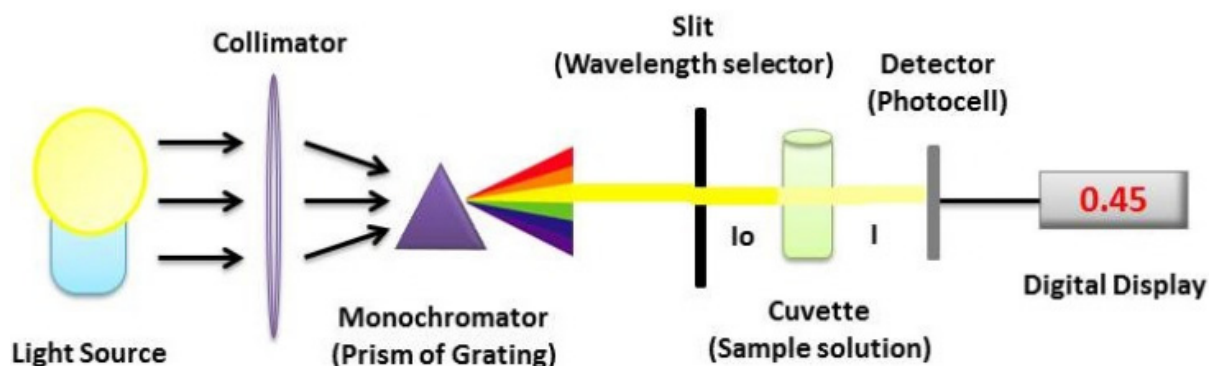

Figure 2. General scheme of the components of a spectrophotometer.[12]

Considering the light sources emit multiple wavelengths at the same time, it is necessary to perform a wavelength discrimination process to select a specific wavelength, thus monochromators are used. In the thesis, particles were diluted in mili-Q water to an iron concentration of around 4 mM. Absorbance measurements were acquired using a NIRQuest (Ocean Optics) spectrophotometer for the NIR and a Shamrock 500i (Andor) spectrograph for the visible region using cuvettes with a light path of 1 cm and a fibre coupled halogen white light source.

These experiments were carried in our group at the Catalan Institute of Nanoscience and Nanotechnology (ICN2). I performed the analysis of the results, with the help of Dr. Javier Saiz and Dr. Borja Sepúlveda.

6. Hyperthermia

Magnetic Hyperthermia

When magnetic nanoparticles are exposed to an alternating magnetic field, their magnetic moments will trend to align in the direction of the field. Essentially, the energy that the particles absorbed initially from the magnetic field is released as thermal energy. There are several mechanisms by which this transformation can take place: hysteresis losses and relaxation processes (Néel and Brownian).

Hysteresis losses: hysteresis losses are phenomena that take place in multi-domain and blocked single-domain ferrimagnetic nanoparticles as a consequence of the rotation of the magnetic

spins in the particle (**Fig. 3a**). The generated thermal energy is proportional to the area of the hysteresis loop and consequently is related to the M_S and H_c.

Néel and Brownian relaxation: when magnetic nanoparticles are exposed to an alternating magnetic field, there is a delay in the relaxation (or return to minimal energy state) of the magnetic moment. In other words, the orientation of the magnetic moment of the particle in a direction that is different to the applied field is not favoured and particles will reorient its moment to reduce energy. This can happen in two ways: if the magnetic moment rotates within the particle, the process is called Néel relaxation (**Fig. 3b**); if it is the particle as a whole what rotates, it is known as Brownian relaxation (**Fig. 3c**). The energy difference between both the initial state and the final one (relaxed) is transformed into heat.
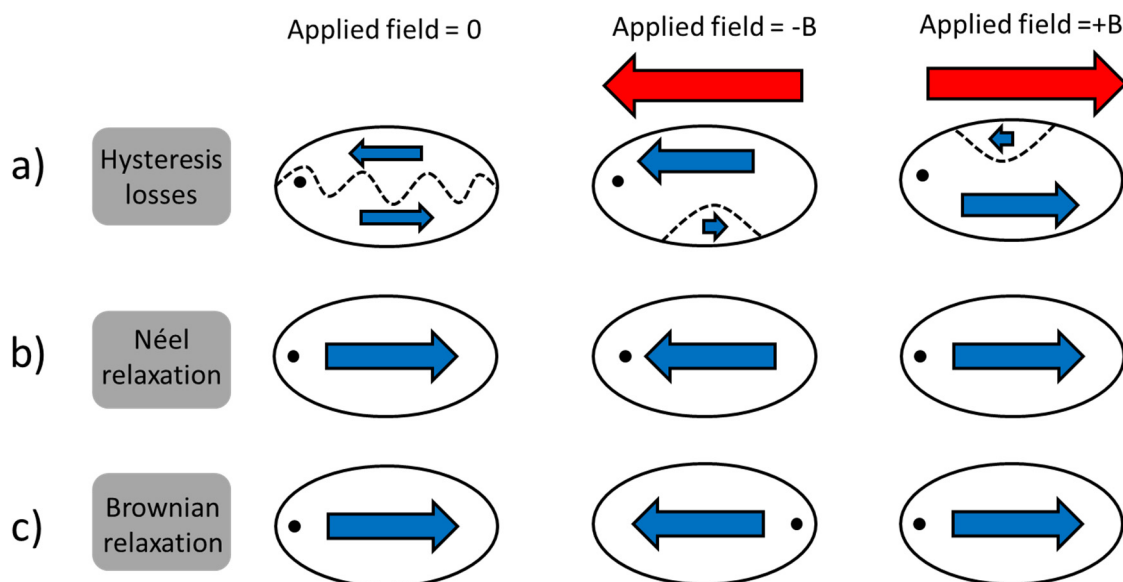

Figure 3. Different heat generation mechanisms in magnetic nanoparticles under application of an alternating magnetic field. Note that particles represented in a) are multi-domain, while those of b) and c) are single-domain. Blue arrows represent the magnetic moments direction. Red arrows represent the direction of the applied field and dashed lines in a) represent the domain walls. The black dot serves as a reference for the particle orientation.

The heating power in magnetic hyperthermia is generally represented by the Specific Absorption Rate (SAR), which gives an idea on how much power particles can generate per unit of material and is described by Equation 2.6:

Eq. 2.6
$$SAR = \frac{c_P}{m} \cdot \frac{dT}{dt},$$

where C_p represents the heating capacity of the medium (usually water); m is the mass of nanoparticles and $\frac{\partial T}{\partial t}$ represents the temperature increase per unit of time when the field is applied.

 The main challenge with magnetic hyperthermia is to achieve particles with high SAR values using safe clinical conditions (i.e., the product of both frequency and field intensity should not exceed $5 \cdot 10^9$ A·m^{-1}·s^{-1}),[13] which are desirable in order to minimize the required dosage of nanoparticles to achieve therapeutic effects in magnetic hyperthermia.[14] However, in the SAR calculation equation neither frequency nor field intensity are taken into account and thus, SAR can vary importantly if the samples are measured in different field conditions. This makes it difficult to compare the capacity as heaters between particles tested in different conditions. For this reason, an alternative (although yet less standardized) parameter was introduced: the Intrinsic Loss Power (ILP).[15] Since it has been found that SAR depends roughly linearly on the frequency and as the square of the field, ILP is defined as (Eq. 2.7):

Eq. 2.7
$$ILP = \frac{SAR}{f \cdot H^2}$$

The heating capacity of the particles was measured by applying an alternating magnetic field, H, of 213 Oe (17 kA/m) at a frequency f = 183 kHz, using an experimental set-up based on a 6 kW Fives Celes® power supply. The sample was placed in a polystyrene sample holder inside a glass tube thermostated at 25°C using an ethylene glycol flow and the temperature was recorded through an optical fibre thermometer dipped into the sample dispersion. The total exposition to the alternating magnetic field was 5 min for each measurement. To determine the reproducibility, the measurements were collected in triplicate.

These experiments were carried in the Chemistry Department of the University of Florence by Dr. Elvira Fantechi. The analysis of the results was carried out also with the collaboration of Dr. Elvira Fantechi.

Optical Hyperthermia (Photothermia)

Whereas SAR is, to some extent, an intrinsic property of the material and independent from the concentration (unless exceptions like aggregation due to an excessive concentration, etc.), optical hyperthermia is based on light absorption and therefore it is ruled by the Beer-Lambert

law. Hence SAR cannot be used to compare the heating efficiency of optic heaters and usually the photothermal conversion efficiency (η) is used instead. The latter can be calculated as (Eq. 2.8):[16]

Eq. 2.8
$$\eta = \frac{h \cdot S \cdot \Delta Tmax - Qdis}{I \cdot (1 - 10^{-A\lambda})} \,,$$

where h is the heat transfer coefficient, S is the laser irradiating area, ΔT_{max} is the optically induced temperature change when the thermal equilibrium is reached, Q_{dis} is the heat dissipation from the experimental setup, I is the incident laser power and A_λ is the absorbance of the nanoparticles at the laser wavelength. The product of $h \cdot S$ is given by:[17]

Eq. 2.9
$$h \cdot S = \frac{m_{water} \cdot C_{water}}{\tau_S} \,,$$

where m_{water} and C_{water} are the mass and heat capacity of deionized water and τ_S is the setup time constant, which is calculated by:

Eq 2.10
$$\tau_S = \frac{-t}{\ln \frac{T_{amb} - T}{T_{amb} - T_{max}}} \,,$$

where t is the decay time (the time that has passed since the stopping of the irradiation), T_{amb} and T_{max} are, respectively, the room and maximum temperature reached during the measurement respectively and T is the temperature.

The photothermal performance of the particles was measured by irradiating the particle dispersion with a laser at either 808 nm or 1064 nm, through a 1 cm cuvette containing 800 µL of sample, while monitoring the temperature with an infrared non-contact thermometer. The applied laser power was 84 mW independently of the wavelength. A blank of water (800 µL) without particles was measured and the heat generated by water alone was subtracted from the measurements with particles.

These experiments were carried in our group at the Catalan Institute of Nanoscience and Nanotechnology. The experiments, as well as the analysis of the results, were carried out with the help of Dr. Borja Sepúlveda.

7. Magnetic Resonance Imaging (MRI)

MRI is a non-invasive imaging technique that is used in modern medicine to investigate the internal structure and anatomy of patients. To generate the images, large magnetic field gradients and radio waves pulses are applied. Compared to other techniques, MRI has the advantage of not needing ionising radiation, such as computered axial tomography or positron-emission tomography.[18]

In this technique strong magnetic fields are applied to force the protons (mostly belonging to either water or fat molecules) to align with the field. Then, a radiofrequency pulse is applied, exciting the aligned protons and forcing them to spin out of their alignment position. When the radiofrequency pulse is over, the protons will realign with the magnetic field and the difference of energy between the excited and the equilibrium ground state is released as a radio frequency signal. The time it takes for the protons to return to equilibrium state is called relaxation time. After a certain period of time following the initial radio frequency pulse, the emitted signals by the protons are measured by a coil. The relaxation times and the amount of released energy vary depending on the environment and the chemical nature of the molecules surrounding the protons. Fourier transformation is applied to convert the frequency information contained in the signal from each location in the imaged plane to different intensity levels, which are then plotted as pixels in the resulting image. By varying the sequence of radiofrequency pulses and the magnetic gradient, different types of images can be obtained created. The time between the applied pulses is called repetition time, whereas the time between the application of the radiofrequency pulse and the reception of the signal from the protons is called time-to-echo.[18]

The relaxation times can be measured in two ways: T_1 and T_2. T_1 corresponds to spin-lattice relaxation processes and the direction of the magnetisation measured is the same as the one of the static field that is applied to align the protons. T_1-weighted images are produced by using short time-to-echo and repetition times (typically around 15 and 500 ms respectively). The magnetization is allowed to recover before measuring the resonance signal. On the other hand, T_2 corresponds to spin-spin relaxation processes and the direction of the magnetization is transversal to that of the static magnetic field. T_2-weighted images are produced by using longer time-to-echo and repetition times compared to T_1-weighted images (typically around 90 and 4000 ms). In T_2-weighted imaging, the magnetization is allowed to decay before measuring the resonance signal by changing the echo time.

Because the faster the protons realign, the more intense the signal becomes, some agents might be administered to enhance the contrast prior to the imaging. Contrast agents work by shortening the relaxation times of either T_1 or T_2. In the case of T_1-weighted images, this results in a brightening of the area (**Fig. 5 a**), whereas in the case of T_2 contrast agents, this leads to a darkening (**Fig. 5 b**).[19] For this reason it is usually said that T_1 and T_2 contrast agents are positive and negative contrast agents, respectively.[20] The efficacy of contrast agents is described by the relaxivity, which correlates the induced relaxation time shortening with the amount of contrast agent. Some examples of T_1 contrast agents are lanthanide and gadolinium chelates, which currently are the most popular; as for the T_2 contrast agents, iron oxide and iron platinum nanoparticles are relatively popular.
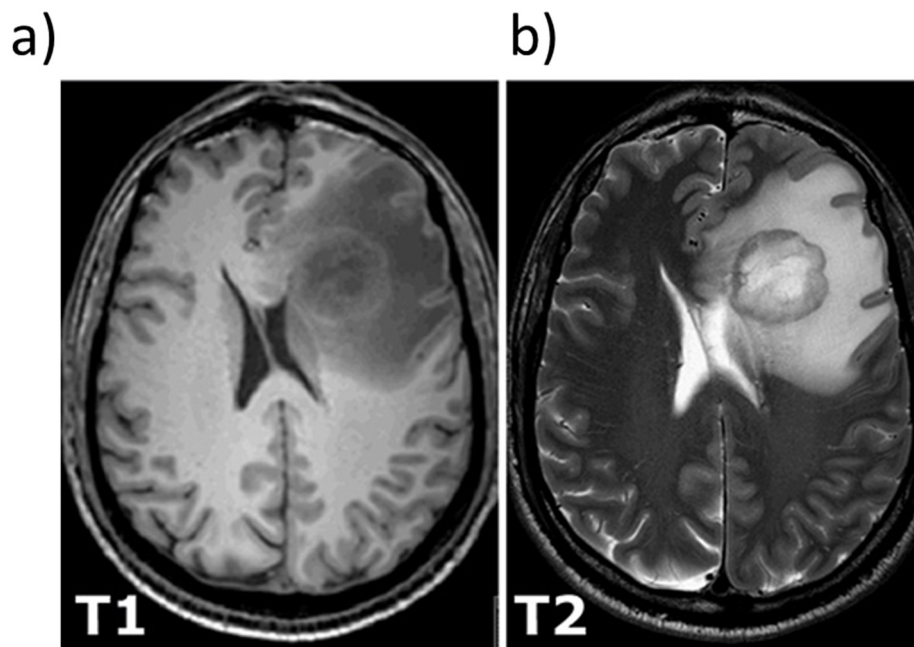

Figure 5. T_1-(a) and T_2-(b) weighted images of a brain tumour with surrounding oedema. Adapted from Collins.[19]

In this work, magnetic resonance imaging studies were performed in a 70 kOe Bruker BioSpec 70/30 USR. For the measurement of the transversal relaxation times, T_2, phantoms containing nanoparticles at various concentrations in 1% agarose were prepared. The relaxivities, r_2, were obtained as the slope of the linear regression of the relaxation rates (R), as the inverse of the relaxation times ($R_2 = 1/T_2$) versus the Fe concentration.

These experiments were carried by Dr. Silvia. Lope Piedrafita at the Servei de Ressonància Magnètica Nuclear of the Universitat Autònoma de Barcelona. The subsequent results analysis was carried out by me with her help.

8. References

(1) Nan Yao, Z. L. W. *Handbook of Microscopy for Nanotechnology*; Yao, N., Wang, Z. L., Eds.; Kluwer Academic Publishers: Boston, **2005**; 38-39.

(2) Yedra, L.; Xuriguera, E.; Estrader, M.; López-Ortega, A.; Baró, M. D.; Nogués, J.; Roldan, M.; Varela, M.; Estradé, S.; Peiró, F. Oxide Wizard: An EELS Application to Characterize the White Lines of Transition Metal Edges. *Microsc. Microanal.* **2014**, 20 (3), 698–705.

(3) Colliex, C.; Manoubi, T.; Ortiz, C. Electron-Energy-Loss-Spectroscopy near-Edge Fine Structures in the Iron-Oxygen System. *Phys. Rev. B* **1991**, 44 (20), 11402–11411.

(4) Walz, F. The Verwey Transition - a Topical Review. *J. Phys. Condens. Matter* **2002**, 14 (12), R285–R340.

(5) Aragón, R.; Buttrey, D. J.; Shepherd, J. P.; Honig, J. M. Influence of Nonstoichiometry on the Verwey Transition. *Phys. Rev. B* **1985**, 31 (1), 430–436.

(6) Özdemir, Ö.; Dunlop, D. J.; Moskowitz, B. M. The Effect of Oxidation on the Verwey Transition in Magnetite. *Geophys. Res. Lett.* **1993**, 20 (16), 1671–1674.

(7) Yin, L. Dynamic Light Scattering. In *Nanotechnology Research Methods for Foods and Bioproducts*; Wiley-Blackwell: Oxford, UK. **2012**; 1152, 145–161.

(8) Dynamic Light Scattering: Applications of Photon Correlation Spectroscopy, Pecora, R. Ed. Springer US. **1985**.

(9) MALVERN. Instruments. Zetasizer Nano User Manual. *Electron. Commun. Japan (Part I Commun).* **2013**, No. 11.

(10) Blees, M. H. Foundations of Colloid Science. *Colloids Surfaces A Physicochem. Eng. Asp.* **2002**, 210 (1), 125-126.

(11) Tang, J.; Myers, M.; Bosnick, K. A.; Brus, L. E. Magnetite Fe_3O_4 Nanocrystals: Spectroscopic Observation of Aqueous Oxidation Kinetics †. *J. Phys. Chem. B* **2003**, 107 (30), 7501–7506.

(12) BiochemistryDen. Spectrophotometer Instrumentation : Principle and Applications https://www.biochemden.com/spectrophotometer-instrumentation-principle/ (accessed May 8, 2019).

(13) Maier-Hauff, K.; Ulrich, F.; Nestler, D.; Niehoff, H.; Wust, P.; Thiesen, B.; Orawa, H.; Budach, V.; Jordan, A. Efficacy and Safety of Intratumoral Thermotherapy Using Magnetic Iron-Oxide Nanoparticles Combined with External Beam Radiotherapy on Patients with Recurrent Glioblastoma Multiforme. *J. Neurooncol.* **2011**, 103 (2), 317–324.

(14) Wu, W.; Wu, Z.; Yu, T.; Jiang, C.; Kim, W.-S. Recent Progress on Magnetic Iron Oxide Nanoparticles: Synthesis, Surface Functional Strategies and Biomedical Applications. *Sci. Technol. Adv. Mater.* **2015**, 16 (2), 023501.

(15) Kallumadil, M.; Tada, M.; Nakagawa, T.; Abe, M.; Southern, P.; Pankhurst, Q. a. Suitability of Commercial Colloids for Magnetic Hyperthermia. *J. Magn. Magn. Mater.* **2009**, 321 (10), 1509–1513.

(16) Roper, D. K.; Ahn, W.; Hoepfner, M. Microscale Heat Transfer Transduced by Surface Plasmon Resonant Gold Nanoparticles. *J. Phys. Chem. C* **2007**, 111 (9), 3636–3641.

(17) Li, Z.; Aranda-Ramos, A.; Güell-Grau, P.; Tajada, J. L.; Pou-Macayo, L.; Lope Piedrafita, S.; Pi, F.; G. Roca, A.; Baró, M. D.; Sort, J.; Nogués, C.; Nogués, J.; Sepúlveda, B. Magnetically Amplified Photothermal Therapies and Multimodal Imaging with Magneto-Plasmonic Nanodomes. *Appl. Mater. Today* **2018**, 12, 430–440.

(18) Xiao, Y.-D.; Paudel, R.; Liu, J.; Ma, C.; Zhang, Z.-S.; Zhou, S.-K. MRI Contrast Agents: Classification and Application (Review). *Int. J. Mol. Med.* **2016**, 38 (5), 1319–1326.

(19) Collins, L. Applied Imaging Technology. *Australas. Phys. Eng. Sci. Med.* **2002**, 25 (2), 87-88.

(20)   McRobbie, D. W.; Moore, E. A.; Graves, M. J. ; Price M. R. Liney, G. P. *MRI from Picture to Proton*, Ed. Cambridge University Press. **2007**

CHAPTER 3: NANOCUBES

1. INTRODUCTION

Although most of the research performed so far on iron oxide magnetic nanoparticles has been carried out using spherical particles,[1,2] as it has been already pointed out, anisotropic structures have numerous advantages over the isotropic ones. In the particular case of nanocubes, it is important to emphasize that for an equal volume, cubes have a larger surface than spheres, which may be advantageous for many applications (*e.g.*, protein grafting or catalysis). Besides, the magnetic properties are also different, since the cubic morphology leads to an increase of both shape and surface anisotropies, which affects the superparamagnetic blocking temperature[3] or the Verwey transition.[4,5]

However, the synthesis of non-spherical Fe_3O_4 nanoparticles is far more challenging than spherical ones, since magnetite has a cubic crystal structure and, consequently, isotropic growth is more favoured.[6] In the literature, the synthesis of magnetite nanocubes has been attempted using different approaches. For example, magnetotactic bacteria can naturally synthesize magnetite nanocubes from 30 to 180 nm.[7] However, the process is slow (considering it requires working with cell cultures), not scalable and the size control is quite poor. Alternatively, chemical approaches include both aqueous[8] and organic-based syntheses.[9,10,11] The synthesis of nanocubes in aqueous media also requires a long time since the growth mechanism (and, hence, the control of the size and shape) is not trivial. Moreover, subtle changes in the experimental conditions, which are difficult to control, can drastically affect the particle size and the size distribution.[8]

On the other hand, thermal decomposition of organic iron precursors presents significant advances in controlling the size of iron oxide nanoparticles, with improved crystallinity and a narrow size distribution. For these reasons all of the syntheses that were tried during this work are based on thermal decomposition.

Most of these syntheses use either iron (III) oleate or iron (III) acetylacetonate as iron precursor.[9,10,11] In the first case, iron (III) oleate is decomposed in non-polar solvents (typically 1-octadecene, squalene or eicosane) in the presence of sodium oleate, and the size can be finely tuned from 9 to 23 nm,[11] reaching exceptionally larger sizes, up to 45 nm.[12–14] The second approach is using iron (III) acetylacetonate as precursor and dibenzyl ether as solvent in the presence of oleic acid as surfactant, which has the advantage of being a one-pot synthesis. This

reaction is considerably faster than the one based on iron (III) oleate and yields typically very large particles with sizes of more than 100 nm.[10] The size can be reduced down to about 20 nm by replacing oleic acid by shorter ligands like decanoic acid.[10] Given the individual advantages of each of these approaches, both of them will be tested and compared in this work.

2. SYNTHESES BASED ON PUBLISHED PROCEDURES

2.1 Iron oleate-based synthesis

The synthesis was originally described by Park *et al.*[15] but it was adapted and optimised for our laboratory conditions.

For the synthesis, the chemicals, oleic acid >90% (Sigma); Iron (III) chloride trihydrate >90% (VWR Chemicals); toluene >99% (Sigma); hexane >97% (VWR Chemicals); ethanol >96% (VWR Chemicals); 1-octadecene >90% (Sigma); and sodium oleate >82% (Sigma) were used as supplied without further purification

Synthesis of the iron oleate. $FeCl_3 \cdot 3H_2O$ (10 g) were dissolved in 60 mL of water and added to a solution of sodium oleate (57 g) dissolved in a mixture of hexane (150 mL) and ethanol (90 mL). The mix was refluxed while stirring for 4 hours at around 60°C. To remove the excess of salts and solvents, the resulting product was decanted in a separation funnel and iron oleate was washed with water three times, being the last step of decantation overnight. Finally, the product was rotavaporated at around 60°C for two hours to remove ethanol and hexane.

Synthesis of the nanocubes. 20 mL of a solution of 1-octadecene containing iron oleate (1 g), oleic acid (0.20 g) and sodium oleate (0.21 g) were placed in a 100 mL three neck round bottom flask connected to a Schlenk line. This mixture was heated to 130 °C at a rate of 10 °C/min and kept at this temperature in vacuum (~$3 \cdot 10^{-2}$ mbar) for 30 minutes under vigorous magnetic stirring. Subsequently, the slurry was heated up to the reflux temperature (~320 °C) at a rate of 3 °C/min under argon flow and kept at this temperature for 30 minutes. Finally, the reaction was cooled down to room temperature.

The resulting product was washed with a 1:1 hexane: ethanol mixture and centrifuged for 10 minutes at 4000 g, discarding the surnatant. The washing was repeated three times and the nanoparticles were redispersed in toluene. This procedure yields iron oxide nanocubes with an average edge length of 11.3$\pm$1.2 nm.

68

The particle size can be controlled by adjusting the total concentration of reagents. For example, 13.8±1.3 nm nanocubes could be obtained by increasing three-fold the total reagent concentration.

The TEM images of the as-obtained nanocubes (**Fig. 1a,b**) reveal a well-defined cubic structure with an edge length of 11.3±1.2 nm and a narrow particle size distribution, with a good polydispersity index (PDI) of 11% (**Fig. 1c**). Although apart from the total reagent concentration, other parameters were tested for controlling the size (*i.e.*, atmosphere, solvent composition, oleic acid and sodium oleate concentration), their influence resulted in shape deviations or an increase of the polydispersity and, thus, these results are not included in this Chapter.
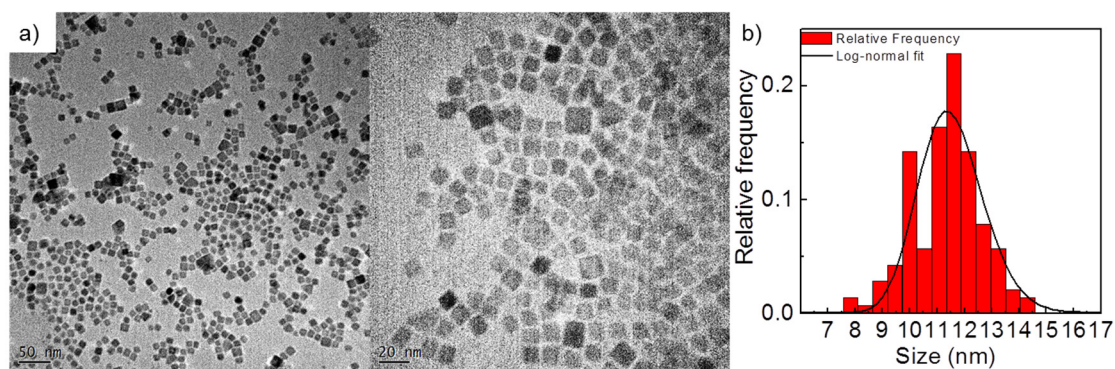

Figure 1. a) TEM images of the magnetite nanocubes obtained from the synthesis. b) Particle size distribution of the standard nanocubes and its fit to a log-normal function.

It has often been reported that the final product of this type of synthesis is a mixture of wüstite (FeO) and magnetite forming a FeO/Fe$_3$O$_4$ core/shell system.[12,16] FeO is an antiferromagnetic material with a Néel temperature of 198 K. Taking into account that the temperature dependence of the magnetization (**Fig. 2**) did not show any noticeable slope change at that temperature in the ZFC curve, it could be concluded that FeO was not present.
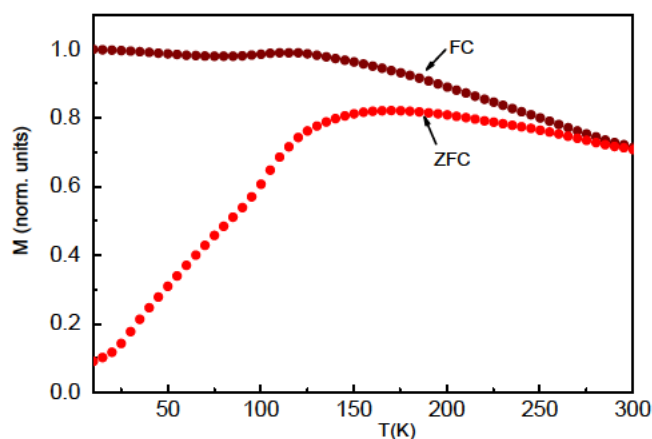
Figure 2.ZFC (red circles) and FC (blue circles) curves of the nanocubes

However, Verwey transition (namely, a crystallographic phase transition from cubic spinel into monoclinic that takes place for lower temperatures than 120 K in Fe_3O_4 and that involves abrupt changes in magnetic properties and electrical conductivity)[17] was not present either.

In conclusion, the iron oleate-based synthesis yielded nanoparticles with a clearly cubic structure and a narrow size distribution. However, although several experimental conditions were tested, the range in which the size could be tuned, while maintaining the cubic shape, was quite small (typically from 10 to 20 nm).[11] Moreover, this synthesis involves the preparation of iron (III) oleate in a previous step, which unfortunately increases the required synthesis time and may lead to some variability between syntheses. Indeed, recent studies have reported that traces of chlorine ions remaining in iron oleate or the extractive process used in its synthesis can dramatically influence the final nanoparticle structure.[18]

2.2 Synthesis using iron (III) acetylacetonate and dibenzyl ether

The synthesis was originally described by Kim *et al.*[10] but it was adapted and optimised for our laboratory conditions.

For the synthesis, all of the chemicals, iron (III) acetylacetonate >97% (Fluka); oleic acid >90% (Sigma); dibenzyl ether >90% (Acros Organics); chloroform >99% (VWR Chemicals); and 4-biphenylcarboxylic acid >99% (Sigma) were used as supplied without further purification.

Synthesis of the nanocubes. Iron (III) acetylacetonate (0.71 g) was added to a mixture of oleic acid (1.13 g) and dibenzyl ether (10 mL), which was used as solvent. This mixture was degassed at room temperature for 30 min in vacuum (~10^{-2} mbar) under vigorous magnetic

70

stirring. Then, the slurry was heated up to the reflux temperature (~290 °C) at a rate of 20 °C/min under argon atmosphere and kept at this temperature for 30 minutes. Finally the reaction was cooled down to room temperature in argon. In order to purify the nanocubes, the resulting product was washed three times with a mix of toluene and hexane (4:1) and centrifuged for 5 minutes at 4000 rpm discarding the surnatant. Finally, the nanoparticles were redispersed in toluene. This standard procedure yields nanoparticles of 130±15 nm.

To control the particle size, the authors recommended the addition of 4-biphenylcarboxylic acid to the reaction. For example, when 0.4 g of 4-biphenylcarboxylic acid were added to the reaction and the amount of oleic acid was increased to 1.27 g, while keeping the rest of the conditions the same, the size was reduced to 25±5 nm. Note that the purification methodology had to be modified to remove the remains of the 4-biphenylcarboxylic acid. Namely, the reaction mixture was placed in two falcon tubes and 40 ml of toluene and 10 of hexane were added followed by centrifugation at 4000 rpm for 5 minutes. The obtained precipitate was resuspended in the same mix of organic solvents as before and centrifuged. The product was now redispersed in 40 ml of chloroform and centrifuged again. A last step of washing was carried out by resuspending in hexane and centrifuging. Finally, the particles were resuspended in toluene and stored.

The characterisation by TEM and SEM of the standard synthesis of nanocubes showed a particle cubic structure with an edge length of 130±15 nm and a narrow particle size distribution, with a good polydispersity index (PDI) of 11% (**Fig. 3**).
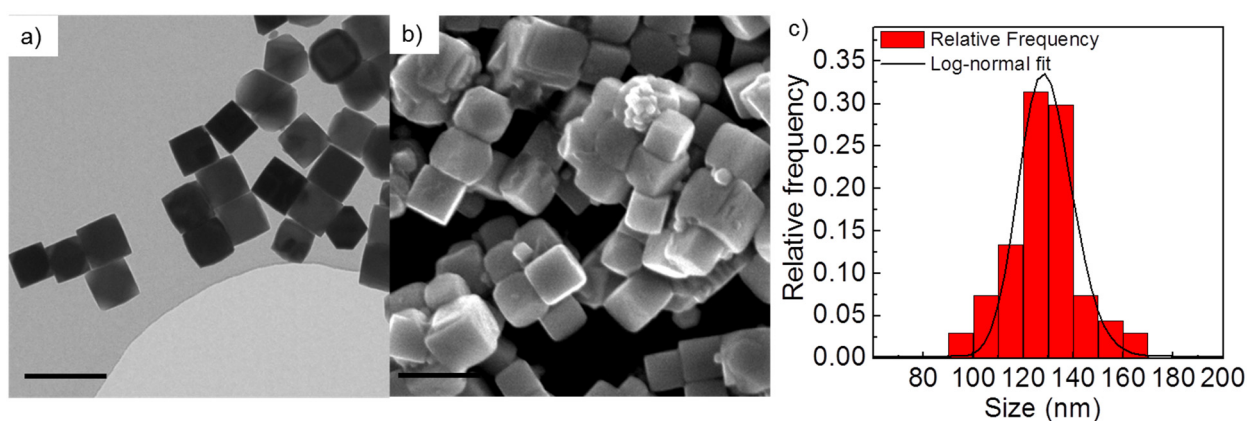

Figure 3. (a) TEM and (b) SEM images of the magnetite nanocubes obtained from the standard iron (III) acetylacetonate synthesis. The scale bars correspond to 200 nm. (c) Particle size distribution of the standard nanocubes and its fit to a log-normal function.

The temperature dependence of the ZFC magnetization (**Fig. 4a**) reveals a clear change in M, at about 110 K. This is a typical feature of the Verwey transition, which is characteristic for magnetite (Fe_3O_4)[2,3] and not present in maghemite (γ-Fe_2O_3). Importantly, no other iron oxide phases such as FeO were observed. The room temperature hysteresis loop presents a saturation magnetization of M_S = 81 emu/g and a coercivity of H_C = 160 Oe (**Fig. 4b**). The M_S value is close to that of bulk magnetite (~90 emu/g), which seems reasonable considering that the mass of the organic surfactant was not taken into account. Interestingly, the loop does not reveal any constriction at low fields, expected for vortex states.[4,5] This is probably due to two factors, (i) the fact that the cubes are randomly oriented and, consequently, the magnetic behaviour of all the orientations is averaged out[5] and (ii) the strong dipolar interactions, which will tend to lead to a collective behaviour rather than the individual properties of the cubes.[6]
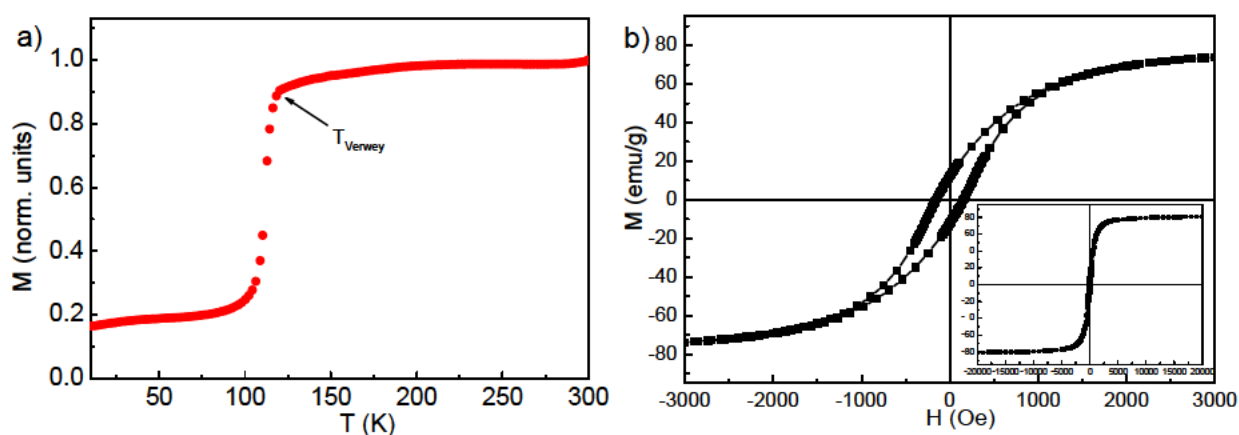

Figure 4. (a) Temperature dependence of the zero field cooled magnetization of the Fe_3O_4 cubes for H = 20 Oe. The Verwey transition temperature, T_{Verwey}, is highlighted by an arrow. (b) Enlarged hysteresis loop of the Fe_3O_4 cubes at room temperature. Shown in the inset is the complete hysteresis loop.

The XRD pattern (**Fig. 5**) shows that the structure of the particles is that of a cubic spinel, consistent with either Fe_3O_4 or γ-Fe_2O_3. However, the presence of prominent peak at ~18°, suggests that the structure is Fe_3O_4.
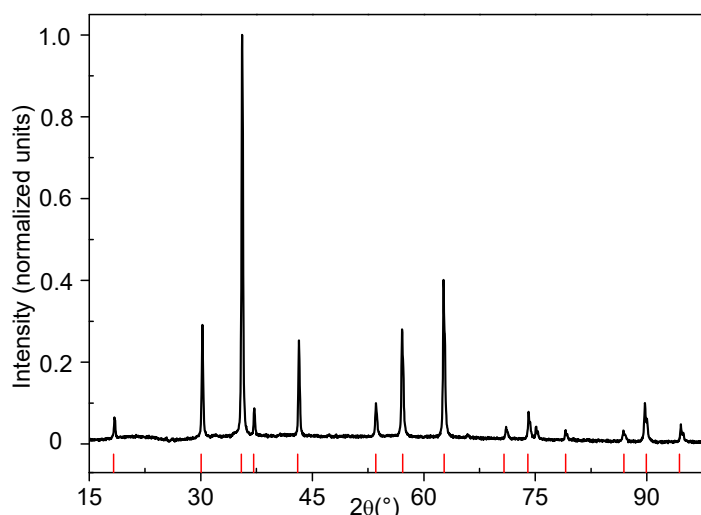
Figure 5. X-ray diffraction pattern of the nanocubes obtained from the standard iron (III) acetylacetonate synthesis (black line) compared to a Fe_3O_4 reference (red lines).

The size control was achieved by the addition of 4-biphenylcarboxylic acid to the synthesis, leading to smaller cubes of around 25 ± 5 nm, while keeping a moderate PDI (22%) (**Fig. 6a, b**). Moreover, the ZFC-FC curves confirmed the presence of Verwey transition, indicating that the composition is mainly preserved as Fe_3O_4 (**Fig. 6c**).
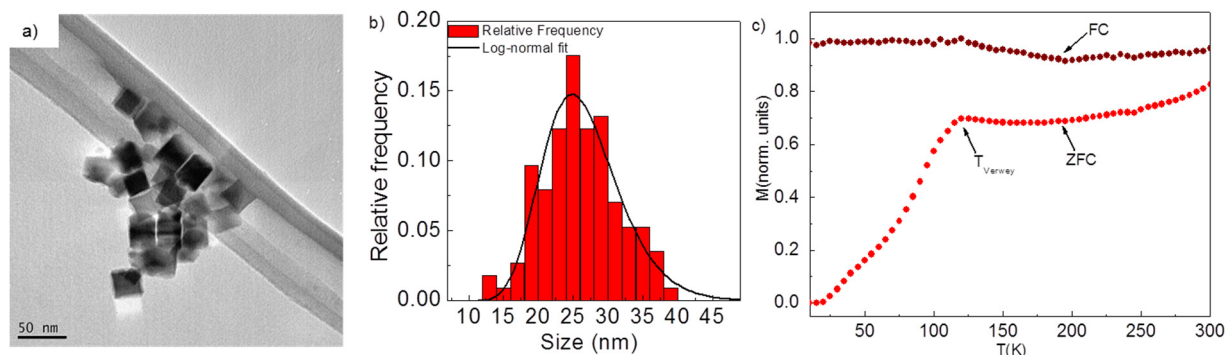

Figure 6. (a) Representative TEM image of the smaller nanocubes and (b), its corresponding particle size distribution and its fit to a log-normal function. (c) Temperature dependence of the zero field cooled (ZFC) and field cooled (FC) magnetization of the Fe_3O_4 cubes. The Verwey transition temperature, T_{Verwey}, is highlighted by an arrow.

The size reduction followed a monotonic dependence with the mass of the 4-biphenylcarboxylic acid (**Fig. 7a**) in the reaction. However, beyond 0.4 g 4-biphenylcarboxylic acid, the size reduction was much less sensitive to the addition of 4-biphenylcarboxylic acid and the polydispersity increased. Moreover, the cubic shape was partially lost, leading to

slightly amorphous particles for added amounts higher than 0.6 g, indicating such concentrations are beyond the optimal conditions range (**Fig. 7 b**).
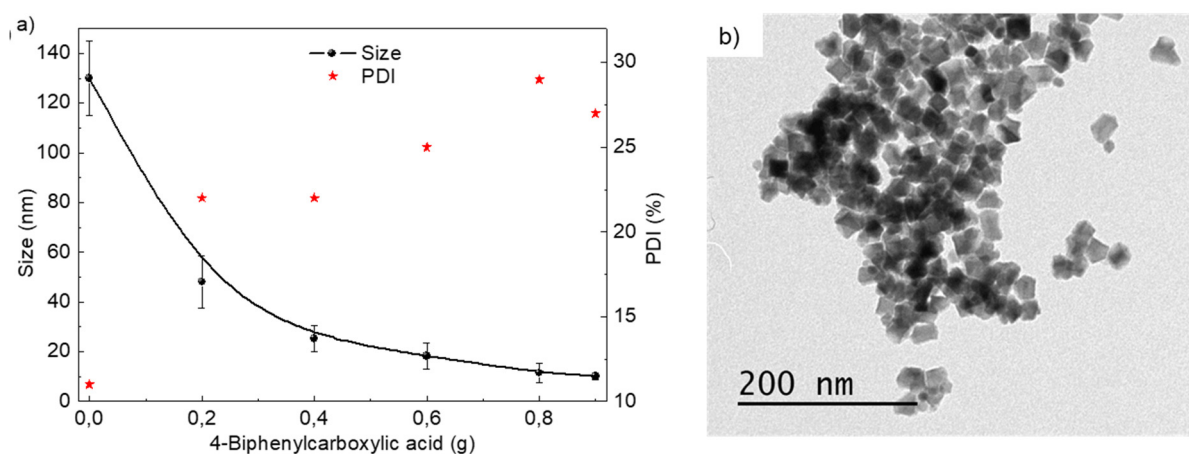

Figure 7. (a) Dependence of the particle size (black circles) and PDI (red stars) on the amount of added 4-biphenylcarboxylic acid. (b) TEM image of the particles synthesized after adding 0.6 g of 4-biphenylcarboxylic acid.

In general, this synthesis worked very well for large particle sizes and also provided a better size control than the synthesis based on iron oleate, allowing tuning the size between 25 and 130 nm. Other advantages of this synthesis are that it is a one-pot synthesis, making it presumably more reproducible (as the number of required experimental steps is reduced). On the other hand, the PDI was rather high for smaller sizes and sizes similar to those obtained by the iron oleate-based synthesis could not be obtained, since the cubic shape and size distribution narrowness were lost. Although there is no doubt that large nanocubes can be useful for some applications, due to the high colloidal stability required for biomedical applications smaller cubes would be preferred. Therefore, we concluded it should be advisable to find a synthesis that is more focused on smaller particle sizes.

2.3 Synthesis replacing oleic by decanoic acid as surfactant

The synthesis was originally described by Guardia *et al*.[9]

All chemicals, iron (III) acetylacetonate >97% (Fluka); chloroform >99% (VWR Chemicals); decanoic acid >98% (Sigma); and dibenzyl ether >90% (Acros Organics) were used as supplied without further purification.

In a typical synthesis of nanocubes, iron acetylacetonate (0.353 g) and decanoic acid (0.69 g) were mixed in dibenzyl ether (25 mL). The solution was degassed for 45 min in vacuum (~10⁻

^{2} mbar) under vigorous magnetic stirring at room temperature, after which an argon flow was passed. The temperature was increased at a rate of 5°C/min up to 200 °C and kept in these conditions for 2.5 hours. Finally, the temperature was increased to reflux (~ 290 °C) at a rate of 10 °C/min. After 60 min, the mixture was cooled down. After cooling down to room temperature, the reaction mixture was placed in two falcon tubes and 25 mL chloroform and 25 mL acetone were added followed by centrifugation at 4000 rpm for 5 minutes. The pellet was resuspended in 15 mL of chloroform and 35 mL of acetone and centrifuged again. The last washing step was repeated and particles were eventually redispersed in chloroform and stored. This standard procedure yields nanoparticles of 19±3 nm

The size of the nanoparticles could be controlled by simply adjusting the vacuum temperature or the heating rates. For example, carrying out the vacuum step at 60 °C and extending the vacuum time to 60 min led to 12 nm nanoparticles. On the other hand, larger nanocubes (of 25 and 38 nm) could be obtained by following the same experimental procedure than for the 19 nm cubes but using slower heating rates (of 6 and 4 °C/min, respectively) to reach the reflux temperature.

 The structural characterisation by TEM of the nanocubes showed particles of 19±3 nm, with a PDI of 18% and a very well-defined cubic morphology (**Fig. 8**).
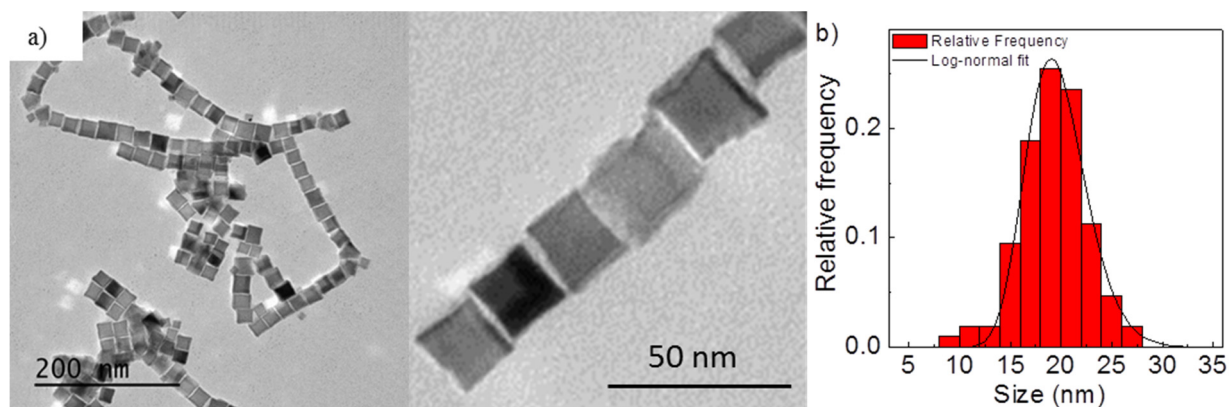

Figure 8. (a) TEM images of the 19 nm nanocubes at different magnifications. (b) Particle size distribution and its fit to a log-normal function.

Although the size of the particles could be easily controlled, the shape of the particles worsened, particularly for larger particles (**Fig. 9**).
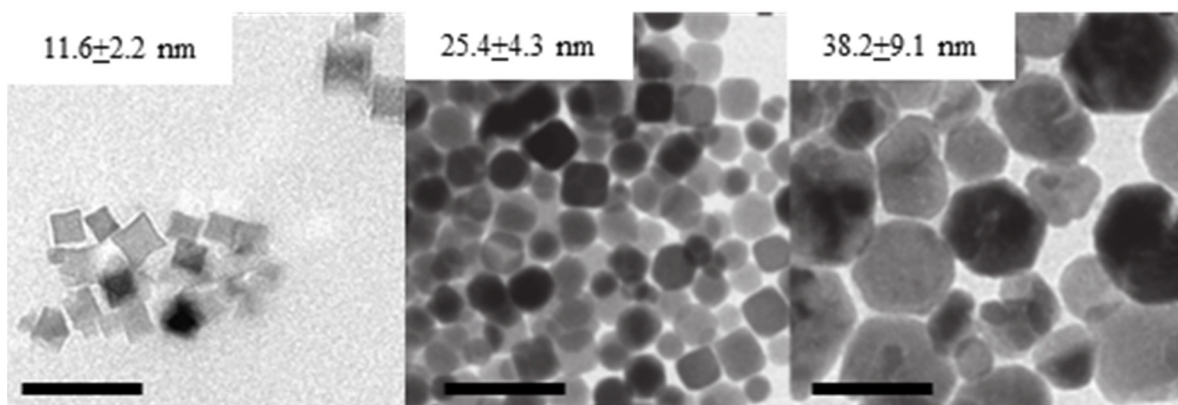
Figure 9. TEM images of particles of different sizes, synthesized following the procedures described in the text. All scale bars correspond to 50 nm.

In conclusion, this synthesis combines the advantages of being experimentally less complex than syntheses requiring iron oleate while being also able to produce smaller particles than the one using oleic acid and iron (III) acetylacetonate, which could be more useful for eventual biomedical applications than the large particles. On the other hand, despite being a one-pot synthesis, it is much slower (requiring more than 5 hours per reaction) and the size control is considerably reduced, as only particles of 19 nm showed a well-defined cubic structure and a narrow size distribution. Another factor that should be taken into account, is that the particles synthesized using this methodology are coated with decanoic acid instead of oleic, which is a shorter fatty acid. Since the particles are stabilised by steric hindrance, shorter fatty acid provides a weaker steric hindrance and for many applications it is crucial to have colloidally stable nanoparticles for an optimum performance since an uncontrolled irreversible aggregation will ruin their applicability. To guarantee homogenous aqueous dispersions it is, therefore, key to ensure that the synthesis yields particles that are as less aggregated as possible. Consequently, it would be preferable a synthesis that renders oleic acid-coated nanoparticles.

3. DEVELOPMENT OF A NEW SYNTHESIS PATHWAY

The first conclusion that can be inferred from all the syntheses we have attempted is that, so far, there is no one-pot synthesis that can be used to produce small nanoparticles (*i.e.*, smaller than 20 nm) with a very well-defined cubic shape and a narrow size distribution in a reproducible way. However, this range is of special interest since the transition from blocked to superparamagnetic state (which, for example, affects the colloidal stability) is expected to be around this size for Fe_3O_4.[4] A reduced particle size could be also interesting as the surface area of nanocubes increases dramatically for sizes smaller than 20 nm (**Fig. 10**), which may be

advantageous for many applications (*e.g.*, protein grafting or catalysis). Despite such small sizes can be synthesized using a protocol based on iron (III) oleate, it would be much more appealing that the synthesis could be carried out using only stable and commercially available reagents (like iron (III) acetylacetonate) that do not require any previous processing.
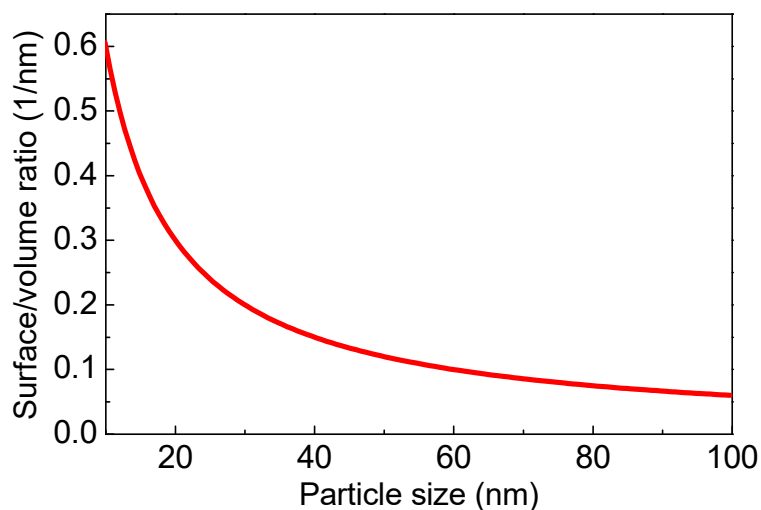

Figure 10. Surface-to-volume ratio as a function of size for nanocubes.

The second conclusion is that none of the formerly described syntheses is able to cover a large range of sizes, from large ferrimagnetic to small superparamagnetic particles. Up to now, when smaller or larger particles beyond the optimal range of a specific synthesis were required, it was necessary to change the synthesis method, otherwise the cubic shape was not retained, the particles became polydisperse or the crystallinity worsened.

Hence, the current somewhat limited control in the growth of magnetite nanocubes over a broad range of sizes with good particle size distribution and high crystallinity using a single and fast synthesis pathway, clearly highlights the need to develop new versatile synthetic approaches to grow Fe_3O_4 nanocubes.

Therefore, we have developed a novel synthesis pathway that allows producing cubic particles of small sizes in only one step but that it can be adapted to produce also larger particles if needed.

All chemicals, iron (III) acetylacetonate >99% (Acros Organics); cobalt (II) acetylacetonate 97% (Sigma); manganese (II) acetylacetonate (Sigma); oleic acid >90% (Sigma); dibenzyl ether >99% (Acros Organics); sodium oleate >82% (Sigma); 1-octadecene >90% (Sigma);

poly(maleic anhydride-alt-1-octadecene) (Sigma); and 1-tetradecene >92% (Sigma) were used as supplied without further purification.

Synthesis of Fe₃O₄ nanocubes. In the standard synthesis, iron (III) acetylacetonate (0.446 g; 1.27 mmol), sodium oleate (0.23g; 0.80 mmol) and oleic acid (1.48 g; 5.20 mmol) were added to a mixture of 1-octadecene (10 mL), dibenzyl ether (10 mL) and 1-tetradecene (3 mL). This mixture was heated to 60 °C at a rate of 5 °C/min and kept at this temperature in vacuum (~3·10^{-2} mbar) for one hour under vigorous magnetic stirring. Subsequently, the slurry was heated up to the reflux temperature (~290 °C) at a rate of 3 °C/min under argon flow and kept at this temperature for 60 minutes. Finally, the reaction was cooled down to room temperature.

In order to purify the nanocubes, the resulting product was washed with a mixture of isopropanol (50 mL), acetone (40 mL) and methanol (10 mL) and centrifuged for 10 minutes at 10600 g, discarding the surnatant. The product was washed again with chloroform (20 mL), isopropanol (40 mL) and methanol (30 mL) and centrifuged. Finally, the nanoparticles were redispersed in toluene. This standard procedure results in iron oxide nanocubes with an average edge length of 15.3±1.3 nm.

The size could be easily tuned over a wide range by adjusting the experimental conditions, *e.g.*, amount of iron (III) acetylacetonate, heating rate, temperature at which vacuum is performed or the solvent volume. For instance, if the amount of iron (III) acetylacetonate was reduced to 0.400 g (1.12 mmol) while keeping the rest of parameters unchanged, 9.1±0.7 nm nanocubes are obtained. On the other hand, 24.5±1.9 nm nanocubes were obtained when the amount of iron (III) acetylacetonate is increased up to 0.610 g (1.73 mmol) and the heating rate is increased to 15 °C/min. Larger cubes (~80 nm) could be obtained by modifying the reagent concentration. Namely, iron (III) acetylacetonate (0.530 g; 1.50 mmol) and oleic acid (0.85 g; 3.01 mmol) are added to a mixture of 1-octadecene (5 mL), dibenzyl ether (5 mL) and 1-tetradecene (1.5 mL). This mixture is degassed at room temperature for 60 min in vacuum. Afterwards, the blend was heated up to the reflux temperature at a rate of 20 °C/min under argon atmosphere and kept at this temperature for 60 minutes. After cooling down to room temperature, the product was centrifuged and washed with a mixture of toluene and hexane 1:1 twice. This procedure leads to cubes about 81.5±6.5 nm in edge length.

4. RESULTS

Standard synthesis

The transmission electron microscopy (TEM) images of the nanocubes obtained from the standard synthesis (**Fig.11 a, b**) reveal a well-defined cubic structure with an edge length of 15.3 ± 1.2 nm and a narrow particle size distribution, with a PDI of 8% (**Fig. 11c**). Moreover, the scanning electron microscopy (SEM) images of the nanoparticles (**Fig. 11d**) show very well ordered cubic superstructures, which confirms the good cubic shape and narrow particle size distribution of the nanocubes.[21]

The crystallinity of the material was studied by high resolution TEM (HRTEM) images, as shown in **Fig. 11e**. The fast Fourier transform (FFT) of the image (**Fig. 11f**) confirms the cubic spinel structure of the nanoparticles.
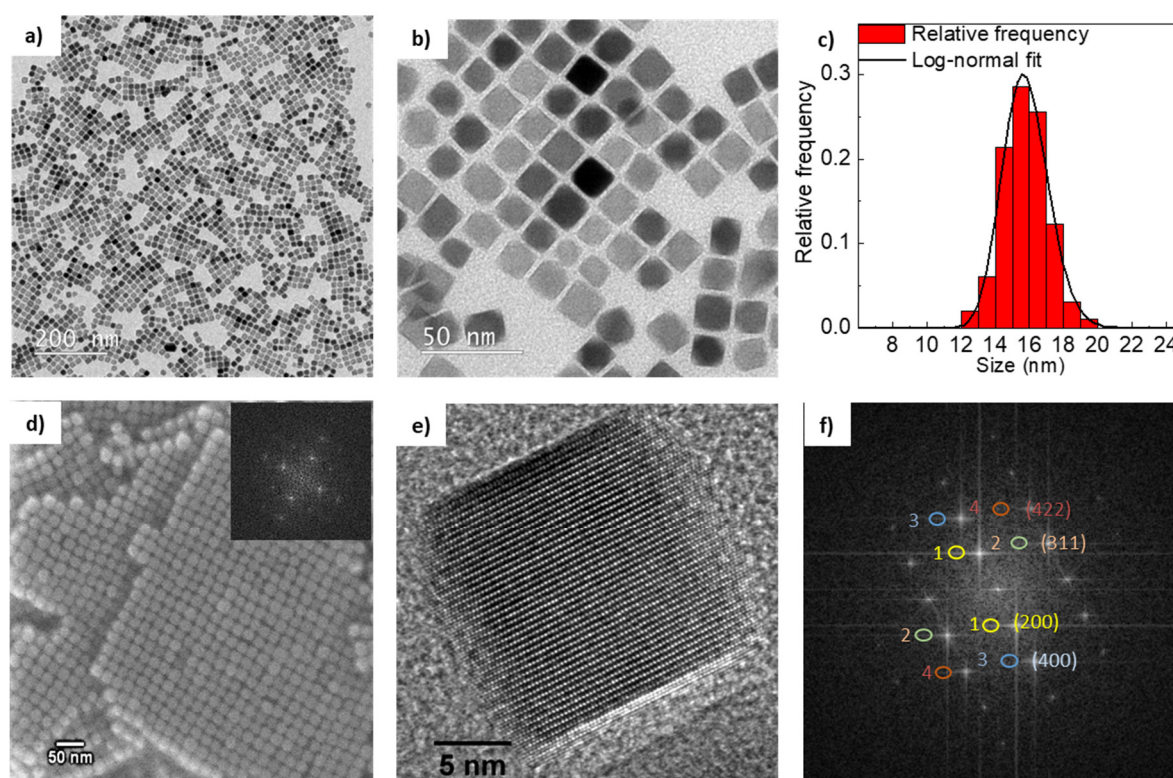

Figure 11. TEM images of the magnetite nanocubes obtained from the standard synthesis (a) at low magnification, (b) at high magnification. (c) Particle size distribution of the standard nanocubes and its fit to a log-normal function. (d) SEM image of the self-assembly of the nanocubes obtained from the standard synthesis. Shown in the inset is the corresponding FFT (which evidences a simple cubic symmetry). (e) HRTEM image of a single particle and (f) its corresponding FFT. The highlighted spots in (f) correspond to the expected cubic spinel (space group Fd$\bar{3}$m) (200) – 0.429 nm, (311) – 0.253 nm, (400) – 0.212 nm and (422) – 0.189 nm reflections seen along the [013] zone axis.

The electron energy loss spectroscopy (EELS) analysis of the nanocubes at the Fe- and O-edges indicates that the samples are composed of Fe_3O_4 (**Fig. 12a, b**). Namely, the spectra at the oxygen K-edge and the Fe L-edge of the standard nanocubes (15.3 nm) are consistent with Fe_3O_4 (**Fig. 12a, b**).[22] On the other hand, the EELS mapping of the Fe oxidation state (obtained from the distance between the Fe L_2- and L_3-edges using the Oxide Wizard script)[23] demonstrates that the oxidation state of the particles is rather homogeneous at about 2.67 (*i.e.*, Fe_3O_4), hence, discarding any major presence of FeO (oxidation state +2) or γ-Fe_2O_3 (oxidation state +3) in the particles (**Fig. 12c**).
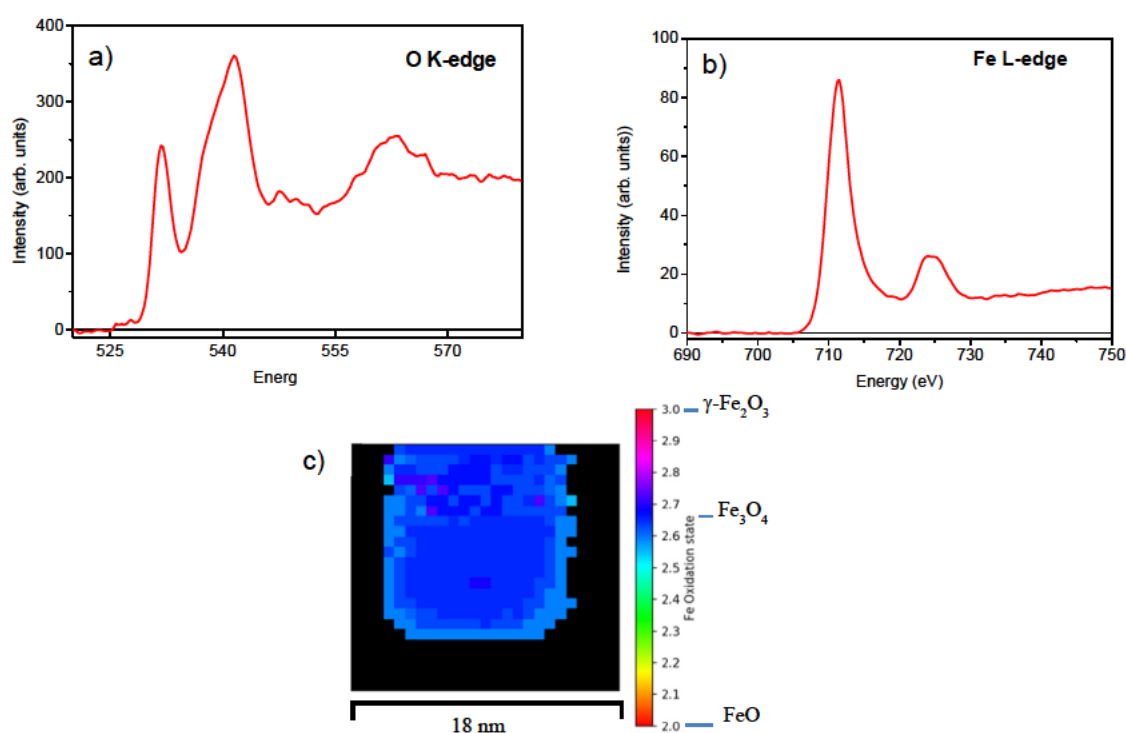

Figure 12. (a) Oxygen K-edge spectrum, (b) Fe L-edge spectrum and (c) EELS 2D mapping of the Fe oxidation state of the standard nanocubes (15.3 nm).

The x-ray diffraction (XRD) pattern (**Fig. 13**) matches that of a cubic spinel lattice with a lattice parameter of a = 8.378(5) nm, consistent with Fe_3O_4 and γ-Fe_2O_3. In fact, the prominent peak at 18° indicates that the nanocubes are composed of Fe_3O_4 rather than γ-Fe_2O_3, in agreement with the EELS analysis. It is worth emphasizing that no other phases (*e.g.*, FeO) are present in the pattern. The crystallite size was evaluated using the Scherrer equation, giving a value of 14.6(4) nm. This value is quite close to the size obtained by TEM (15.3 nm), indicating that the particles are single-crystal.
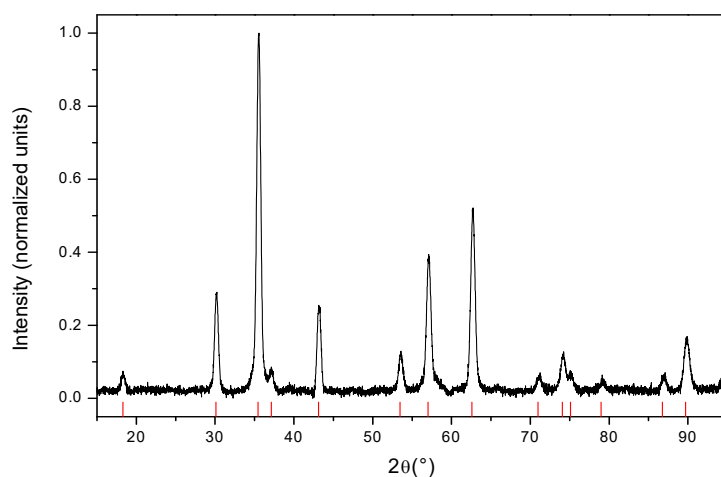
Figure 13. X-ray diffraction pattern of the nanocubes obtained from the standard synthesis (black line) compared to a Fe_3O_4 reference (red lines).

The magnetic measurements show that the saturation magnetization, M_S, of the nanocubes is 84 emu/g at room temperature rather close to the M_S of bulk magnetite ($M_S \sim 90$ emu/g), which further confirms the good crystallinity of the particles previously shown by XRD and HRTEM. As expected from their size, the particles exhibit a superparamagnetic behaviour at room temperature (with negligible coercivity, $H_c \approx 0$ Oe and remanence, $M_R \approx 0$ emu/g; **Fig. 14a**). As shown in the inset of **Fig. 14a**, at 10 K the particles show a moderate coercivity ($H_c = 200$ Oe). Moreover, the temperature dependence of the magnetization, M(T), indicates that the blocking temperature, T_B (taken as the maximum in the zero-field cooled magnetization curve; **Fig. 14b**), is slightly above room temperature. In addition, M(T) exhibits a kink at low temperatures (**Fig. 14b**). This is a unique feature of the Verwey transition, which occurs in Fe_3O_4 but not in γ-Fe_2O_3.[24] Thus, this confirms the EELS analysis that the nanocubes are pure Fe_3O_4.
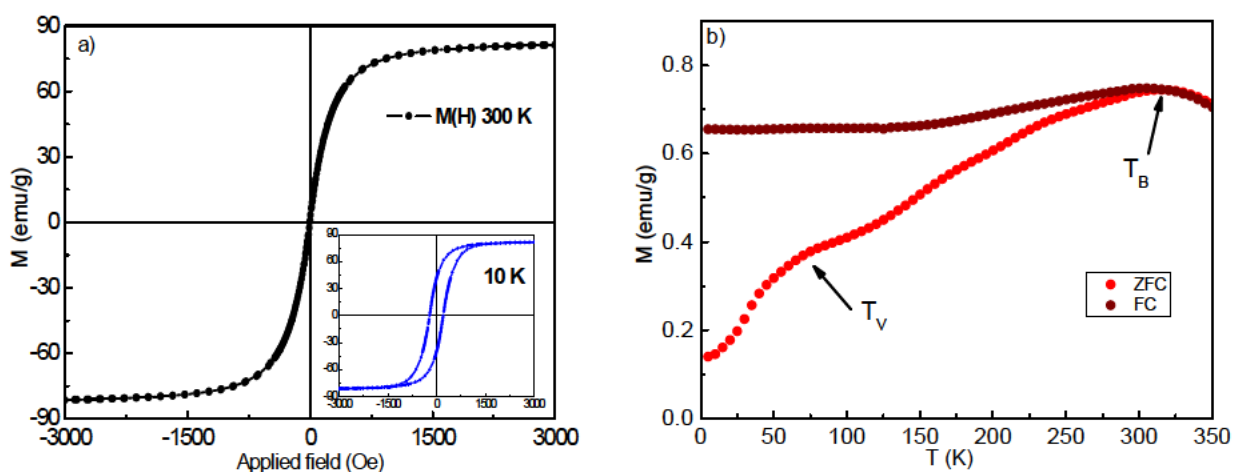
Figure 14. (a) Hysteresis loops at 300 K of the nanocubes obtained from the standard synthesis (15.3 nm). Shown in the inset is the loop at 10 K. (b) Temperature dependence of the field cooled (FC) and zero field cooled (ZFC) magnetization at H = 5 Oe. The blocking temperature, T_B, and the Verwey transition, T_V, are highlighted by arrows.

Size control

Several parameters were evaluated to control the particle size, such as solvent mixture polarity, boiling point, addition of a nucleation step, heating rate, temperature at which vacuum was performed, oleic/sodium oleate ratio, or solvent, among others (see **Table 1**).

Fe (III) acetylacetonate (g)	Oleic acid (g)	Na oleate (g)	Dibenzyl ether/Octadecene /Tetradecene (mL)	Vacuum temperature (°C)	Heating rate (°C/min)	Edge (nm)	PDI (%)
0.420	1.48	0.23	10:10:3	60	3	10	7
0.443	1.48	0.23	10:10:3	60	3	15	8
0.530	1.48	0.23	10:10:3	60	3	17	7
0.610	1.48	0.23	10:10:3	60	15	24	9
0.690	1.48	0.23	10:10:3	60	15	23	11
0.530	1.48	0.23	10:10:3	60	15	25	6
0.530	0.850	0.01	7.5:7.5:2.25	Room temperature	20	53	9
0.530	0.850	0.01	5:5:1.5	Room temperature	20	80	14
0.446	1.48	0.23	10:10:3	Room temperature	3	24	6
0.446	1.48	0.23	10:10:3	60	3	14	10
0.446	1.48	0.23	10:10:3	100	3	12	6

Table 1. Summary of the synthesis conditions of the different nanocubes described in the text

Although **Table 1** is a compilation of empirical results, some general trends can be inferred. For example, within a given range of experimental conditions, usually an increase in the iron precursor nominal concentration usually leads to larger sizes. Also, faster heating rates and/or

the total solvent volume reduction typically result in larger sizes. Finally, it is also worth mentioning that generally a higher vacuum temperature leads to smaller particles. All of these results are in line with the growth process that will be described in detail in the discussion. Nevertheless, it is important to emphasize that these trends should be considered only as rough guidelines within certain conditions range and beyond these limits other effects could predominate. For example, (i) if the heating rate is too fast, it might be difficult to achieve homogeneous heat diffusion within the synthesis flask, which can lead to polydispersity in either size or shape; (ii) performing vacuum at too high temperatures can cause the evaporation of the most volatile components, such as 1-tetradecene, which would result in dramatic changes in the chemical composition of the mixture; (iii) adding too little iron (III) acetylacetonate can cause an insufficient amount of monomers so that the nucleation cannot take place; (iv) conversely, too much iron (III) acetylacetonate can result in its incomplete dissolution, leading to a heterogeneous mixture.

Notably, based on the standard synthesis described above, among all the tested parameters, the amount of iron acetylacetonate turned out to be the most convenient way to finely tune the size without losing the cubic shape. In fact, the particle size varies monotonically with the iron acetylacetonate amount (**Fig. 15f**). For example, by decreasing the amount of iron acetylacetonate from 0.446 to 0.420 g the edge length decreases from 15.3 to 10.2 nm (**Fig. 15b**), whereas when the iron acetylacetonate amount is increased to 0.61 g, the edge length increases to 24.5 nm (**Fig. 15c**). However, if the iron acetylacetonate amount decreases exceedingly (below 0.420 g), although particle size can be further reduced to 9.1 nm, the cubic shape is partially lost, *i.e.*, the particles become more spherical and irregularly-shaped; (**Fig. 15a**). Similarly, if too much iron acetylacetonate is used in the reaction, although the size does not change considerably (*e.g.*, 24.5 nm for 0.610 g of iron acetylacetonate), the particle shape tends to become more cuboctahedral in detriment of the cubic shape, as shown in **Fig. 15e**).

As an alternative way to control the size, the temperature at which the vacuum stage was performed was changed between 100 ºC and room temperature achieving a final size of 11.8 nm and 23.7 nm, respectively (**Fig. 15g, i**). Nevertheless, similar to the control of the amount of iron acetylacetonate, this approach cannot be used to obtain particles larger than about 25 nm.
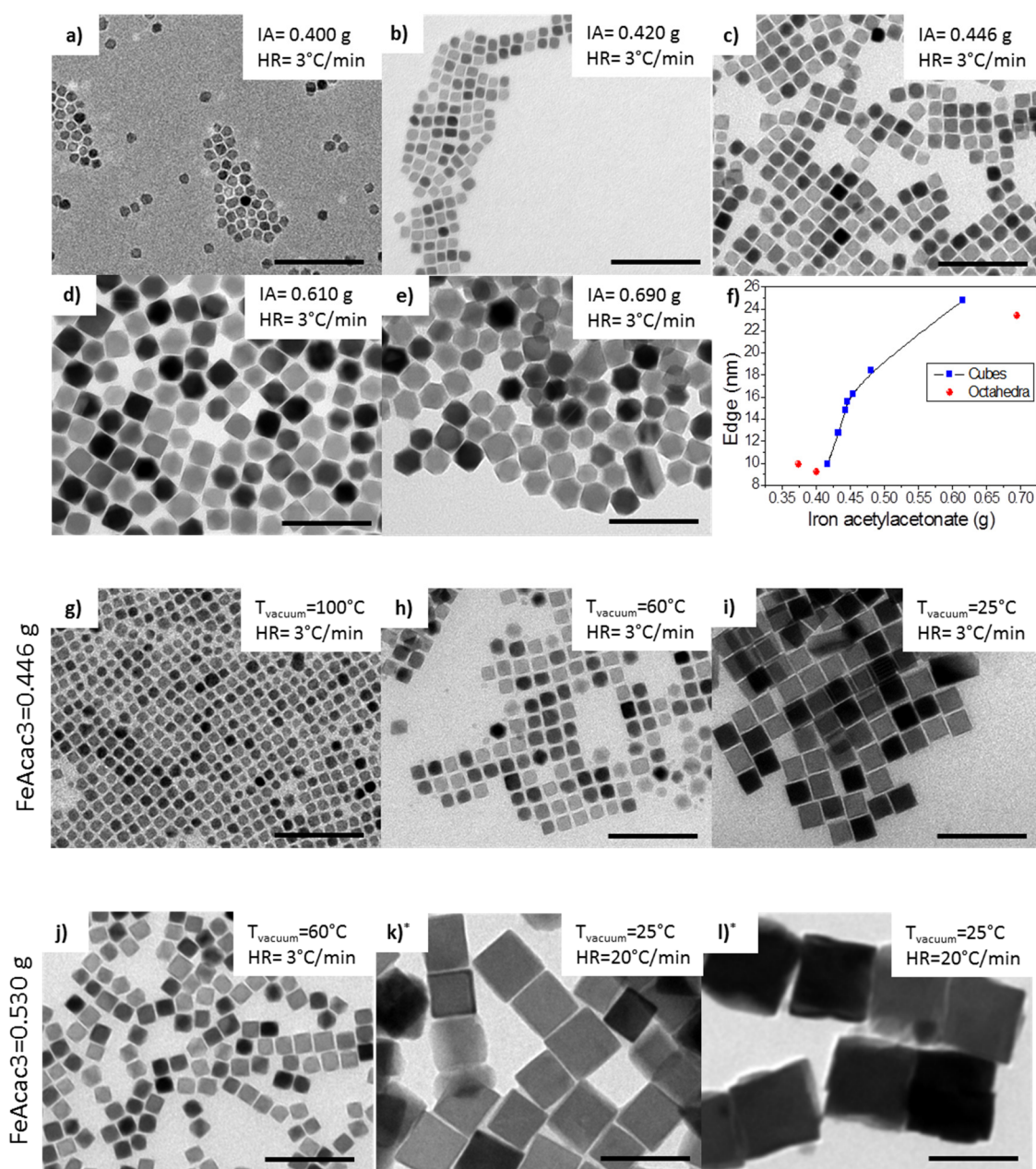
Figure 15. (a-e) TEM images of the effect of the iron acetylacetonate amount on the particle size and shape. (f) Dependence of the nanoparticle size on the amount of iron acetylacetonate. Note that the cubic particles are shown with blue squares, while other shapes are represented with red circles. (g-i) TEM images of the effect of temperature at which the vacuum stage is carried out for a fixed amount of iron acetylacetonate, FeAcac3 = 0.446 g. (j-l) TEM images of the effect of the heating rate carried out for a fixed amount of iron acetylacetonate, FeAcac3 = 0.533 g. "IA" and "HR" refer to iron acetylacetonate amount and heating rate, respectively. All the scale bars correspond to 100 nm.

*The syntheses corresponding to panels (k) and (l) were carried out in the same conditions but with different dilution factor; see **Table 1**.

Interestingly, this limitation can be overcome with only minor changes to the standard reaction and without changing any of the reactants. For example, a higher heating rate will produce a lower number of nuclei that will have an increased chance for the iron to keep on growing. Thus, when 0.530 g of iron acetylacetonate were used with a heating rate of 3 °C/min, 17.4 nm cubes were obtained (**Fig. 15j**). However, if the heating rate is increased to 15 °C/min, while keeping the rest of the conditions the same, particle size increases up to 25 nm (**Table 1**). Importantly, increasing the total reagent concentration (*i.e.*, reducing the solvent volume) while applying a faster heating rate led to larger cubic particles. For example, if the heating rate is raised to 20 °C/min and the solvent volume is reduced to 17.3 mL (instead of 23 mL) the size increases to 52.6 nm (**Fig. 15k**). Using an even smaller solvent volume (11.5 instead of 17.3 mL) while keeping the rest of the conditions the same, 80 nm cubes were obtained (**Fig. 15l**).

Interestingly, the PDI of the nanoparticles was kept low across all the studied size range. Although the PDI reached a maximum of 14% for the largest sizes, it remained between 6-9% for the particles in the range from 9-53 nm (**Fig. 16**, red symbols), thus they can be considered as monodisperse.

To assess the morphological quality of the particles, we used a simple "cubicity" parameter. Namely, since the ratio between the diagonal of a perfect square and its side is $\sqrt{2}$, by comparing the diagonal/side ratio with $\sqrt{2}$ we can have a quantitative idea on how close we are to an ideal-cube. Thus, while for a perfect cube the cubicity = diagonal/($\sqrt{2}$edge) × 100 should be 100%, for a sphere or a cuboctahedron the cubicity should decrease to 70% or 50%, respectively. Interestingly, the cubicity was beyond 90% throughout all the studied range (**Fig. 16**), clearly indicating that cubic morphology is preserved.
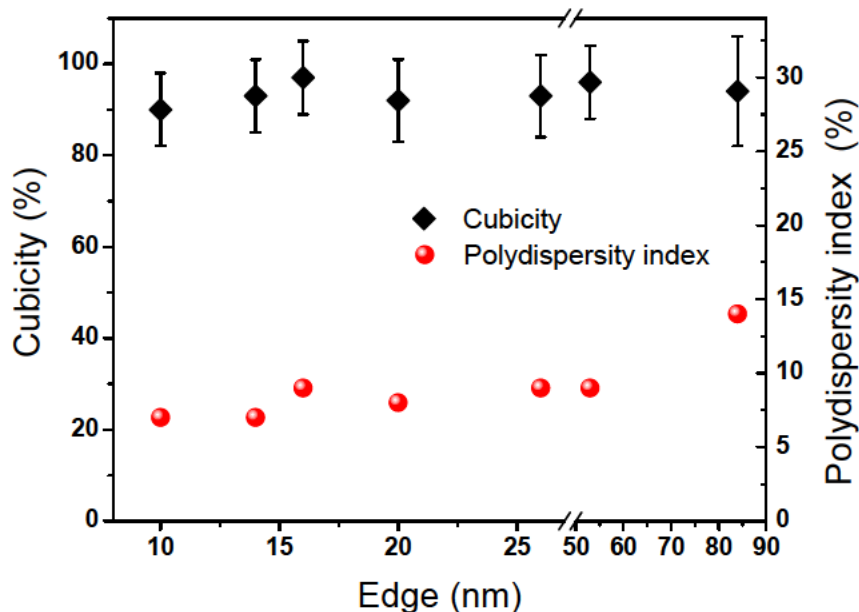
Figure 16. Cubicity (in black) and polydispersity index, PDI (in red) as a function of particle size. Note the break and the change of increment in the x-axis for large sizes.

Importance of the particle size on the colloidal stability

The achieved accurate control on the nanocubes size and the low PDI allow us to show the importance of the particle size on the colloidal stability of the magnetite suspensions. For many applications it is crucial to have colloidally stable nanoparticles for an optimum performance, especially for magnetic hyperthermia, drug delivery or magnetic resonance imaging, as an uncontrolled irreversible aggregation will harm their applicability. Stable single-particle colloidal dispersions are also necessary for an adequate water transfer of the nanoparticles for biomedical applications. To guarantee homogenous aqueous dispersions it is, therefore, key to ensure that the synthesis yields single particles, as the aggregated nanoparticles during the synthesis will remain aggregated once transferred to water. To verify whether the synthesis produces single-particles or aggregates, the hydrodynamic size was measured on freshly synthesized nanoparticles (*i.e.*, before transferring them to water). If particles are not aggregated, the ratio of the hydrodynamic and TEM particle sizes should be close to 1. Remarkably, a very abrupt change in the colloidal stability for particles larger than 16 nm is observed. Namely, while particles with sizes up to 16 nm showed a size ratio close to 1 (see inset in **Fig. 17**), indicating that most of the cubes were in a single-particle state in dispersion, whereas for 17 nm particles and beyond aggregation is observed (**Fig. 17**). We hypothesized that the degree of aggregation is probably related to the magnetic state[25,26] of the nanoparticles.
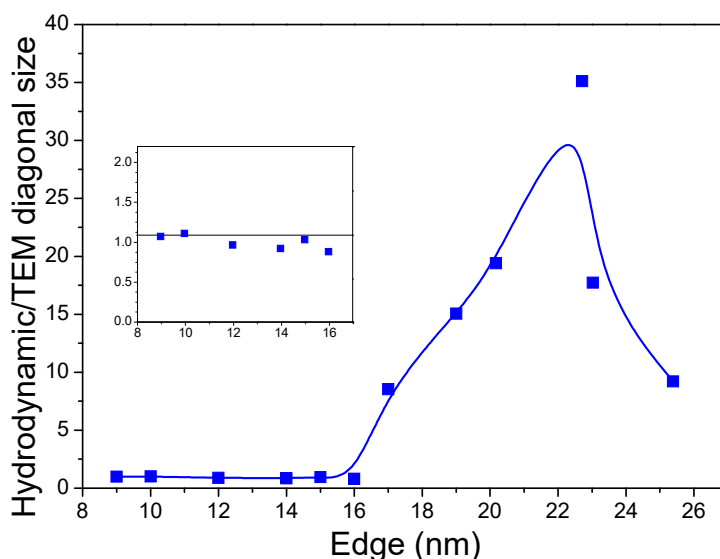
Figure 17. Hydrodynamic size/TEM diagonal as a function of the particle size. Shown in the inset is an enlargement for small sizes. Note that the diagonal rather than the edge length is used to account for the fact that the nanoparticles rotate during the hydrodynamic diameter measurements.

Origin of the aggregation

To further investigate the origin of the aggregation, measurements of the room temperature remanence, M_R, were carried out for samples of different edge lengths (**Fig. 18**, red symbols). However, note that since the magnetic measurements were carried out in powder samples, the results cannot be directly compared to the DLS measurements, where the particles are free to move. Nevertheless, since magnetic interactions are known to be a key factor in aggregation, magnetic measurements can give some clues about the role of the magnetization in the aggregation process. In fact, there is a clear correlation between the aggregation state and M_R, where the non-aggregated particles have a superparamagnetic behaviour [*i.e.*, H_c(300K) and $M_R \sim 0$]. Thus, the correlation found between the coercivity and the hydrodynamic size suggests that the origin of the aggregation is likely magnetic dipolar interactions. Hence, small particles, which show coercivity values close to 0 (and therefore no remanence), should remain stable, while particles beyond 17 nm, which are ferrimagnetic, will aggregate due to the dipolar interactions. However, in particles larger than 22 nm, the aggregation size seems to decrease as the particle size keeps increasing. This could be because of the formation of particle arrangements with flux-close states or the formation of vortex states or eventually multi-domain states in larger particles, both with reduced remanent magnetizations (and weaker dipolar interactions).[25,26] However, the systematic study of the magnetic properties of the nanoparticles is beyond the scope of this work.
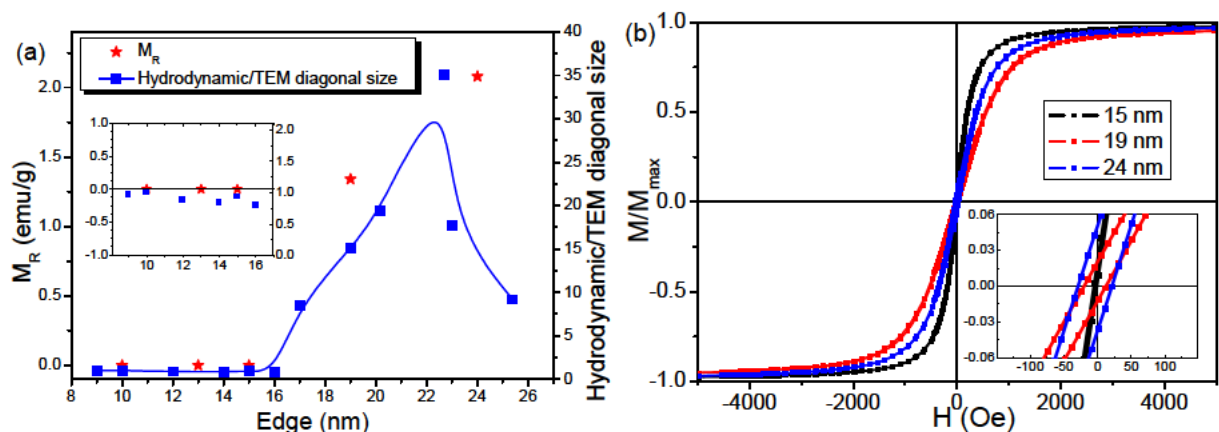
Figure 18. (a) Hydrodynamic size/TEM diagonal size (blue squares) and room temperature coercivity, M_R, (red stars) as a function of the particle size. Shown in the inset is an enlargement for small sizes. Note that the diagonal rather than the edge length is used to account for the fact that the nanoparticles rotate during the hydrodynamic diameter measurements. (b) Hysteresis loops at room temperature for the 15, 19 and 24 nm edge nanocubes (in black, red and blue, respectively). Shown in the inset is a magnification of the loops at low fields.

To have a more visual view of the effect of the colloidal stability, magnetite nanocubes within a range from 9 to 25 nm were dispersed and stored for 72 h. As can be seen in **Fig. 19**, only particles with sizes below 17 nm remained stable.
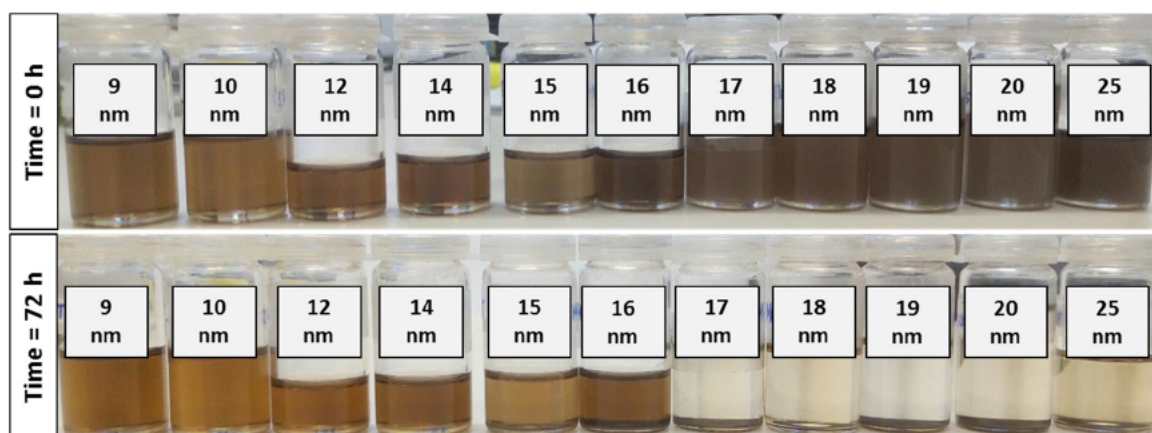

Figure 19. Toluene dispersions of nanocubes of different sizes right after sonication and redispersion (Time = 0 h; top row) and after being stored for 72 h (Time = 72 h; bottom row).

These results highlight the relevance of the nanometric range size control to ensure the colloidal stability and to optimize the features for biomedical applications.

5. DISCUSSION

Discussion of the synthesis protocol

Given the relevance of the size to maximize the performance in biomedical applications, it is worth discussing the rationale behind the achieved control in the nanocubes synthesis.

For equal volume, the surface-to-volume ratio of cubes is about 25% larger than for spheres. This implies a larger surface energy for cubes at all sizes. However, as the size of the nanocubes becomes smaller (particularly below 25 nm) the surface-to-volume ratio dramatically increases (see **Fig. 10**). Consequently, cubic shapes become increasingly less energetically favourable than spherical ones as size decreases. Therefore, to synthesize nanocubes it is crucial to provide a chemically stable environment whose properties remain unchanged during the growth stage, since any perturbation can destabilize the growth of the particles leading to deviations in either the size or the shape towards other more thermodynamically favourable structures. Taking into account these aspects, we have carefully designed a chemical synthesis for magnetite nanocubes by rationally choosing the iron precursor, surfactants, solvents, heating rate and other steps of the reaction.

Thermal decomposition of metal organic precursors in the presence of fatty acids (commonly, oleic acid), which can act as both surfactant and reductor, represents a good synthetic strategy since it produces highly crystalline monodisperse particles with narrower size distribution than other methods like coprecipitation, microemulsions, laser or spray pyrolysis.[25] In the case of iron oxide nanoparticles, the most popular iron precursors are iron oleate, iron pentacarbonyl and iron acetylacetonate. Since iron oleate is not commercially available, it must be synthesized prior to the synthesis of the nanoparticles, which adds a tedious step to the synthesis process. Moreover, the exact details of the synthesis and purifying steps deeply affect the quality of the resulting nanoparticles, introducing a high degree of variability. Moreover, the synthesis often yields a mixture of several iron oxide phases rather than pure magnetite.[27] Iron pentacarbonyl generally leads to metallic iron particles which are further oxidized to magnetite or maghemite.[28] However, this compound is chemically unstable and the crystallinity of the resulting nanoparticles is not very high.[29] On the other hand, iron acetylacetonate is a highly stable and a commercially available reagent, which makes it a more desirable candidate for the synthesis of high quality iron oxide nanoparticles.

Considering that thermal decomposition occurs at high temperature and iron acetylacetonate is a moderately polar molecule, a polar high-boiling solvent should be used. Thus, iron acetylacetonate is usually used with dibenzyl ether as solvent. However, dibenzyl ether has been reported to be unstable at high temperatures leading to benzaldehyde, especially in the presence of oxygen.[30,31] This instability results in dramatic changes of the solvent properties, like the polarity, boiling point or conductivity. For example, during the synthesis of iron oxide nanoparticles it has been observed that the boiling temperature of the mixture decays several degrees as the growth stage advances due to the emergence of more volatile molecules.[32] This lack of a stable environment for the growth of the particles hinders the formation of small monodisperse and well-defined cubic structures.

The key factors that determine the final structure of iron oxide particles synthesized by thermal decomposition have been studied in detail and some factors, like the ratio of oleic acid to iron, have been identified as critical.[33] However, Qiao *et al*. recently proposed that the final shape and size is determined mainly by the balance between the chemical potential of the monomers (μ_m, see below) and the chemical potential of the different crystal planes.[31] In the particular case of magnetite, the {111} planes are the most densely packed and have the lowest chemical potential.[34] On the other hand, the {100} planes are the least densely packed and have the highest reactivity, while the {110} planes have an intermediate packing and chemical potential. Therefore, the chemical potential of these planes can be ranked as: $\mu_{\{100\}} > \mu_{\{110\}} > \mu_{\{111\}}$.

Note that the chemical potential of the monomers is defined as $\mu_m = \mu_m^0 + RT\ln[C_m \cdot \gamma_m]$, where μ_m^0 is the chemical potential of the monomers in a reference state and is a constant; R is the ideal gas constant; T is for temperature; C_m is the concentration of monomers and γ_m is the activity coefficient of the monomers in solution.

As the temperature of the mixture increases, the iron acetylacetonate exchanges iron cations with the oleate anions to form monomers.[35] These monomers accumulate and once oversaturation is reached, nuclei are generated.[36] At this point, the chemical potential of monomers is higher than those of the crystal planes ($\mu_m > \mu_{\{100\}} > \mu_{\{110\}} > \mu_{\{111\}}$) and they can change from the solvated state (high chemical potential) to any of the planes of lower chemical potential.[37] This stage is called diffusional growth. Although in nuclei all of these facets are exposed and thermodynamically the growth in any plane is permitted, the rate at which monomers are deposited is different for every facet and it depends on the kinetic constants, which are inversely proportional to the energy barrier of the process. Since the {111} planes

are the most densely packed and thus they have a high steric hindrance, the arrival of new monomers will be inhibited. Therefore, the energy barrier that monomers have to overcome to deposit on this plane is higher than on the other planes, consequently the {111} facets will grow the slowest.

The initial simultaneous growth in the three directions (ruled only by the differences in deposition rates) leads to the formation of octahedrons (see **Fig. 20**). As the reaction advances, the chemical potential of the monomers falls (*i.e.*, because of the C_m decay) to a point where the {100} planes cannot grow anymore ($\mu_{\{100\}} > \mu_m > \mu_{\{110\}} > \mu_{\{111\}}$). However, the {110} and {111} facets keep growing, which makes the octahedra turn into tetradecahedra (see **Fig. 20**). Similarly, when the μ_m decays sufficiently, deposition on the {110} planes stops, while it continues on the {111} facets, leading to the transition from tetradecahedra into cubes (see **Fig. 20**). If the amount of remaining monomers is sufficiently high to continue the deposition in {111} planes, the cubes vertices will continue to grow, resulting in star-like structures. However, because of the large hydrodynamic size of the iron oleate monomers it is very difficult for them to overcome the steric hindrance of the {111} planes making the growth of stars rather inefficient.
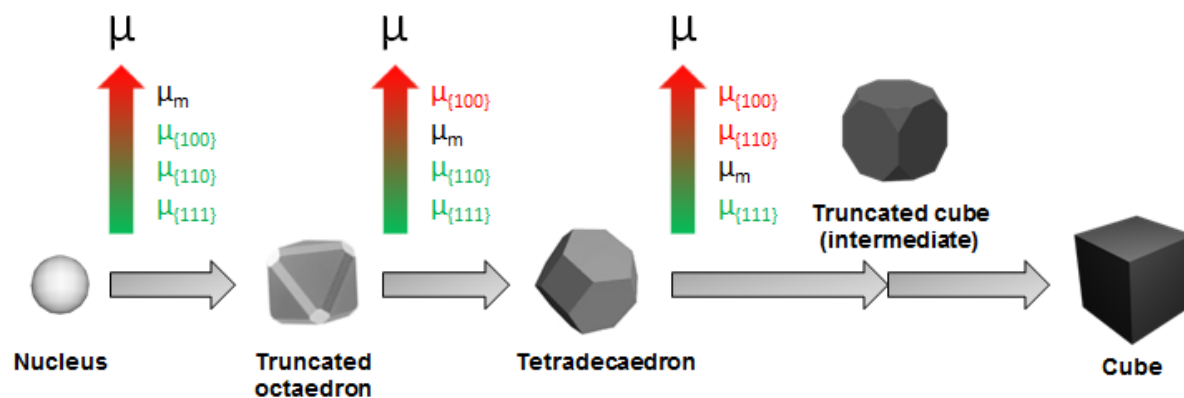
Figure 20. Schematic representation of the transition from a nucleus into a cube as μ_m decays. The green (red) colour for the μ of the crystal planes depends if their chemical potential is lower (higher) than μ_m [31]

Since several parameters control the chemical potential of the monomers, *μ_m*, diverse approaches can be envisaged to engineer the morphology of the nanoparticles. However, μ_m^0 and R are constants and, thus they do not influence the shape of the particle. Additionally, taking into account that the growth stage is carried out at the boiling temperature of the solvent, if the solvent composition is stable, T can be considered as a constant that will be defined

91

mainly by the properties of the solvent used for the synthesis. This implies that C_m and γ_m are the parameters than can be controlled to tune the chemical potential.

C_m is the balance between the rate at which monomers are generated and consumed during the synthesis. In our case, this can be controlled by the total amount of iron and surfactants and also by tuning the ratio between oleic acid and sodium oleate, as will be explained later. The other parameter, γ_m, depends on how strong is the interaction between the solvent and the monomers, and it can be adjusted by either changing the iron ligands or the solvent. Since non-polar solvents have stronger molecular interactions with the long aliphatic chains of the monomers, they should decrease the activity coefficient of the monomers; consequently, they should ease the formation of cubic structures, while polar solvents should tend to favour octahedral-like structures. This effect becomes critical when using dibenzyl ether, since at high temperatures it usually decomposes into molecules like benzaldehyde, which are even more polar than the dibenzyl ether itself. As a consequence of this rise in polarity, interactions between the solvent and the aliphatic chains of the monomers become weaker, increasing γ_m, which in turn increases μ_m so much that the growth on all facets is permitted. This implies that although initially cubes can grow using dibenzyl ether, as it starts to decompose the morphology control is lost. In the extreme situation, eventually a secondary nucleation becomes possible, resulting in polydisperse particles.

Based on the above arguments, one could think that replacing dibenzyl ether for 1-octadecene, which is more stable and less polar, could be a good solution. However, replacing dibenzyl ether by 1-octadecene is not possible because iron acetylacetonate is poorly dissolved in such a non-polar solvent. Nevertheless, even if a total substitution of dibenzyl ether is not feasible, still a partial substitution is possible to minimize the effects of the dibenzyl ether instability. This is why in our approach we decided to use a mixture of 1-octadecene and the minimum amount of dibenzyl ether necessary to dissolve iron acetylacetonate. 1-octadecene has a higher boiling point than dibenzyl ether (315 vs 298 °C), consequently, the resulting mixture has an intermediate boiling point between both solvents. However, given the lability of the ether bond in dibenzyl ether, we considered it would be favourable to intentionally decrease the boiling temperature of the mixture to prevent the risk of dibenzyl ether decomposition. This is why 1-tetradecene was added to the mixture since it has a similar structure to that of 1-octadecene but with a much lower boiling point (252 °C). The volume of 1-tetradecene in the solvent mixture was adjusted so the overall boiling point of the mixture was around 290 °C. Importantly, the resulting solvent mixture showed a very stable boiling temperature over time, in contrast to

pure dibenzyl ether as can be seen in **Fig. 21** and reported before.[30] Note that reaching the boiling temperature in the final step of the synthesis is highly desirable to induce a rapid oversaturation of monomers that triggers a burst homogeneous nucleation. It is important to stress that the nucleation does not occur only because a critical concentration of monomers is surpassed, but rather because of the sudden increase in the γ_m (and consequently their activity) when the solvent mixture starts to boil, which triggers the burst nucleation. This will make the nuclei appear mostly at the same time and to grow at the same rate, resulting in more monodisperse nanoparticles.[38] Another reason why it is advisable to reach such a high temperature is to promote the complete reduction of iron (III) to iron (II), a required step to form magnetite.[27]
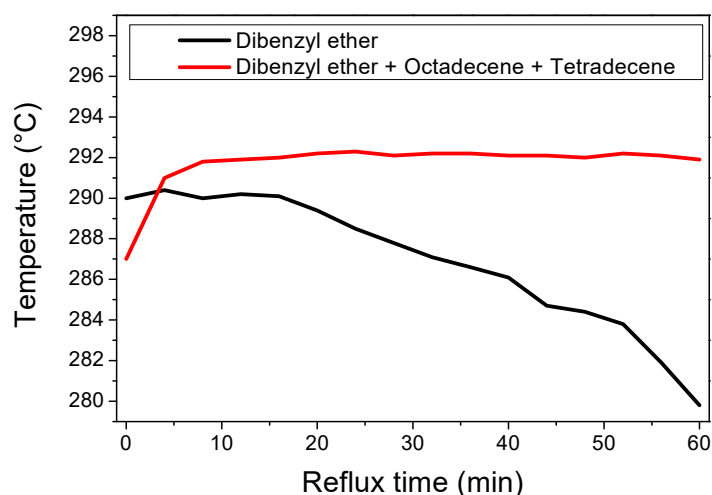

Figure 21. Evolution of the synthesis temperature with the reflux time for both dibenzyl ether alone and the solvent mixture described in the text.

As previously mentioned, controlling the chemical potential of the monomers during the growth stage is crucial to control the final shape of the particles. Based on this fact, we assumed that a more constant chemical potential of the monomers during the diffusion growth stage will produce better defined structures. For this reason we combined the use of oleic acid with its sodium salt, sodium oleate. Sodium oleate can also coordinate with iron but it must first dissociate from sodium. This dissociation is disfavoured in non-polar solvents, where it takes place only in a small proportion, slowing down the formation of monomers. However, as the reaction proceeds and oleate anions are consumed, the dissociation equilibrium should gradually be shifted towards the dissociated form, keeping a smoother monomer generation rate and thus a low and more constant chemical potential over time. An additional reason to replace part of the oleic acid by sodium oleate is because it is known that the acidic form can

condensate with itself at the high temperatures of the synthesis (near 300°C) *via* heterolytic cleavage (*i.e.*, ketonic decarboxylation).[27] As by-products of this reaction, a heavy ketone (oleone), CO_2 and water are generated. Reducing the occurrence of this reaction is highly desirable, since these by-products can generate abrupt bubbling, changing the local concentrations and chemical properties (adding heterogeneity to the mixture) and also because the generated water can react with dibenzyl-ether to produce benzaldehyde changing the overall polarity of the mixture or its boiling point. However, in the sodic form, the heterolytic cleavage necessary for this reaction is strongly disfavoured. Nevertheless, similarly to the case of dibenzyl ether, a total substitution of oleic acid for sodium oleate is not possible since it is poorly dissolved in the mixture at room temperature and cannot dissociate to exchange iron from iron acetylacetonate and generate the monomers. We empirically found that the number of sodium oleate moles should be around 15% of oleic acid mol. Finally, one last reason to add sodium oleate is that the sodium cations generated in the reaction are highly hygroscopic, hence they can trap any water molecules formed during the synthesis. This avoids the reported[39] negative influence of water on the shape of the nanoparticles.

To confirm the size and shape evolution mechanism, aliquots were taken at different reflux times (after the mixture just starts to boil, at t = 0, 10, 30 and 60 min) and analysed using TEM. Although in the aliquots taken in the first 10 minutes the number of particles that could be recovered was exceedingly low (probably because due to their small size they could not be precipitated after washing) to perform any systematic analysis, the images at 30 min and 60 min confirmed the transition from octahedral into cubic structure after the first 30 minutes of reflux (**Fig. 22a, b**). Notably, when the same experiment was carried out with only oleic acid (but keeping the total concentration of surfactant the same), the growth of the particles was faster but resulted in octahedral-shaped particles, as expected from an initially higher but much less constant μ_m during the reflux time (**Fig. 22c, d**). In addition, in the case of oleic acid the growth was practically finished after the first 30 min and extending the reflux time to 60 min only lead to a size increase of 1 nm, whereas in the reaction with oleic acid and sodium oleate, the particles experienced more drastic size and morphology changes over time.
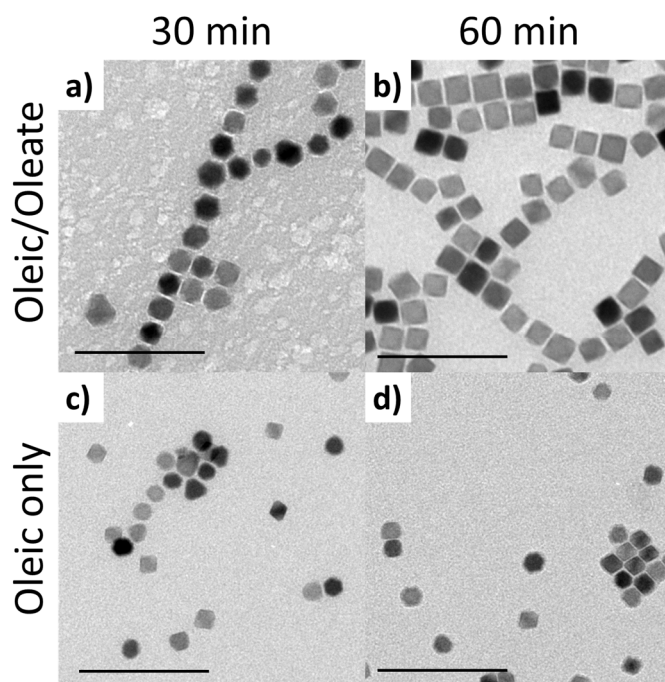
Figure 22. TEM images of the particles obtained at different reflux times using a combination of both oleic acid and sodium oleate at (a) 30 min and (b) 60 min and using only oleic acid (but keeping to the total concentration of surfactant the same) at (c) 30 min and (d) 60 min. Scale bars correspond to 100 nm.

Size control

There are different approaches to control the size of the nanocubes without changing the solvent or the iron precursor, like replacing oleic acid by a shorter ligand such as decanoic acid.[9] However, since decanoic acid is a shorter fatty acid than oleic acid, the steric hindrance it can provide is weaker. Taking into account the magnetic character of the final product, decanoic acid will provide less protection against aggregation due to dipolar interactions. Since our goal is having colloidally stable nanocubes, we chose oleic acid as surfactant.

The main parameter to control the size in our synthesis is the amount of iron (III) acetylacetonate. Since the limiting factor for the growth of the particles is the availability of monomers that can be incorporated into the structures, higher or lower amounts of iron precursor lead to larger or smaller nanoparticles, respectively.

Moreover, the synthetic approach has an initial stage where vacuum is done at 60°C for 1 hour to ensure the elimination of both water and oxygen traces in the solvents. During this step, the exchange between iron acetylacetonate and oleic acid is favoured, leading to the formation of monomers of iron oleate. As the temperature at which vacuum is performed increases, the number of monomers will increase. A higher number of monomers when the nucleation step

95

begins will produce a higher number of nuclei, decreasing the amount of iron available for the later growth stage and thus leading to smaller particles. For the same reason, a slow heating rate (3°C/min) was chosen to reach the boiling temperature.

Finally, to achieve particles larger than about 25 nm a slightly modified approach is necessary. Increasing the reagent concentration (by reducing the solvent volume) allows the particles to grow for a longer time because in this way a lower total number of monomers is required to have a high enough μ_m to overcome the energy barrier for the deposition on the surface of the particles. However, as mentioned before, if μ_m is too high the cubic morphology can be lost. For this reason, the heating rate was increased to (i) have a lower number of nuclei and (ii) avoid all the monomers to be generated in the same time, thus keeping a moderate μ_m for a longer time. Thus, the combination of the higher concentration and faster heating rate allows the synthesis of large nanocubes.

In conclusion, unlike all of the other tested approaches, the new developed procedure allows synthesizing Fe_3O_4 nanocubes with a precise size tunability over a broad range (9 – 80 nm), keeping the cubic morphology and a small PDI (< 10%) all over the range. The as-obtained material has proven to be crystalline and pure, with magnetite as the main iron oxide phase, as inferred from both the structural and magnetic characterisations. In addition, the procedure has also the advantages of being very fast (with a total reaction time of only 2.5 hours) and highly reproducible due to the enhanced chemical stability of the reaction environment.

6. CONCLUSIONS

Several published chemical pathways to produce nanocubes have been tried in this work. Although all of them provided cubic particles, they all were limited to a narrow size range or to sizes that were not suitable for biomedical applications, or showed some problems related to the purity or crystallinity, etc. Despite the potential interest of magnetic cubic nanoparticles for multiple purposes, their synthesis in a controllable and reproducible manner is a challenge that had not been fully resolved. Consequently, we proceeded to engineer a new chemical synthesis starting from the assumptions that i) the loss of size control and reproducibility stem from the chemical instability of the growth environment and ii) the chemical potential of the monomers, which has recently been reported as the main factor determining the particle shape, could be tuned by adjusting the ratio of oleate anions in both the acidic and basic forms. The results showed that the new pathway can provide particles that meet all the criteria of a "good

synthesis": size monodispersity, reproducibility, phase purity, high crystallinity and well-defined shape. In addition, we have carefully described the mechanisms controlling the size and shape of the nanoparticles. Therefore, this new synthetic pathway enables the facile and accurate tuning of the nanocubes size, which, as we will see, is crucial to optimize their properties, for example, for biomedical applications.

7. REFERENCES

(1)   Laurent, S.; Forge, D.; Port, M.; Roch, A.; Robic, C.; Vander Elst, L.; Muller, R. N. Magnetic Iron Oxide Nanoparticles: Synthesis, Stabilization, Vectorization, Physicochemical Characterizations, and Biological Applications. *Chem. Rev.* **2010**, 110 (4), 2574–2574.

(2)   Ling, D.; Hyeon, T. Chemical Design of Biocompatible Iron Oxide Nanoparticles for Medical Applications. *Small* **2013**, 9 (9-10), 1450–1466.

(3)   Salazar-Alvarez, G.; Qin, J.; Šepelák, V.; Bergmann, I.; Vasilakaki, M.; Trohidou, K. N.; Ardisson, J. D.; Macedo, W. A. A.; Mikhaylova, M.; Muhammed, M.; Baró, M. D.; Nogués, J. Cubic versus Spherical Magnetic Nanoparticles: The Role of Surface Anisotropy. *J. Am. Chem. Soc.* **2008**, 130 (40), 13234–13239.

(4)   Nemati, Z.; Alonso, J.; Rodrigo, I.; Das, R.; Garaio, E.; García, J. Á.; Orue, I.; Phan, M.-H.; Srikanth, H. Improving the Heating Efficiency of Iron Oxide Nanoparticles by Tuning Their Shape and Size. *J. Phys. Chem. C* **2018**, 122 (4), 2367–2381.

(5)   Mitra, A.; Mohapatra, J.; Meena, S. S.; Tomy, C. V.; Aslam, M. Verwey Transition in Ultrasmall-Sized Octahedral Fe_3O_4 Nanoparticles. *J. Phys. Chem. C* **2014**, 118 (33), 19356–19362.

(6)   Lisjak, D.; Mertelj, A. Anisotropic Magnetic Nanoparticles: A Review of Their Properties, Syntheses and Potential Applications. *Prog. Mater. Sci.* **2018**, 95, 286–328.

(7)   Mirabello, G.; Lenders, J. J. M.; Sommerdijk, N. A. J. M. Bioinspired Synthesis of Magnetite Nanoparticles. *Chem. Soc. Rev.* **2016**, 45 (18), 5085–5106.

(8)   Andrés Vergés, M.; Costo, R.; Roca, A. G.; Marco, J. F.; Goya, G. F.; Serna, C. J.; Morales, M. P. Uniform and Water Stable Magnetite Nanoparticles with Diameters around the Monodomain–multidomain Limit. *J. Phys. D. Appl. Phys.* **2008**, 41 (13), 134003.

(9)   Guardia, P.; Di Corato, R.; Lartigue, L.; Wilhelm, C.; Espinosa, A.; Garcia-Hernandez, M.; Gazeau, F.; Manna, L.; Pellegrino, T. Water-Soluble Iron Oxide Nanocubes with High Values of Specific Absorption Rate for Cancer Cell Hyperthermia Treatment. *ACS Nano* **2012**, 6 (4), 3080–3091.

(10)   Kim, D.; Lee, N.; Park, M.; Kim, B. H.; An, K.; Hyeon, T. Synthesis of Uniform Ferrimagnetic Magnetite Nanocubes. *J. Am. Chem. Soc.* **2009**, 131 (2), 454–455.

(11)   Kovalenko, M. V.; Bodnarchuk, M. I.; Lechner, R. T.; Hesser, G.; Schäffler, F.; Heiss, W. Fatty Acid Salts as Stabilizers in Size- and Shape-Controlled Nanocrystal Synthesis: The Case of Inverse Spinel Iron Oxide. *J. Am. Chem. Soc.* **2007**, 129 (20), 6352–6353.

(12)   Estrader, M.; López-Ortega, A.; Golosovsky, I. V.; Estradé, S.; Roca, A. G.; Salazar-Alvarez, G.; López-Conesa, L.; Tobia, D.; Winkler, E.; Ardisson, J. D.; Macedo, W. a. a.; Morphis, A.; Vasilakaki, M.; Trohidou, K. N.; Gukasov, A.; Mirebeau, I.; Makarova, O. L.; Zysler, R. D.; Peiró, F.; et al. Origin of the Large Dispersion of Magnetic Properties in Nanostructured Oxides: Fe_xO/Fe_3O_4 Nanoparticles as a Case Study. *Nanoscale* **2015**, 7 (7), 3002–3015.

(13)   Torruella, P.; Arenal, R.; de la Peña, F.; Saghi, Z.; Yedra, L.; Eljarrat, A.; López-Conesa, L.; Estrader, M.; López-Ortega, A.; Salazar-Alvarez, G.; Nogués, J.; Ducati, C.; Midgley, P. a.; Peiró, F.; Estradé, S. 3D Visualization of the Iron Oxidation State in FeO/Fe_3O_4 Core–Shell Nanocubes from Electron Energy Loss Tomography. *Nano Lett.* **2016**, 16 (8), 5068–5073.

(14)   Ichikawa, R. U.; Roca, A. G.; López-Ortega, A.; Estrader, M.; Peral, I.; Turrillas, X.; Nogués, J. Combining X-Ray Whole Powder Pattern Modeling, Rietveld and Pair Distribution Function Analyses as a Novel Bulk Approach to Study Interfaces in Heteronanostructures: Oxidation Front in FeO/Fe_3O_4 Core/Shell Nanoparticles as a Case Stu. *Small* **2018**, 14 (30), 1800804.

(15)   Park, J.; An, K.; Hwang, Y.; Park, J.-G.; Noh, H.-J.; Kim, J.-Y.; Park, J.-H.; Hwang, N.-M.; Hyeon, T. Ultra-Large-Scale Syntheses of Monodisperse Nanocrystals. *Nat. Mater.* **2004**, 3 (12), 891–895.

(16)   Wetterskog, E.; Tai, C.-W.; Grins, J.; Bergström, L.; Salazar-Alvarez, G. Anomalous Magnetic Properties of Nanoparticles Arising from Defect Structures: Topotaxial Oxidation of $Fe_{1-x}O|Fe_{3-\delta}O_4$ Core|Shell Nanocubes to Single-Phase Particles. *ACS Nano* **2013**, 7 (8), 7132–7144.

(17)   Özdemir, Ö.; Dunlop, D. J.; Moskowitz, B. M. The Effect of Oxidation on the Verwey Transition in Magnetite. *Geophys. Res. Lett.* **1993**, 20 (16), 1671–1674.

(18)   Feld, A.; Weimer, A.; Kornowski, A.; Winckelmans, N.; Merkl, J.-P.; Kloust, H.; Zierold, R.; Schmidtke, C.; Schotten, T.; Riedner, M.; Bals, S.; Weller, H. Chemistry of Shape-Controlled Iron Oxide Nanocrystal Formation. *ACS Nano* **2019**, 13 (1), 152–162.

(19)   Walz, F. The Verwey Transition - a Topical Review. *J. Phys. Condens. Matter* **2002**, 14 (12), R285–R340.

(20)   García, J.; Subías, G. The Verwey Transition - A New Perspective. *Journal of Physics Condensed Matter*. **2004**, R145–R178.

(21)   Disch, S.; Wetterskog, E.; Hermann, R. P.; Salazar-Alvarez, G.; Busch, P.; Brückel, T.; Bergström, L.; Kamali, S. Shape Induced Symmetry in Self-Assembled Mesocrystals of Iron Oxide Nanocubes. *Nano Lett.* **2011**, 11 (4), 1651–1656.

(22)   Colliex, C.; Manoubi, T.; Ortiz, C. Electron-Energy-Loss-Spectroscopy near-Edge Fine Structures in the Iron-Oxygen System. *Phys. Rev. B* **1991**, 44 (20), 11402–11411.

(23)   Yedra, L.; Xuriguera, E.; Estrader, M.; López-Ortega, A.; Baró, M. D.; Nogués, J.; Roldan, M.; Varela, M.; Estradé, S.; Peiró, F. Oxide Wizard: An EELS Application to Characterize the White Lines of Transition Metal Edges. *Microsc. Microanal.* **2014**, 20 (3), 698–705.

(24)   Walz, F. The Verwey Transition - a Topical Review. *J. Phys. Condens. Matter* **2002**, 14 (12), R285–R340.

(25) Liu, X. L.; Fan, H. M. Innovative Magnetic Nanoparticle Platform for Magnetic Resonance Imaging and Magnetic Fluid Hyperthermia Applications. *Curr. Opin. Chem. Eng.* **2014**, 4, 38–46.

(26) Almeida, T. P.; Muxworthy, A. R.; Kovács, A.; Williams, W.; Brown, P. D.; Dunin-Borkowski, R. E. Direct Visualization of the Thermomagnetic Behavior of Pseudo–single-Domain Magnetite Particles. *Sci. Adv.* **2016**, 2 (4), e1501801.

(27) Kemp, S. J.; Ferguson, R. M.; Khandhar, A. P.; Krishnan, K. M. Monodisperse Magnetite Nanoparticles with Nearly Ideal Saturation Magnetization. *RSC Adv.* **2016**, 6 (81), 77452–77464.

(28) Hyeon, T.; Su Seong Lee; Park, J.; Chung, Y.; Hyon Bin Na. Synthesis of Highly Crystalline and Monodisperse Maghemite Nanocrystallites without a Size-Selection Process. *J. Am. Chem. Soc.* **2001**, 123 (51), 12798–12801.

(29) Levy, M.; Quarta, A.; Espinosa, A.; Figuerola, A.; Wilhelm, C.; García-Hernández, M.; Genovese, A.; Falqui, A.; Alloyeau, D.; Buonsanti, R.; Cozzoli, P. D.; García, M. A.; Gazeau, F.; Pellegrino, T. Correlating Magneto-Structural Properties to Hyperthermia Performance of Highly Monodisperse Iron Oxide Nanoparticles Prepared by a Seeded-Growth Route. *Chem. Mater.* **2011**, 23 (18), 4170–4180.

(30) Guardia, P.; Riedinger, A.; Nitti, S.; Pugliese, G.; Marras, S.; Genovese, A.; Materia, M. E.; Lefevre, C.; Manna, L.; Pellegrino, T. One Pot Synthesis of Monodisperse Water Soluble Iron Oxide Nanocrystals with High Values of the Specific Absorption Rate. *J. Mater. Chem. B* **2014**, 2 (28), 4426–4434.

(31) Qiao, L.; Fu, Z.; Li, J.; Ghosen, J.; Zeng, M.; Stebbins, J.; Prasad, P. N.; Swihart, M. T. Standardizing Size- and Shape-Controlled Synthesis of Monodisperse Magnetite (Fe_3O_4) Nanocrystals by Identifying and Exploiting Effects of Organic Impurities. *ACS Nano* **2017**, 11 (6), 6370–6381.

(32) Gilbert, K. E.; Gajewski, J. J. Coal Liquefaction Model Studies: Free Radical Chain Decomposition of Diphenylpropane, Dibenzyl Ether, and Phenyl Ether via B-Scission Reactions. *J. Org. Chem.* **1982**, 47 (25), 4899–4902.

(33)   Moya, C.; Batlle, X.; Labarta, A. The Effect of Oleic Acid on the Synthesis of $Fe_{3-x}O_4$ Nanoparticles over a Wide Size Range. *Phys. Chem. Chem. Phys.* **2015**, 17 (41), 27373–27379.

(34)   Barbieri, A.; Weiss, W.; Van Hove, M. A.; Somorjai, G. A. Magnetite Fe_3O_4(111): Surface Structure by LEED Crystallography and Energetics. *Surf. Sci.* **1994**, 302 (3), 259–279.

(35)   LaMer, V. K.; Dinegar, R. H. Theory, Production and Mechanism of Formation of Monodispersed Hydrosols. *J. Am. Chem. Soc.* **1950**, 72 (11), 4847–4854.

(36)   Lee, J.; Yang, J.; Kwon, S. G.; Hyeon, T. Nonclassical Nucleation and Growth of Inorganic Nanoparticles. *Nat. Rev. Mater.* **2016**, 1 (8), 16034.

(37)   Peng, Z. A.; Peng, X. Mechanisms of the Shape Evolution of CdSe Nanocrystals. *J. Am. Chem. Soc.* **2001**, 123 (7), 1389–1395.

(38)   Wang, Y.; He, J.; Liu, C.; Chong, W. H.; Chen, H. Thermodynamics versus Kinetics in Nanosynthesis. *Angew. Chemie - Int. Ed.* **2015**, 54 (7), 2022–2051.

(39)   Cotin, G.; Kiefer, C.; Perton, F.; Ihiawakrim, D.; Blanco-Andujar, C.; Moldovan, S.; Lefevre, C.; Ersen, O.; Pichon, B.; Mertz, D.; Bégin-Colin, S. Unravelling the Thermal Decomposition Parameters for The Synthesis of Anisotropic Iron Oxide Nanoparticles. *Nanomaterials* **2018**, 8 (11), 881.

CHAPTER 4: NANORODS

1. INTRODUCTION

In the 1970-80s there was a considerable interest in iron oxide non-spherical nanoparticles (*i.e.*, nanorods) since they were the basis of some of the magnetic recording media at that time.[1] In recent years, iron oxide nanorods have gained a renewed interest due to their appealing properties for biomedical applications. For example, due to the higher surface to volume ratio, compared to spheres, nanorods have longer blood circulation times,[2] stronger retention and interaction with tumour cells and better targeting specificity.[3] Moreover, because of their high magnetic moment, magnetic nanorods can be useful to achieve a higher efficiency in magnetic separation and manipulation.[4] Nanorods are also interesting candidates for MRI since due to their shape they tend to have high r_2 relaxivity values.[5,6] Finally, they have been shown to present enhanced heating performance in magnetic hyperthermia, even when compared with other anisotropic structures such as cubes, making them a good candidate for this kind of therapy.[7] The elongated shape of this type of particles offers some very special properties: from a crystallographic point of view, due to the variation of particle shape, the atomic arrangements in each facet of the nanocrystal can be altered, resulting in new properties and different chemical reactivities.[8] Interestingly, from a structural point of view, nanorods are very singular due to the huge surface to volume ratio. For example, a sphere of Fe_3O_4 of 18 nm and a nanorod of 57x8 nm have an equivalent volume. However, these spheres have a surface area of 65.8 m^2/g, whereas the nanorods have 103.4 m^2/g, which represents a 1.6-fold increase.

Moreover, from a magnetic point of view, nanorods are also very special. For instance, due to the shape anisotropy, rod-like nanoparticles exhibit an anisotropic response to the application of a magnetic field: if the magnetic field is applied parallel to the long axis of the particle, the hysteresis loop will adopt a square-like shape, with a large H_c value and M_R approximately equal to M_s. However, if the magnetic field is applied perpendicular with respect to the long axis, the hysteresis loop will be S-shaped, usually with small coercivity and with $M_R \ll M_s$.[9]

However, despite the fore mentioned advantages, not much research has been published on the use of magnetic iron oxide nanorods. Although the synthesis of Fe_3O_4 nanorods has been pursued since the late 20th century,[10] their synthesis represents a tough challenge because the high surface energy and the cubic spinel structure of Fe_3O_4 favour the formation of more spherical-like structures.[11,12,13] After so many years of research, there is a large number of

different proposed routes for the synthesis of Fe₃O₄ nanorods. In this work, several published synthetic approaches were tested and compared to find an appropriate pathway that satisfies all the criteria we need to consider a synthesis as reliable. The following is a summary of some of the most relevant approaches that were tested.

2. SYNTHESES BASED ON LITERATURE RECIPES

2.1 Synthesis of β-FeOOH rods followed by reduction

This synthesis was originally described by Mohapatra *et al.*[6] but it was adapted and modified to the conditions of our laboratory. In this approach, the rod structures are firstly synthesized by hydrolysis of iron salts in water. These initial structures are not made of Fe_3O_4 yet, but of β-FeOOH, a more oxidized iron oxide phase. In principle, the different crystal structure (monoclinic) of this iron oxide phase should ease the formation of needle-like shaped particles. Afterwards, these particles are reduced into iron Fe_3O_4 by applying a reducing agent at high temperatures.

The chemicals, $FeCl_3 \cdot 6H_2O$ (Merck); ethanol >96% (VWR Chemicals); polyvinylpyrrolidone K30 (Fluka); and oleylamine >80% (Acros Organics) were used as supplied without further purification.

Synthesis of β-FeOOH nanorods. In a typical synthesis, $FeCl_3 \cdot 6H_2O$ (1.10 g) and polyvinylpyrrolidone (1.5 g) were dissolved in a solution of ethanol (30 mL) and mili-Q water (50 mL). The mixture was placed in a round-bottom flask connected to a Schlenk line, heated at 4 °C/min to reflux temperature (80 °C) and kept in these conditions for 18 hours while magnetically stirring. The particles were centrifuged at 4000 g for 5 min and washed with ethanol twice. This process resulted in elongated particles of 32x7 nm.

Reduction of β-FeOOH into Fe_3O_4. Approximately 200 mg of β-FeOOH nanorods were redispersed in a round bottom flask containing oleylamine (10 mL). The dispersion was degassed by applying vacuum (~10^{-2} mbar) at room temperature while stirring for 30 min. After this step, an argon atmosphere was set and the mixture was heated to 200 °C at a rate of 20 °C/min and kept in these conditions for 4 hours. After cooling down to room temperature, the particles were washed with ethanol and centrifuging twice.

The TEM images of the synthesized β-FeOOH nanorods (**Fig. 1a**) show that, indeed, the as-obtained particles are porous nanorods with a particle size distribution (**Fig. 1b**) of 32±6 nm

(PDI of 20%) in length and 7.0±1.7 nm in width. In addition, the XRD pattern suggested that the as-synthesized nanorods are mainly made of β-FeOOH (**Fig. 1c**).
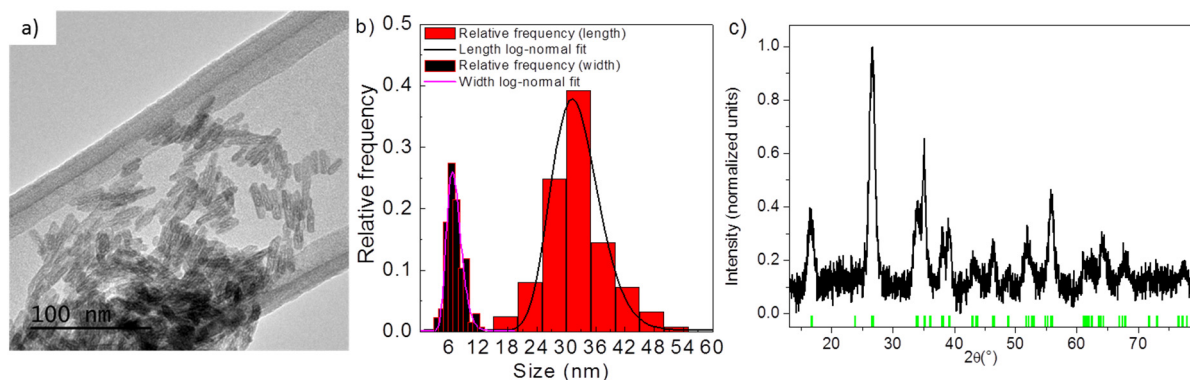

Figure 1. a) TEM image of the β-FeOOH nanorods. b) Distributions of the length (red columns) and width (black columns) of the nanorods and their respective fit to a log-normal function. c) X-ray diffraction pattern of the particles compared to a β-FeOOH reference (green lines).

After the reduction with oleylamine, the morphology of the particles was checked via TEM (**Fig. 2a**). The images showed that the overall nanorod structure was not altered by the process. However, the XRD pattern indicated that the reduction into Fe_3O_4 was not completely achieved, as most of the peaks did not match the positions of the Fe_3O_4 reference and, instead, a mixture of phases was obtained with a low crystallinity, as inferred from the rather broad the peaks (**Fig. 2b**). Moreover, many of the nanorods have a porous structure, which could negatively affect the crystallinity and thus the eventual magnetic properties.
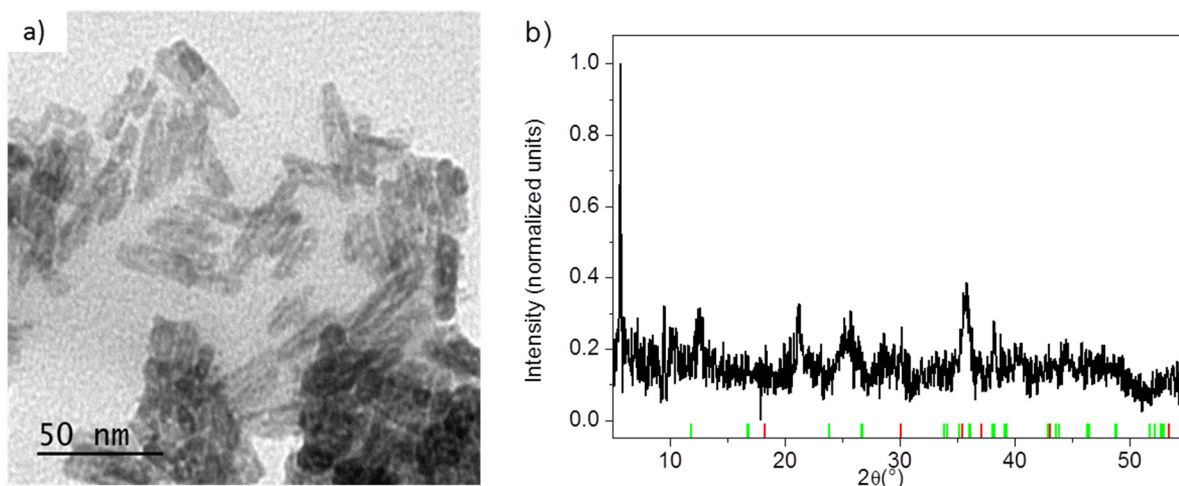
105

Figure 2. a) TEM image of the nanorods after phase reduction. b) X-ray diffraction pattern of the nanorods compared to references of β-FeOOH (green lines) and Fe_3O_4 (red lines).

In conclusion, this technique allowed the synthesis of iron oxide needle-like nanoparticles. The experimental methodology is simple and does not require a complex setup, although it is quite time-consuming, as the growth of the rods requires several hours and an extra step for the reduction into magnetite. However, due to the very low purity and the poor crystallinity of the Fe_3O_4 after reduction we decided to keep searching other synthetic alternatives.

2.2 Synthesis of nanorods using ionic liquids

This synthesis was originally described by Wang *et al.*[14] and is a thermal decomposition approach, where a zero-valent iron precursor ($Fe(CO)_5$) is decomposed in an ionic liquid (1-butyl-3-methylimidazolium bis(triflylmethyl-sulfonyl) imide, (a.k.a. [BMIM]·[Tf_2N]) in the presence of surfactants. The advantages of this approach are that it is a one-pot synthesis and that, according to the authors, the shape can be tuned to produce either nanocubes or nanorods by simply adjusting the ratio between surfactants, making it, a priori, a very versatile approach.

The chemicals, iron pentacarbonyl (VWR Chemicals); [BMIM]·[Tf_2N] (Sigma); oleic acid >90% (Sigma); 1,2-tetradecanediol >90% (Sigma); ethanol >96% (VWR Chemicals); and oleylamine >80% (Acros Organics) were used as supplied without further purification.

For the synthesis, 1,2-tetradecanediol (87 mg) was dissolved in a flask containing a solution oleic acid (40 µL) and oleylamine (43 µL) in 5 mL of [BMIM]·[Tf_2N]. The mixture was degassed applying vacuum (~10^{-2} mbar) for 10 minutes at 110 °C. After degassing, argon was pumped into the system and iron pentacarbonyl (100 µL) was injected in the mix and the

106

temperature was increased to reflux (at around 310 °C) at a rate of 1.7 °C/min. The reflux temperature was maintained for 1 hour and then the reaction was cooled down to room temperature.

The particles were washed with a mixture of oleic acid and oleylamine (40μL each) in hexane (6 mL) and centrifuged twice for 5 min at 4000 g.

The TEM images show that a rod-like structure was achieved (**Fig. 3a**). However, the amount of material is not even enough to perform a statistical analysis, it is difficult to find particles and yet, the most representative example of particles are those shown in **Fig. 3b**, which are irregular and without a clearly defined structure.
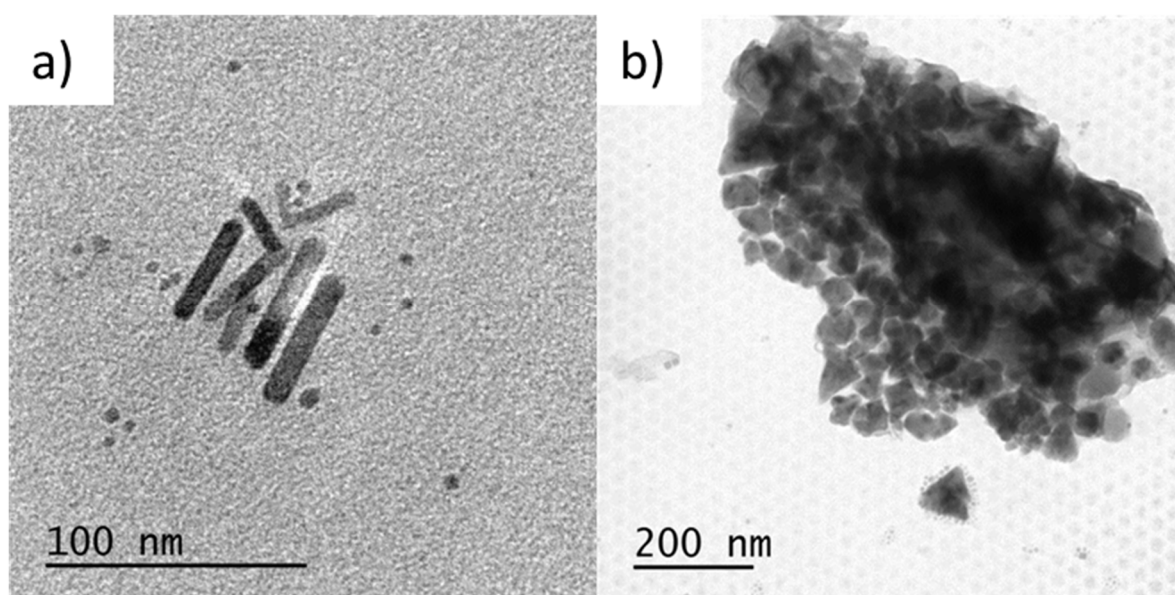

Figure 3. a) TEM image of some nanorods and b) a representative image of majority of the particles that were present in the product.

Although the resulting product was black (typical for Fe_3O_4) and it can be collected by a magnet, indicating the presence of a magnetic iron phase, due to the very low specificity (nanorods represented indeed a very minor part of the as-obtained particles) and the low yield, this synthesis was discarded.

2.3 Synthesis of nanorods based on hydrothermal coprecipitation

This synthesis was originally described by Lian *et al.*[15] but it was adapted and optimized to the conditions of our laboratory. This approach is based on the basic precipitation of different iron salts in water in hydrothermal conditions using urea as a precipitating agent precursor. The

novelty of this approach relies on the fact that, unlike other coprecipitation syntheses, the origin of the formation of Fe_3O_4 nanorods comes from the decomposition of the urea into carbon dioxide and ammonium, which takes place only at high temperatures and leads to a sudden pH increase. The uniform rise in pH prevents the occurrence of very high local supersaturation, allowing a homogeneous nucleation throughout the solution.

The chemicals, iron (III) chloride hexahydrate (Merck); iron (II) sulphate heptahydrate (Merck); and urea >99.5% (VWR Chemicals) were used as supplied without further purification.

For the synthesis, iron (III) chloride hexahydrate and (0.505 g), iron (II) sulphate heptahydrate (0.515 g) and urea (0.445 g) were added to 30 mL of water that had been degassed at room temperature previously to remove traces of oxygen. The mixture was heated at a rate of 15 °C/min up to 95°C in a closed flask with argon atmosphere and kept at this temperature for 18 hours. After cooling down to room temperature, the particles were washed with methanol and centrifuged at 4000 g for 10 minutes twice. This procedure resulted in nanorods of around 90x21 nm.

The size could be controlled by adjusting the concentration of the chemicals. For example, increasing the total concentration by a factor of four resulted in particles of 300x70 nm.

The TEM images (**Fig. 4a**) showed the presence of nanorods with an average length of 90$\pm$60 nm (PDI of 55%) and a width of 21$\pm$6 nm (**Fig. 4b**). The XRD pattern of the as-synthesized nanorods showed well-defined peaks that mainly matched the pattern of a Fe_3O_4 reference, especially that of 18° (**Fig. 4c**), despite some other peaks could not be indexed (*e.g.*, at 21 °).
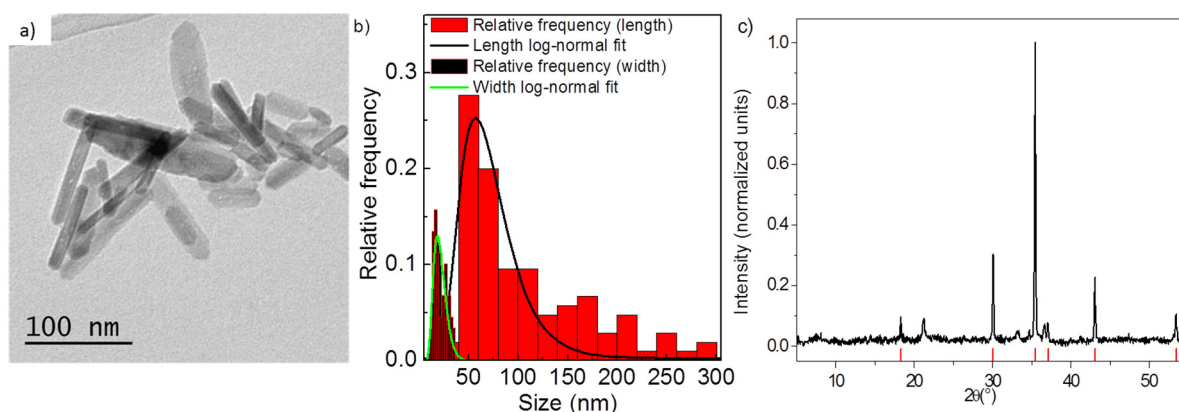
Figure 4. a) Representative TEM image of the nanorods and b) distributions of both the length (red columns) and width (black columns) of the nanorods and their fit to a log-normal function (black and green respectively). c) X-ray diffraction pattern of the particles compared to a Fe_3O_4 reference (red lines).

This synthesis allowed us to obtain particles of magnetite with a very well defined rod-like shape, which is better than the other tested synthesis approaches. However, the size dispersity is really high, with PDI values larger than 50%. Moreover, despite to some extent the size could be controlled by adjusting the total concentration of reagents, it could only be increased, as when the concentration is reduced progressively below that of the standard synthesis, no significant size reduction is observed and, eventually, the reaction simply does not take place. Moreover, due to the large size and the absence of surfactants during the synthesis, the particles were completely aggregated even after being freshly synthesized. Some attempts were carried out to include a surfactant (polyvinylpyrrolidone) during the synthesis or to coat the particles after the synthesis, but no significant improvement was obtained. Due to the poor control on size and the high state of aggregation, this synthesis was discarded for the purpose of this work.

3. SOLVOTHERMAL SYNTHESIS

The direct synthesis of Fe_3O_4 nanorods is clearly challenging and the conclusions obtained so far after many failed experiments are that: either the shape or size control is rather poor (to say the least); or the structures require further processing to become Fe_3O_4 (*i.e.*, annealing, reduction, etc.). However, in 2012, H. Sun *et al.*[13] described a different approach to synthesize Fe_3O_4 nanorods in one single step. Although this synthesis is based on a previously published synthesis to produce γ-Fe_2O_3 elongated nanoparticles,[16] the main innovation of this approach is that the reaction is carried out at high pressures and temperatures so as to allow the released gases to react with the particles during their growth and, thus, no further processing is required to obtain Fe_3O_4.

The chemicals, iron pentacarbonyl (VWR Chemicals); hexadecylamine >90% (Sigma); oleic acid >90% (Sigma); 1-octanol >90% (Sigma); and ethanol >96% (VWR Chemicals) were used as supplied without further purification.

For the standard synthesis, hexadecylamine (0.6 g) and oleic acid (1.79 g) were added to 8 mL of 1-octanol. The mixture was heated to 55 °C for 30 min while stirring so hexadecylamine is dissolved and homogeneously distributed. Afterwards, the mixture was cooled down to room temperature and iron pentacarbonyl (2 mL) was injected and blended for other 30 minutes more. Then, the resulting liquid was transferred into a 15 mL Teflon vessel and placed inside a steel autoclave. The autoclave was heated to 200 °C for 7 hours in an oven. After cooling down to room temperature, the particles were washed with ethanol and centrifuged for 10 minutes at 10600 g twice. The procedure resulted in nanorods of 35x6 nm.

As indicated by Sun et al,[13] the size could be tuned by changing the concentration of surfactants. Thus, decreasing the amount of hexadecylamine to only 0.2 g resulted in nanorods of 74x11 nm. Although the size could not be reduced in a reproducible way to obtain particles with sizes smaller than 30-35 nm, larger nanorods could be obtained by adjusting the amounts of reagents. For instance, carrying out the same proceeding but mixing 4.48 g of oleic acid, 0.367 g of hexadecylamine and 3.33 mL of iron pentacarbonyl in 13.3 mL of 1-octanol resulted in nanorods of 200x30 nm.

The TEM characterisation of the standard sample (**Fig. 5a**) indicated the presence of nanorods with a particle size of 35±7 nm (PDI 19%) in length and 5.8±1.1 nm (**Fig. 5b**). The XRD pattern shows a peak at 18 ° which is characteristic from magnetite but the overall profile is compatible with either Fe_3O_4 or γ-Fe_2O_3, so it is not possible to unequivocally distinguish both phases using only this technique (**Fig. 5c**). However, the clear presence of the Verwey transition suggested that the composition is mainly Fe_3O_4 (**Fig. 5d**).
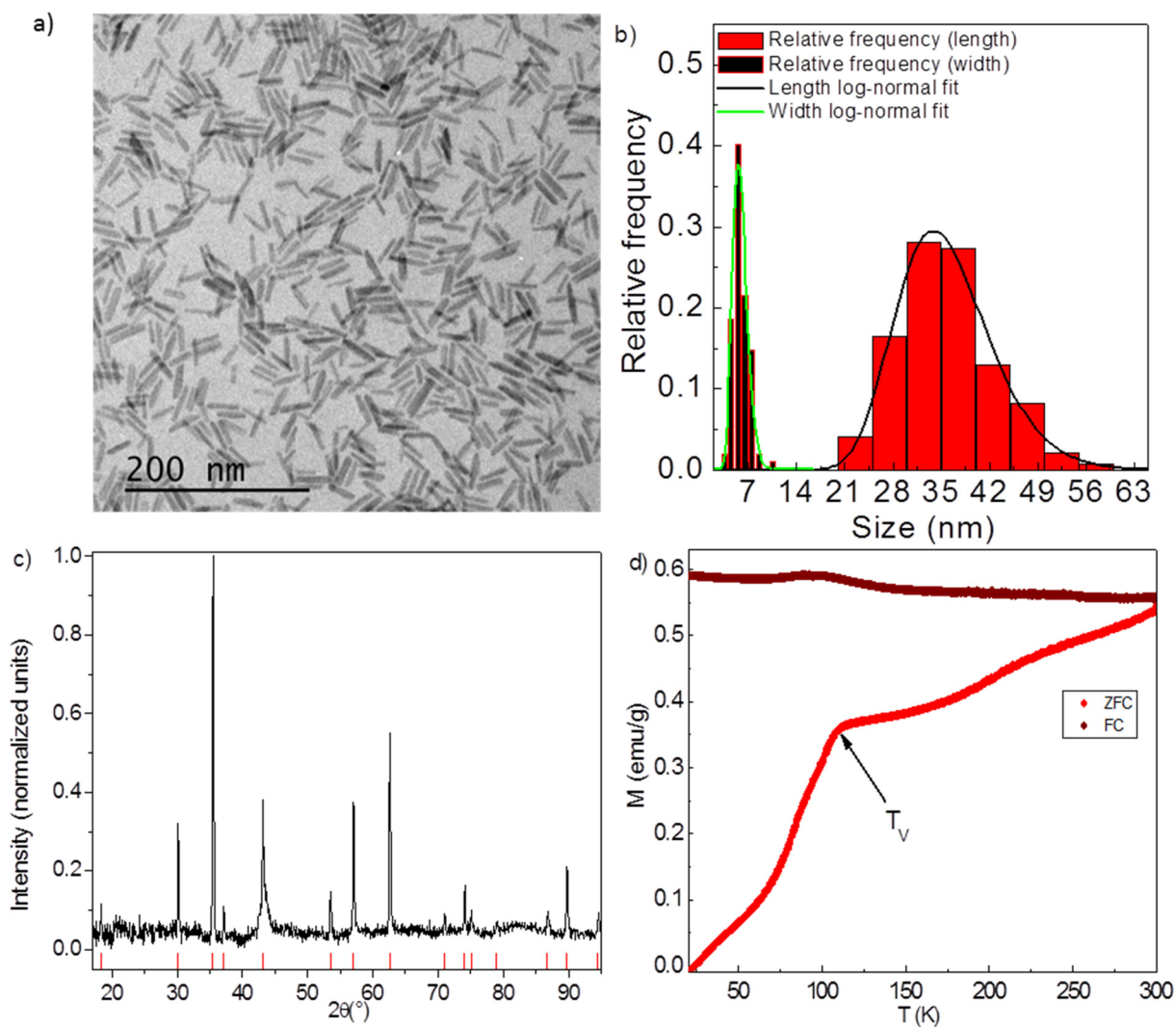
Figure 5. a) TEM image of the nanorods and b) size distribution (length in red columns; and width in black columns) and their fit to a log-normal function (black and green respectively). c) X-ray diffraction pattern of the particles compared to a Fe_3O_4 reference (red lines). Note that in this case, the x-ray diffraction measurements were carried out in the European Synchrotron Radiation Facility (Grenoble, France). d) ZFC and FC magnetization curves of the Fe_3O_4 nanorods. The Verwey transition temperature, T_V, is highlighted by an arrow.

The size could be tuned to produce particles in a very wide range of sizes (between 35 and 400 nm) while keeping the high shape definition and a moderate PDI (<20%), as can be seen in the images of **Fig. 6**.
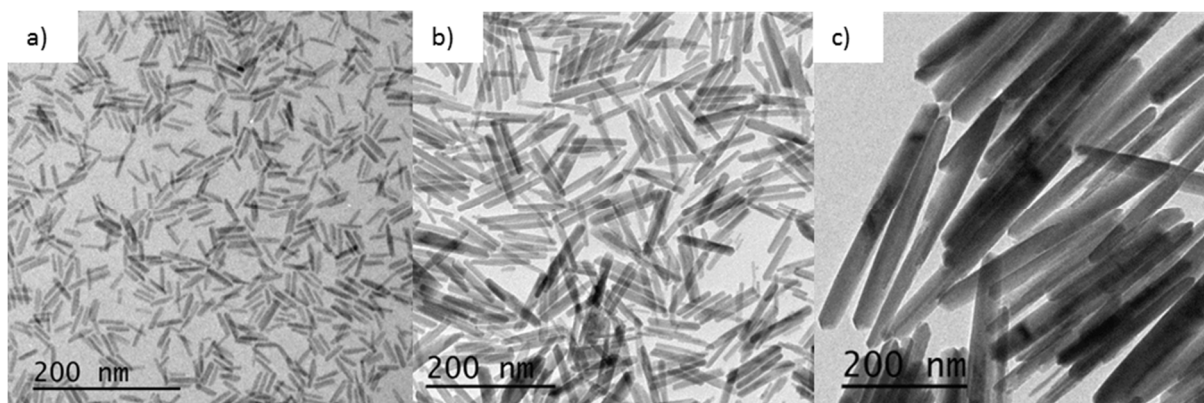
Figure 6. TEM images of nanorods of (a) 32x6, (b) 85x10; and (c) 400x40 nm.

Discussion on the chemical mechanism.

In the article of 2011 by Palchoudhury *et al*.,[16] which settled down the basis for this solvothermal synthesis, the authors claimed that carrying out the thermal decomposition of iron (III) oleate in 1-octadecene at 150-200 °C resulted in γ-Fe$_2$O$_3$ elongated particles. However, Sun *et al*. suggested that maybe the reaction mechanism involves the hydrolysis and not the thermal decomposition of iron (III) oleate because (i) the temperature at which the reaction is carried out is too low for thermal decomposition to take place, as it requires temperatures around 300 °C; (ii) during a thermal decomposition reaction, the reducing gases such as H$_2$ and CO are released would reduce Fe^{3+} into Fe^{2+} and the final product should be a more reduced iron oxide phase such as Fe$_3$O$_4$ or FeO, rather than γ-Fe$_2$O$_3$; and (iii), the authors reported that if the iron (III) oleate is thoroughly dried before the reaction, nanorods were not obtained, indicating that the impurities of iron (III) oleate (like water, which is used for washing after the synthesis of iron (III) oleate) might play a major role. Taking into account these considerations, Sun *et al*. hypothesized that if reduction takes place simultaneously during the growth of the nanostructures, Fe$_3$O$_4$ nanorods could be obtained. Consequently, they designed a synthesis that uses iron pentacarbonyl as iron source, oleic acid as surfactant and hexadecylamine to produce water for the hydrolysis and whose mechanism of reaction of reaction would be as follows:

1) In a first step, iron pentacarbonyl is oxidized by oleic acid, which acts as both oxidant and surfactant:

$$2Fe(CO)_5 + 6C_{17}H_{33}COOH \rightarrow 2Fe(C_{17}H_{33}COO)_3 + 10CO + 3H_2$$

2) In a parallel reaction, oleic acid condenses with oleylamine to produce a heavy amide as by-product and water, which will be used in the eventual hydrolysis of iron (III) oleate:

$$C_{17}H_{33}COOH + C_{16}H_{31}NH_2 \rightarrow C_{17}H_{33}CONHC_{16}H_{33} + H_2O$$
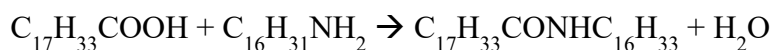
3) In the last step, the water generated during the condensation hydrolyses the iron (III) oleate while the hydrogen released in the first reaction acts as a reductor, producing magnetite:

$$3(C_{17}H_{33}COO)_3 Fe + 4H_2O + 1/2H_2 \rightarrow Fe_3O_4 + 9\ C_{17}H_{33}COOH$$
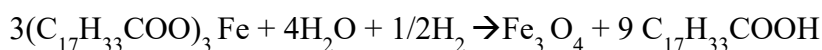
In this work, several reaction parameters (*i.e.*, solvent polarity, replacing hexadecylamine by other amines, the influence of the aliphatic chain of the surfactants, the influence of the amount of oleic acid …) were studied. However, for practical reasons, only some of the most relevant results will be described.

The role of hexadecylamine:

Sun *et al.* indicated that the dimensions of the synthesized nanorods can be tuned by simply varying the amount of hexadecylamine.[13] However, if one observes in detail the mechanism of reaction (in particular, the second step) it is easy to figure out that the role of hexadecylamine can be complex and even somehow contradictory, resulting, probably, in a non-linear response. On the one hand, one could assume that the more hexadecylamine is added, the more water will be generated and, given it is a reagent in the last step of the reaction, more Fe_3O_4 should be produced and hence a larger growth would be expected. However, on the other hand, hexadecylamine condenses with oleic acid, thus reducing its amount, which is one of the reactants of the first reaction. Therefore, fewer monomers of iron (III) oleate should be generated and consequently less growth would be expected. Indeed, whether the reduction of its availability due to the condensation with the hexadecylamine will eventually have a noticeable effect or not will depend on the ratio between both the oleic acid and the hexadecylamine. For example, if the amount of oleic acid molecules is much higher than that of hexadecylamine, the loss of oleic acid molecules can be negligible. Conversely, if the amount of both reagents is comparable, the influence can be considerable.

The truth is that the role of alkylamines in reactions involving metal carboxylates as precursors (such as metal-oleates) can be quite complex. Although the study of the ability of amines to act as surfactant has been extensively studied in literature, only a few articles have focused on the

interaction between the amines and the rest of the components in the reaction medium, such as other surfactants, and reported the formation of stable acid-base complexes in solution.[17] In a recent study, Sharifi *et al*. showed that the formation of this complexes can modulate the affinity of oleic acid to metal cations.[18] For example, they observed that in thermal decomposition reactions carried out in aprotic solvents, if too little amine is added, oleic acid remains mainly protonated, which harnesses its ability to coordinate with the metals. However, if the amount of amine in the reaction is too large, oleic acid remains mainly complexed and consequently it is not available to coordinate with metals. Therefore, the authors suggested the existence of an optimal ratio between both amine and carboxylic acid and that either for higher or lower ratios than the optimal, the influence will be similar, as in both scenarios the availability of oleate anions is reduced, thus decreasing its coordinating capacity. Conversely, a strong coordination to the surface of the growing particles should result in an inhibition of the growth and thus, the particle size becomes smaller. From our experience, the described trend can explain some of our experimental results.

For example, we conducted a study varying the amount of hexadecylamine while keeping the rest of the parameters the same and analysed the dimensions of the resulting nanorods. The results also displayed a "v-shaped" plot, with a size minimum for a ratio of oleic acid to hexadecylamine molecules of 10:1(**Fig. 7**). It is also interesting to confirm the existence of an optimal ratio between the amine and the carboxylate as it was predicted. In our case, the PDI ranged from 16% for the smallest particles, to 20% for the largest, suggesting that the polydispersity increase could be related to a decreased availability of oleate anions to regulate the particle growth. Remarkably, the aspect ratio varied in parallel with the length of the nanorods, ranging from 9.8 for the longest rods to 5.7 for the shortest ones. Therefore, these two parameters cannot be controlled independently by varying only the amount of hexadecylamine.
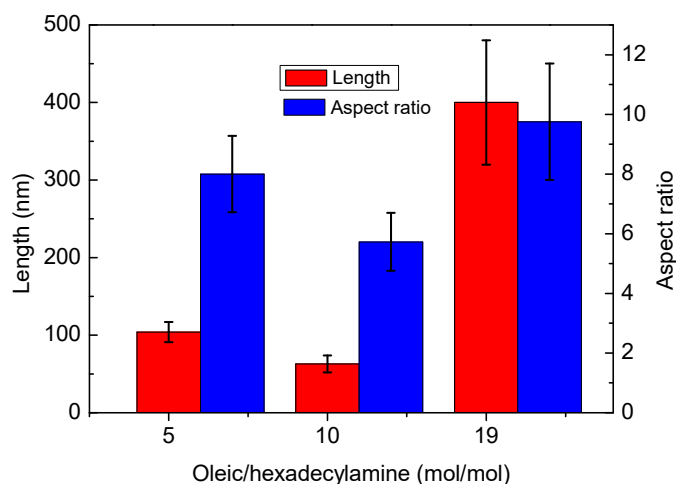
Figure 7. Length and aspect ratio (red and blue columns, respectively) as a function of the oleic acid to hexadecylamine ratio.

However, note that in our study, the trend is somehow different. In particular, Sharifi[18] reports that the ratio of oleic to hexadecylamine at which the minimum size is achieved is 3:1. However, in our work, the minimum size appears at a ratio of 10:1. Several factors can be taken into account to find a possible explanation to the origin of these differences. For example, although the size vs oleic to hexadecylamine ratio does exhibit a minimum for a given ratio, in our case the size becomes much larger for lower ratios (large amounts of hexadecylamine) than for higher ratios. This difference can be explained if one considers that, while in the study of Sharifi the sum of both oleic and oleylamine mol was kept constant, in this work, the hexadecylamine amount was varied while keeping constant the amount of oleic acid. Therefore, a low ratio of oleic to hexadecylamine involved a higher total amount of surfactants and, consequently, it is expected that the growth is smaller than for higher ratios.

Another factor that should be considered is that in the article by Sharifi *et al*., [18] the study is performed using a thermal decomposition synthesis. However, the one we performed is based on hydrolysis, where the reaction is carried out at much lower temperatures and consequently the affinity constant of the acid-base complex can be different, shifting the ratio at which the minimum appears. Finally, in the article by Sharifi,[18] the study is performed using oleic acid and oleylamine. Both of them are more similar molecules whose structure differs only in the functional group whereas, in our study, there are important differences in the aliphatic chain as well. For instance, hexadecylamine has a shorter and completely saturated carbon chain, while that of oleic acid is longer and with an unsaturation in the C9 position. This can result in a

115

much different solubility in the reaction mixture. For these reasons, it seems reasonable that the minimum size is achieved at a different carboxylic to amine ratio than that described in the literature.

Although varying the amount of hexadecylamine to tune the size of the nanorods might seem an appealing choice due to the simplicity of the approach, it has to be taken into account that some parallel and undesired consequences can arise. For example, despite the reaction is carried out some degrees above the boiling point of the solvent, the heavy amide that is produced has a much higher boiling point and, therefore, as the reaction advances, the overall boiling point of the mixture can be shifted towards higher temperatures. If the amount of the generated amide is high enough, the boiling point of the mixture can be displaced beyond the temperature of the reaction and thus a sudden decrease in the pressure inside the autoclave can take place. The pressure decay could lead to a much lower retention of gases like H_2 in the solution, which are reactants for the last stage of the reactions sequence. If this would happen, the particles that are formed or that keep growing before and after the increase of the boiling point beyond the temperature of reaction would grow in very different conditions, leading to an increased size and shape polydispersity. In addition, because the amide is a much less polar molecule than any of the pristine molecules present in the medium, the stability of the monomers in solution (and thus their activity coefficient which, as explained in the former chapter, is crucial to determine the final structure) can be severely modified as the reaction advances due to changes in the overall polarity. The viscosity properties of the medium can also change and consequently the rate at which monomers diffuse during the growth stage can also be altered, affecting the growth rate of the particles or, in any case, varying the properties of the environment during the reaction. This effect can become key at high concentrations of hexadecylamine and especially important if one considers that the solubility of the amide in the octanol is rather limited and it is not difficult to reach saturation and thus make it precipitate inside the reaction, increasing the heterogeneity of the medium. Indeed, this by-product appears often as a solid after the reaction, leading to the clustering some of the particles.

From an experimental point of view, confirming all of these hypotheses is a challenge, especially considering that the reaction is carried out inside an autoclave at high pressure and temperature and therefore it is not possible to place sensors to monitor the reaction or to acquire aliquots in real time to perform the pertinent analyses. Elucidating the exact influence of hexadecylamine in the reaction would require an exhaustive analysis that is beyond the scope

of this thesis. In any case, it seems obvious that other alternatives to control the size should be found so as to avoid undesired side-effects.

The influence of the pressure

Given the large number of gas molecules that are involved in the reaction mechanism (*i.e.*, water, hydrogen, carbon monoxide, etc.), it is expected that changes in the pressure should affect the reaction. Therefore, we performed a study to determine its influence by simply varying the autoclave filling level (namely, by scaling up the total amount of reactants and solvents). This represents a dual way to increase the pressure as, on the one hand, due to the larger amount of reactants that are placed inside the reactor, a higher number of gas molecules are released and, on the other hand, the fuller the reactor is, less space will remain for the generated gases to expand and thus, their retention in solution is increased. The enhanced retention of water and H_2 within the mixture is expected to result in a larger particle size, as both of them are reactants for the eventual formation of Fe_3O_4. The results confirmed this hypothesis. Namely, the size increased for higher pressures and the length could be tuned from 27 to 66 nm, while keeping the aspect ratio constant at around 6 (**Fig. 8**).
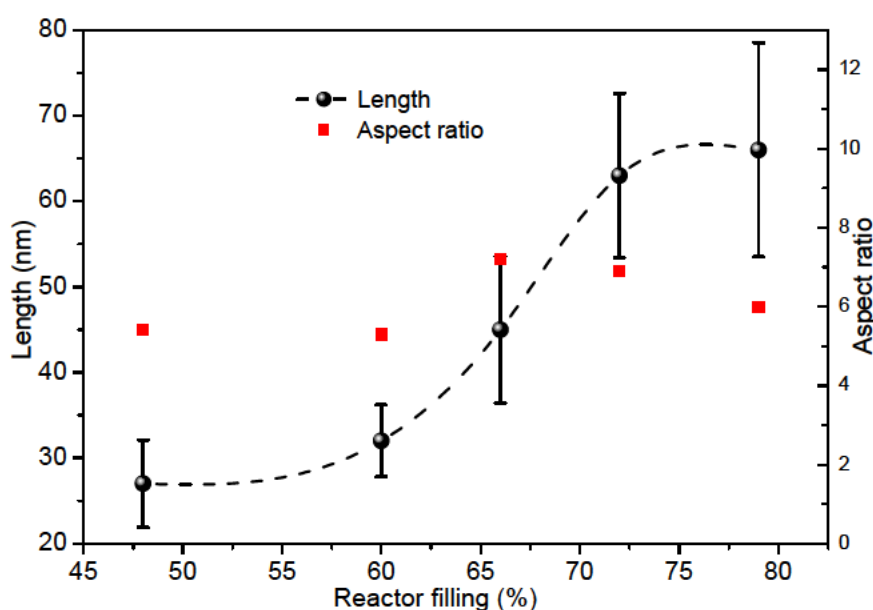

Figure 8. Length (black circles) and aspect ratio (red squares) of the nanorods as a function of the filling level of the reactor. The filling percentage was estimated by adding the volume of the solvent and the oleic acid and dividing it by the capacity of the reactor.

Although the range within the dependence is linear might seem somehow limited, it is interesting as this range of sizes can be convenient for many applications where colloidal

stability is required, as larger particles will probably aggregate due to dipolar inter-particle interactions and the lack of stirring during the synthesis. Because the reaction must be carried out inside a tightly sealed reactor, it is experimentally not feasible to have a control on the pressure inside the chamber. It could happen, for example, that at high pressures, the reactor cannot contain all of the released gases and some leaks appear; or it could also happen that the solvent is already saturated of gases. Conversely, if the filling level is too low, the gases can escape to the headroom before reacting and thus only the molecules that are consumed immediately after their generation will react. These effects could be potential explanations to the loss of linearity for too high or too low filling percentages. Nevertheless, controlling the pressure has proven to be an interesting and simple alternative to control the particle size without changing any of the other chemical parameters.

Controlling the aspect ratio.

Despite the size could be controlled to some extent, the aspect ratio, which one of the most important structural properties of nanorods showed no clear dependence on any of the tested parameters. For example, in the case of the study of the influence of the hexadecylamine amount, the aspect ratio oscillated between 5.4 and 7.2 in an apparently random fashion. However, tuning the aspect ratio can be very interesting because it can dramatically affect the magnetic properties. For example, tuning the aspect ratio can be an interesting way to increase the shape anisotropy by tuning the demagnetizing field. However, if the aspect ratio is larger than 10, the shape anisotropy is approximately the same as a nanowire with an infinite aspect ratio.[19] Moreover, exceedingly long wires can become colloidally unstable due to the increased magnetic moment and the concomitant stronger dipolar interactions. Thus, adjusting the aspect ratio to a value of 10 could be a way to optimize the shape anisotropy without compromising the particle stability. From a biomedical point of view, this can be very interesting as a higher demagnetizing factor would imply a higher relaxivity in MRI, although for biomedical applications, a high colloidal stability is required. Therefore, a tight control on aspect ratio is needed to optimize the properties.

Some articles reported a set of different experimental conditions to empirically adjust the aspect ratio, although it always involved the simultaneous change of the length and the width and not the change of length while keeping the width contant.[7] Furthermore, from these studies no clear trend can be inferred to correlate the change in the chemical conditions and the final influence

on the aspect ratio. To the best of our knowledge, no research paper has ever reported a way to finely control the aspect ratio of iron oxide nanorods as a totally independent parameter.

Because tuning the size by varying the amount of surfactants can have unexpected consequences, it is appealing to find an alternative to tune the aspect ratio in a simple and straightforward way. Taking into account the results observed during the development of the synthesis of nanocubes, we hypothesized that a partial substitution of oleic acid by its sodium salt (sodium oleate) can help to tune the morphology of the particles for the same reasons than in the case of cubes: both oleate species have different solubility in the medium, different ability to release the counter-ion and thus different reaction kinetics, etc. In this particular case, the hygroscopic behaviour of sodium ions becomes especially relevant, as they can trap the water molecules formed in the condensation of oleic acid and hexadecylamine and thus slow down its release and subsequent reaction with iron (III) oleate, leading to a decreased chemical potential of water. The convergence of these effects could promote a differential facet growth. Therefore, we proceeded to make different syntheses by varying only the fraction of oleic acid molecules that were replaced by sodium oleate.

The synthesis was carried out by mixing hexadecylamine (0.83 g; 3.44 mmol), iron pentacarbonyl (2.75 mL; 19.0 mmol) and oleic acid (2.46 g; 8.71 mmol) in 11 mL of octanol. The mixing procedure, temperatures and reaction times were the same as described above. However, the number of oleic acid molecules was progressive replaced by sodium oleate (*i.e.*, 10% substitution = 7.84 mmol of oleic acid plus 0.87 mmol of sodium oleate, etc.).The TEM images showed clearly that the width could actually be kept constant at around 6 nm while increasing the length (and thus the aspect ratio) with increasing proportions of sodium oleate (**Fig. 9,** upper row). The response was linear in a range of up to 15% of sodium oleate, which allowed tuning the aspect ratio in a wide range, from 3.7 to 17.1 (**Fig. 9,** lower panel). The loss of linearity for high percentages of sodium oleate percentages might be related to its limited solubility in such a non-polar medium.
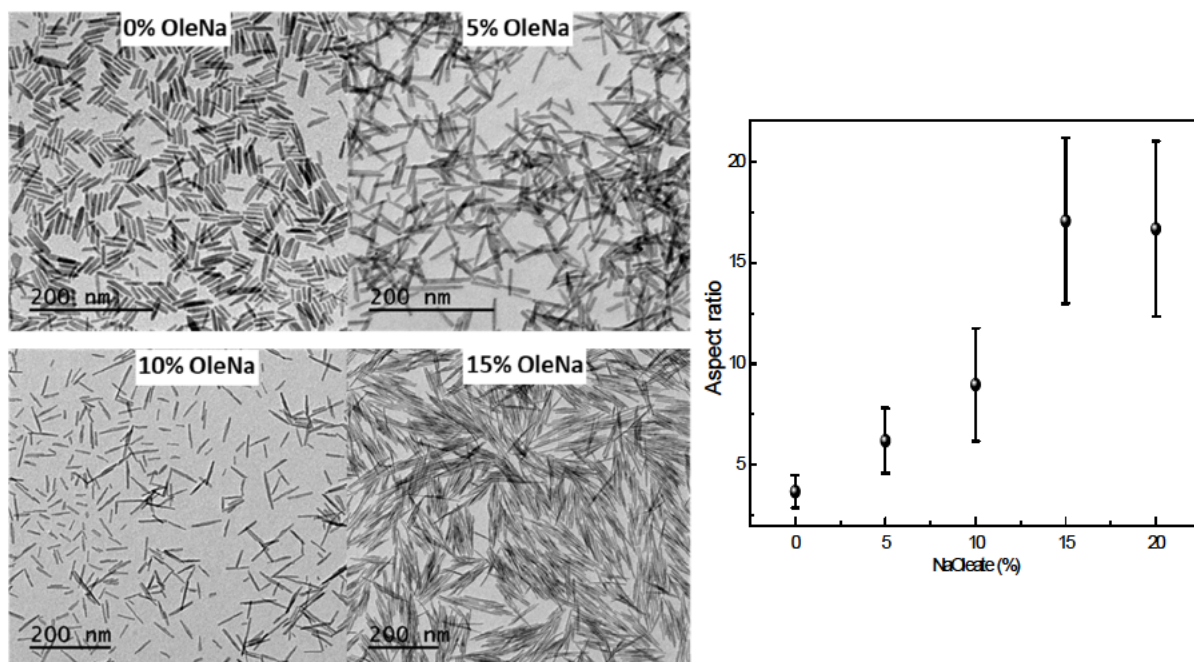
Figure 9. Left panels: TEM images of the nanorods. The insets indicate the percentage of oleic acid moles that have been replaced by sodium oleate. All scale bars correspond to 100 nm. Right panel: aspect ratio of the nanorods as a function of the sodium oleate substitution.

It is remarkable that, despite the deep structural changes, the composition was preserved even for the highest sodium oleate percentages, as could be inferred from the XRD patterns, where all display the same lattice parameter (**Fig. 10**).
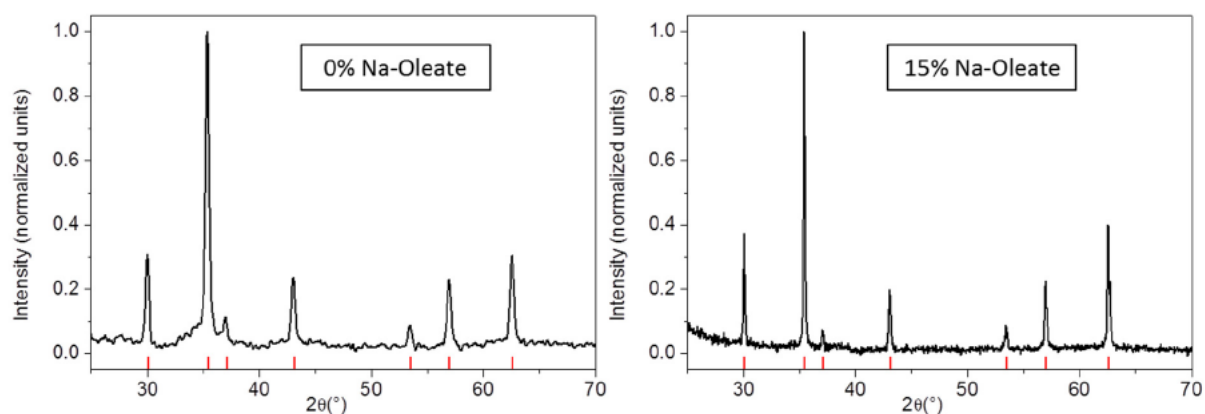

Figure 10. XRD patterns of the nanorods synthesized without sodium oleate (left) and replacing a 15% of the oleic moles by sodium oleate.

4. CONCLUSIONS

The synthesis of magnetite nanorods is rather complex. In this work, different approaches have been explored with different degrees of success. Among all of the different approaches that have been tried, the solvothermal synthesis is the only one that produces (i) monodisperse nanorods, (ii) low degree of aggregation, (iii) good crystallinity and (iv) a pure Fe_3O_4 phase. Thus, this approach satisfies all the criteria of a high-quality synthesis. In addition, the size range that can be achieved using this methodology is convenient for different applications. Although some ways to control the size was reported previously in the literature, in this work other alternatives for controlling the structural properties have been found, such as using the pressure to tune the size. Another novelty of this work is that it has been found a new way to finely tune the aspect ratio within a wide range using a simple approach. These novel approaches can improve the optimization of the properties of the Fe_3O_4 nanorods for diverse applications

5. REFERENCES

(1)   Sharrock, M. P.; Bodnar, R. E. Magnetic Materials for Recording: An Overview with Special Emphasis on Particles. *J. Appl. Phys.* **1985**, 57 (8), 3919–3924.

(2)   Geng, Y.; Dalhaimer, P.; Cai, S.; Tsai, R.; Tewari, M.; Minko, T.; Discher, D. E. Shape Effects of Filaments versus Spherical Particles in Flow and Drug Delivery. *Nat. Nanotechnol.* **2007**, 2 (4), 249–255.

(3)   Xia, Y.; Yang, P.; Sun, Y.; Wu, Y.; Mayers, B.; Gates, B.; Yin, Y.; Kim, F.; Yan, H. One-Dimensional Nanostructures: Synthesis, Characterization, and Applications. *Adv. Mater.* **2003**, 15 (5), 353–389.

(4)   Son, S. J.; Reichel, J.; He, B.; Schuchman, M.; Lee, S. B. Magnetic Nanotubes for Magnetic-Field-Assisted Bioseparation, Biointeraction, and Drug Delivery. *J. Am. Chem. Soc.* **2005**, 127 (20), 7316–7317.

(5)   Nikitin, A. A.; Khramtsov, M. A.; Savchenko, A. G.; Abakumov, M. A.; Mazhuga, A. G. Anisotropic Iron-Oxide Nanoparticles for Diagnostic MRI: Synthesis and Contrast Properties. *Pharm. Chem. J.* **2018**, 52 (3), 231–235.

(6)   Mohapatra, J.; Mitra, A.; Tyagi, H.; Bahadur, D.; Aslam, M. Iron Oxide Nanorods as High-Performance Magnetic Resonance Imaging Contrast Agents. *Nanoscale* **2015**, 7 (20), 9174–9184.

(7)   Das, R.; Alonso, J.; Nemati Porshokouh, Z.; Kalappattil, V.; Torres, D.; Phan, M.-H.; Garaio, E.; García, J. Á.; Sanchez Llamazares, J. L.; Srikanth, H. Tunable High Aspect Ratio Iron Oxide Nanorods for Enhanced Hyperthermia. *J. Phys. Chem. C* **2016**, 120 (18), 10086–10093.

(8)   Orza, A.; Wu, H.; Xu, Y.; Lu, Q.; Mao, H. One-Step Facile Synthesis of Highly Magnetic and Surface Functionalized Iron Oxide Nanorods for Biomarker-Targeted Applications. *ACS Appl. Mater. Interfaces* **2017**, 9 (24), 20719–20727.

(9)   Pecko, D.; Arshad, M. S.; Sturm, S.; Kobe, S.; Rozman, K. Z. Magnetization-Switching Study of fcc Fe–Pd Nanowire and Nanowire Arrays Studied by In-Field Magnetic Force Microscopy. *IEEE Trans. Magn.* **2015**, 51 (10), 1–4.

(10)   Min Chen; Bo Tang; Nikles, D. E. Preparation of Iron Nanoparticles by Reduction of Acicular β-FeOOH Particles. *IEEE Trans. Magn.* **1998**, 34 (4), 1141–1143.

(11)   Milosevic, I.; Jouni, H.; David, C.; Warmont, F.; Bonnin, D.; Motte, L. Facile Microwave Process in Water for the Fabrication of Magnetic Nanorods. *J. Phys. Chem. C* **2011**, 115 (39), 18999–19004.

(12)   Venkateswarlu, S.; Kumar, B. N.; Prathima, B.; SubbaRao, Y.; Jyothi, N. V. V. A Novel Green Synthesis of Fe_3O_4 Magnetic Nanorods Using Punica Granatum Rind Extract and Its Application for Removal of Pb(II) from Aqueous Environment. *Arab. J. Chem.* **2019**, 12 (4), 588–596.

(13)   Sun, H.; Chen, B.; Jiao, X.; Jiang, Z.; Qin, Z.; Chen, D. Solvothermal Synthesis of Tunable Electroactive Magnetite Nanorods by Controlling the Side Reaction. *J. Phys. Chem. C* **2012**, 116 (9), 5476–5481.

(14)   Wang, Y.; Yang, H. Synthesis of Iron Oxide Nanorods and Nanocubes in an Imidazolium Ionic Liquid. *Chem. Eng. J.* **2009**, 147 (1), 71–78.

(15) Lian, S.; Wang, E.; Kang, Z.; Bai, Y.; Gao, L.; Jiang, M.; Hu, C.; Xu, L. Synthesis of Magnetite Nanorods and Porous Hematite Nanorods. *Solid State Commun.* **2004**, 129 (8), 485–490.

(16) Palchoudhury, S.; An, W.; Xu, Y.; Qin, Y.; Zhang, Z.; Chopra, N.; Holler, R. A.; Turner, C. H.; Bao, Y. Synthesis and Growth Mechanism of Iron Oxide Nanowhiskers. *Nano Lett.* **2011**, 11 (3), 1141–1146.

(17) Klokkenburg, M.; Hilhorst, J.; Erné, B. H. Surface Analysis of Magnetite Nanoparticles in Cyclohexane Solutions of Oleic Acid and Oleylamine. *Vib. Spectrosc.* **2007**, 43 (1), 243–248.

(18) Sharifi Dehsari, H.; Harris, R. A.; Ribeiro, A. H.; Tremel, W.; Asadi, K. Optimizing the Binding Energy of the Surfactant to Iron Oxide Yields Truly Monodisperse Nanoparticles. *Langmuir* **2018**, 34 (22), 6582–6590.

(19) Lisjak, D.; Mertelj, A. Anisotropic Magnetic Nanoparticles: A Review of Their Properties, Syntheses and Potential Applications. *Prog. Mater. Sci.* **2018**, 95, 286–328.

CHAPTER 5: PHASE TRANSFER

1. INTRODUCTION

For biomedical applications it is required that the particles are dispersible in aqueous environments such as blood, culture media, etc. In fact, not only dispersibility is required, but also colloidal stability over time, as aggregates larger than 200 nm could result in thrombosis within the capillary of the circulatory system.[1]

However, most of the synthesis pathways that lead to controlled sizes and shapes are based on organic synthesis. In particular, all of the synthesis routes that have been described in this thesis yield oleate coated nanoparticles which make them stable in organic media. Therefore, it is necessary to carry out a phase transfer process to make particles undergo from hydrophobic to hydrophilic.

Certainly, the phase transfer process can be almost as important as the synthesis itself, as it can alter dramatically the final properties of the particles. For example, it has been reported that the coating can influence noticeably some magnetic properties such as magnetic moment, surface anisotropy, susceptibility and coercivity.[2] Considering that for biomedical applications, particles with a high magnetic saturation but yet well dispersed are often required, these effects must be taken into account to carefully select the coating. In biomedical applications such as magnetic hyperthermia, some studies have shown how different coatings can lead to different aggregation states, resulting in very different performances, even for the same core.[3] Despite some researches have pointed that in some cases, the reversible and controlled self-assembling of particles (*e.g.*, nanocubes forming chains) can improve the efficiency in magnetic hyperthermia,[4] in general the heating efficiency decays for increasingly aggregated particles as a consequence of the strong magnetic interactions, hence it is preferable to avoid aggregation. A similar behaviour is observed in MRI, where it is desirable to have non-aggregated particles so as to maximize the particle surface that is exposed and thus the diffusion of the water molecules onto it.[5] In the particular case of MRI, it is also important to take into account the thickness of the coating, as some studies have pointed out that an exceedingly thick coatings can decrease the relaxivity values due to the shielding of the magnetic core.[6] Finally, it is worth to mention that the coating controls the biodistribution and clearance within the organism. For example, it has been shown that intravenously injected iron oxide nanoparticles can accumulate preferentially in different organs (such as liver or spleen) and be eliminated at different rates

depending solely on the nature of the coating.[7] In fact, some coatings allow the attachment of molecules such as antibodies for targeting specific cells, increasing the accumulation in specific areas and consequently the efficacy of the treatment and on the same time, reducing their accumulation in non-desired regions, which can help to reduce the side effects.[8]

There is an extensive amount of literature describing methodologies for phase transferring and stabilisation of inorganic particles in aqueous media using different approaches: ligand exchange to replace the original surfactant,[9–12] coating the particles with polymers,[13–15] chemical modification of the original surfactant[16] and silica coating[17] to name a few. Some of these methodologies have become very popular for different reasons. For instance, due to the experimental simplicity of the approach, ligand exchanging with tetramethylammonium hydroxide (TMAOH) has been frequently used in the literature.[11] In this process, TMAOH, a positively charged quaternary amine, replaces the oleate coating and interacts electrostatically with the hydroxyl groups on the surface of the metallic nanoparticles (**Fig. 1**). The positive charges attract hydroxide anions present in the water, thus generating a highly negatively charged layer (<-40 mV) around the particle. Other approaches involve a more complex methodology but yield excellent results. For example, coating the particles with polyethylene glycol (PEG) provides a very good stability due to the presence of highly hydrophilic ether bonds all along the polymer chains.[18] In addition, there is a vast variety of PEG derivatives commercially available (*i.e.*, conjugated with amines, aldehydes, epoxides, heterocycles, *etc.*), which makes PEG coating a very versatile approach.
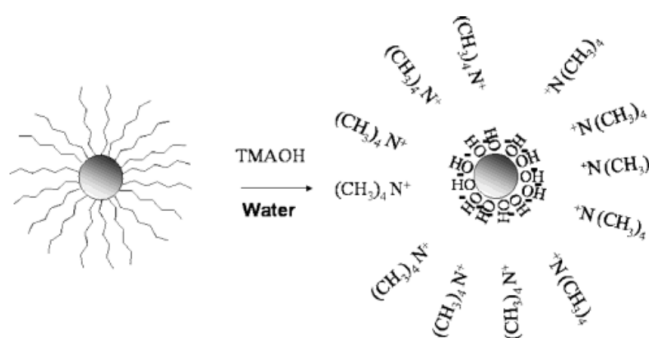

Figure 1. Scheme showing the process of ligand exchanging with TMAOH. The original oleic acid coating (left) is displaced with TMAOH cations (right).[11]

In general, the main function of the coating is to overcome the Van der Waals attractive forces and, in the particular case of magnetic nanoparticles, the magnetic dipolar forces, that would cause the aggregation of the particles. Consequently, some criteria should be established to carefully select the most convenient phase transfer process for the final applications. For

example, it is mandatory that the coating process does not alter the morphology of the particles. In addition, ideally the coated particles should have a small hydrodynamic diameter, which should be kept over the time. Therefore, non-reversible (or barely reversible) transferring processes would be preferred, so as the coating is as stable as possible. This condition discards, for example, TMAOH, as it is based on weak electrostatic interactions and consequently, can be desorbed in saline media, such as buffers or biological fluids.[19]

If possible, the coating should provide also functionalisable groups to allow the grafting with biomolecules that can, for example, target selectively malignant cells. Despite in the literature there is a vast variety of methodologies that allow the attachment of biomolecules such as antibodies or other proteins by exploiting reversible or weak interactions between the particles and the molecules (such as ionic adsorption), presumably processes involving the creation of a covalent bond (such as an amide or disulphide bonds between the particles and the proteins) are more convenient, since they are non-reversible processes.[20] In any case, it would also be convenient that these functional groups were electrically charged to provide electrostatic repulsion. Indeed, it is generally considered that particles with Z-potential values larger than $\pm$ 30 mV are stable due to the large electrostatic inter-particle repulsion.[21] Considering that plasma proteins have a low isoelectric point (such as serum albumin, whose isoelectric point is around 5) and thus are negatively charged at physiological pH values, the ionisable group of the coating should also be negatively charged to avoid the aggregation with the plasma proteins. Consequently, we considered that ideally the coating should have carboxylic groups to i) confer negative charge to avoid aggregation between particles and/or plasma proteins; and ii) allow the functionalisation of targeting molecules through the creation of amide bonds. This restricts considerably the number of choices. For example, despite there are some commercially available carboxylic PEG derivatives, to the best of our knowledge there is no straightforward methodology that ensures that the carboxyl groups are available for the further functionalisation and usually multiple chemical modifications and several days of work are required.[14] Moreover, the use of PEG derivatives might involve other problems, like the high price of carboxyl PEG derivatives or that it has been reported that the long chains of this type of polymers might harness the performance of the particles as contrast agent.[6,22]

Summarizing, the ideal methodology should: i) not alter the morphology or the chemical composition of the particle so as to preserve its properties; ii) yield small hydrodynamic diameters; iii) involve barely reversible processes to ensure long-term stability; and iv) the

coating should have carboxylic groups on its structure that remain available for grafting and that provide a highly negative charge (Z-potential <-30 mV).

2. TESTED CONVENTIONAL METHODOLOGIES

Due to the difficulty of stabilizing hydrophobic magnetic nanoparticles in water, many different approaches were tested, such as coating with polyvinylpyrrolidone, silica, ligand exchange with citrate and caffeic acid or using phosphonate derivatives to replace the original coating, etc. However, for practical reasons, only those that led to the most relevant results will be described in some detail.

2.1 Oxidative cleavage of oleic acid

In this strategy, originally described by Lee *et al.*, [16] the unsaturation present in the oleic acid is exploited to make particles hydrophilic. In their methodology, ozone is used to oxidize the double bond of oleic acid and break the molecule, introducing a carboxyl terminus or an aldehyde (**Fig. 2**). Both of these groups are hydrophilic and exposed to the solvent, thus resulting in hydrophilic nanoparticles.
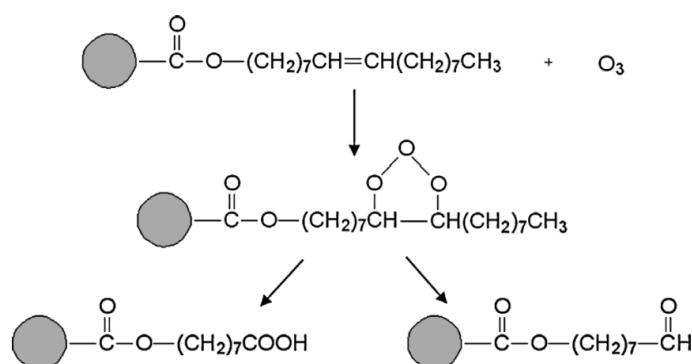

Figure 2. Scheme showing the reaction mechanism of the ozonolysis of oleic acid on the surface of a particle. Adapted from Lee *et al.*[16]

The ozonolysis can be a moderately aggressive treatment and the authors noticed that the colour of the iron oxide particles changed from black to dark brown, which may be an indication of the oxidation of Fe_3O_4 into $\gamma\text{-}Fe_2O_3$. For this reason, the protocol described by Si *et al.*, was used instead of the original approach.[23] In this methodology, the oxidation of the oleic acid is carried out by using a solution containing a mild oxidizing agent, instead of using ozone gas to minimize the transformation to maghemite.

Briefly, a dispersion containing approximately 50 mg of iron oxide nanoparticles (cubes of 17.0±1.9 nm) in 5 mL toluene was added into a 20 mL mixture of ethyl acetate (10 mL) and acetonitrile (10 mL). Then, an aqueous solution of sodium periodate (400 mg in 15 mL) was added with vigorous stirring at room temperature for 2 hours. Afterwards, the stirring was stopped and the mixture was separated into two phases. The black aqueous phase (now containing the particles) was collected, washed with ethanol and centrifuged for 10 minutes at 4000 g twice. Finally, the particles were redispersed in water and stored.

The TEM images revealed that the morphology was mainly preserved and no significant differences could be appreciated after the transferring process (**Fig. 3**). In addition, the intense black colour was kept after the transference, suggesting that the oxidizing agent was mild enough so as not to oxidize the particles.
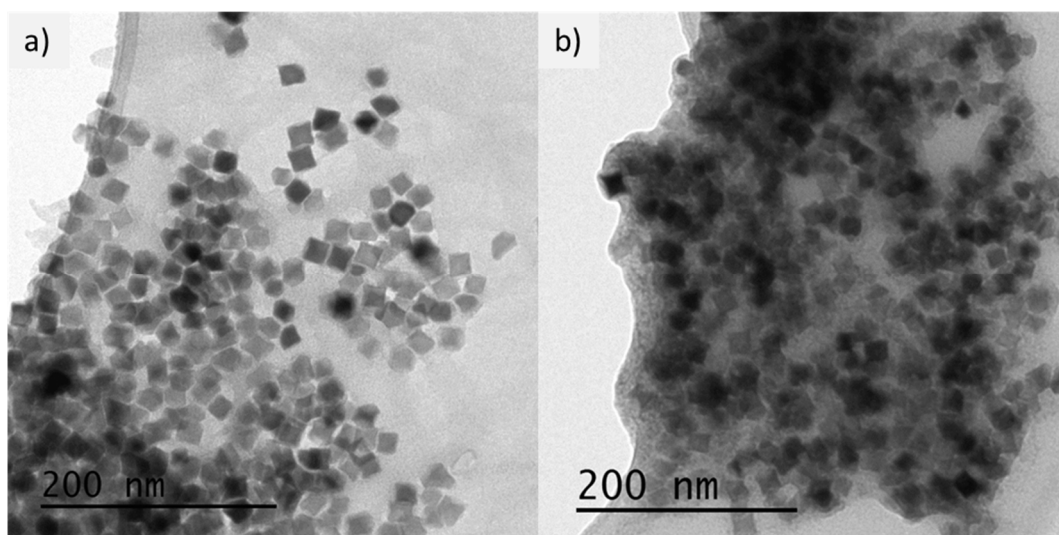

Figure 3. TEM image of a) the as-synthesized nanocubes and b) the same cubes after being transferred by oxidative cleavage.

The Z-potential measurements indicated a moderate negative charge, of -25 mV. The negative value of the Z-potential indicates the presence of negatively charged molecules on the surface, which presumably are due to carboxyls. However, the hydrodynamic diameter measurements revealed a large aggregate size (>150 nm). Considering that the longest dimension of the particles (the diagonal) is around 25 nm, it can be deduced that the particles are considerably aggregated. In fact, the particles remained only dispersed for a short period of time (a few hours) and then precipitated unless they were vigorous stirred. A possible explanation for the origin of this effect could be that the coexistence of both aldehyde and carboxyl groups on the surface of the particles could be insufficient to keep the particles stable. The moderate Z-

potential suggests that it would be required that the whole surface is entirely covered by carboxyl groups to maintain the stability. Another possible explanation to the moderate Z-potential could be that, as the oxidation is carried out with sodium periodate, some sodium ions could be electrostatically adsorbed on the surface, partially neutralising the charge. Therefore, this approach was not suitable for our purposes.

2.2 Ligand exchange with 2,3-dimercaptosuccinic acid (DMSA)

The use of DMSA as a chelating agent to stabilize iron oxide nanoparticles was proposed in 1997 by Fauconnier et al.[9] DMSA can coordinate in different ways to the iron oxide surfaces. For example, in some situations both of the carboxyl groups can be involved in the coordination to the surface of the particle, whereas in some other cases, one of them remains aiming to the exterior (**Fig. 4**). This situation is especially useful as the free carboxyl can provide negative charge to the particles and can be used for the attachment of biomolecules.[24] Interestingly, the thiol groups can react with other thiols present in the nearby DMSA molecules, thus creating a cross-linking effect that ensures that DMSA cannot be released from the surface of the particles.[25] The DMSA molecule has four protonable groups: two thiols and two carboxyls. Because of the removal of electron density that the thiols perform on the carboxyl groups, the latter have a much lower pK_a than those typical of carboxylic acids (~4.8), with values as low as 2.31 and 3.69.[26] Due to this enhanced acidity, DMSA can protonate the oleate anions which are present on the surface of the as-synthesized particles and force its release. Subsequently, the resulting deprotonated DMSA molecule can coordinate to the surface of the particle, thus replacing the pristine oleate coating.
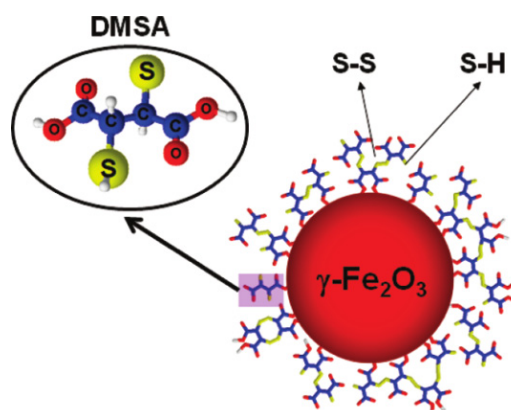
Figure 4. DMSA molecules coordinated to the surface of a maghemite nanoparticle in different ways. Note that some molecules are cross-linked through the disulphide bonds. Adapted from Soler *et al.*[25]

The protocol used to transfer the particles was the same as described by Roca *et al.*[27] Briefly, a dispersion of iron oxide nanoparticles (in our case, nanocubes of 16 ± 3 nm) in toluene (approximately 50 mg in 5 mL) was washed with ethanol and centrifuged for 10 minutes at 4000 g. The particles were redispersed in 25 mL of toluene and then a solution of DMSA (90 mg) in dimethyl sulfoxide (5 mL) was added. The mixture was sonicated for 5 min and magnetically stirred overnight. The DMSA coated nanoparticles appeared attached to the walls of the flask and the surnatant, containing toluene, dimethyl sulfoxide and oleic acid, was discarded. The particles were recovered by eluting with a mixture of ethanol and acetone 1:1 and washed and centrifuged for 10 minutes at 4000 g with this mixture twice. After that, particles were redispersed in water and stored.

The morphology was checked via TEM and the conservation of the cubic shape after the ligand exchange was confirmed (**Fig. 5**). The Z-potential measurements revealed a Z-potential of -37.9 mV, which is considerably high and beyond the value that is needed to consider that the particles should remain stable due to the high electrostatic repulsion ($\pm$ 30 mV). Again, the negative value indicates the presence of free carboxyls, this time with a higher density than in the previous protocol, as inferred from the larger Z-potential value. Nevertheless, the measured hydrodynamic diameter indicated the presence of large aggregates, with a value of 125 nm. Although this result indicates a lower aggregation state compared to that obtained by the oxidative cleavage of oleic acid, it is still very high.
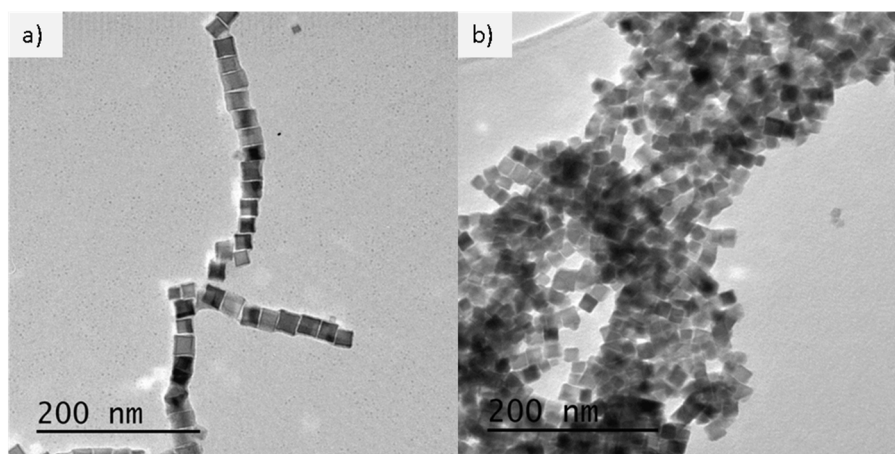
Figure 5. TEM images of the nanocubes before (a) and (b) after transferring to water by ligand exchange with DMSA.

A hypothetic explanation to this aggregation is related to the process of transferring: once the DMSA has displaced enough oleic molecules from the particle surface that are being transferred, the particles are not stable in the medium (mostly toluene) anymore. Consequently, the particles aggregate to hide the hydrophilic regions from the solvent, which is very non-polar, and precipitate onto the surface of the flask. As a consequence, the exchange might be incomplete and thus clusters of particles are transferred instead of single particles. For smaller or non-magnetic nanoparticles, the mechanical stirring could be enough to break these aggregates and force the particles to expose their surface and keep exchange ligands. However, due to the magnetic nature of our particles, this stirring might not be sufficiently strong.

2.3 Conclusions of the conventional methods

Despite the two described methodologies are those that provided the best results of the diverse approaches attempted, the quality of the resulting aqueous colloids is insufficient to meet all the criteria that were initially stablished. For example, although both of them did not alter significantly the morphology of the particles and provided free carboxylic groups, as revealed by the Z-potential measurements, the aggregate size is too large to ensure a long-term stability. Although both methodologies are based on very different principles, the stabilisation mechanism of both of them relies merely on the electrostatic repulsion. The fact that, despite achieving high Z-potential values, particles remain aggregated suggests that maybe electrostatic repulsion is not sufficient to stabilize this type of magnetic material. Consequently, finding other alternative strategies for phase transferring seems crucial.

3. AMPHIPHILIC COATINGS

Although electrostatic repulsion is a powerful mechanism to stabilize nanoparticles, in the case of magnetic nanoparticles, it might be not strong enough to ensure their colloidal stability, as it has been observed from the results of the experiments performed so far, especially for particles with core sizes larger than 15 nm. It is also important to bear in mind that these particles are intended for biomedical applications and, consequently, should remain stable in biological fluids. However, as some authors reported, the presence of a large amount of ions in the biological media might screen the electrostatic charges on the surface of the nanoparticles, leading to a non-reversible magnetic aggregation.[5] To understand the enhanced aggregation in biological media, one should consider that, according to the theory of Derjaguin-Landau-Verwey-Overbeek (or DLVO theory) the electrostatically charged particles are surrounded by a counter-ion sphere, resulting in the so-called electric double layer (**Fig. 6a**). Colloidal stability would be the result of the balance between the electrostatic repulsion of this secondary layer and the Van der Waals forces. Depending on the interparticle distance (r), the result of this balance could lead to a completely non-aggregated state, reversible aggregation or irreversible aggregation in the case of small particles distances (**Fig 6b**). These states are separated by energy barriers and, for particles where the electrostatic repulsion is much stronger than the Van der Waals forces, the minimum energy is obtained for completely separated nanoparticles.

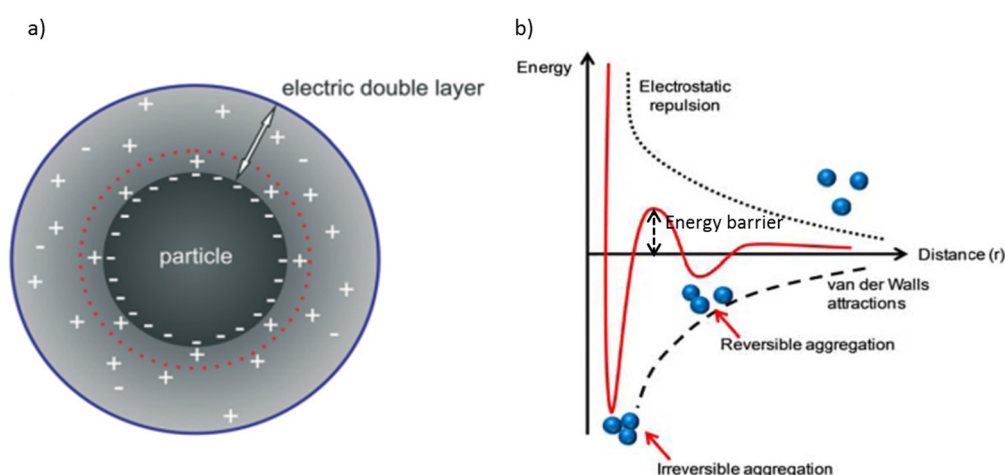**Figure 6.** a) Electric double layer around an electrostatically stabilized particle, consisting of an inner counter-ion shell, or Stern layer (beneath the red-dotted line) and an outer diffuse layer. Reprinted from Polte *et al*.[28] b) Energy profile obtained by representing the attractive and repulsive forces contributions to the total energy as a function of *r*. Adapted from Solaiman *et al*.[29]

In the case of magnetic nanoparticles, magnetic attraction should be considered as well. This attraction depends exponentially on r and consequently, irreversible aggregation can take place at longer distances, meaning that stronger electrostatic repulsion forces are required to stabilize magnetic nanoparticles.[30] However, the ions present in the biological fluids screen the electrostatic charges and thus they decrease the energy barriers between states proportionally to the total ion concentration (**Fig. 7**). Therefore, although electrostatic repulsion by itself might help to stabilize the particles, other stabilization mechanisms may be needed.
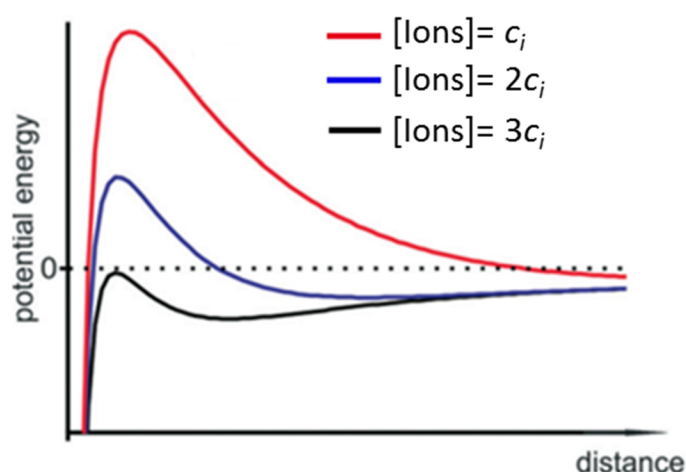

Figure 7. Total interaction potential energy as a function of the distance between two particles at different ion concentrations (c_i). Adapted from Polte *et al.*[28]

An alternative mechanism that could help to avoid irreversible aggregation against the presence of ions is steric hindrance, which is essentially a physical barrier that prevents the particles getting too close to each other, thus avoiding irreversible aggregation. This is the premise on which some coatings, such as silica or polymeric shells, are based. Among the coatings that can provide steric hindrance, amphiphilic coatings deserve special attention. These consist of molecules with both hydrophobic and hydrophilic regions. These regions self-assemble to orient the hydrophilic regions towards the solvent and hiding the hydrophobic regions from the solvent, which act this way as spacers between particles. In addition, the hydrophilic regions are usually electrostatically charged, therefore combining both electrostatic and steric hindrances in a single coating, which usually results in a good stability. Apart from this enhanced stability, the use of amphiphilic coatings can actually have other advantages. For example, it has been observed that they can yield single particles, which has positive effects for some applications (MRI, for example). Despite, in general, single particles are rather sensitive to enzymatic degradation, which results in a rapid clearance and a reduced time of

application, amphiphilic molecules have shown to increase their resistance against enzymatic degradation and consequently particles are more persistent when coated by a double-chained amphiphilic molecule than by the completely hydrophilic chains of PEG.

Considering the important benefits of working with this type of coatings, we proceeded to try two different approaches: encapsulating the particles with a lipid bilayer; and using an amphiphilic co-polymer (poly (maleic anhydride alt-1-octadecene), PMAO).

3.1 Lipid bilayer

Mimicking Nature can often be a source of simple, yet effective solutions. Actually, cell membranes could be the solution to the problem of stabilizing hydrophobic nanostructures in aqueous media. Cell membranes consist essentially of a double layer of amphiphilic molecules, such as fatty acids, phospholipids, etc., where the hydrophilic regions are exposed in both the outer and inner faces while the hydrophobic moieties of each layer are facing each other, thus being hidden from the solvent. This structure is stabilized mainly by the hydrophobic interactions between both layers and the hydrophilic interactions with the solvent. In the case of the oleic acid coated nanoparticles, one of the layers is already present in the particles after the synthesis so, in principle, it is only required to add a secondary layer so as to make the particles become hydrophilic. This approach would have apparently some advantages such as not requiring removing the original coating of the particles and ensuring biocompatibility, as oleic acid is a naturally present molecule in organisms and thus the introduction of xenobiotics would not be required.

This simple idea is actually not new and several different attempts can be found on literature, trying to develop suitable protocols to coat particles with a secondary fatty acid layer.[31–35] Although the methodology is different in the diverse approaches, they all can be summarized more or less as follows. First, the particles are dispersed in a non-polar medium (like hexane) and oleic acid is added to the medium at different ratios respect to the mass of the particles. Then, water is added to the mixture and stirred to force the mixing with the non-polar phase (e.g., by sonication, mechanical stirring…). Afterwards, the mixture is left to rest (typically 24 hours) until the complete separation of both the organic and aqueous phase takes. Finally, the aqueous phase is recovered and the particles are washed and purified. Despite requiring a phase separation step of one day, these methodologies are apparently simple and cost-effective. However, although the fundamentals of the approach might seem simple, from an experimental

point of view it is rather challenging. In fact, after trying to reproduce one by one each of the cited protocols, several problems were found. For example, the optimal amount of oleic acid that should be added according to the different authors looks somehow empirical and is very different from article to article, with a difference of up to several orders of magnitude. Second, the phase separation is not always complete, which results in some particles remaining in the organic phase. Third, the amount of surfactant has a critical role, as if too little is added, the mixture of both phases does not take place or large aggregates are encapsulated instead of single particles; whereas, if a large excess of surfactant is added, random micelles are generated (**Fig. 8**). The latter case is especially dangerous, as oil-in-water micelles can be produced (*i.e.*, hexane droplets coated with a bilayer that makes them water dispersible), which are really toxic in contact with cells. Even if an optimal amount of oleic acid was added, it is very difficult to avoid the formation of these micelles. Furthermore, the addition of an excessive amount of surfactant involved the generation of a massive amount of foam, which adds heterogeneity to the system, and consequently, to the final result. Therefore, after considering the results of these experiments, we proceeded to develop a new protocol for bilayer coating.
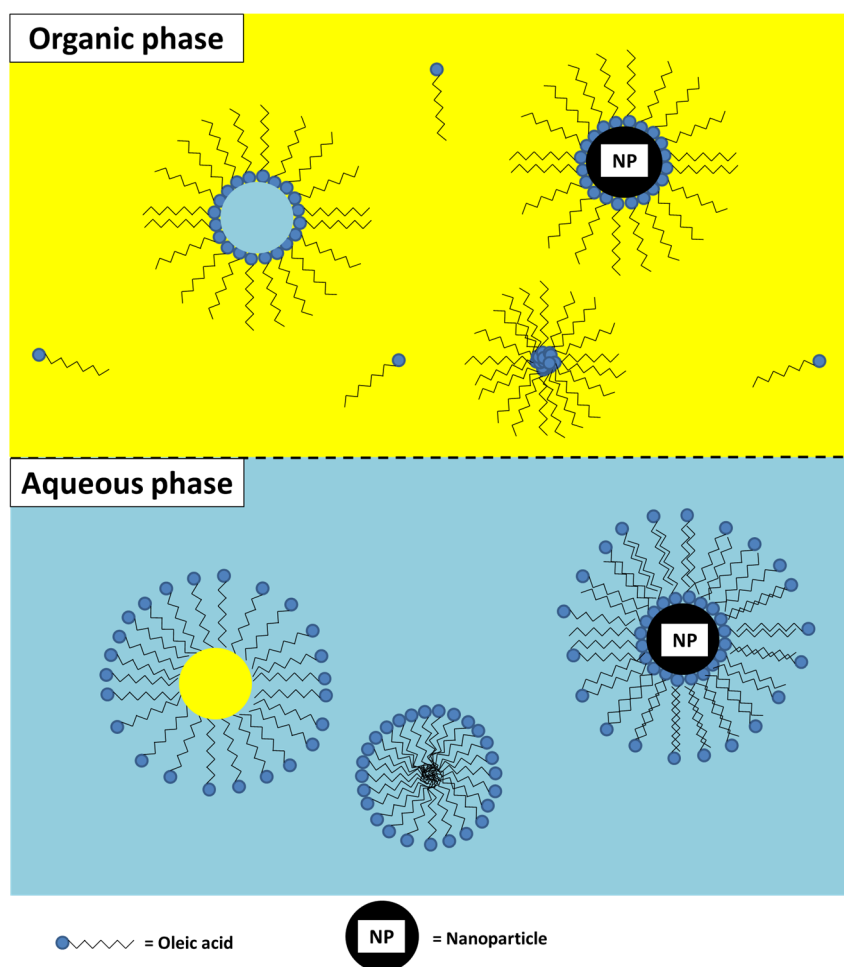
Figure 8. Scheme showing the possible structures that can be present after phase separation in both organic and non-polar (in yellow) and water (in blue) phases when an excess of oleic acid is used to transfer the particles. Note that, up to six different self-assembled structures have been generated in the process.

The first fact that caught our attention is that, in all the described protocols, both the non-polar solvent and the water were mixed together. Although this is necessary to disperse the particles in the first stages so their surface is exposed, the non-polar solvents can also destabilize the bilayers in the already transferred particles, thus decreasing the yield of the transfer, leading to polydisperse aggregates, etc. Therefore, a possible improvement could be carry out the full process in a single phase which, by the way, would avoid also the long phase separation step. As bilayers are based mainly on hydrophobic interactions, the process should be carried out in water to induce these hydrophobic interactions. However, oleic acid is not miscible with water and consequently cannot be used for this process. Fortunately, a possible solution to overcome this problem is to replace oleic acid by its sodium salt which, owing to its negative charge, is soluble in water. By proceeding in this way, no chemicals other than the sodium oleate and water will be required.

The second observation that captured our interest is the huge difference between the reported optimal values of oleic acid that concentration are required to create a secondary layer according to the literature, varying even in several orders of magnitude.[34,35] These values were obtained empirically after some trial experiments. However, in my opinion, a more rational approach would be needed to obtain optimal results. It is clear that if a too small amount of surfactant (in our case, sodium oleate) is used, the coating will not be complete or only aggregates will be encapsulated; however, if the amount of surfactant is larger than a critical value, called critical micelle concentration (CMC), the formation of non-specific micelles will take place. Namely, the CMC is the concentration of surfactant below which all the molecules are free monomers and above which micelles appear. Therefore, working at a concentration equal to the CMC seems the optimal point, as in this way the amount of free oleate molecules is maximized but micelle formation cannot take place, thus avoiding the formation of other structures as by-products. For a given temperature, the CMC value depends on the characteristics of the surfactant. In the case of sodium oleate, although the exact CMC value is still not univocally established, since it depends strongly on the experimental methodology employed for its determination, after comparing several literature references, a value of ~3 mM was considered.[36]

If the concentration of oleate anions remains at the CMC, the formation of double layers should not take place. However, when particles are forced to enter the aqueous phase (*i.e.*, by sonication), the nominal concentration of oleate molecules in the solvent increases beyond the CMC threshold, triggering the formation of micelles directly on the surface of the nanoparticles. This process results in the formation of a single structure (bilayer-coated nanoparticles), as the concentration of surfactant is insufficient to allow the formation of other structures (**Fig. 9a**). Moreover, a benefit of working with a concentration of surfactant which is just as low as needed is to avoid the formation of foam. Finally, another advantage of this methodology is that, considering the availability of multiple oleyl derivatives (such as thiols, amines, alcohols, etc.), it makes it very versatile, as multiple functional groups can be implemented with only minor changes in the methodology (**Fig. 9b**).
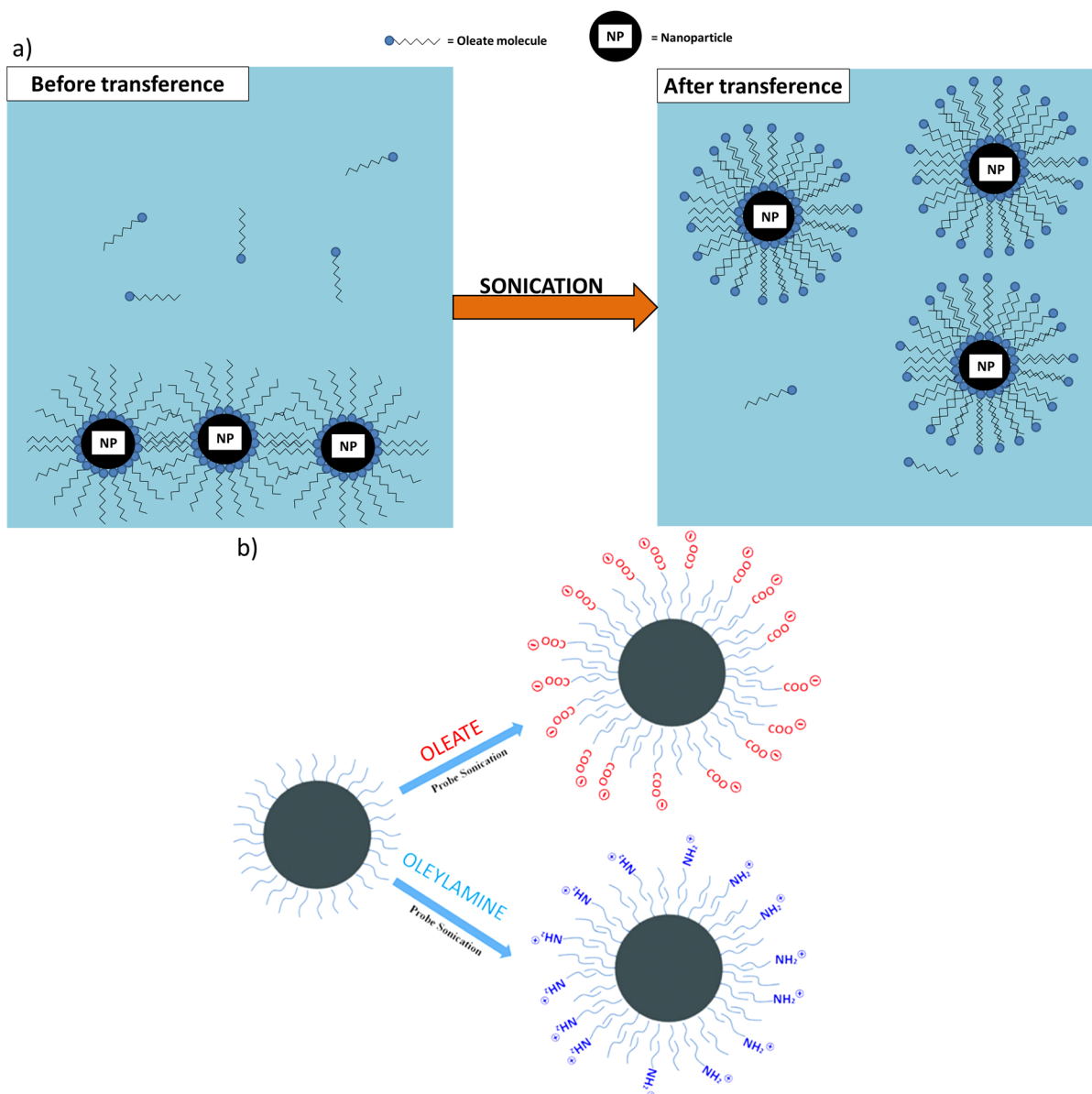
Figure 9. a) Scheme showing the process of single-phase bilayer coating. Note that now only one type of structure is generated. b) Particles coated with a secondary layer of oleate (top) and oleylamine (bottom) using the same procedure.

In a typical transference process, the particles (for these experiments, 18 nm nanocubes) were first washed with acetone and dried under vacuum to erase any traces of solvents. Approximately 10 mg of nanocubes in powder were placed on a 15 mL falcon tube and 21.8 mL of a solution of sodium oleate 3 mM (CMC) was added. The volume of the sodium oleate solution that was added was calculated so the number of sodium oleate molecules per nm^2 of particle was equal to 60. This number was calculated to maximize the surfactant-to-surface ratio without requiring too large volumes of solution, as this will result in more diluted dispersions and would harness the subsequent sonication step, as sonicating a large volume

might require a very high sonication power. The mixture was sonicated in a bath until complete homogenisation (about 5 minutes) and afterwards, the resulting dispersion was sonicated using a probe sonicator at maximum power for 5 more minutes while cooling in a water bath to avoid overheating. Subsequently, the particles were filtered through a syringe filter (0.22 µm pore size) to discard aggregates. Finally, the particles were centrifuged for 20 min at 10.600 g and redispersed in water.

In order to create a hybrid bilayer with oleylamine, the methodology was slightly modified. In its neutral form, oleylamine is a highly immiscible with water. To allow the water solubility, HCl had to be added to acidify the oleylamine. To the best of our knowledge, there are no available data on the CMC value of oleylamine. Therefore, given the structural similarity with oleate, I assumed that this value was similar to that of sodium oleate (~3 mM). Oleylamine (22 µL) was placed on a flask and HCl (15 µL) was added to protonate the oleylamine. The amount of HCl was selected so the number of mol of both HCl and oleylamine were the same. Water (21.8 mL) was added and then the mixture was magnetically stirred and sonicated until complete homogenisation. After this, the mixture was added to a falcon tube containing the particles (10 mg) and the rest of the procedure is the same as in the case of oleate coating.

The TEM images of the particles coated with a double layer of oleate molecules showed that the cubic structure was not altered after the transference and also the presence of single particles and a few dimers and trimers (**Fig. 10**).
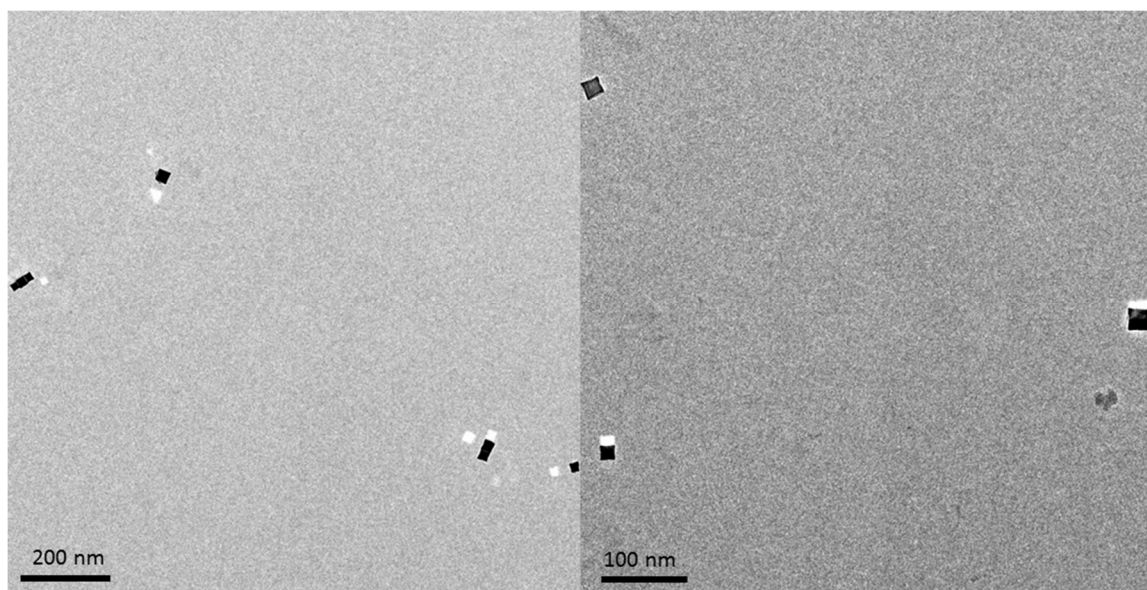

Figure 10. TEM images of the nanocubes coated with a double layer of oleate anions.

The Z-potential measurements showed values of -34.6±1.5 mV for the oleate coated particles and +29.7±0.3 mV for those coated with oleylamine, confirming the successful coating with different ligands. As for the hydrodynamic diameter measurements, the values were 48±5 nm and 81±6 nm for the oleate and oleylamine coated nanoparticles respectively. Considering the longest dimension of the 18 nm edge nanocubes is 31 nm (the inner diagonal) and that the thickness of the bilayer is about 4 nm,[37] one could expect a value of approximately 40 nm for single-particles. In the case of oleate coated nanoparticles, the obtained value is pretty similar and it can be assumed that most of particles are individually coated, although some minor aggregates can coexist, as it has been observed in the TEM images. Conversely, in the case of oleylamine coated particles, particles are more aggregated. This is probably due to the fact that oleylamine was not fully protonated when entering in contact with the water and, consequently, it was partially lost when transferring it onto the falcon containing the particles. This could explain also the lower Z-potential value. However, no more trials were performed to improve this issue, as this was only a proof of concept.

It is very important to mention that the vast majority of the material was lost after the centrifugation step, as most of the particles remained in the surnatant. Apparently, 20 minutes were not enough to cause the precipitation of most single-particles and a stronger centrifugation force (or much longer times) would be necessary to recover the single particles. Interestingly, when the hydrodynamic diameter measurements were performed on the surnatant instead of the redispersed particles after centrifugation, the measured size was 39.0 ± 0.8 nm, indicating a higher presence of single-particles.

Unfortunately, the full optimisation of the process would have required much more work and thus some questions remained unanswered. For example: the total sonication time was only 10 minutes, whereas in some other protocols, it requires several hours. It would be interesting to investigate if longer sonication times could improve the results. On the other hand, although a ratio of 60 molecules of surfactant per nm^2 of surface was chosen as a starting point, it should be investigated whether this is actually the optimal ratio. It would be also interesting to study if longer centrifugation times could improve the single-particles recovery. Contrariwise, as seen in other experiments, centrifuging for several hours in a non-thermalized centrifuge can rise the temperature of the falcons up to 60-70 °C and it should be confirmed if bilayers can resist such high temperatures. Moreover, considering there is no cross-linkage between monomers, if the particles are highly diluted, it might be possible that bilayers disassemble so

the concentration of free surfactant rises up to reach equilibrium. If so, is this process fast enough to represent a problem? Given the size of the particles, it is expected that they are ferrimagnetic (the transition from superparamagnetism to ferrimagnetism in cubes takes place at around 15 nm, as seen from our previous results). Therefore, maybe the results would have been better if the experiments had been carried out with smaller superparamagnetic nanoparticles. As for the oleylamine coating, it is possible that the results had been improved if oleylammonium bromide had been used instead of oleylamine, as it is already ionised and soluble in water. Answering all of these questions would have required many more experiments and months of work and, for this reason, the research was discontinued during the thesis.

Nevertheless, the results obtained here are very promising, as this protocol represents an important advance in several aspects. For example, (i) it is the only protocol that is completely carried out in a single phase, avoiding the use of organic solvents, which is interesting for particles intended for biomedical applications; (ii) it does not require a slow phase separation step. Namely, it is the fastest protocol described so far, as it only takes 10-15 minutes to coat the particles; (iii) it has been proven to be versatile, as secondary layers with different molecules have been created, allowing to tune the electrostatic charge, the functional group, etc.; (iv) the colloidal properties are better than any of the other techniques tried so far in this Thesis.

3.2 Amphiphilic co-polymer coating

Poly (maleic anhydride-alt-1-octadecene) (PMAO) is a polymer consisting of long hydrophobic aliphatic chains linked to each other by anhydride rings. In a similar way to double layers, the non-polar chains interact with the chains of the capping oleates present in the surface of the hydrophobic particles. During the process of intercalation, the anhydride rings are hydrolysed using a base, which generates two carboxyls per anhydride, thus generating a large negative charge (**Fig. 11**). The process was first described by Pellegrino *et al.*,[15] although in this work it has been modified and adapted and some steps have been simplified for practical reasons.
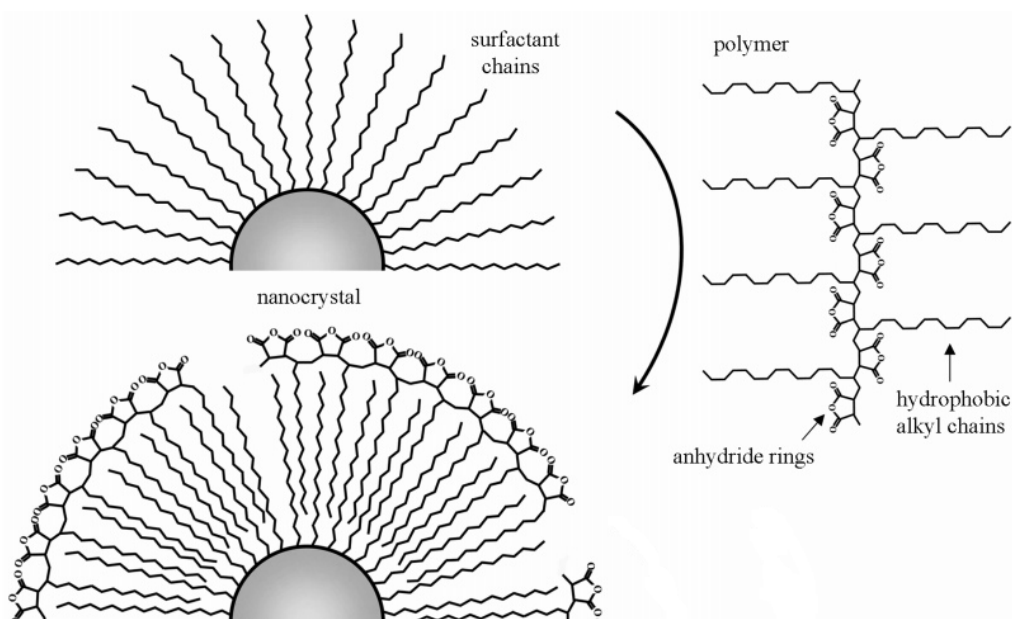
Figure 11. Scheme showing the coating of hydrophobic nanocrystals with PMAO. Adapted from Pellegrino *et al.*[15]

In a typical transference, the particles (in this case, 10 mg of 15.3 nm nanocubes) were dispersed in chloroform (12.3 mL) and PMAO (272 mg) was added so the density of monomers per nm^2 of particles is equal to 500 and the concentration of particles is 0.09 μM. After sonicating for 10 min, the chloroform was removed by rotaevaporation. The resulting precipitate was covered with 12.3 mL of borate buffer (50 mM at pH 9) and sonicated overnight until the complete redispersion of the particles. The mixture was further ultrasonicated with a probe sonicator for 30 minutes and filtered through a syringe filter (0.22 μm pore size). Finally, the particles were centrifuged at 10600 g for 4 hours and redispersed in mili-Q water.

The TEM images confirmed the preservation of the shape (**Fig. 12**) and the presence of mainly single-particles.
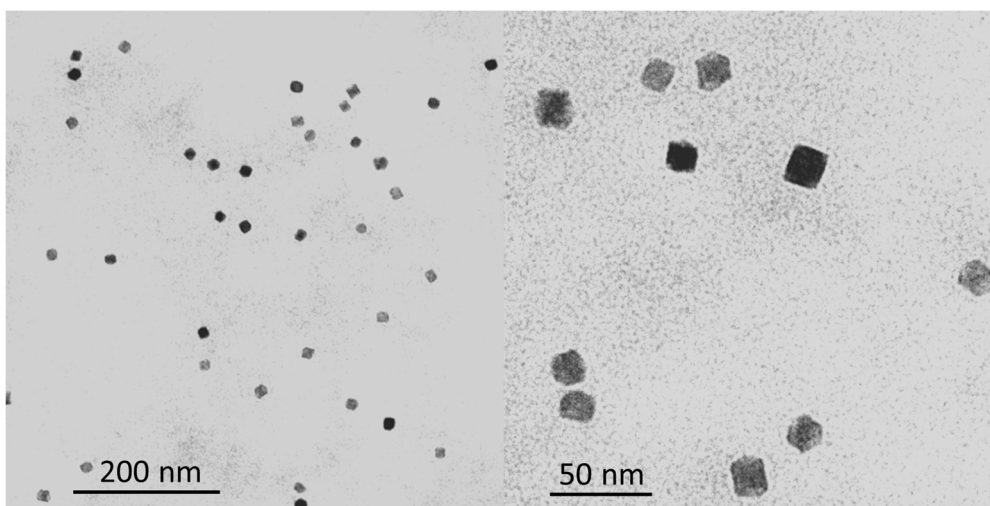
Figure 12. TEM images of the nanocubes coated with a PMAO.

The DLS characterization resulted in a hydrodynamic size and a Z-potential of 34±6 nm and -35±5 mV, respectively. Considering that the thickness of this coating has been estimated to be about 4 nm in thickness, thus increasing approximately 8 nm the hydrodynamic diameter, it can be assumed that the particles were mainly well-dispersed and colloidally stable as single-particles.

4. CONCLUSIONS

Although many examples can be found on literature where an ionic coating is enough to stabilize small inorganic particles, working with relatively large hydrophobic magnetic nanoparticles makes stabilization far more challenging. From the results obtained from different approaches, it is clear that steric hindrance is crucial to achieve total stability, especially if particles should remain well-dispersed in saline media such as biological fluids. Interestingly, amphiphilic coatings have turned out to provide very good results and met all the criteria that were set (not altering the morphology, providing negative charge through carboxyl groups, a low hydrodynamic diameter, etc.). Remarkably, in this work, a new protocol for coating the particles with lipid bilayers has been developed. However, despite the promising results, the optimisation of the full protocol would require a more systematic study that is beyond of the scope of this thesis. Consequently, considering the limited time and the need for stable particles (for example, for *in vitro* studies) and the excellent results achieved with PMAO, this coating was selected as the preferred methodology for transferring our particles into water.

5. REFERENCES

(1)   Chen, L.T.; Weiss, L. The Role of the Sinus Wall in the Passage of Erythrocytes Through the Spleen. *Blood* **1973**, 41 (4), 529–537.

(2)   Haracz, S.; Hilgendorff, M.; Rybka, J. D.; Giersig, M. Effect of Surfactant for Magnetic Properties of Iron Oxide Nanoparticles. *Nucl. Instruments Methods Phys. Res. Sect. B Beam Interact. with Mater. Atoms* **2015**, 364, 120–126.

(3)   Guibert, C.; Dupuis, V.; Peyre, V.; Fresnais, J. Hyperthermia of Magnetic Nanoparticles: Experimental Study of the Role of Aggregation. *J. Phys. Chem. C* **2015**, 119 (50), 28148–28154.

(4)   Myrovali, E.; Maniotis, N.; Makridis, A.; Terzopoulou, A.; Ntomprougkidis, V.; Simeonidis, K.; Sakellari, D.; Kalogirou, O.; Samaras, T.; Salikhov, R.; Spasova, M.; Farle, M.; Wiedwald, U.; Angelakeris, M. Arrangement at the Nanoscale: Effect on Magnetic Particle Hyperthermia. *Sci. Rep.* **2016**, 6 (1), 37934.

(5)   Nikitin, A. A.; Khramtsov, M. A.; Savchenko, A. G.; Abakumov, M. A.; Mazhuga, A. G. Anisotropic Iron-Oxide Nanoparticles for Diagnostic MRI: Synthesis and Contrast Properties. *Pharm. Chem. J.* **2018**, 52 (3), 231–235.

(6)   Tong, S.; Hou, S.; Zheng, Z.; Zhou, J.; Bao, G. Coating Optimization of Superparamagnetic Iron Oxide Nanoparticles for High T_2 Relaxivity. *Nano Lett.* **2010**, 10 (11), 4607–4613.

(7)   Kolosnjaj-Tabi, J.; Lartigue, L.; Javed, Y.; Luciani, N.; Pellegrino, T.; Wilhelm, C.; Alloyeau, D.; Gazeau, F. Biotransformations of Magnetic Nanoparticles in the Body. *Nano Today* **2016**, 11 (3), 280–284.

(8)   Puertas, S.; Batalla, P.; Moros, M.; Polo, E.; del Pino, P.; Guisán, J. M.; Grazú, V.; de la Fuente, J. M. Taking Advantage of Unspecific Interactions to Produce Highly Active Magnetic Nanoparticle−Antibody Conjugates. *ACS Nano* **2011**, 5 (6), 4521–4528.

(9)   Fauconnier, N.; Pons, J. N.; Roger, J.; Bee, A. Thiolation of Maghemite Nanoparticles by Dimercaptosuccinic Acid. *J. Colloid Interface Sci.* **1997**, 194 (2), 427–433.

(10)   De Montferrand, C.; Hu, L.; Milosevic, I.; Russier, V.; Bonnin, D.; Motte, L.; Brioude, A.; Lalatonne, Y. Iron Oxide Nanoparticles with Sizes, Shapes and Compositions Resulting in Different Magnetization Signatures as Potential Labels for Multiparametric Detection. *Acta Biomater.* **2013**, 9 (4), 6150–6157.

(11)   Salgueiriño-Maceira, V.; Liz-Marzán, L. M.; Farle, M. Water-Based Ferrofluids from $Fe_x Pt_{1-x}$ Nanoparticles Synthesized in Organic Media. *Langmuir* **2004**, 20 (16), 6946–6950.

(12)   De Palma, R.; Peeters, S.; Van Bael, M. J.; Van Den Rul, H.; Bonroy, K.; Laureyn, W.; Mullens, J.; Borghs, G.; Maes, G. Silane Ligand Exchange to Make Hydrophobic Superparamagnetic Nanoparticles Water-Dispersible. *Chem. Mater.* **2007**, 19 (7), 1821–1831.

(13)   Rando, D. G.; Brandt, C. A.; Ferreira, E. I. Use of N-Methylene Phosphonic Chitosan to Obtain an Isoniazid Prodrug. *rasilian J Pharm Sci 2004; 40: 335-44.* **2004**, 40 (3), 334–344.

(14)   Xie, J.; Xu, C.; Kohler, N.; Hou, Y.; Sun, S. Controlled PEGylation of Monodisperse Fe_3O_4 Nanoparticles for Reduced Non-Specific Uptake by Macrophage Cells. *Adv. Mater.* **2007**, 19 (20), 3163–3166.

(15)   Pellegrino, T.; Manna, L.; Kudera, S.; Liedl, T.; Koktysh, D.; Rogach, A. L.; Keller, S.; Rädler, J.; Natile, G.; Parak, W. J. Hydrophobic Nanocrystals Coated with an Amphiphilic Polymer Shell: A General Route to Water Soluble Nanocrystals. *Nano Lett.* **2004**, 4 (4), 703–707.

(16)   Lee, S.-Y.; Harris, M. T. Surface Modification of Magnetic Nanoparticles Capped by Oleic Acids: Characterization and Colloidal Stability in Polar Solvents. *J. Colloid Interface Sci.* **2006**, 293 (2), 401–408.

(17)   Graf, C.; Vossen, D. L. J.; Imhof, A.; Van Blaaderen, A. A General Method to Coat Colloidal Particles with Silica. *Langmuir* **2003**, 19 (17), 6693–6700.

(18)   Mohapatra, A.; Uthaman, S.; Park, I.-K. Polyethylene Glycol Nanoparticles as Promising Tools for Anticancer Therapeutics. In *Polymeric Nanoparticles as a Promising Tool for Anti-cancer Therapeutics*. Elsevier, **2019**. 205–231.

(19)   Alejo, T.; Merchán, M. D.; Velázquez, M. M. Adsorption of Quantum Dots onto Polymer and Gemini Surfactant Films: A Quartz Crystal Microbalance Study. *Langmuir* **2014**, 30 (33), 9977–9984.

(20)   Jung, Y.; Jeong, J. Y.; Chung, B. H. Recent Advances in Immobilization Methods of Antibodies on Solid Supports. *Analyst* **2008**, 133 (6), 697-701.

(21)   Bhattacharjee, S. DLS and Zeta Potential - What They Are and What They Are Not? *J. Control. Release* **2016**, 235, 337–351.

(22)   Arias, L.; Pessan, J.; Vieira, A.; Lima, T.; Delbem, A.; Monteiro, D. Iron Oxide Nanoparticles for Biomedical Applications: A Perspective on Synthesis, Drugs, Antimicrobial Activity, and Toxicity. *Antibiotics* **2018**, 7 (2), 46.

(23)   Si, J. C.; Xing, Y.; Peng, M. L.; Zhang, C.; Buske, N.; Chen, C.; Cui, Y. L. Solvothermal Synthesis of Tunable Iron Oxide Nanorods and Their Transfer from Organic Phase to Water Phase. *CrystEngComm* **2014**, 16 (4), 512–516.

(24)   Jun, Y.-W.; Huh, Y.-M.; Choi, J.-S.; Lee, J.-H.; Song, H.-T.; Kim, S.; Yoon, S.; Kim, K.-S.; Shin, J.-S.; Suh, J.-S.; Cheon, J. Nanoscale Size Effect of Magnetic Nanocrystals and Their Utilization for Cancer Diagnosis via Magnetic Resonance Imaging. *J. Am. Chem. Soc.* **2005**, 127 (16), 5732–5733.

(25)   Soler, M. A. G.; Lima, E. C. D.; Nunes, E. S.; Silva, F. L. R.; Oliveira, A. C.; Azevedo, R. B.; Morais, P. C. Spectroscopic Study of Maghemite Nanoparticles Surface-Grafted with DMSA. *J. Phys. Chem. A* **2011**, 115 (6), 1003–1008.

(26)   Aposhian, H. V.; Aposhian, M. M.. Meso-2,3-Dimercaptosuccinic Acid: Chemical, Pharmacological and Toxicological Properties of an Orally Effective Metal Chelating Agent. *Annu. Rev. Pharmacol. Toxicol.* **1990**, 30, 279–306.

(27)   Roca, A. G.; Veintemillas-Verdaguer, S.; Port, M.; Robic, C.; Serna, C. J.; Morales, M. P. Effect of Nanoparticle and Aggregate Size on the Relaxometric Properties of MR Contrast Agents Based on High Quality Magnetite Nanoparticles. *J. Phys. Chem. B* **2009**, 113 (19), 7033–7039.

(28)   Polte, J. Fundamental Growth Principles of Colloidal Metal Nanoparticles-a New Perspective. *CrystEngComm* **2015**, 17 (36), 6809–6830.

(29)   Solaiman, S. M.; Yamauchi, Y.; Kim, J. H.; Horvat, J.; Dou, S. X.; Alici, G.; Ooi, L.; Martinac, B.; Shiddiky, M. J. A.; Gopalan, V.; Hossain, M. S. A. Nanotechnology and Its Medical Applications: Revisiting Public Policies from a Regulatory Perspective in Australia. *Nanotechnol. Rev.* **2017**, 6 (3), 25–26.

(30)   Cousin, F.; Dubois, E.; Cabuil, V. Tuning the Interactions of a Magnetic Colloidal Suspension. *Phys. Rev. E - Stat. Physics, Plasmas, Fluids, Relat. Interdiscip. Top.* **2003**, 68 (2), 021405.

(31)   Li, W.; Hinton, C. H.; Lee, S. S.; Wu, J.; Fortner, J. D. Surface Engineering Superparamagnetic Nanoparticles for Aqueous Applications: Design and Characterization of Tailored Organic Bilayers. *Environ. Sci. Nano* **2015**, 3, 85–93.

(32)   Smolensky, E. D.; Park, H.-Y. E.; Berquo, T. S.; Pierre, V. C. Surface Functionalization of Magnetic Iron Oxide Nanoparticles for MRI Applications–effect of Anchoring Group and Ligand Exchange Protocol. *Contrast Media Mol Imaging* **2011**, 6 (4), 189–199.

(33)   Soares, P. I. P.; Laia, C. A. T.; Carvalho, A.; Pereira, L. C. J.; Coutinho, J. T.; Ferreira, I. M. M.; Novo, C. M. M.; Borges, J. P. Iron Oxide Nanoparticles Stabilized with a Bilayer of Oleic Acid for Magnetic Hyperthermia and MRI Applications. *Appl. Surf. Sci.* **2016**, 383, 240–247.

(34)   Prakash, A.; Zhu, H.; Jones, C. J.; Benoit, D. N.; Ellsworth, A. Z.; Bryant, E. L.; Colvin, V. L. Bilayers as Phase Transfer Agents for Nanocrystals Prepared in Nonpolar Solvents. *ACS Nano* **2009**, 3 (8), 2139–2146.

(35)   Mei, Z.; Dhanale, A.; Gangaharan, A.; Sardar, D. K.; Tang, L. Water Dispersion of Magnetic Nanoparticles with Selective Biofunctionality for Enhanced Plasmonic Biosensing. *Talanta* **2016**, 151, 23–29.

(36)   Stand, O. F. Critical Micelle Concentrations of Aqueous Surfactant Systems. *J. Pharm. Sci.* **1972**, 61 (2), 135–137.

(37)   Han, S. Molecular Dynamics Simulation of Oleic Acid/oleate Bilayers: An Atomistic Model for a Ufasome Membrane. *Chem. Phys. Lipids* **2013**, 175-176, 79–83.

CHAPTER 6: BIOMEDICAL APPLICATIONS

1. INTRODUCTION

In order to confirm the suitability for biomedical applications of magnetic nanoparticles, some background experiments need to be carried out. First it is crucial to prove that the material is not cytotoxic. Moreover, it is also very important to verify that cells are able to internalize the particles, which is usually a required condition to cause therapeutic effects. Note that the rate at which cells endocytose the particles can be enhanced by grafting the particles with biomolecules that target preferably cancer cells. As a targeting molecule, a protein involved in the metabolism of iron, called transferrin, was chosen, since cancer cells tend to overexpress its membrane receptor as a response to an increased demand of iron.[1] From the diagnosis viewpoint, a key issue to treat tumours is to determine precisely their location. In this sense, magnetic nanoparticles can be used for this purpose since they act as contrast agents in MRI. In fact, shape anisotropic nanoparticles (like ours) have been proposed to improve the resolution in r2-based MRI images.

Regarding the therapeutic effect of magnetic particles, most of their uses are based on hyperthermia. Although the magnetic hyperthermia of magnetic nanoparticles (and in particular iron oxides) has been known for a long time, recent studies have shown that, despite iron oxides are not plasmonic materials, they can also induce a high temperature increase under the irradiation of an appropriate light source with the extra advantage of allowing magnetic active targeting.[2]

Finally, it has recently been reported that magneto-plasmonic nanoparticles can be used for *in-situ* temperature sensing based on the viscosity changes induced by temperature variations.[3] This could be particularly useful during hyperthermia sessions, where it is important to control the temperature to minimize the damage to nearby health tissues due to thermal ablation.

To tackle these issues, experiments of cytotoxicity and internalisation (both with and without a targeting biomolecule) were conducted on human cell lines. The potential of the nanoparticles as a contrast agent was evaluated by NMR measurements, whereas the performance in two kinds of hyperthermia (magnetic and optical) was studied as well. Eventually, the particles were used for nanothermometry, which is a relatively new way of real time *in situ* monitoring temperature and could be useful to avoid thermal ablation necrosis during hyperthermia sessions.

2. CYTOTOXICITY AND TARGETING

2.1 Cytotoxicity study

The cytotoxicity of the nanoparticles was assessed by incubating cell cultures with different amounts of particles to determine the threshold beyond which an important decay on the viability is induced. Furthermore, the influence of the shape was evaluated by incubating cells with both nanocubes and nanorods.

The HeLa cells (ATCC, Manassas, VA) were cultured as recommended in Dulbecco's modified Eagle medium (DMEM) containing Glutamax™ and D-glucose (4.5 g/L, Life Technology SAS), supplemented with 10% heat-inactivated foetal calf serum (FCS, Life Technology SAS) and 1% penicillin/streptomycin. Cells were cultured in a moist atmosphere (5% CO_2) at 37 °C in 75 cm^2 tissue-culture flasks (for growth and maintenance) or in 24-well plates (Corning) for the incubation with the particles.

Cells were incubated with nanoparticles (either 27 nm nanocubes or 40x6 nm nanorods) at iron concentrations of up to 26 mM for 1 hour. After that, they were carefully washed with culture medium. After the incubation time, the number of cells as well as their viability was measured using Trypan Blue assay.[4] Cells without nanoparticles were used as a control and thus the cell viability is normalized respect to this control.

The results (**Fig. 1**) showed some differences between both nanocubes and nanorods. The latter turned out to have more influence on the cell viability compared to nanocubes. This effect has been reported in literature and correlated to the surface-to-volume ratio of the particles and it can be explained by the higher induced membrane damage and the enhanced radical oxygen species production, whose production is catalysed by the iron oxide surfaces.[5] The nanocubes induced a maximum decay (for [Fe] = 26 mM) on the cell viability of 10%, whereas this value becomes 20% for nanorods. Considering these results, an iron concentration of 4 mM was chosen for the *in vitro* experiments, where the toxicity due to the presence of the particles is negligible.
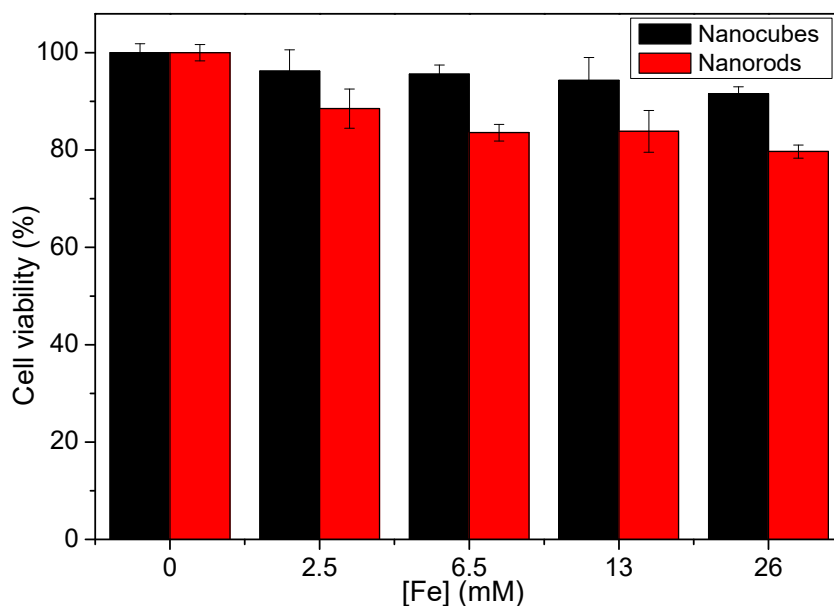
Figure 1. Cell viability as a function of the concentration of iron for both nanocubes and nanorods (black and red columns, respectively).

2.2 Targeting

Transferrin is a protein whose molecular weight is around 80 kDa and is responsible for the plasmatic iron transportation in mammals. Some studies have reported that around 74% of tumour cells overexpress its membrane receptor, therefore suggesting a potential target for future therapies.[1] Consequently, we proceeded to functionalize the nanoparticles with transferrin to promote their accumulation and internalisation in malignant cells. Although there are several strategies to graft nanoparticles with proteins, (*i.e.*, ionic adsorption, cross-linkage through the creation of disulphide bonds, etc.), in our case the immobilisation through the creation of a covalent bond between the carboxyl groups of the surfactant and the amine groups of the transferrin was chosen, as it yields to a non-reversible and highly stable link.[6,7] This strategy is usually referred to as "EDC coupling", as it involves the usage of 1-ethyl-3-(3-dimethylaminopropyl) carbodiimide (EDC). This molecule is used to activate the carboxyl groups of the surface of the nanoparticles. Then, N-hydroxysuccinimide (NHS) reacts with the intermediate generated in the previous step and eventually the primary amines present in the protein react leading to an amide bond that acts as linker between the nanoparticle and the protein (**Fig. 2**).
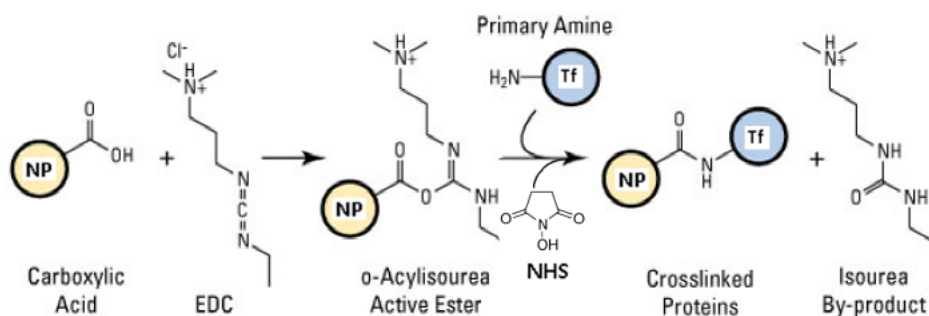
Figure 2. Scheme showing the grafting of transferrin (Tf) onto the surface of a nanoparticle (NP). Adapted from Thermo Fisher Scientific web site.[8]

The followed protocol was the same as described by Piraux et al.[9] Briefly, 0.5 mg of nanoparticles were magnetically precipitated, washed and redispersed in 500 μL of 2-(N-morpholino) ethanesulfonic acid (MES; 100 mM, pH 6), containing NHS and EDC at concentrations of 3.75 and 1.5 mM, respectively. The mixture was vortexed at room temperature for 1.5 hours to activate the carboxyl groups. Afterwards, the particles were magnetically precipitated and washed twice with phosphate-buffered saline (PBS; 10 mM, pH 7.4) and eventually redispersed in 1 mL of PBS containing different amounts of transferrin (from 0.25 to 2 mg per mg of nanoparticle). The particles were incubated with the protein by vortexing overnight at 4°C. Eventually, the particles were washed twice with PBS to remove the excess of protein and stored in PBS at 4°C.

The presence of proteins on the surface of the nanocubes was confirmed by using attenuated total reflectance (ATR) measurements, a spectroscopic technique based on infrared absorption. The samples were prepared by simply depositing a few drops of the particle dispersion (either raw or transferrin grafted) onto the sample holder of the spectrometer. The comparison of the spectra of the raw nanocubes and the grafted nanocubes revealed some significant differences: the shifting of the peak at 1591 cm^{-1} and the apparition of two peaks at 1645 and 1545 cm^{-1} would confirm the apparition of an amide bond (presumably between the particle and the transferrin) as a result of the shifting of the band corresponding to the –C=O and the apparition of a –C-N bond (**Fig. 3a**).[10] The peak at 1371 cm^{-1}, present in the raw nanocubes but mostly not in the grafted nanocubes, corresponds to secondary alkanes and is very likely due to the presence of methanol traces from the cleaning step prior to the deposition of the sample.

154

To monitor the amount of transferrin that is immobilised on the surface of the nanocubes, the ratio of nitrogen to iron (N/Fe) was measured using x-ray photoelectron spectroscopy (XPS). The samples were prepared by depositing a few drops of dispersion onto a glass sample holder and let them dry at room temperature. The results indicated that for amounts higher than 1.5 mg of transferrin per mg of nanocubes, the N/Fe ratio does not increase in a linear way anymore, indicating that the surface is becoming saturated (**Fig. 3b**). Therefore, to optimize the amount of protein attached during the grafting process, a ratio of 1.5 mg of transferrin per mg of particle was chosen.
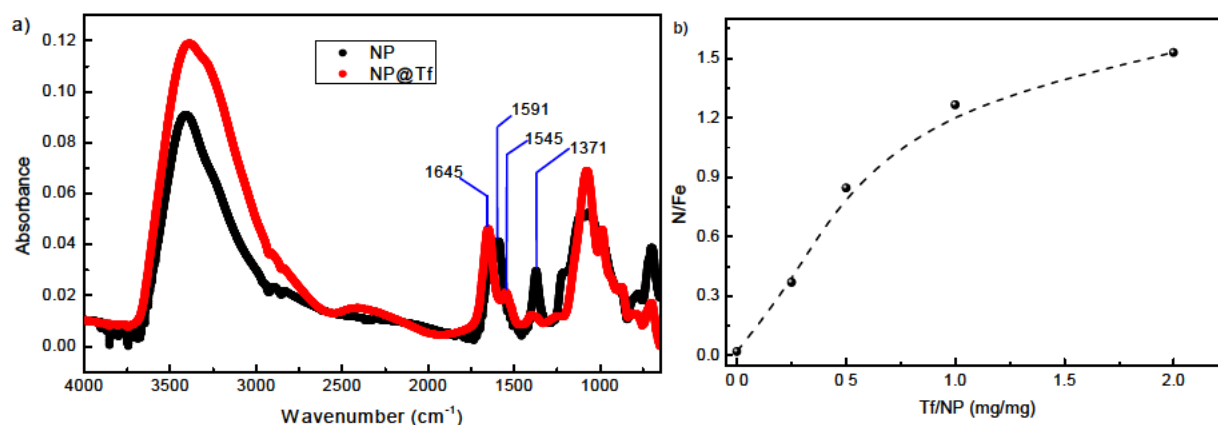

Figure 3. a) Infrared spectra of the raw (NP; black curve) and the transferrin grafted (NP@Tf; red curve) nanoparticles. b) N/Fe ratio (measured by XPS) as a function of the transferrin (Tf) to nanoparticle (NP) mass ratio that was used during the functionalisation.

Interestingly, when the same methodology was applied to 40x6 nm nanorods, the grafting was confirmed as well, but even at ratios as high as 16 mg transferrin/mg of nanoparticles, no saturation point could be found. This effect could be explained if one takes into account that nanorods have a much higher surface area than nanocubes (138.5 m^2/mg and 10.5 m^2/mg respectively) and therefore, presumably they can attach a higher amount of protein on their surface.

To study the targeting efficacy of the transferrin grafting, HeLa cells were incubated with the particles (either cubes or nanorods, both raw and grafted) for 1 hour at an iron concentration of 4 mM and then washed with culture medium as indicated previously. The viability was determined afterwards and the cells were dissolved in a mixture of HCl and HNO_3 and the iron content was determined *via* ICP. The percentage of nanoparticles that had been internalised was calculated by the ratio between the initial iron concentration (4 mM) and the one determined by ICP after dissolving the cells. The data (cell viability and internalisation

percentage) were compared to a control of cells that were not incubated with particles. The results showed that the cell viability did not change in an important way with respect to the control, indicating that the grafted nanoparticles keep the low cytotoxicity. However, contrarily to what it was expected, the percentage of internalisation decreases for grafted particles when compared to the raw ones, both for nanocubes and nanorods (**Fig. 4a**).
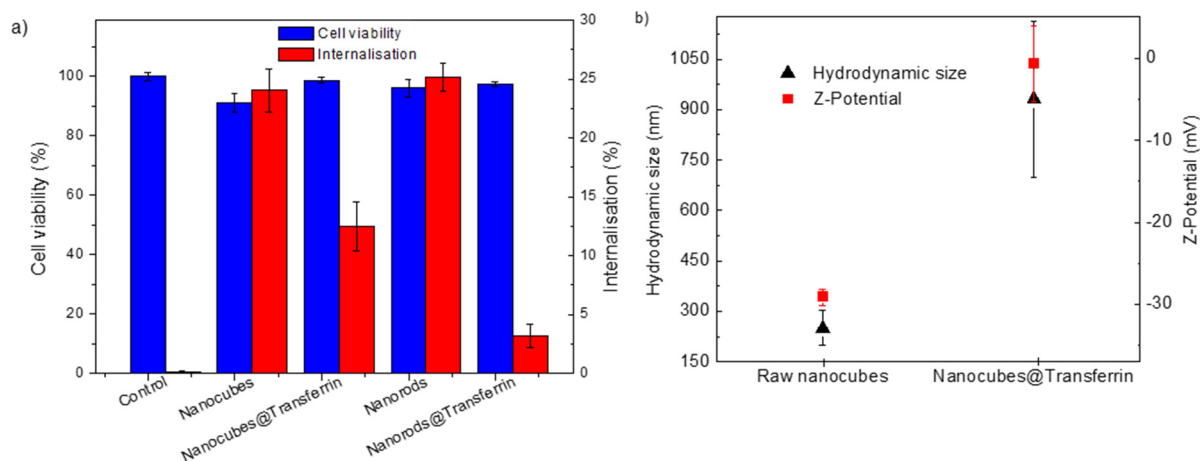

Figure 4. a) Cell viability and percentage of nanoparticles internalisation (blue and red columns, respectively) for cells incubated with nanocubes and nanorods both raw and grafted, as indicated by the "@transferrin" suffix. b) Hydrodynamic size and Z-potential measurements for raw and transferrin coated nanocubes ("Nanocubes@Transferrin").

Some studies had previously reported the loss of the targeting capacity of transferrin grafted nanoparticles in complex biological media, where the presence of other proteins can result in the formation of a protein corona around the particle could harness the coupling of transferrin to its corresponding membrane receptor.[11] However, in our case, not only the grafting does not result in an improvement of the internalisation, but it also yields to a decay. Therefore, another explanation should be investigated. We hypothesized that a possible reason could be the large degree of aggregation that particles showed during the functionalisation process. The origin of the aggregation could be explained if one takes into account that the grafting process involves working in saline media, with a large amount of ions that can neutralise the inter-particle electrostatic repulsion and several steps of magnetic precipitation. In addition, the EDC coupling process itself involves the chemical modification of the carboxyl groups of the particles to make them reactive, which results in their neutralisation, therefore cancelling the electrostatic stabilisation. To analyse the aggregation degree, hydrodynamic diameter and Z-potential measurements were conducted. The Z-potential indicated a virtually total neutralisation of the electrostatic charge which was shifted from -29.1 ± 1.1 to -0.7 ± 4.6 mV

after the grafting. This resulted in the increase of the hydrodynamic diameter from 250 to 930 nm, indicating that the particles were mainly aggregated (**Fig. 4b**). As a consequence, the particles were not stable during the incubation with the cells and remained mainly as large aggregates on the bottom of the culture wells. Using the Bradford assay (a spectrophotometric method for protein quantification),[12] the protein concentration in the surnatant of the grafting reaction was determined and compared to the initial value. By a simple matter balance, the amount of protein that was immobilised on the nanoparticles was estimated to be approximately 200 µg per mg of particle.

It seems reasonable to assume that, considering that the loss of electrostatic repulsion during the EDC coupling is what causes the aggregation, using a coating that also can provide steric stabilisation (like PMAO or a lipid bilayer) could be a possible solution to overcome this issue. Unfortunately, these experiments were carried out using DMSA coated nanoparticles as, at that time, the PMAO coating had not been tested yet and the yield of the bilayer coating was still too low to allow carrying out this kind of experiments.

3. MAGNETIC RESONANCE IMAGING

The size effect on the nuclear magnetic resonance response of the nanocubes was assessed by measuring the r_2 relaxivity for 13.3, 15.3 and 19.3 nm nanocubes. As can be seen in **Fig. 5a,b**, the increase in size from 13.3 to 15.3 nm enables a 40% enhancement in the r_2 value (from 332 to 455 $s^{-1}mM^{-1}$). However, a further increase to 19.3 nm has a minimal effect on r_2 (460 $s^{-1}mM^{-1}$). This is in agreement with earlier studies which reported a raise of r_2 with size for superparamagnetic nanoparticles and a saturation of r_2 as the particles become ferrimagnetic and evidences the importance of the size control also for NMR imaging.[13] These values were compared to those of commercial spherical particles of 22 nm in diameter (22±2 nm in diameter; Ocean Nanotech®) which, despite having a similar volume to the 15 nm edge nanocubes, they showed a 1.6 times smaller r_2 value (293 $s^{-1}mM^{-1}$; **Fig. 5c**). Notably, the values for the nanocubes are considerably higher than commercially available contrast agents such as Feridex® and Resovist ®, whose r_2 values are 105 and 176 $s^{-1}mM^{-1}$, respectively. Eventually, to highlight the importance of shape anisotropy the r_2 relaxivity of 35x5 nm nanorods was determined as well. The rods showed an r_2 value of 589 $s^{-1}mM^{-1}$, which is higher than any of the other particles tested so far (**Fig. 5d**). As a result of their high shape anisotropy, nanorods show an enhanced demagnetizing factor, increasing the maximum range at which nanorods can

alter the relaxation time of protons.[14] In addition, due to their large surface to volume ratio, a higher number of water molecules can diffuse onto the surface of the particles.[15]
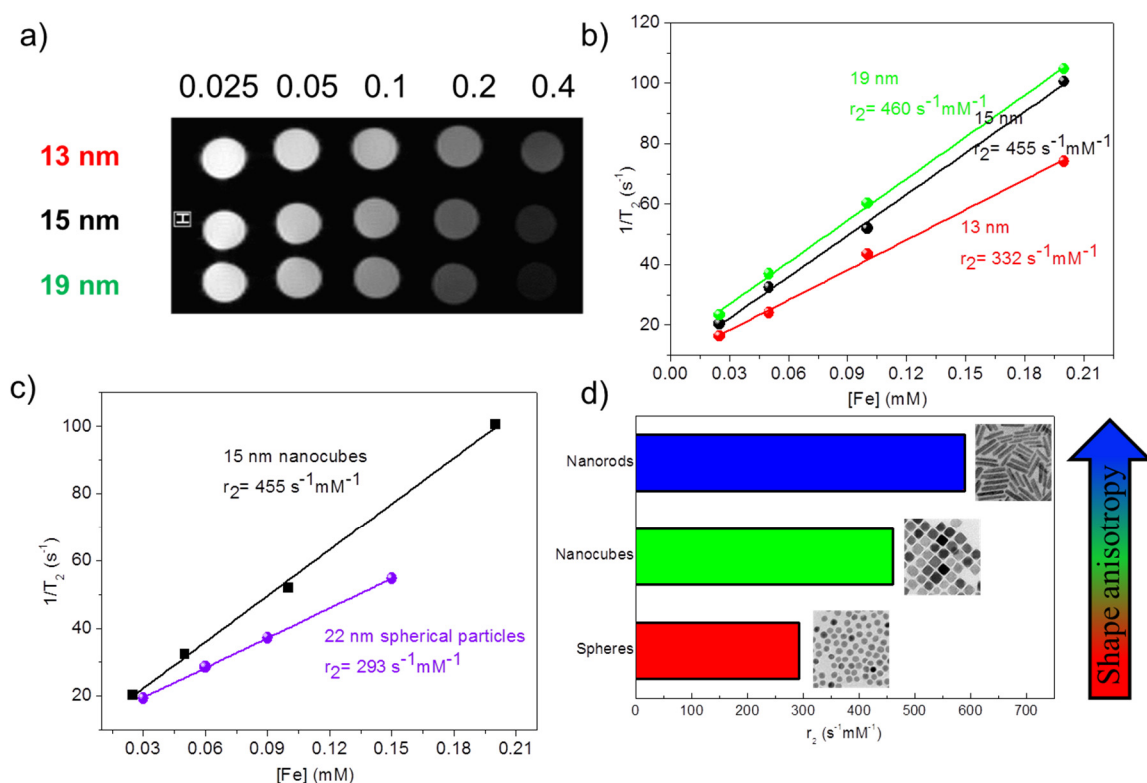

Figure 5. a) T_2-weighted magnetic resonance images of agarose phantoms for nanoparticles of different sizes and different concentrations (the numbers above the image indicate the [Fe] concentration in mM). b) Dependence of the NMR R_2 ($1/T_2$) values on the [Fe] concentration for the three samples. c) Relaxivities of the 15 nm nanocubes (black squares) compared to the commercial 22 nm spherical particles (purple circles). d) Comparison of the r_2 values between particles with different degrees of shape anisotropy.

4. HYPERTHERMIA

To evaluate the efficacy of the nanoparticles as therapeutic agents, two different types of hyperthermia were tested: magnetic hyperthermia and photothermia.

4.1 Magnetic hyperthermia

To analyse the magnetic hyperthermia efficiency, the nanocubes were exposed to an alternating field (H = 17 kA/m, frequency, f = 183 kHz). It is worth emphasizing that these conditions are rather mild, as the product H·f ($3.1 \cdot 10^9$ A·m^{-1}·s^{-1}) is clearly below the safety limit for clinical applications (*i.e.*, $5 \cdot 10^9$ A·m^{-1}·s^{-1}). Despite the moderate field, the heat generated after 5 min of magnetic actuation produced large temperature increases, ΔT, for the three particle sizes. It is worth highlighting that, under identical field and iron concentration (6.9 mg Fe/mL; 123.6

mM), a size increase of just 2 nm (from 13.3 nm to 15.3 nm) induced an 85% enhancement of the ΔT (**Fig. 6**). Moreover, the size increase up to 19 nm generated an additional 30% raise in the ΔT, which reached 65°C (**Fig. 6**).[16] The specific absorption rate (SAR) values exhibited a similar trend, showing a non-linear increase with the cube size. For example, an increase of only 2 nm in the particle size (from 13.3 to 15.3 nm) generates a 65 W/g gain in SAR, while an increase of 4 nm from 15.3 to 19.3 nm only leads to an increase of 17 W/g. Correspondingly, the intrinsic loss power (ILP) values obtained from the SAR were 2.08, 3.31 and 3.63 $nH \cdot m^2 \cdot kg^{-1}$ for the 13.3, 15.3 and 19.3 nm cubes, respectively. The non-linear SAR/ILP evolution is most likely linked to the transition between superparamagnetic and blocked states in the particles that was observed at a size of about 16 nm.[17,18] Namely, the drastic increase in ΔT between the 13 and 15 nm samples is probably related to the fact that the 15 nm nanocubes are very close to becoming ferrimagnetic at room temperature. Hence, the application of an alternating field should induce considerable hysteresis losses in these particles. Interestingly, the ΔT and SAR values of the commercial Fe_3O_4 spherical particles, with a volume (5553 nm^3) slightly larger than the 15 nm cubes (3582 nm^3), measured in the same conditions, are considerably worse than those of the nanocubes (**Fig. 6**). In fact, the ILP of the spherical nanoparticles, 1.1 $nH \cdot m^2 \cdot kg^{-1}$, is only one third of the one for the 15 nm nanocubes. Additionally, the ILP values of the nanocubes are also higher than the reported ones for commercially available Fe-based ferrofuids[19] and are comparable with other cubic iron oxide nanoparticles, which is an appealing result in view of the very mild conditions used in our study.[12,20,21] The results highlight the importance of the anisotropic morphology, good crystallinity, nanometric control of the size and lack of agglomeration to optimize the response for magnetic hyperthermia applications.[22,23]
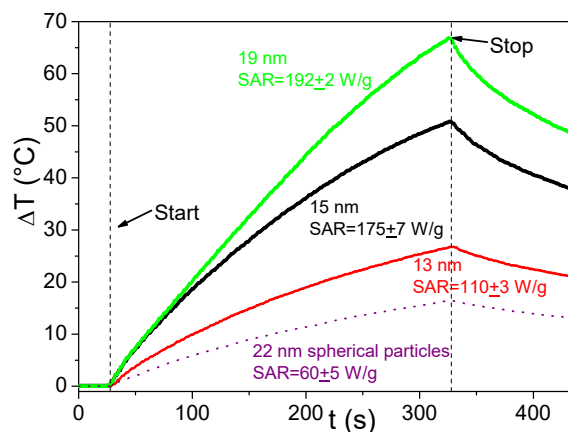
Figure 6. Temperature increase as a function of time for the different nanocubes and the commercial spherical particles exposed to an alternating magnetic field (17 kA/m – 183 kHz). "Start" and "Stop" indicate the beginning and the end of the application of the magnetic field.

Some experiments were conducted using nanorods (40x6 nm; 1131 nm^3) as well, which showed a SAR value of 140 W/g at 471 KHz and 14 kA/m (ILP = 1.45 nH·m^2·kg^{-1}). These values are intermediate between those obtained by cubes and spheres and relatively modest, especially if one considers that it has been reported in literature that nanorods show much better heating power compared to cubes and spheres.[24] However, it is important to mention that these nanorods were coated with DMSA, whereas in the experiments with cubes and spheres the particles were coated with amphiphilic polymers, ensuring colloidal stability. The lack of strong stabilizing forces in the case of magnetic nanorods can be particularly dramatic, due to their prominent dipolar interactions.[25] Thus, the higher degree of aggregation is likely the explanation for the low heating power, as it has been reported that uncontrolled aggregation can affect the magnetic hyperthermia properties.[23] More detailed studies of the coating influence are planned for the future.

4.2 Photothermia

Although most of the uses of iron oxides in biomedicine are based on their magnetic properties, in recent years there has been an increased interest in exploiting their optical properties for biomedical applications.[26] For example, they show a great potential as nanoheaters in photothermal therapy, where laser light is locally converted into heat to destroy diseased malignant cells. Most of the work in photothermal therapy in iron oxides and other materials (*e.g.*, Au nanoparticles) has been carried out using near infrared radiation since in this range light can penetrate deeper in tissues (*i.e.*, biological window). The ranges of wavelengths that can be used for biomedical applications are those belonging to the so-called biological windows

of the electromagnetic spectrum, which are two regions where the biological tissues such as blood, skin and fat have a reduced absorption (**Fig. 7a**). Although usually studies have been carried out using wavelengths around $\lambda \sim 800$ nm (*i.e.*, first biological window, $\lambda \sim 650\text{-}950$ nm), in recent years there has been an increased interest in using the second biological window ($\lambda \sim 1000\text{-}1350$ nm). Actually, this range offers several advantages over the first optical window for biomedical uses: (i) the maximum permissible exposure (MPE) is higher for lasers in the second biological window than in the first one (**Fig. 7b**), allowing longer exposures to radiation without damage to heathy tissues and (ii) light penetrates considerably deeper into skin for at $\lambda \sim 1064$ nm (the typical λ in the second biological window) than for $\lambda \sim 808$ nm (the typical λ in the first biological window).[27] However, the range of materials suitable for photothermal therapies in the second biological window is somewhat limited.
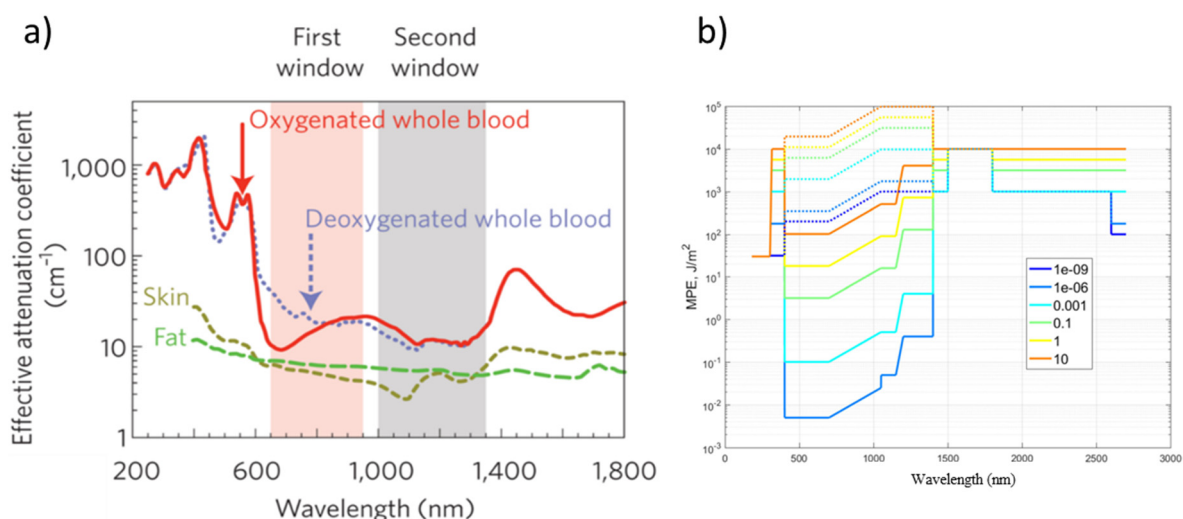

Figure 7. a) Absorbance spectra of different biological tissues in the UV-Vis-NIR regions.[28] b) MPE as a function of the wavelength for some exposure times. Solid lines refer to eye MPE, while dotted lines refer to skin MPE. The time in the legend is expressed in seconds.[29]

So far, the interest in the photothermal properties of both Fe_3O_4 and $\gamma\text{-}Fe_2O_3$ has been mainly focused in the first biological window.[21,30,31] Interestingly, although both iron oxides are very similar from a structural point of view, their optical properties differ strongly. Therefore, we conducted a detailed study to determine: i) which of them is the best material for photothermal therapy; ii) the optimal wavelength to excite the particles; and iii) the optical heating performance of our material and how powerful is it if compared with other popular optical heaters. For these purposes, a comprehensive spectroscopic study was carried out (which

included simulations and experimental data) and heating measurements using different laser sources.

For comparison, maghemite particles were prepared. The synthesis was carried using the polyol method,[9] which yielded 10 nm-diameter γ-Fe$_2$O$_3$ nanoparticles. The procedure was carried out as follows: iron acetate (4.3 g; 25 mmol) was dissolved in diethylene glycol (250 ml) and distilled water (0.45 mL). The solution was then refluxed with mechanical stirring for 3 hours. The mixture was cooled to room temperature and centrifugation gave a black magnetic powder, which was washed several times with hot water to obtain the maghemite form of iron oxide (γ-Fe$_2$O$_3$).[32] Due to their small size, these nanoparticles are very easily oxidized, especially if this reactivity is enhanced by heating at relatively mild temperatures (>50 °C).[33]

The TEM images of the γ-Fe$_2$O$_3$ nanoparticles indicate a spherical structure with diameter of 9.5+2.2 nm and a moderately narrow particle size distribution with a PDI of 19% (**Fig. 8a,b**). The x-ray diffraction pattern shows that the sample is a cubic spinel (**Fig. 8c**). However, the absence of a peak at 18° indicates that γ-Fe$_2$O$_3$ is the predominant iron oxide phase rather than Fe$_3$O$_4$.
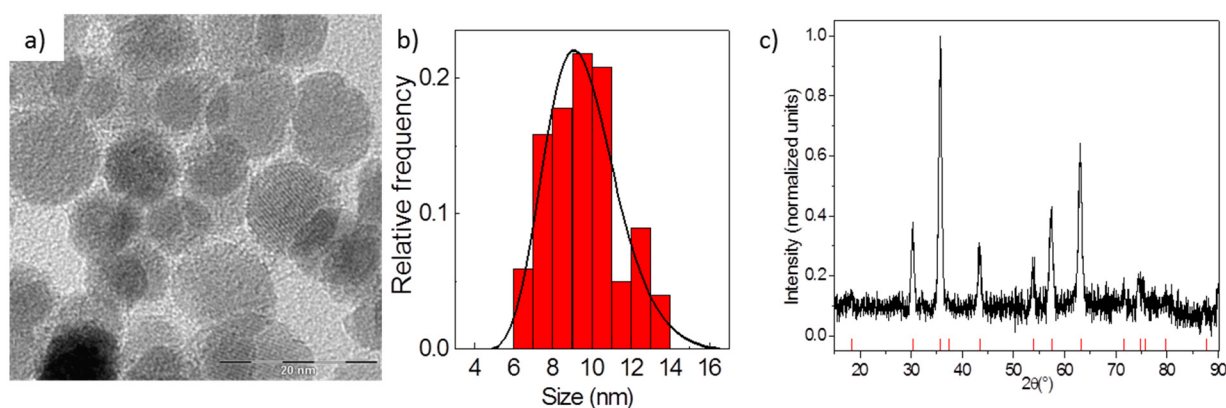

Figure 8. a) TEM image of the maghemite nanoparticles and b) its corresponding particle size distribution, fitted to a log-normal function. The scale bar corresponds to 20 nm; c) X-ray diffraction pattern of the γ-Fe$_2$O$_3$ nanoparticles (black line) compared to a γ-Fe$_2$O$_3$ reference (red lines).

Spectroscopic study

It is worth to emphasize that while γ-Fe_2O_3 is a semiconductor with a band gap of 2.0 eV, Fe_3O_4 is a half-metal with a band gap of 0.2 eV.[34,35] Moreover, in Fe_3O_4 charge-transfer transitions between Fe^{2+} and Fe^{3+} ions provide a wide an intense absorption band in the NIR, which is not present in γ-Fe_2O_3.[36,37] To have a better understanding of the optimal material and wavelength for photothermia between the two oxides, we carried out optical absorption (C_{abs}) and scattering (C_{scat}) cross sections simulations based on their bulk optical properties (**Fig. 9a,b**).[35,37,38] Remarkably, the simulations showed striking differences between the γ-Fe_2O_3 and Fe_3O_4 particles. In particular, while a rapid decrease in C_{abs} is observed for γ-Fe_2O_3 in the NIR, the C_{abs} increases considerably for Fe_3O_4 in the second NIR biological window range. It is worth noting that the C_{abs} of Fe_3O_4 shows a dip in the 700-800 nm region, which covers the largest part of the first biological window. In addition, it can be observed that the ratio between absorption and scattering (C_{abs}/ C_{scat}) is higher for Fe_3O_4 than for Fe_2O_3, especially for longer wavelengths, such as those in the second biological window (**Fig. 9b**). Two relevant consequences are expected for the optically induced heating form the simulated C_{abs} results: (i) poor efficiency for γ-Fe_2O_3 in the whole NIR range and (ii) a much higher efficiency for Fe_3O_4, with an important enhancement in the second biological window, a region which has been far less exploited than the first biological window despite its potential advantages.[28]

To confirm the results of the simulations, the absorbance spectra of Fe_3O_4 (nanocubes of 26 $\pm$ 2 nm edge length) and γ-Fe_2O_3 particles nanoparticles were acquired and compared (**Fig. 9c**). The experimental data clearly confirmed the presence of a strong absorption band for Fe_3O_4 in the second biological window and a dip in the $\lambda \sim 800$ nm range. Although, considering only the absorption spectrum of magnetite, it might seem appealing to work at long wavelengths (*i.e.*, 1200 nm and beyond), because biological tissues are mainly made of water, it is also important to consider the absorption of radiation due to water molecules. Therefore it is crucial to find to find the optimal region where the absorption of iron oxides is maximized respect to that of water, as working in such regions would allow achieving a maximum absorbance of the nanoparticles with a minimum heating of the nearby healthy tissues. Consequently, the spectrum of water was subtracted from the absorption spectra of both maghemite and magnetite to obtain the differential spectra, which revealed a local maximum in the region from 1060-1070 nm (**Fig. 9d**). Interestingly, there are commercially available lasers in this region, specifically at 1064 nm. Indeed, the 1.5-fold increase in the absorbance of Fe_3O_4 from $\lambda \sim 808$

nm (which is a typical laser wavelength used for photothermal treatments in the first window) to $\lambda \sim 1064$ nm highlights the high potential of the second biological window for biomedical applications using Fe_3O_4. In contrast, the absorbance of γ-Fe_2O_3 at $\lambda \sim 1064$ nm is less than half that of Fe_3O_4, while they have similar absorbance values at $\lambda \sim 808$ nm. Furthermore, working at 1064 nm represents some additional advantages, since i) the MPE is much higher than at 808 nm (1.0 and 0.3 W/cm^2, respectively);[39] and ii) the optical penetration in skin tissues for lasers with wavelengths in the 1064-1070 nm region is maximized (**Fig. 9e**).
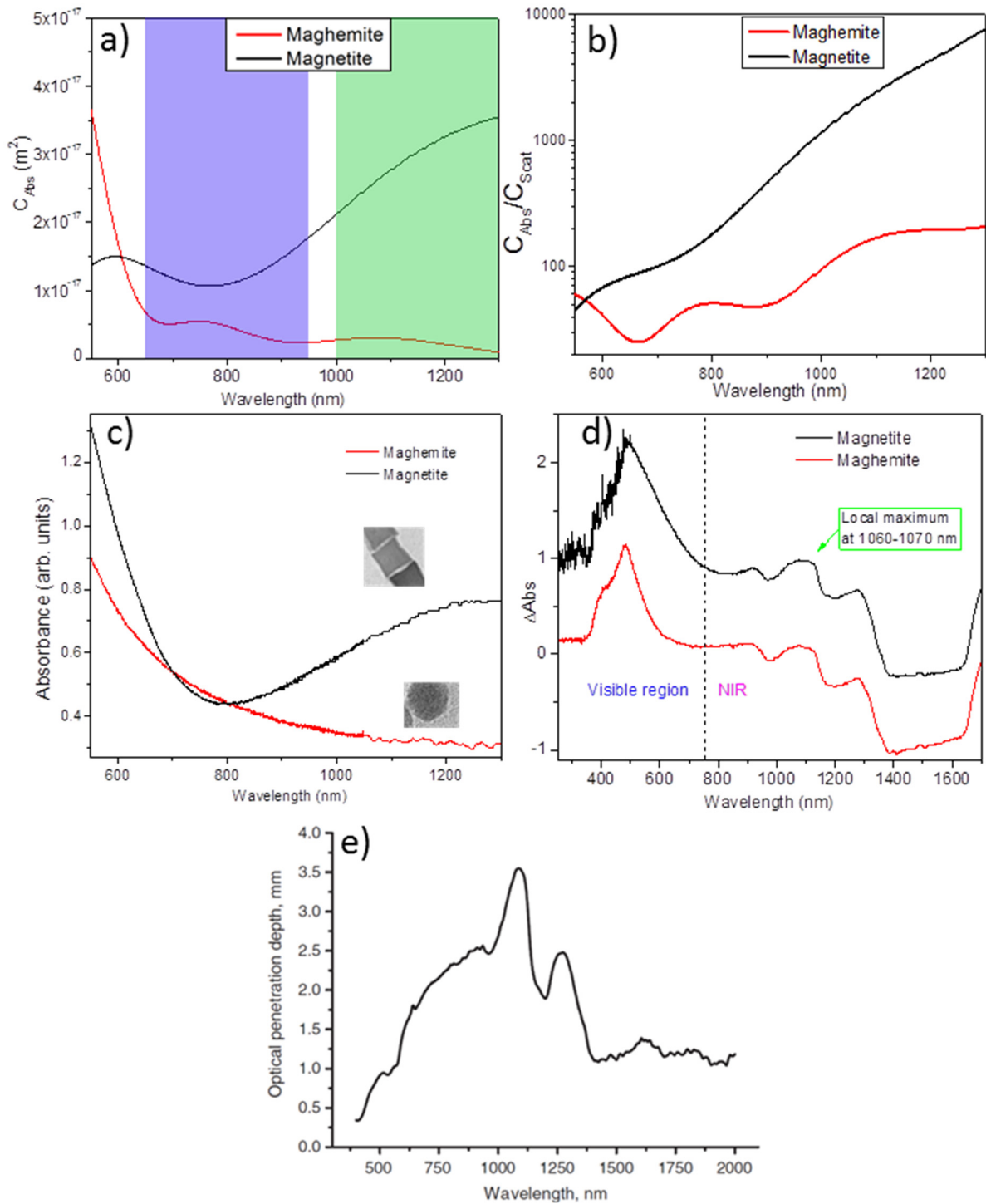
Figure 9. a) Simulated absorption spectra for magnetite (black) and maghemite (red) with regions corresponding to either the first (blue area) and second biological windows (green area) ; b) Simulated absorption to scattering ratio (C_{Abs}/C_{Scat}) as a function of the wavelength for magnetite (black) and maghemite (red); c) experimental visible and NIR absorption spectra of magnetite (black) and maghemite (red); d) differential spectra of magnetite (black) and maghemite (red) respect to water; e) Optical penetration depth (in mm) of light into skin at different wavelengths.[27]

Heating performance

The main conclusions from the spectroscopic study are that i) magnetite is a much more powerful radiation absorber than maghemite (not only because the absorbance spectrum shows higher values but also because of the reduced scattering) and ii), the wavelengths between 1060-1070 nm represent an optimal region for the heat generation, as the Fe_3O_4 absorption spectrum shows a maximum respect to water. Hence, to establish the correlation between higher absorbance and improved heating capabilities of the nanoparticles, photothermal experiments were performed for both γ-Fe_2O_3 and Fe_3O_4 nanoparticles using lasers in the first ($\lambda \sim 808$ nm) and second ($\lambda \sim 1064$ nm) biological windows. The temperature vs time profiles evidence that Fe_3O_4 is a much more powerful optical heater than γ-Fe_2O_3 at $\lambda \sim 808$ nm and the differences between both materials become even more evident at $\lambda \sim 1064$ nm (**Fig. 10a**). Interestingly, the calculation of their photothermal conversion efficiencies (**Fig. 10b**) showed that the differences in the heating capacity of γ-Fe_2O_3 and Fe_3O_4 are not only because of the difference in absorption between both materials, but also to the reduced scattering of both particles at 1064 nm and especially for Fe_3O_4. In fact, the simulations revealed that a higher absorption/scattering ratio in Fe_3O_4 could be the origin of the differences in the heating efficiencies. Therefore, the heating efficiencies of γ-Fe_2O_3 and Fe_3O_4 shown in **Fig. 10b** evidence that Fe_3O_4 at $\lambda \sim 1064$ nm is the best choice for photothermal treatments using iron oxides. These results highlight the importance of combining high absorption cross-section and small isolated nanoparticle instead of particle clusters for minimizing the light scattering that does not contribute to heating, thereby maximizing the photothermal conversion efficiency. Notably, the heating efficiency for magnetite at $\lambda \sim 1064$ nm (0.69) is even slightly higher than gold nanorods (0.67), that have been pointed out by some authors as the most efficient plasmonic heaters.[40] This is also due to the negligible scattering of single Fe_3O_4 nanocubes compared to plasmonic nanoparticles at resonance. Another possible reason for the high efficiency of the nanocubes could be the high crystallinity: these cubes were synthesized using a methodology developed in our group[41] and that has been proven to yield highly crystalline particles which, according to some authors, could improve the photothermal efficiency of iron oxide nanoparticles.[42]
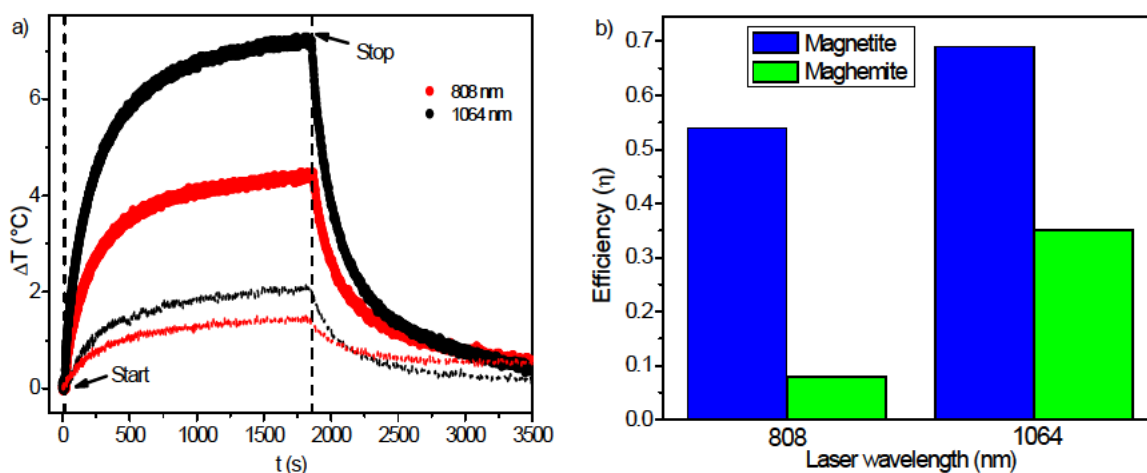
Figure 10. a) Heating curves using 808 and 1064 nm lasers (red and black curves respectively) for both magnetite (solid lines) and maghemite particles (dashed line). "Start" and "Stop" indicate the beginning and the end of the application of the laser irradiation; b) Comparison of the heating efficiencies for magnetite (blue) and maghemite particles (green) upon heating with either 808 or 1064 nm lasers.

In vitro hyperthermia treatment on cells

To confirm the potential of the Fe_3O_4 nanocubes as heat mediators for hyperthermia we have carried out an *in vitro* study on cancerous HeLa cells. For these tests, photothermia as a stand-alone technique was chosen, instead of its combination with magnetic hyperthermia. The main reason to discard magnetic hyperthermia is that it requires much higher concentrations of nanoparticles than photothermia to reach the same temperature, *i.e.*, for the photothermal heating performance trials, [Fe] = 4 mM was enough, whereas magnetic hyperthermia required [Fe] = 124 mM. Another important reason is that, despite the performance of the particles as magnetic heaters is acceptable, the heating capacity of the particles can be importantly affected after being endocytosed, since due to the tight confinement within the cells after internalisation, the magnetic properties of the particles undergo dramatic changes because of aggregation, which can decrease their ability to heat under the application of a magnetic field.[23] Indeed, some studies have reported a 15-fold decay in the magnetic heating power for particles after being internalised by cells.[43] Conversely, some researchers have suggested that for photothermal therapies, the endosomal sequestration could have a boosting effect on the optical heating capacity.[30]

For the *in vitro* trials, cells were incubated with nanoparticles at an iron concentration of [Fe] = 4 mM for 1 hour and carefully washed with culture medium. Subsequently, they irradiated by a 1064 nm laser for 10 minutes. The applied intensity was 0.3 W/cm^2, *i.e.*, below the safety limit for human tissues of 0.33 W/cm^2 for a 808 nm laser, which so far is the most commonly

employed laser for photothermal therapies.[44] To optimize the hyperthermia treatment, cells were initially thermalized at 37°C and were withdrawn from the thermostat immediately before irradiation. Therefore, the temperature elevation was observed from close to 37 °C to the plateau reached after 10 min irradiation. After the treatment, the number of cells as well as their viability was measured using Trypan Blue assay. Control experiments with cells without laser application and without nanoparticles were also carried out. Since water (and cell medium) slightly absorbs in the NIR range a control experiment with light irradiations but without nanoparticles was carried out. Irradiation alone produced an increase in the temperature of the cell culture of 4°C and a cell viability decay of around $3.0 \pm 1.2\%$ with respect to the control without irradiation and with no particles. The presence of nanoparticles alone, *i.e.*, without irradiation, caused a viability decay of around $9 \pm 1\%$. However, the application of irradiation in the presence of nanocubes generated a fast T increase of up to 21°C (**Fig. 11a**), which led to a viability decrease of $84 \pm 2\%$, which clearly confirms the ability of the 1064 nm laser irradiation when using Fe_3O_4 nanocubes to induce significant cell death (**Fig. 11b**).
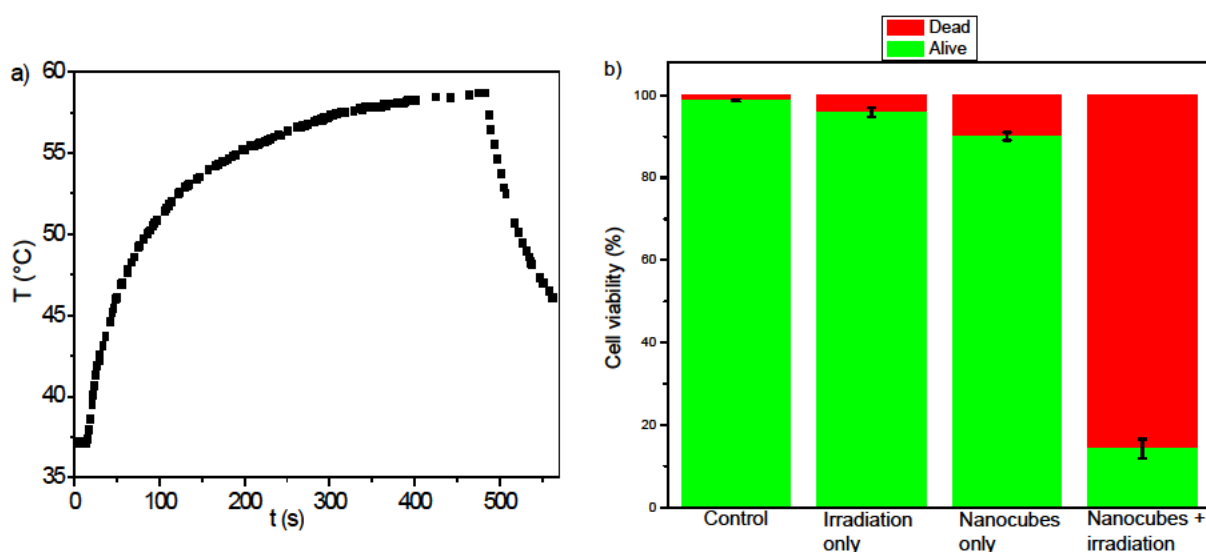
Figure 11. a) Heating curve of the cells incubated with nanocubes during the photothermal treatment and b) cell viability in the different conditions.

5. NANOTHERMOMETRY

A key aspect to gain control in photothermia therapies is the possibility to have a tight real-time control of the temperature changes generated during the treatment to selectively kill malignant cells by apoptosis and to prevent damage to the nearby healthy tissue. Given the anisotropic shape of the Fe_3O_4 nanocubes and their magnetic character, the particles are

excellent candidates for opto-magnetic modulation. Interestingly, the nanocubes transmittance spectrum of linearly polarized light in the visible and NIR ranges shows an important decrease under the application of a low amplitude constant magnetic field (40 Oe) (**Figure 12a**), even though the geometric anisotropy of the cubes is moderate compared to other structures such as rods. Moreover, this change becomes more obvious for longer wavelengths (*i.e.,* in the second biological window). This feature was exploited for simultaneous heating/thermometry studies in-situ using only the 1064 nm laser. Namely, upon the application of a magnetic field, H, ferrimagnetic nanoparticles rotate to align their magnetic moments parallel to H, which induces changes in the transmittance. When H is alternating, the speed at which the particles can align with H is limited by the viscosity of the medium, which is evidenced by a phase lag (*i.e.*, a phase shift) between the changes in transmittance and oscillation of H at a given frequency. Since the viscosity of the medium decreases as the temperature increases, the viscous drag is smaller at higher temperatures and consequently the phase shift between the transmittance an H also decreases. Thus, the changes in phase shift can be used to monitor the temperature of the dispersion after proper calibration.[3] As can be seen in **Fig. 12 b**, the phase shift clearly changes as the λ ∼ 1064 nm laser is switched on and off, *i.e.*, as the photothermal process upon laser irradiation starts and ends. Importantly, the temperature measured by an infrared thermometer and the phase shift are clearly correlated. Note that the phase shift change is initially faster than the temperature change registered by infrared thermometry. The lag between both ways of thermometry is due to the fact that nanocubes are measuring the local heating of the liquid in the immediate surrounding of the particles, which is very fast, while in the case of the infrared thermometry the heating must first diffuse over the whole liquid and reach the surface, adding some delay. The capability to locally measure the temperature changes in-situ an in real time is key for the future photothermal *in vivo* applications, since it will allow a more accurate control of the treatments, thus minimizing any possible side effects.
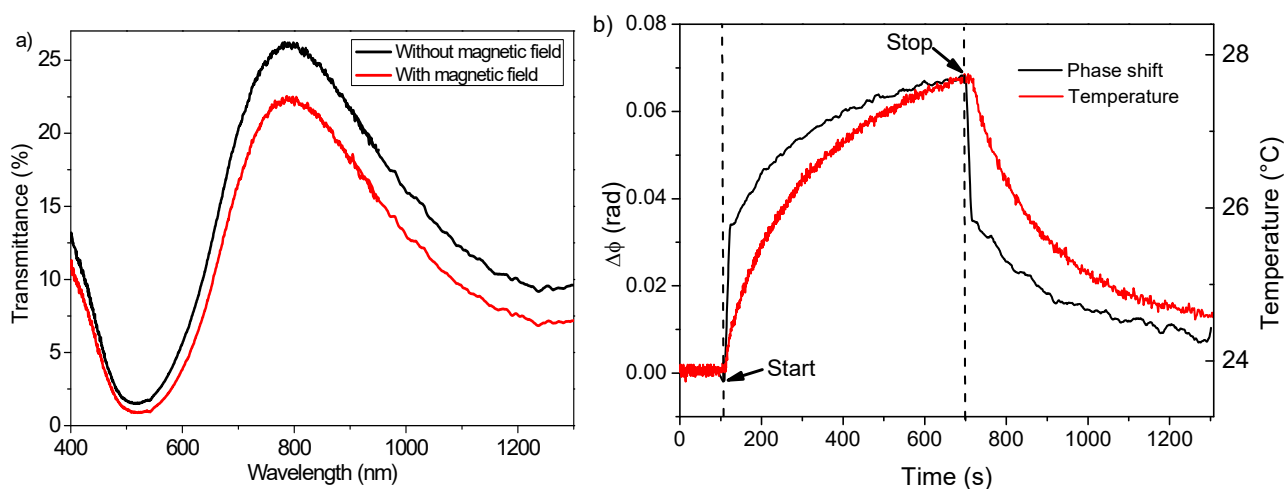
Figure 12. a) Transmittance spectra of the nanocubes with and without application of a dc-magnetic field (red and black curves, respectively); and b) phase lag of the nanocubes rotation (black curve) and infrared monitored temperature (red curve) vs time. "Start" and "Stop" indicate the beginning and the end of the application of the laser irradiation.

6. CONCLUSIONS

In this chapter, the biocompatibility and low cytotoxicity of the nanoparticles synthesized in this work has been validated. Unfortunately, although experiments to target malignant cells using transferrin were attempted, the results were not satisfactory, likely because of aggregation. However, it is believed that this issue could be easily overcome if the DMSA coating was replaced by an amphiphilic coating, which could ensure the colloidal stability despite the aggressive conditions of the functionalisation process. Nevertheless, the particles were successfully internalised by the cells despite the relatively short incubation times. Moreover, they have proven to be suitable as a diagnostic tool, yielding r_2 relaxivity values that represent an important improvement with respect to other iron oxide-based commercial products, thus reinforcing the potential interest of shape anisotropic particles.

As for the therapeutic potential, the nanoparticles showed a good heating capacity in magnetic hyperthermia, with large T increases despite the mild conditions of the applied magnetic fields. However, it is in optical heating where they have turned out to show a great potential for hypothetical real clinic situations. Based on a thorough spectroscopic study, it has been shown that magnetite should be the preferred iron oxide for photothermal applications in medicine, as it provides higher absorption values and an enhanced efficiency due to the lower scattering to absorption ratio. In addition, the second biological window, despite it is a far less explored

region, has proven to host the optimal wavelengths that should be used for photothermia using iron oxides. Owing to these findings, it has been possible to achieve great T increases with low dosages, which resulted in the massive killing of cancer cells (up to 84%) with a single session of only 10 minutes. Furthermore, thanks to its anisotropic structure, it has been possible to use the particles for *in situ* temperature sensing with a faster response than other techniques such as infrared thermometry. This could potentially ease the precise, real-time, temperature monitoring during future photothermal sessions. All of these results reinforce the idea of exploiting anisotropy to design new nanotheranostic tools, allowing multimodal applications (diagnosis, therapy and temperature sensing) using a single and versatile material.

7. REFERENCES

(1)   Högemann-Savellano, D.; Bos, E.; Blondet, C.; Sato, F.; Abe, T.; Josephson, L.; Weissleder, R.; Gaudet, J.; Sgroi, D.; Peters, P. J.; Basilion, J. P. The Transferrin Receptor: A Potential Molecular Imaging Marker for Human Cancer. *Neoplasia* **2003**, 5 (6), 495–506.

(2)   Shen, S.; Kong, F.; Guo, X.; Wu, L.; Shen, H.; Xie, M.; Wang, X.; Jin, Y.; Ge, Y. CMCTS Stabilized Fe_3O_4 Particles with Extremely Low Toxicity as Highly Efficient Near-Infrared Photothermal Agents for in Vivo Tumor Ablation. *Nanoscale* **2013**, 5 (17), 8056-8066.

(3)   Li, Z.; Lopez-Ortega, A.; Aranda-Ramos, A.; Tajada, J. L.; Sort, J.; Nogues, C.; Vavassori, P.; Nogues, J.; Sepulveda, B. Simultaneous Local Heating/Thermometry Based on Plasmonic Magnetochromic Nanoheaters. *Small* **2018**, 14 (24), 1800868.

(4)   Shen, S.; Wang, S.; Zheng, R.; Zhu, X.; Jiang, X.; Fu, D.; Yang, W. Magnetic Nanoparticle Clusters for Photothermal Therapy with near-Infrared Irradiation. *Biomaterials* **2015**, 39, 67–74.

(5)   Lee, J. H.; Ju, J. E.; Kim, B. Il; Pak, P. J.; Choi, E. K.; Lee, H. S.; Chung, N. Rod-Shaped Iron Oxide Nanoparticles Are More Toxic than Sphere-Shaped Nanoparticles to Murine Macrophage Cells. *Environ. Toxicol. Chem.* **2014**, 33 (12), 2759–2766.

(6)   Lee, N.; Yoo, D.; Ling, D.; Cho, M. H.; Hyeon, T.; Cheon, J. Iron Oxide Based Nanoparticles for Multimodal Imaging and Magnetoresponsive Therapy. *Chem. Rev.* **2015**, 115 (19), 10637–10689.

(7)   Puertas, S.; Batalla, P.; Moros, M.; Polo, E.; del Pino, P.; Guisán, J. M.; Grazú, V.; de la Fuente, J. M. Taking Advantage of Unspecific Interactions to Produce Highly Active Magnetic Nanoparticle−Antibody Conjugates. *ACS Nano* **2011**, 5 (6), 4521–4528.

(8)   Scientific, T. F. Carbodiimide Crosslinker Chemistry. (Accessed Jul 31, 2019) https://www.thermofisher.com/es/es/home/life-science/protein-biology/protein-biology-learning-center/protein-biology-resource-library/pierce-protein-methods/carbodiimide-crosslinker-chemistry.html

(9)   Piraux, H.; Hai, J.; Verbeke, P.; Serradji, N.; Ammar, S.; Losno, R.; Ha-Duong, N.-T.; Hémadi, M.; El Hage Chahine, J.-M. Transferrin Receptor-1 Iron-Acquisition Pathway — Synthesis, Kinetics, Thermodynamics and Rapid Cellular Internalization of a Holotransferrin–maghemite Nanoparticle Construct. *Biochim. Biophys. Acta - Gen. Subj.* **2013**, 1830 (8), 4254–4264.

(10)   Honig, D.E., Near-infrared Analysis, *Anal. Instrum.* **1985**. 14(1), 1–62.

(11)   Salvati, A.; Pitek, A. S.; Monopoli, M. P.; Prapainop, K.; Bombelli, F. B.; Hristov, D. R.; Kelly, P. M.; Åberg, C.; Mahon, E.; Dawson, K. a. Transferrin-Functionalized Nanoparticles Lose Their Targeting Capabilities When a Biomolecule Corona Adsorbs on the Surface. *Nat. Nanotechnol.* **2013**, 8 (2), 137–143.

(12)   Bradford, M. M. A Rapid and Sensitive Method for the Quantitation of Microgram Quantities of Protein Utilizing the Principle of Protein-Dye Binding. *Anal. Biochem.* **1976**, 72 (1-2), 248–254.

(13)   Lee, N.; Choi, Y.; Lee, Y.; Park, M.; Moon, W. K.; Choi, S. H.; Hyeon, T. Water-Dispersible Ferrimagnetic Iron Oxide Nanocubes with Extremely High r_2 Relaxivity for Highly Sensitive in Vivo MRI of Tumors. *Nano Lett.* **2012**, 12 (6), 3127–3131.

(14)   Lisjak, D.; Mertelj, A. Anisotropic Magnetic Nanoparticles: A Review of Their Properties, Syntheses and Potential Applications. *Prog. Mater. Sci.* **2018**, 95, 286–328.

(15) Nikitin, A. A.; Khramtsov, M. A.; Savchenko, A. G.; Abakumov, M. A.; Mazhuga, A. G. Anisotropic Iron-Oxide Nanoparticles for Diagnostic MRI: Synthesis and Contrast Properties. *Pharm. Chem. J.* **2018**, 52 (3), 231–235.

(16) Hergt, R.; Dutz, S. Magnetic Particle Hyperthermia—biophysical Limitations of a Visionary Tumour Therapy. *J. Magn. Magn. Mater.* **2007**, 311 (1), 187–192.

(17) Guardia, P.; Di Corato, R.; Lartigue, L.; Wilhelm, C.; Espinosa, A.; Garcia-Hernandez, M.; Gazeau, F.; Manna, L.; Pellegrino, T. Water-Soluble Iron Oxide Nanocubes with High Values of Specific Absorption Rate for Cancer Cell Hyperthermia Treatment. *ACS Nano* **2012**, 6 (4), 3080–3091.

(18) Lacroix, L.-M.; Malaki, R. B.; Carrey, J.; Lachaize, S.; Respaud, M.; Goya, G. F.; Chaudret, B. Magnetic Hyperthermia in Single-Domain Monodisperse FeCo Nanoparticles: Evidences for Stoner–Wohlfarth Behavior and Large Losses. *J. Appl. Phys.* **2009**, 105 (2), 023911.

(19) Kallumadil, M.; Tada, M.; Nakagawa, T.; Abe, M.; Southern, P.; Pankhurst, Q. A. Suitability of Commercial Colloids for Magnetic Hyperthermia. *J. Magn. Magn. Mater.* **2009**, 321 (10), 1509–1513.

(20) Marcelo, G.; Catalina, F.; Bruvera, I.; Marquina, C.; Goya, G. Specific Power Absorption of Silica-Coated Magnetite Cubes. *Curr. Nanosci.* **2014**, 10 (5), 676–683.

(21) Espinosa, A.; Di Corato, R.; Kolosnjaj-Tabi, J.; Flaud, P.; Pellegrino, T.; Wilhelm, C. Duality of Iron Oxide Nanoparticles in Cancer Therapy: Amplification of Heating Efficiency by Magnetic Hyperthermia and Photothermal Bimodal Treatment. *ACS Nano* **2016**, 10 (2), 2436–2446.

(22) Keisari, Y. *Tumor Ablation*; Keisari, Y., Ed.; Springer Netherlands: Dordrecht, 2013.

(23) Guibert, C.; Dupuis, V.; Peyre, V.; Fresnais, J. Hyperthermia of Magnetic Nanoparticles: Experimental Study of the Role of Aggregation. *J. Phys. Chem. C* **2015**, 119 (50), 28148–28154.

(24) Das, R.; Alonso, J.; Nemati Porshokouh, Z.; Kalappattil, V.; Torres, D.; Phan, M.-H.; Garaio, E.; Garcia, J. A.; Sánchez Llamazares, J. L.; Srikanth, H. Tunable High Aspect Ratio Iron Oxide Nanorods for Enhanced Hyperthermia. *J. Phys. Chem. C* **2016**, 10086–10093. (25) Son, S. J.; Reichel, J.; He, B.; Schuchman, M.; Lee, S. B. Magnetic Nanotubes for Magnetic-Field-Assisted Bioseparation, Biointeraction, and Drug Delivery. *J. Am. Chem. Soc.* **2005**, 127 (20), 7316–7317.

(26) Huang, W.; Tsai, P.; Chen, Y. Multifunctional Fe_3O_4@Au Nanoeggs as Photothermal Agents for Selective Killing of Nosocomial and Antibiotic-Resistant Bacteria. *Small* **2009**, 5 (1), 51–56.

(27) Bashkatov, A. N.; Genina, E. A.; Kochubey, V. I.; Tuchin, V. V. Optical Properties of Human Skin, Subcutaneous and Mucous Tissues in the Wavelength Range from 400 to 2000 nm. *J. Phys. D. Appl. Phys.* **2005**, 38 (15), 2543–2555.

(28) Smith, A. M.; Mancini, M. C.; Nie, S. Bioimaging: Second Window for in Vivo Imaging. *Nat. Nanotechnol.* **2009**, 4 (11), 710–711.

(29) Angelini, F.; Colao, F. Optimization of Laser Wavelength, Power and Pulse Duration for Eye-Safe Raman Spectroscopy. *J. Eur. Opt. Soc. Publ.* **2019**, 15 (1), 2.

(30) Espinosa, A.; Kolosnjaj-Tabi, J.; Abou-Hassan, A.; Plan Sangnier, A.; Curcio, A.; Silva, A. K. A.; Di Corato, R.; Neveu, S.; Pellegrino, T.; Liz-Marzán, L. M.; Wilhelm, C. Magnetic (Hyper)Thermia or Photothermia? Progressive Comparison of Iron Oxide and Gold Nanoparticles Heating in Water, in Cells, and In Vivo. *Adv. Funct. Mater.* **2018**, 28 (37), 1803660.

(31) Hai, J.; Piraux, H.; Mazarío, E.; Volatron, J.; Ha-Duong, N. T.; Decorse, P.; Lomas, J. S.; Verbeke, P.; Ammar, S.; Wilhelm, C.; El Hage Chahine, J.-M.; Hémadi, M. Maghemite Nanoparticles Coated with Human Serum Albumin: Combining Targeting by the Iron-Acquisition Pathway and Potential in Photothermal Therapies. *J. Mater. Chem. B* **2017**, 5 (17), 3154–3162.

(32) Piraux, H.; Hai, J.; Gaudisson, T.; Ammar, S.; Gazeau, F.; El Hage Chahine, J. M.; Hémadi, M. Transferrin-Bearing Maghemite Nano-Constructs for Biomedical Applications. *J. Appl. Phys.* **2015**, 117 (17), 17A336.

(33)   Tartaj, P.; González-Carreño, T.; Ferrer, M. L.; Serna, C. J. Metallic Nanomagnets Randomly Dispersed in Spherical Colloids: Toward a Universal Route for the Preparation of Colloidal Composites Containing Nanoparticles. *Angew. Chemie Int. Ed.* **2004**, 43 (46), 6304–6307.

(34)   Litter, M. I.; Blesa, M. A. Photodissolution of Iron Oxides. IV. A Comparative Study on the Photodissolution of Hematite, Magnetite, and Maghemite in EDTA Media. *Can. J. Chem.* **1992**, 70 (9), 2502–2510.

(35)   Liu, H.; Di Valentin, C. Band Gap in Magnetite above Verwey Temperature Induced by Symmetry Breaking. *J. Phys. Chem. C* **2017**, 121 (46), 25736–25742.

(36)   Kovalenko, M. V.; Bodnarchuk, M. I.; Lechner, R. T.; Hesser, G.; Schäffler, F.; Heiss, W. Fatty Acid Salts as Stabilizers in Size- and Shape-Controlled Nanocrystal Synthesis: The Case of Inverse Spinel Iron Oxide. *J. Am. Chem. Soc.* **2007**, 129 (20), 6352–6353.

(37)   Tang, J.; Myers, M.; Bosnick, K. A.; Brus, L. E. Magnetite Fe_3O_4 Nanocrystals: Spectroscopic Observation of Aqueous Oxidation Kinetics †. *J. Phys. Chem. B* **2003**, 107 (30), 7501–7506.

(38)   He, Y. P.; Miao, Y. M.; Li, C. R.; Wang, S. Q.; Cao, L.; Xie, S. S.; Yang, G. Z.; Zou, B. S.; Burda, C. Size and Structure Effect on Optical Transitions of Iron Oxide Nanocrystals. *Phys. Rev. B - Condens. Matter Mater. Phys.* **2005**, 71 (12), 125411.

(39)   *Auburn University Laser Safety Manual*; **2007**. https://cws.auburn.edu/shared/content/files/1401/laser-safety.pdf

(40)   Li, Z.; Aranda-Ramos, A.; Güell-Grau, P.; Tajada, J. L.; Pou-Macayo, L.; Lope Piedrafita, S.; Pi, F.; G. Roca, A.; Baró, M. D.; Sort, J.; Nogués, C.; Nogués, J.; Sepúlveda, B. Magnetically Amplified Photothermal Therapies and Multimodal Imaging with Magneto-Plasmonic Nanodomes. *Appl. Mater. Today* **2018**, 12, 430–440.

(41)   Muro-Cruces, J.; Roca, A. G.; López-Ortega, A.; Fantechi, E.; Del-Pozo-Bueno, D.; Estradé, S.; Peiró, F.; Sepúlveda, B.; Pineider, F.; Sangregorio, C.; Nogues, J. Precise Size Control of the Growth of Fe_3O_4 Nanocubes over a Wide Size Range Using a Rationally Designed One-Pot Synthesis. *ACS Nano* **2019**, 13 (7), 7716–7728.

(42)   Chen, H.; Burnett, J.; Zhang, F.; Zhang, J.; Paholak, H.; Sun, D. Highly Crystallized Iron Oxide Nanoparticles as Effective and Biodegradable Mediators for Photothermal Cancer Therapy. *J. Mater. Chem. B* **2014**, 2 (7), 757–765.

(43)   Plan Sangnier, A.; Preveral, S.; Curcio, A.; K. A. Silva, A.; Lefèvre, C. T.; Pignol, D.; Lalatonne, Y.; Wilhelm, C. Targeted Thermal Therapy with Genetically Engineered Magnetite magnetosomes@RGD: Photothermia Is Far More Efficient than Magnetic Hyperthermia. *J. Control. Release* **2018**, 279 (April), 271–281.

(44)   Laser Institute of America, L. I. A. ANSI Z136.1: American National Standard for Safe Use of Lasers. *SPIE Med. Imaging* **2007**, 90400Q.

CHAPTER 7: CONCLUSIONS

In this thesis, the challenge of improving the state of the art in nanotheranostics has been tackled by carefully tuning and controlling the shape anisotropy of nanostructures of iron oxide (magnetite, Fe_3O_4). It is worth emphasizing that the aim was using Fe_3O_4 nanostructures as stand-alone nanotherapeutic agents, *i.e.*, without the need of additional materials. For this purpose, the synthesis of different anisometric morphologies such as nanocubes and nanorods has been pursued.

For the synthesis of cubes, different approaches found in literature were tested. Although in all of them nanocubes could be obtained within a certain range of sizes, some problems were encountered (*e.g.*, limited range of sizes, poor control of the size distribution, low crystallinity, loss of cubicity, *etc.*) that did not allow to obtain cubes with optimal properties. Thus, we proceeded to develop our own synthesis procedure by first identifying the problems that harnessed the production of high-quality particles (*i.e.*, due to the lack of a chemically stable environment, impure precursors, *etc.*) and then using a rational approach to overcome these issues. The resulting protocol satisfied all the quality criteria and yielded particles with optimal properties in a reproducible way. Since the parameters that control the size and shape were successfully identified, it has been possible to establish some guidelines to finely tune the size as required for the different biomedical applications.

On the other hand, the controlled synthesis of nanorods was far more challenging because, due to the cubic spinel structure of Fe_3O_4, isotropic growth is favoured and hence very few of the published procedures yielded rod-like particles in a reproducible way and with optimal properties. Among all the tested approaches, only the solvothermal synthesis resulted in high quality nanoparticles. Although the original publication reported some ways to tune the size, in this work several approaches to have a more precise size and aspect ratio control have been proposed. For example, a way to tune the aspect ratio as an independent parameter has been identified (by controlling the oleic acid/sodium oleate proportion), as well as an alternative way to control the particle size by simply adjusting the pressure. Nevertheless, because the synthesis of nanocubes is simpler, faster and more reproducible, for most of the experiments in this work, cubes were used instead of rods.

The stabilisation of the synthesized nanoparticles in aqueous environments is a necessary step prior to any biomedical application. However, due to the high magnetic moment and the

177

original hydrophobic coating, this step turned out to be more complex than expected. After trying many different published approaches, it was concluded that a coating that can combines both steric and electrostatic repulsion is necessary to ensure good colloidal stability in biological media. In the process, a new way to coat particles with functionalisable lipid bilayers has been developed. However, since this protocol still requires further work, an already published protocol to coat particles with polymeric amphiphilic shells was chosen as the most convenient phase transfer procedure.

Eventually, the biomedical potential of the nanoparticles was assessed. First, the biocompatibility of the material was confirmed by measuring the cytotoxicity on human cell cultures. Although the targeting attempts did not provide satisfactory results (probably because of problems related to the colloidal stability), good cell internalisation was confirmed for all the types of particles tested. The ability of the particles to be used as a diagnostic tool was confirmed after evaluating their properties as contrast agents in MRI. Interestingly, the obtained relaxivity values are considerably superior to iron oxide-based commercial agents. As for the therapeutic capacity, the magnetic heating power was measured, resulting in moderately good values, especially if compared with spheres which are, still, the most commonly employed type of particles. These two results confirm the advantages of working with shape anisotropic nanoparticles.

Based on the combination of simulations and experimental data, it was established that Fe_3O_4 has a great potential to work also as a photothermal mediator. The existence of a unique absorption band in the second biological window, still virtually unexploited in iron oxides, provides a powerful heating capacity that resulted in the destruction of the vast majority of cancer cells in *in vitro* experiments that required only short sessions and, compared to typical magnetic hyperthermia therapies, very low dosages. Furthermore, due to the shape anisotropy, it has been possible to use the particles for real time monitoring of the local temperature, which can be useful for future thermal therapies and emphasizes, even more, the benefits of shape anisotropy.

In conclusion, the results of this thesis have led to the successful synthesis of anisotropic fully functionalisable structures with high colloidal stability and a demonstrated biocompatibility with excellent properties for multimodal purposes such as, magnetic and optical hyperthermia, contrast agents in MRI and nanothermometry, making from these particles a very versatile material for nanomedicine.

FUTURE WORK

The new growth approaches and novel applications developed in this thesis have advanced considerably the synthesis and biomedical use of anisotropic Fe_3O_4 nanoparticles. However, it must be emphasized that further work is required to make anisotropic Fe_3O_4 nanoparticles a competitive nanotheranostic tool.

For example, despite the synthesis of nanocubes is well controlled now, further work should be carried out to fully understand the mechanisms of nanorods growth to improve the reproducibility, increase the size range or shorten the reaction times.

In addition, although the polymeric coatings yielded excellent results, it would also be interesting to continue the research on the very promising and versatile coating based on bilayers. In particular, it would be interesting to test this transfer methodology with particles of different morphologies, such as nanorods of different sizes and aspect ratio, and different materials, e.g., other ferrites. It is also crucial to test the long-term stability of the bilayers as well as their resilience in biological environments. In fact, the simplicity and cost-effectiveness of this approach could ease the eventual development of commercial magnetic nanoparticles for biomedical applications in future.

Due to the lack of time, the biomedical experiments, such as magnetic and photothermal heating, using nanorods could not be carried out in a systematic manner. Thus, it would be really interesting to compare the performance of nanocubes with those of nanorods, where the tunability of its aspect ratio opens the door to many new possibilities, such as enhanced contrast capacity and, very likely, improved magnetic heating performance. Moreover, due to its high anisotropy, new ways to induce cell death are possible, such as mechanically induced death by particle rotation under the application of a dynamic magnetic field. In addition, the higher shape anisotropy may also be used for an enhanced sensing capacity in nanothermometry.

More experiments should be carried out on human cell lines to test different conditions in hyperthermia. For example, although the cell internalisation can decrease dramatically the magnetic heating capacity of particles, it could be interesting to test if an amphiphilic coating is able to avoid this effect, thus preserving their performance as heaters. The implementation of magnetic hyperthermia would push the limits of hyperthermal therapies, especially in the body regions were laser irradiation is not feasible.

To improve the hyperthermia performance (both magnetic and optic), another interesting experiment would be to find out the conditions to induce the cell death only *via* apoptosis (and not by necrosis), since this would minimize the side effects.

Finally, the next step in this this research should be performing *in vivo* experiments to demonstrate that the promising preliminary *in vitro* results still hold for animal models.

In summary, despite the innovative approaches developed and the encouraging results obtained, it is necessary to continue the work so that this kind of therapies can, hopefully, be applied some day in real clinic situations.